

# **A NEW NONLINEAR HYDROLOGIC RIVER ROUTING MODEL**

A Dissertation  
Presented to  
The Academic Faculty

By

Dong Ha Kim

In Partial Fulfillment  
Of the Requirements for the Degree  
Doctor of Philosophy in the  
School of Civil and Environmental Engineering

Georgia Institute of Technology  
December 2011

# A NEW NONLINEAR HYDROLOGIC RIVER ROUTING MODEL

Approved by:

Dr. Aris Georgakakos, Advisor  
School of Civil and Environmental  
Engineering  
*Georgia Institute of Technology*

Dr. Terry Sturm  
School of Civil and Environmental  
Engineering  
*Georgia Institute of Technology*

Dr. Jian Luo  
School of Civil and Environmental  
Engineering  
*Georgia Institute of Technology*

Dr. Huaming Yao  
School of Civil and Environmental  
Engineering  
*Georgia Institute of Technology*

Dr. Magnus Egerstedt  
School of Electrical and Computer  
Engineering  
*Georgia Institute of Technology*

Date Approved: November 08, 2011

## ACKNOWLEDGEMENTS

I wish to extend my sincere appreciation to the many people and organizations that have made this work possible during my time at the Georgia Institute of Technology. To my advisor, Dr. Aris Georgakakos, I extend my deepest gratitude for his relentless support, time, advice, and sincere criticism. Without his guidance, I would not have achieved the level of intellectual and professional development that I have. I cannot thank him enough for what he has done for me. I would also like to thank my committee members, Dr. Huaming Yao, Dr. Terry Sturm, Dr. Magnus Egerstedt, and Dr. Jian Luo, for their time and guidance. To my colleagues at the Georgia Water Resources Institute, Amy Tidwell, Martin Kistenmacher, Fred Kimaite, Christian Braneon, Chia-Jeng Chen, and Feng Zhang, I would like to extend my thanks for their friendship, moral support, and encouragement over the years. Most of all, I am thankful for the time we have spent together while all of us were going through this tough time of our lives. To Ms. Jane Chisholm, who has proofread my papers, I sincerely appreciate your support, kindness, care, and smile. To Bubhae and Sungak Buddhist monks, I am truly grateful for their spiritual wisdom that has seen me through the trying times of the past years. Foremost, to my parents, who have always been there to give me the greatest strength to persevere, I cannot begin to acknowledge the extent of their endless love, support, patience, and sacrifice.

## TABLE OF CONTENTS

<b>ACKNOWLEDGEMENTS .....</b>	<b>III</b>
<b>LIST OF TABLES .....</b>	<b>VII</b>
<b>LIST OF FIGURES .....</b>	<b>IX</b>
<b>SUMMARY .....</b>	<b>XV</b>
<b>CHAPTER 1: INTRODUCTION.....</b>	<b>1</b>
1.1 Statement of problems .....	1
1.2 Research objective .....	3
1.3 Methodology .....	3
1.4 Thesis organization .....	5
<b>CHAPTER 2: A LITERATURE REVIEW.....</b>	<b>6</b>
2.1 Hydrologic routing model.....	6
2.1.1 Kinematic wave model .....	7
2.1.2 Diffusion wave model.....	9
2.1.3 Muskingum model .....	11
2.1.4 Muskingum-Cunge model .....	13
2.1.5 Kalinin-Milyukov model .....	19
2.1.6 Multilinear cascade model .....	20
2.2 Hydraulic routing model .....	24
2.3 State-space model/optimal control theory in reservoir and river systems .....	30
2.4 Uncertainty characterization in hydrologic models .....	34

## **CHAPTER 3: A NONLINEAR HYDROLOGIC RIVER ROUTING MODEL..... 37**

3.1	Modeling framework .....	37
3.1.1	Assumptions.....	37
3.1.2	Model identification and calibration procedure .....	40
3.1.3	Discrete-time linear quadratic regulator (LQR).....	44
3.2	Application to the Equatorial Lake system.....	47
3.2.1	Approach.....	47
3.2.2	Equatorial Lakes .....	48
3.2.3	Model identification and calibration procedure .....	50
3.2.4	Results.....	54
3.2.4.1	Results for the first experiment.....	55
3.2.4.2	Results for the second experiment .....	59
3.2.4.3	Results for the experiments three through six.....	66
3.3	Application to the Main Nile .....	78
3.3.1	Main Nile .....	78
3.3.2	Model identification and calibration procedure .....	80
3.3.3	Results.....	86
3.3.4	Summary remarks on the river routing model .....	94

## **CHAPTER 4: BAYESIAN FORECASTING FRAMEWORK..... 96**

4.1	Uncertainty characterization .....	96
4.2	General BFF procedure.....	97
4.3	Theoretical background .....	102
4.3.1	Prior density in the space of transformed variates .....	102
4.3.2	Likelihood function in the space of transformed variates.....	103
4.3.3	Posterior density in the space of transformed variates.....	104
4.3.4	Prior and posterior functions in the space of the original variates.....	107
4.3.5	Predictive distribution in the space of the original variates .....	109
4.4	Application of BFF to the Equatorial Lakes .....	110
4.4.1	Introduction.....	110
4.4.2	Input uncertainty processor.....	111
4.4.2.1	Inflow forecast .....	111
4.4.2.2	Ensemble outflow forecast and distribution fitting.....	113
4.4.3	Model uncertainty processor.....	117
4.4.3.1	Marginal distributions of actual and model-estimated outflows.....	117
4.4.3.2	Normal quantile transform.....	121
4.4.3.3	Prior density in the transformed space and its validation .....	122
4.4.3.4	Likelihood function in the transformed space and its validation.....	127

4.4.4	Integrator.....	133
4.4.5	Linear one-step transition model .....	137
4.5	Application of the BFF to the Main Nile .....	141
4.5.1	Introduction.....	141
4.5.2	Input uncertainty processor.....	142
4.5.2.1	Inflow forecast .....	142
4.5.2.2	Ensemble forecast of outflow and distribution fitting .....	144
4.5.3	Model uncertainty processor.....	146
4.5.3.1	Marginal distributions of actual and model-estimated outflows.....	146
4.5.3.2	Normal quantile transform.....	150
4.5.3.3	Prior density in the space of the transformed variates and its validation.....	151
4.5.3.4	Likelihood function in the transformed space and its validation.....	155
4.5.4	Integrator.....	160
4.5.5	Linear one-step transition model .....	164
4.6	Summary remarks on the BFF .....	167

**CHAPTER 5: ACCOMPLISHMENTS, CONCLUSIONS, AND**

**RECOMMENDATIONS..... 169**

5.1	Accomplishments and Conclusions .....	169
-----	---------------------------------------	-----

5.2	Recommendations for future work .....	170
-----	---------------------------------------	-----

**APPENDIX A..... 172**

**APPENDIX B..... 182**

**APPENDIX C..... 184**

**REFERENCES..... 188**

## LIST OF TABLES

Table 3-1. Elevation ranges and active storages of the lakes (Hydromet 1992).....	50
Table 3-2. Evaluation of river routing model for the first experiment. ....	58
Table 3-3. Evaluation of river routing model for the second experiment.....	63
Table 3-4. Evaluation of river routing model for the third experiment. ....	77
Table 3-5. Evaluation of river routing model for the fourth experiment. ....	77
Table 3-6. Evaluation of river routing model for the fifth experiment. ....	77
Table 3-7. Evaluation of river routing model for the sixth experiment. ....	78
Table 3-8. Evaluation of the river routing model for the Main Nile from January 1, 1914 to December 21, 1963. ....	91
Table 3-9. Evaluation of the new river routing model for the Main Nile. ....	94
Table 4-1. $R^2$ of fitted Weibull distributions $\Pi_j(u_j)$ for $j = 1, \dots, m$ . ....	117
Table 4-2. $R^2$ of fitted Weibull distributions $\Gamma_j(u_j^*)$ for $j = 0, \dots, m$ . ....	120
Table 4-3. $R^2$ of fitted Weibull distributions $\Lambda_j(u_j)$ for $j = 1, \dots, m$ . ....	121
Table 4-4. Parameters of prior densities in the space of the transformed variates .....	123
Table 4-5. $R^2$ values of the regression lines in the normal probability plots for the prior densities in the space of the transformed variates. ....	126
Table 4-6. Parameters of the likelihood functions in the space of the transformed variates. .....	129
Table 4-7. $R^2$ values of the regression lines in the normal probability plots for the likelihood functions in the space of the transformed variates. ....	131
Table 4-8. Comparison of the ranges of $u_j^*$ from the pre-BFF and BFF distributions. The O mark indicates that the observed outflow falls within the forecasted ranges. ....	136
Table 4-9. $R^2$ of fitted Weibull distributions $\Pi_j(u_j)$ for $j = 1, \dots, m$ . ....	146

Table 4-10. $R^2$ of fitted Weibull distributions $\Gamma_j(u_j^*)$ for $j = 0, \dots, m$ .....	149
Table 4-11. $R^2$ of fitted Weibull distributions $\Lambda_j(u_j)$ for $j = 1, \dots, m$ .....	150
Table 4-12. Parameters of the prior densities in the space of the transformed variates. ....	152
Table 4-13. $R^2$ values of the regression lines in the normal probability plots for the prior densities in the space of the transformed variates.....	154
Table 4-14. Parameters of the likelihood functions in the space of the transformed variates. ....	156
Table 4-15. $R^2$ values of the regression lines in the normal probability plots for the likelihood functions in the space of the transformed variates.....	158
Table 4-16. Comparison of the ranges of $u_j^*$ from the pre-BFF and BFF distributions.....	163

## LIST OF FIGURES

Figure 2-1. Computational procedure of a multilinear model. ....	21
Figure 3-1. Schematic view of a cascaded series of M conceptual reservoirs of a river reach. ....	40
Figure 3-2. The Equatorial Lake system. ....	49
Figure 3-3. Estimated release functions for the first experiment. ....	56
Figure 3-4. Model verification during the entire time period (calibration + validation) for the first experiment. ....	57
Figure 3-5. Model verification during validation for the first experiment. ....	57
Figure 3-6. Sensitivity analysis for the first experiments. ....	59
Figure 3-7. Estimated release functions for the second experiment. ....	60
Figure 3-8. Model verification over the entire time period for the second experiment. ....	61
Figure 3-9. Correlation analysis. ....	62
Figure 3-10. Model verification during validation for the second experiment. ....	62
Figure 3-11. Release functions for the original system. ....	65
Figure 3-12. Release functions for stable systems. ....	66
Figure 3-13. 5% disturbed NBS of each lake and 5% disturbed outflow of Lake Albert. ....	67
Figure 3-14. 10% disturbed NBS of each lake and 10% disturbed outflow of Lake Albert. .	68
Figure 3-15: 15% disturbed NBS of each lake and 15% disturbed outflow of Lake Albert. .	68
Figure 3-16. 20% disturbed NBS of each lake and 20% disturbed outflow of Lake Albert. .	69
Figure 3-17. Simulated release functions for the third experiment. ....	70
Figure 3-18. Simulated release functions for the fourth experiment. ....	70
Figure 3-19. Simulated release functions for the fifth experiment. ....	71

Figure 3-20. Simulated release functions for the sixth experiment. ....	71
Figure 3-21. Model verification during the entire time period (calibration + validation) for the third experiment. ....	72
Figure 3-22. Model verification during the entire time period (calibration + validation) for the fourth experiment. ....	73
Figure 3-23. Model verification during the entire time period (calibration + validation) for the fifth experiment. ....	73
Figure 3-24. Model verification during the entire time period (calibration + validation) for the sixth experiment. ....	74
Figure 3-25. Model verification during validation for the third experiment. ....	74
Figure 3-26. Model verification during validation for fourth experiment. ....	75
Figure 3-27. Model verification during validation for the fifth experiment. ....	75
Figure 3-28. Model verification during validation for the sixth experiment. ....	76
Figure 3-29. The Eastern Nile system with existing and planned development [Georgakakos and Yao, 2000]. ....	79
Figure 3-30. The Main Nile system with existing and planned development [Georgakakos and Yao, 2000]. ....	79
Figure 3-31. Inflow-Outflow hydrograph for the river routing application, January 1, 1914 to December 21, 1963. Time in 10-day intervals; 10-day average discharge in million cubic meters per day. ....	87
Figure 3-32. Optimal release and loss functions for the application reach modeled as a cascade of three conceptual reservoirs with a calibration time from January 1, 1914 to December 21, 1963. ....	90
Figure 3-33. Comparison of observed and simulated outflows of the application reach (at Dongola) modeled as a cascade of three conceptual reservoirs from January 1, 1914 to December 21, 1963 in 10-day intervals. ....	91
Figure 3-34. Optimal release and loss functions for the application reach modeled as a cascade of three conceptual reservoirs over a calibration time from January 1, 1914 to November 11, 1952. ....	92

Figure 3-35. Comparison of observed and calibrated outflows of the application reach (at Dongola), modeled as a cascade of three conceptual reservoirs over a calibration time from Jan. 1, 1914 to Nov. 11, 1952 in 10-day intervals. ....	93
Figure 3-36. Comparison of observed and validated outflows of the application reach (at Dongola) modeled as a cascade of three conceptual reservoirs over a validation time from Nov. 11, 1952 to Dec. 11, 1963 in 10-day intervals. ....	93
Figure 4-1. The Bayesian forecasting framework methodology. ....	99
Figure 4-2. BFF application data: historical outflow from January 1, 1912 to August 1, 1975; forecasting horizon from August 1, 1975 to November 1, 1977; time in monthly intervals; monthly discharge in billions of cubic meters. ....	111
Figure 4-3. Ensemble forecasts of NBS for Lake Victoria over the forecasting horizon. Time is in monthly intervals. ....	112
Figure 4-4. Ensemble forecasts of NBS for Lake Kyoga over the forecasting horizon. Time is in monthly intervals. ....	112
Figure 4-5. Ensemble forecasts of NBS for Lake Albert over the forecasting horizon. Time is in monthly intervals. ....	113
Figure 4-6. Simulated outflows of Lake Albert over the forecasting horizon. Time is in monthly intervals. ....	114
Figure 4-7. Empirical distributions of $\mathbf{u}_j$ and the fitted Weibull distributions $\Pi_j(u_j)$ for select time steps of the forecasting horizon. ....	116
Figure 4-8. Historical analogs of actual outflows over the forecasting horizon. Time is in monthly intervals. ....	118
Figure 4-9. Historical analogs of model-estimated outflows over the forecasting horizon. Time is in monthly intervals. ....	119
Figure 4-10. Empirical distributions of $\mathbf{u}_j^*$ and the fitted Weibull distributions $\Gamma_j(u_j^*)$ for selected time steps of the forecasting horizon. ....	119
Figure 4-11. Empirical distributions of $\mathbf{u}_j$ and fitted Weibull distributions $\Lambda_j(u_j)$ for selected time steps of the forecasting horizon. ....	120
Figure 4-12. Linearity of $\mathbf{w}_j$ on $\mathbf{w}_{j-1}$ in the prior densities in the space of the transformed variates. Selected $j$ 's are used. ....	124

Figure 4-13. Normal probability plots for the prior densities in the space of the transformed variates. Selected $j$ 's are used. ....	126
Figure 4-14. Residual plots for the prior densities in the space of the transformed variates. ....	127
Figure 4-15. Linearity of $\mathbf{x}_j$ on $\mathbf{w}_{j-1}$ and $\mathbf{w}_{j-1}$ of likelihood functions in the space of the transformed variates. Selected $j$ 's are used. ....	129
Figure 4-16. Normal probability plots for the likelihood functions in the space of the transformed variates. Selected $j$ 's are used. ....	131
Figure 4-17. Residual plots for the likelihood functions in the space of the transformed variates. Selected $j$ 's are used. ....	132
Figure 4-18. Simulated predictive one-step transition distributions from the Monte Carlo simulation and the corresponding average predictive distributions. $j=4$ and $24$ are used. .	135
Figure 4-19. Box plots from the pre-BFF distributions $\Pi_j(u_j)$ (blue) and the BFF predictive distributions $\Omega_j(u_j^*   u_{j-1}^*)$ (red). ....	136
Figure 4-20. The values of ratio $R_1$ over the forecasting horizon. ....	137
Figure 4-21. A moving window for the linear one-step transition model. Historical analogs of the actual outflow of Lake Albert are used. ....	139
Figure 4-22. Ensemble forecasts of the actual outflow of Lake Albert over the forecasting horizon generated by a sequence of linear one-step transition models. ....	140
Figure 4-23. The values of ratio $R_2$ over the forecasting horizon. ....	141
Figure 4-24. BFF application: the historical inflow-outflow hydrograph from January 1, 1914 to November 1, 1952; the forecasting horizon from November 1, 1952 to December 11, 1953; time in 10-day intervals; 10-day average discharge in million cubic meters. ....	142
Figure 4-25. Ensemble forecasts of the Khartoum inflows over the forecasting horizon. Time is in 10-day intervals. ....	143
Figure 4-26. Ensemble forecasts of the Atbara inflows over the forecasting horizon. Time is in 10-day intervals. ....	143
Figure 4-27. Simulated outflows at Dongola over the forecasting horizon. Time is in 10-day intervals. ....	144

Figure 4-28. Empirical distributions of $\mathbf{u}_j$ and the fitted Weibull distributions $\Pi_j(u_j)$ for select time steps of the forecasting horizon. ....	145
Figure 4-29. Historical analogs of the observe outflow at Dongola over the forecasting horizon. Time is in 10-day intervals. ....	147
Figure 4-30. Historical analogs of the model-estimated outflow at Dongola over the forecasting horizon. Time is in 10-day intervals. ....	147
Figure 4-31. Empirical distributions of $\mathbf{u}_j^*$ and fitted Weibull distributions $\Gamma_j(u_j^*)$ for the selected time steps of the forecasting horizon. ....	148
Figure 4-32. Empirical distributions of $\mathbf{u}_j$ and fitted Weibull distributions $\Lambda_j(u_j)$ for the selected time steps of the forecasting horizon. ....	149
Figure 4-33. Linearity of $\mathbf{w}_j$ on $\mathbf{w}_{j-1}$ in the prior densities in the space of the transformed variates. Selected $j$ 's are used. ....	152
Figure 4-34. Normal probability plots for the prior densities in the space of the transformed variates. Selected $j$ 's are used. ....	154
Figure 4-35. Residual plots for the prior densities in the space of the transformed variates. ....	155
Figure 4-36. Linearity of $\mathbf{x}_j$ on $\mathbf{w}_{j-1}$ and $\mathbf{w}_{j-1}$ of the likelihood functions in the space of the transformed variates. Selected $j$ 's are used. ....	157
Figure 4-37. Normal probability plots for the likelihood functions in the space of the transformed variates. Selected $j$ 's are used. ....	158
Figure 4-38. Residual plots for the likelihood functions in the space of the transformed variates. ....	160
Figure 4-39. Simulated predictive one-step transition distributions from the Monte Carlo simulation and the corresponding average predictive distributions. $j=8$ and $24$ are used. .	161
Figure 4-40. Box plots from pre-BFF distributions $\Pi_j(u_j)$ (blue) and BFF predictive distributions $\Omega_j(u_j^*   u_{j-1}^*)$ (red). ....	163
Figure 4-41. The values of ratio $R_1$ over the forecasting horizon. ....	164
Figure 4-42. A moving window for the linear one-step transition model. ....	165

Figure 4-43. Ensemble forecast of the actual outflow at Dongola over the forecasting horizon, generated by a sequence of linear one-step transition models..... 166

Figure 4-44. The values of  $R_1$  and  $R_2$  over the forecasting horizon. .... 166

## SUMMARY

A key element of hydrologic routing models is the storage-discharge relationship assumed to follow a certain mathematical form, usually a linear or a power function, the parameters of which are calibrated based on existing inflow-outflow data. While this assumption simplifies the model calibration process, it also constrains the models to operate by this function throughout their flow range. In view of the complex and nonlinear river flow behavior, this approximation undoubtedly introduces errors.

This research presents a new hydrologic river routing approach that is not limited by the above assumption. River reaches are modeled as cascades of interacting conceptual reservoirs, with storage-discharge functions identified by the data. A novel parameter estimation approach has been developed to identify these functions and all other model parameters based on control theory concepts. After calibration, these functions indeed exhibit different mathematical forms at different regions of their active variation range. The new approach is applied and successfully demonstrated in real world reservoir and river routing applications from the Nile River Basin. A Bayesian forecasting scheme was also developed that uses the new approach to generate flow forecasts with explicit uncertainty characterization.

# CHAPTER 1

## INTRODUCTION

### 1.1 Statement of problems

The most comprehensive and potentially accurate river routing approach is hydraulic river routing based on the complete St. Venant equations. However, its application to actual river (and flood) routing involves (1) large quantities of high quality flow/channel data; (2) computational parameters; (3) computational cost; and (4) modeling experience [Weinmann and Laurenson, 1979; Becker and Kundzewicz, 1987; Garbrecht and Brunner, 1991; Camacho and Lees, 1999]. By contrast, hydrologic river routing schemes are much simpler in terms of the overall model structure and data requirements. The accuracy of hydrologic river routing models is generally less than that of dynamic wave models, but it can be enhanced if outflow measurements are taken into account [Wasimi and Kitanidis, 1983; Georgakakos et al., 1990]. Furthermore, hydrologic routing models can be easily transformed into state-space models and conveniently incorporated into reservoir management schemes [Georgakakos and Marks, 1987; Georgakakos, 1989]. They can also account for input and model uncertainties [Georgakakos et al., 1990].

River routing is an intrinsically nonlinear process, and linear river routing approaches, such as the Muskingum model [Cunge, 1969] and the Kalinin-Milyukov model [Kalinin and Milyukov, 1957], are limited in describing the full range of its nonlinear response. In general, in multi-linear routing models [Becker and Kundzewicz, 1987; Perumal, 1992; Perumal, 1994; Camacho and Lees, 1999], the inflow to the system (i.e., river reach) is averaged over constant

intervals and each is subsequently routed through a series of interacting linear routing sub-models. The entire river reach can thus be viewed as a cascade of interacting conceptual reservoirs in which outflow depends linearly on storage, and the overall output is a combination of the response of each linear sub-model. This is the manner in which multi-linear routing models simulate the nonlinear river routing response while leveraging the mathematical convenience of linear routing schemes.

In most hydrologic routing schemes, the storage-discharge relationships are assumed to have a certain mathematical form, such as a linear or power function [*Cunge*, 1969; *Muzik*, 1974; *Georgakakos*, 1982], and these properties are invariant over the entire range of flows along the reach. Such assumptions can oversimplify or misrepresent the true relationships so that the overall model performance can be underestimated. Is it possible to develop routing models that do not require such assumptions?

Lastly, all models are bound to contain uncertainties associated with input data, time and spatial discretizations, or modeling assumptions. Bayes theory provides a theoretically sound framework that can quantify these uncertainties especially in forecast applications. However, the traditional Bayesian framework yields a probabilistic description of river flow forecasts in the form of probability distributions at given future times. Such forecasts, although useful in flood forecasting applications, are not as useable as part of operational management systems, and require conversion to multi-trace ensemble forms.

## **1.2 Research objective**

This research aims to develop and demonstrate a new hydrologic river routing model and its use in forecasting as part of a Bayesian uncertainty framework. More specifically, the overarching research objectives are as follows:

- Develop and demonstrate a hydrologic river routing approach, including an efficient model identification-calibration procedure, that rectifies the weaknesses of linear routing schemes.
- Incorporate the new river routing scheme within Bayesian forecasting framework (BFF) that characterizes the underlying uncertainties and generates reliable multi-trace ensemble forecasts.

## **1.3 Methodology**

In this work, a new nonlinear hydrologic river routing model is developed to identify storage-outflow and storage-water loss relationships for different reaches of a river or a reservoir. The model is then incorporated into a Bayesian forecasting framework (BFF) that generates multi-trace forecast ensembles which incorporate both input and model uncertainties.

The routing model assumes that a river reach can be viewed as a cascade of conceptual reservoirs, each of which receives water from upstream and releases water downstream according to release and loss functions. Additionally, these release and loss functions are assumed to follow non-decreasing storage-outflow and storage-water losses relationships, respectively. First, the identification of the required number of conceptual reservoirs is addressed by developing models with progressively more conceptual reservoirs and selecting

the configuration that achieves satisfactory correspondence between simulated and observed outflows based on the principle of parsimony. Second, without any assumption on the mathematical structures of the functions, a Linear Quadratic Regulator (LQR) is used to identify storage-outflow and storage-water loss relationships. Consequently, the combination of the cascade model with the identified storage-outflow and storage-water loss relationships for each submodel can take into account the unsteadiness and nonuniformity of flood flows.

Next, the identified and calibrated routing model is used to generate the forecasts of river or lake outflow. First, a historical analog method is used to select ensembles of system inflows. By an ensemble forecasting method, each inflow trace is then simulated with the previously calibrated river routing model for generating ensembles of outflows. To improve the outcome from the ensemble forecasting, a Bayesian forecasting framework (BFF) was developed and used to generate updated outflow ensembles. In BFF, the distributions of the forecasted outflows are estimated by a sequence of conditional predictive distributions, which probabilistically quantify the total uncertainty (model uncertainty + input uncertainty) in an integrated fashion. In addition, a sequence of linear one-step transition models is derived for generating reliable traces of future outflow, which can be used as better inputs to a real-time operational management model for watershed systems.

Both the routing model and the BFF are first tested on the Equatorial Lakes in East Africa which consists of a series of cascading reservoirs and then applied to the Main Nile. The Equatorial Lake system encompasses Lakes Victoria, Kyoga, and Albert and their drainage basins. The Main Nile flows from Khartoum, Sudan, to Aswan, Egypt and extends upstream

400 km. The river routing model is utilized for routing flows from Khartoum past the confluence of Atbara to Dongola, a distance of about 1,083 km. Except for the discharges at Khartoum and Atbara, no other significant inflows enter the Main Nile in this reach.

#### **1.4 Thesis organization**

This thesis includes five chapters. Chapter 2 contains a review of the relevant literature on hydraulic and hydrologic river routing models, state-space models in reservoir and river systems, and uncertainty characterization in hydrologic models.

Chapter 3 details the methods used to construct the nonlinear river routing model. First, the assumptions and the general identification and calibration procedure for the routing model are presented. Next, the routing model is applied to the Equatorial Lakes first and the Main Nile.

Chapter 4 describes the development of the Bayesian forecasting framework (BFF). It begins with characterizing the associated uncertainties and proceeds with the theoretical background of the BFF. The method is then applied to the Equatorial Lakes and the Main Nile. Finally, Chapter 5 summarizes the research accomplishments, conclusions, and recommendations.

## CHAPTER 2

### A LITERATURE REVIEW

#### 2.1 Hydrologic routing model

The laws of conservation of mass and momentum for unsteady flow can be written as [Sturm, 2001]:

$$\frac{\partial A}{\partial t} + \frac{\partial Q}{\partial x} = q_L \quad (1.1)$$

$$\frac{\partial Q}{\partial t} + \frac{\partial}{\partial x} \left( \beta \frac{Q^2}{A} \right) + \frac{\partial}{\partial x} (gh_c A) = gA(S_0 - S_f) + q_L v_L \cos \phi \quad (1.2)$$

in which  $x$  and  $t$  are distance and time, respectively;  $A$  is the cross-sectional area of flow;  $Q$  is the discharge;  $\beta$  is the momentum flux correction factor;  $h_c$  is the vertical distance below the free surface to the centroid of the cross-sectional area of flow;  $S_0$  is the channel bed slope;  $S_f$  is the friction slope;  $q_L$  is the lateral inflow per unit of length in the flow direction; and  $v_L$  is the velocity of the lateral inflow inclined at angle  $\phi$  to the  $x$  direction. These two differential equations comprise the Saint-Venant equations, the solutions of which describe the flood wave propagation in one-dimensional unsteady river flows. Assuming negligible lateral inflow and  $\beta \approx 1$ , the governing Equations (1.1) and (1.2) can be rewritten as:

$$\frac{\partial A}{\partial t} + \frac{\partial Q}{\partial x} = 0 \quad (1.3)$$

$$S_f = S_0 - \frac{\partial y}{\partial x} - \frac{V}{g} \frac{\partial V}{\partial x} - \frac{1}{g} \frac{\partial V}{\partial t} \quad (1.4)$$

in which  $y$  is the flow depth; and  $V$  is the mean flow velocity. The second term on the right-hand side is the pressure gradient term; the third term is the convective acceleration term; and the last term is the local acceleration term. The two acceleration terms are called the inertia term.

### 2.1.1 Kinematic wave model

When the pressure gradient term and the inertia term are assumed to be negligible, the simplified momentum equation along with the continuity equation, leads to the kinematic wave routing model:

$$\frac{dQ}{dt} = \frac{\partial Q}{\partial t} + c_k \frac{\partial Q}{\partial x} = 0 \quad (1.5)$$

in which  $c_k = dQ / dA = dx / dt$  is the absolute kinematic wave celerity. In addition, the discharge can be calculated in a similar fashion to the uniform flow, which defines a unique relationship between depth and discharge:

$$Q = b_0 A^a \quad (1.6)$$

in which  $b_0$  and  $a$  are constant coefficients. The numerical solutions for Equations (1.5) and (1.6) can be obtained by using either the method of characteristic or the finite difference method.

A kinematic wave does not subside or attenuate (the peak discharge remains the same), but it changes shape or become steeper because the kinematic wave celerity increases with increasing  $Q$ , thus increasing  $y$  as a higher discharge moves downstream at a higher speed [Sturm, 2001]. Since natural floods attenuate, the applicability of the kinematic wave routing method has been investigated extensively. Henderson [1966] suggested that the assumptions made for the kinematic wave model can be justified for natural floods in steep rivers whose slopes are of the order of 10 ft per mile or more. Ponce *et al.* [1978] stated that the kinematic wave model is applicable for a stream channel if:

$$\frac{t_r S_0 V_0}{d_0} \geq N \quad (1.7)$$

in which  $t_r$  is the time-of-rise of the inflow hydrograph;  $S_0$  is the bed slope;  $V_0$  is the average velocity; and  $d_0$  is the average flow depth. To obtain 95 % accuracy in one period of translation,  $N = 85$  is suggested. To apply the kinematic wave model, a Froude number less than 2 is suggested by Miller and Cunge [1975].

*Serrano* [2006] derived a new approximate analytical solution to the nonlinear kinematic wave equation in which  $c_k$  varies with flow depth. This was achieved by combining an implicit solution obtained through the method of characteristics with an analytical decomposition [Adomian, 1994] and successive approximation of discharge (*Serrano* 2003; *Serrano* 2004).

### 2.1.2 Diffusion wave model

In practice, real flood waves show a certain amount of diffusion or attenuation. A diffusion wave routing model, extended from the kinematic wave model, can account for the diffusion or attenuation of a wave. By neglecting the inertia term in the momentum equation, the diffusion wave equation is derived for streamflow and channel flow [*Hayami*, 1951; *Lighthill and Whitham*, 1955] :

$$\frac{\partial Q}{\partial t} + c_k \frac{\partial Q}{\partial x} = \nu \frac{\partial^2 Q}{\partial x^2} \quad (1.8)$$

in which the hydraulic diffusivity  $\nu = Q / (2TS_0)$ ;  $S_0$  is the bottom slope; and  $T$  is the channel top width. *Hayami's* diffusion-analogy solution for flood waves can analytically solve the diffusion wave equation with constant  $c_k$  and  $\nu$ . The second alternative to solve the diffusion wave equation is to extend the finite difference approximation of the kinematic wave model by matching physical and numerical diffusion. The finite difference solutions of the kinematic wave equations simulate physical diffusion through artificial or numerical diffusion due to the

numerical approximation. The second approach leads to the development of the Muskingum-Cunge model, which will be described in more detail.

*Price* [2009] adopted a nonlinear, advection-diffusion equation in a conceptual routing model based on physical principles. The numerical solution of the equation is based on a centered difference scheme. The input data of the model are only historic upstream and downstream stage hydrographs and the related in-bank rating curves, local rainfall, and minimal supplementary information. To account for bypassing of the main channel and insufficient in situ hydraulic data for the floodplains, both upstream and downstream above-bank rating curves are extracted as power functions from the corresponding in-bank rating curves and utilized for better estimates of the discharge downstream.

Using the Lambda scheme, *Wang et al.* [2003] converted the Saint-Venant equations into a nonlinear convection-diffusion equation that was discretized spatially using the mixing cell method [*Singh et al.*, 1997] for yielding a first-order nonlinear ordinary differential equation. The integration of the differential equation with respect to time generates an implicit nonlinear differential equation, the analytical solutions of which yield the value of discharge for a given computational cell.

### 2.1.3 Muskingum model

Hydrological models are based on the conservation of mass and the relationship between storage and inflow/outflow. In the Muskingum model, first developed by *McCarthy* [1938], the governing equations are the finite difference approximations of the continuity equation

$$\frac{S_2 - S_1}{\Delta t} = \frac{I_1 + I_2}{2} - \frac{O_1 + O_2}{2} \quad (1.9)$$

and the linear relationship between storage and a weighted function of inflow and outflow:

$$S = K[XI + (1 - X)O]. \quad (1.10)$$

The subscripts  $I$  and  $2$  indicate the beginning and end of the time interval. The parameter  $K$  is considered an average reach travel time and  $X$  is the weighting coefficient related to the effects of inflow and outflow on storage. The combination of the two equations, [*Ponce*, 1989], can estimate  $O_2$  given the observed  $(I_1, I_2)$ , the previously calculated  $O_1$ , and the estimated parameters  $(K, X)$  in such a way that

$$O_2 = C_0 I_2 + C_1 I_1 + C_2 O_1 \quad (1.11)$$

in which the routing coefficients are

$$C_0 = \frac{\Delta t / K - 2X}{2(1 - X) + \Delta t / K} \quad (1.12)$$

$$C_1 = \frac{\Delta t / K + 2X}{2(1 - X) + \Delta t / K} \quad (1.13)$$

$$C_2 = \frac{2(1 - X) - \Delta t / K}{2(1 - X) + \Delta t / K} \quad (1.14)$$

Once  $K$  and  $X$  are computed, then an outflow at each time step is estimated recursively by Equation (1.11), assuming that the initial outflow is equal to the initial inflow.

There are several ways to estimate  $K$  and  $X$  : (1) The least squares method [*Singh and McCann*, 1980]. (2) The graphical method computes the slope of the most suitable straight line to the plot of  $S$  versus  $XI + (1 - X)O$  to yield  $K$  , assuming a value of  $X$  between 0 and 1. (3) The direct optimization method [*Stephenson*, 1979; *O'Donnell*, 1985] directly computes the routing coefficients before  $K$  and  $X$  by minimizing the difference between the observed outflow hydrograph and the computed hydrograph in a least square sense.

The drawbacks of the Muskingum method are: (1) The true relationship between storage and a weighted combination of inflow and outflow can be non-linear or looped curves; and (2) in conventional methods, the parameters  $K$  and  $X$  are assumed to be constant, thereby making the parameters dependent on a set of specific inflow-outflow hydrographs [*Dooge*, 1973]. As a result, there is no guarantee that they can be used for a different flood to produce a similarly accurate outflow prediction [*Sturm*, 2001]. *Guang-Te and Singh* [1992] developed a variable-parameter Muskingum method to allow the parameters to vary in time and space. Depending on the dependency of wave travel time on discharge and storage, three versions of the method were categorized, tested for three data sets, and compared with the conventional Muskingum method in which the parameters had been estimated by trial and error (the graphical method).

The new method used the simplex method to determine the parameters  $K$  and  $X$  that minimized the sum of the squares of difference between observed and computed outflows. The results showed that the variable-parameter Muskingum method could represent the storage hysteresis, which is not described by the conventional graphical method and related versions. In addition, the variable-parameter method was several times more accurate in estimating discharge compared to the conventional methods.

#### 2.1.4 Muskingum-Cunge model

A significant improvement on the Muskingum model was developed by *Cunge* [1969]. While the analytical solution of the differential equation of the Muskingum model does not allow for wave attenuation, the Muskingum scheme allows for subsidence of a wave travelling along a river reach. *Cunge* [1969] investigated this contradiction by assuming single-valued stage/discharge curves and a constant wave celerity in the kinematic wave equation

$$\frac{dQ}{dt} = \frac{\partial Q}{\partial t} + \left( \frac{dQ}{dA} \right) \frac{\partial Q}{\partial x} = \frac{\partial Q}{\partial t} + c \frac{\partial Q}{\partial x} = 0, \quad (1.15)$$

where  $Q$  is the river flow;  $A$  is the cross-sectional flow area;  $x$  and  $t$  are distance along a river and time, respectively; and  $c$  is the kinematic wave celerity. Then the kinematic wave equation, Equation (1.5), is discretized on the  $x-t$  space, using an implicit finite-difference scheme [*Ponce*, 1989]:

$$\frac{X(Q_j^{n+1} - Q_j^n) + (1-X)(Q_{j+1}^{n+1} - Q_{j+1}^n)}{\Delta t} + c \frac{Y(Q_{j+1}^n - Q_j^n) + (1-Y)(Q_{j+1}^{n+1} - Q_j^{n+1})}{\Delta x} = 0, \quad (1.16)$$

where  $n$  and  $j$  indicate the spatial and temporal intervals of each node in each computational grid on the  $x-t$  space, respectively; and  $X$  and  $Y = 0.5$  are the weighting factors. Solving Equation (1.16) for the unknown discharge yields:

$$Q_{j+1}^{n+1} = C_0 Q_j^{n+1} + C_1 Q_j^n + C_2 Q_{j+1}^n \quad (1.17)$$

in which the routing coefficients are

$$C_0 = \frac{c(\Delta t / \Delta x) - 2X}{2(1-X) + c(\Delta t / \Delta x)} \quad (1.18)$$

$$C_1 = \frac{c(\Delta t / \Delta x) + 2X}{2(1-X) + c(\Delta t / \Delta x)} \quad (1.19)$$

$$C_2 = \frac{2(1-X) + c(\Delta t / \Delta x)}{2(1-X) + c(\Delta t / \Delta x)}. \quad (1.20)$$

By defining  $K$  in Equations (1.12) to (1.14) as  $\Delta x / c$ , the Muskingum method is indeed a numerical approximation of the kinematic wave equation in terms of the implicit finite-difference scheme. *Cunge* [1969] and *Ponce et al.* [1979] also showed the difference  $R$  between an implicit finite-difference approximation of the kinematic wave equation and the differential equation, based on the assumption that a discharge at a node in the space-time space can be expanded by the Taylor series:

$$R = c \left[ \left( \frac{1}{2} - X \right) + C \left( \frac{1}{2} - Y \right) \right] \frac{\partial^2 Q}{\partial x^2} \Delta x + c \left\{ (1 - C) \left[ \frac{1}{2} (X + C \cdot Y) - \frac{1}{3} (1 + C) \right] \right\} \frac{\partial^3 Q}{\partial x^3} \Delta x^2 + O(\Delta x^3)$$

(1.21)

in which  $C = c\Delta t / \Delta x$  is the Courant number. The numerical diffusion coefficient and the numerical dispersion coefficient appear in the first-order and second-order error terms in the Equation(1.21). *Cunge* [1969] also analyzed the effects of the routing coefficients of the Muskingum scheme on numerical stability and the magnitude of the numerical attenuation. Furthermore, matching the numerical diffusion coefficient in  $R$  and the physical diffusion coefficient of the Saint-Venant equations (neglecting the inertia term) can calculate the weighting factor  $X$  (with  $Y = 0.5$ ) directly from the flow characteristics and channel properties:

$$X = \frac{1}{2} \left( 1 - \frac{q_0}{S_0 c \Delta x} \right)$$

(1.22)

in which  $q_0$  is the reference discharge per unit of width; and  $S_0$  is the bottom slope. The Muskingum method with  $X$ , calculated by Equation(1.22), is referred to as the Muskingum-Cunge method. However, the attenuation obtained with  $X$  from Equation (1.22) does not take into account the numerical dispersion. Therefore, keeping the value of the Courant number  $C$  as close to one as possible is necessary to properly simulate the physical diffusion in the Muskingum-Cunge scheme.

The Muskingum-Cunge method is limited to diffusion wave routing. Hence, like the Muskingum method, the Muskingum-Cunge method is based on a single-valued stage-discharge relationship and does not account for strong flow nonuniformity and unsteady flows showing substantial loops in stage-discharge relationship. Thus, *Ponce* (1989) pointed out that the Muskingum-Cunge method is suited for river routing in natural streams without significant backwater effects, which can be classified by the diffusion wave criterion:

$$t_r S_0 \left[ \frac{g}{d_0} \right]^{1/2} \geq M \quad (1.23)$$

in which  $t_r$  is the rise time of the inflow hydrograph,  $S_0$  is the bottom slope,  $d_0$  is the average flow depth. In practice,  $M = 15$  is recommended for general use. The dynamic wave routing schemes are recommended in situations where neither kinematic nor diffusion wave solutions, which Muskingum and Muskingum-Cunge methods are based on, are likely to represent river flows. In particular, dynamic wave solutions are applicable to flow over very flat slopes, flow into large reservoirs, strong backwater effects, and flow reversals [*Ponce*, 1989].

The constant-parameter Muskingum-Cunge method has been compared with the variable-parameter Muskingum-Cunge method [*Ponce and Yevjevich*, 1978; *Ponce and Changanti*, 1994]. In the constant-parameter method [*Dooge*, 1973], the Courant number  $C$  and the cell Reynolds number  $D$  [*Roache*, 1972], defined by  $D = q_0 / (S_0 c \Delta x)$ , are calculated with reference flow values and kept constant throughout the computation time. Since  $c$  is constant

in the kinematic wave method, the constant-parameter Muskingum-Cunge method is referred to as a linear mode. In the variable-parameter method, on the contrary, the routing parameters are recalculated for every computational grid as a function of local flow values in which  $c$  varies so that this method is referred to as a nonlinear mode. While the linear mode conserves mass with no loss of water volume in the outflow hydrograph, the nonlinear mode loses a small but perceptible loss of mass. In addition, the steepening of inbank flood waves cannot be displayed well, while the nonlinear mode can simulate the wave steepening.

*Ponce and Yevjevich* [1978] suggested a three-point method and an iterative four-point method to calculate the varying routing parameters based on local flow values, discharge and celerity.

*Ponce and Changanti* [1994] modified the three-point method by estimating the average celerity not from the three known grid points, but from the average unit-width discharge at the three grid points with  $c = \beta(q/d)$ , where  $\beta$  is the exponent of the rating, and  $d$  is the flow depth. As with the modified three-point method, *Ponce and Changanti* [1994] also modified the iterative four-point method by calculating the local average celerity with the average unit-width discharge at the four grid points. *Ponce and Changanti* [1994] applied all these methods including the constant-parameter method for various temporal/spatial grid resolutions and the ratios of peak inflow to baseflows. The results showed the loss of mass was greater for the three-point methods (conventional and modified). In addition, the modified methods conserved more mass than the conventional methods with the loss rate of mass between 1 and 3 percent.

*Ponce and Lugo* [2001] extended the variable-parameter Muskingum-Cunge method into the looped-rating Muskingum-Cunge model to account for looped rating of dynamic waves with the use of a local water surface slope and the Vedernikov number [*Dooge et al.*, 1982; *Ponce*, 1991] in the expression for dynamic hydraulic diffusivity. The dynamic hydraulic diffusivity modifies the hydraulic diffusivity  $\nu_d$  by:

$$\nu_d = \frac{q}{2S_0} (1 - V^2) \quad (1.24)$$

in which  $V$  is the Vedernikov number, defined as the ratio of relative kinematic to relative dynamic celerities [*Vedernikov*, 1945; *Vedernikov*, 1946; *Craya*, 1952; *Chow*, 1959]. The looped-rating Muskingum-Cunge model was developed by modifying the four-point variable-parameter Muskingum-Cunge model [*Ponce and Changanti*, 1994]. The application of the looped-rating model to various bottom slopes, ratios of base to peak flows, and spatial/temporal resolutions showed that as the wave period increased the wave became more diffusive and the loop thickness increased. In addition, the mass gain increased with the loop thickness and the peak inflow/base flow ratio.

*Garbrecht and Brunner* [1991] applied the variable-parameter Muskingum-Cunge method, based on the four-point method, into the compound channel with decoupling the main/overbank flow and variable time intervals. This modified scheme is called DNCFR. The separation of the compound channel provided distinct characterization of the main and overbank flows. In the variable time interval mode, large time increments were used during

interstorm periods, and shorter time increments were selected to account for rapidly-changing discharges during storm events. They used the National Weather Service's full dynamic flow-routing model DAMBRK (1988 version) [Fread, 1984] as the benchmark or standard to test DNCFR. The benchmark testing was preferred over the observed data because processes unrelated to flow routing, such as significant infiltration on overbank floodplains or changing flow resistance caused by submerged vegetation, can smear field data and the effect of these processes is generally hard to measure. The comparison of the results showed that the diffusivity of waves, the peak discharge, and the time to peak of the outflow hydrographs were well represented, within about 4% of the results from DAMBRK on the average. Furthermore, the computation time of DNCFR is, on the average, one order of magnitude faster than the benchmark model. However, the resulting outflow hydrographs showed slightly lagged/lower peak and relatively significant flattening of the rising limbs. *Garbrecht and Brunner* [1991] assumed that the deviations appeared to result from the difference in the calculation of flow characteristics in the decoupled compound channels in both routing models.

### 2.1.5 Kalinin-Milyukov model

Another widely used linear routing model is the Kalinin-Milyukov model, developed by *Kalinin and Milyukov* [1957]. This method is a variation of the Muskingum method in that they discretized the second term in the kinematic wave equation of Equation (1.5) by

$$\frac{\partial Q}{\partial x} \approx \frac{Q(t) - I(t)}{\Delta x}.$$

Plugging this modification into the kinematic wave equation generates:

$$Q(t) = e^{-t/\tau} \left\{ \frac{1}{\tau} \int_0^t I \cdot e^{t'/\tau} dt' + Q_0 \right\} \quad (1.25)$$

in which  $Q_0$  is the outflow at time  $t = 0$  and  $\Delta x / c_k = \tau$  is the time of propagation of the given discharge along the reach of  $\Delta x$ .

The inflow hydrograph for a given reach  $\Delta x$  can be discretized at a certain number of intervals  $\Delta t$  to calculate the discrete outflow for the given reach:

$$Q(t_1 + \Delta t) = Q(t_1) + [I(t_1) - Q(t_1)]k_1 + k_2 \Delta I \quad (1.26)$$

in which  $\Delta I = I(t_1 + \Delta t) - I(t_1)$ ,  $k_1 = 1 - \exp(-\Delta t / \tau)$ , and  $k_2 = 1 - k_1 \tau / \Delta t$ . The Kalinin-Milyukov method is more advantageous than the Muskingum model in that [Miller and Cunge, 1975]: (1)  $\tau$  and  $\Delta x$  can be determined in a coherent manner instead of by trial and error; and (2) it also gives much better results for water stages.

### 2.1.6 Multilinear cascade model

A system is linear if it satisfies: (1) proportionality or homogeneity, and (2) superposition or additivity. Otherwise, the system is nonlinear. Multilinear models, synonymously known as multiple input linear models, multiple linearization models, and non-linear threshold modes, describe a nonlinear system with a set of linear models [Becker and Kundzewicz, 1987].

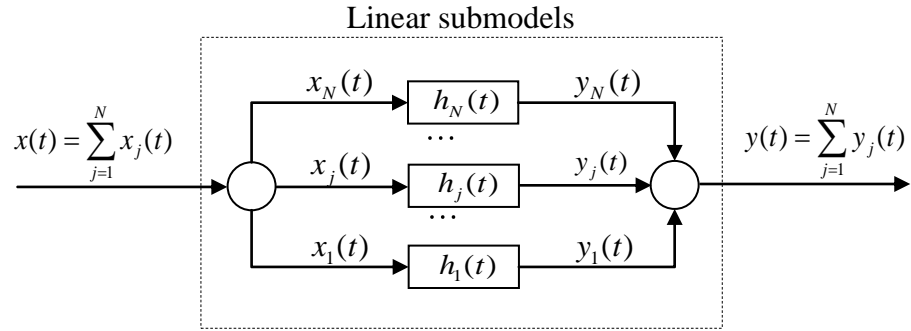


**Figure 2-1.** Computational procedure of a multilinear model.

In addition, the multilinear model is defined as two computational processes: (1) the algorithm of partitioning the input hydrograph  $x(t)$ , shown in Figure 2-1, into elementary input pulses  $x_j(t)$ ; and (2) the combination of the linear sub-models outputs responding to each of the elementary input pulses. The overall output  $y(t)$  of the multilinear model is the combination of every response  $y_j(t)$  of the linear sub-models with the impulse response  $h_j(t)$  to elementary input pulses  $x_j(t)$ , according to the convolution of the impulse response and the input pulses:

$$y(t) = \sum_{j=1}^N y_j(t) = \sum_{j=1}^N \int h_j(\tau) x_j(t - \tau) d\tau . \quad (1.27)$$

Based on the technique used to partition the input hydrograph horizontally or vertically, two schemes are categorized as the amplitude distribution [Keifer and McQuivey, 1974; Becker, 1976; Becker and Kundzewicz, 1987] and the time distribution scheme [Kundzewicz, 1984;

*Becker and Kundzewicz, 1987*] respectively. The horizontal partition represents different zones of discharges, while the vertical distinction produces different zones of time.

*Kundzewicz [1984]* pointed out that these multilinear schemes are not able to take into account significant backwater effects, formation of computational irregularities in the peak discharge of the simulated outflow hydrograph, caused by (1) insufficient partitioning of the inflow hydrograph and (2) the subjectivity involved in selecting the computational ranges of inflow.

To overcome these limitations, except that of the backwater effect, *Perumal [1992]* proposed the multilinear Muskingum flood routing method. Based on the time distribution scheme with a constantly partitioned time interval equivalent to the routing time interval, this method routes each of the input pulses through the Muskingum-Cunge model, the parameters of which depend upon not only flow/channel characteristics, but also the intensities of the input pulses. In a uniform wide rectangular channel with no lateral inflow, the test results showed that this model was able to simulate the solution of the St. Venant equations closely when the rating curve at the inlet of the reach was characterized by narrow loops. In addition, a ‘dip’ or ‘reduced outflow’ at the beginning of the routed hydrograph, which is the well known phenomenon to the users of the Muskingum method, was diminished by increasing the number of routing reaches. However, this procedure increases the number of the model parameters from two to three.

To overcome this drawback, *Perumal [1994]* proposed a cascade of linear sub-models in a discrete time domain, introduced by *O’Connor [1976]*. This multilinear discrete cascade

model is analogous to the Nash model [Nash, 1960] in a continuous time domain, which is a conceptual representation of the Kalinin-Milyukov model, when its parameter for the number of linear reservoirs in a reach is an integer. The parameters of the discrete cascade model vary at each routing time to account for the non-linearity of flood waves more appropriately. The discrete cascade model is derived by taking finite difference approximation of the governing equations of the Nash model. Each pulsed input from the input hydrograph is routed by the input pulse response of the cascade model. The parameters of the sub-model are estimated by (1) relating to the channel/flow characteristics [Dooge, 1973] and (2) using one-to-one relationship between the pulse response of the discrete cascade model and the impulse response of the Nash model. The overall outflow at a certain time  $j\Delta t$  is calculated by adding all the component outflows estimated at the same time. Perumal [1994] tested this model in uniform rectangular channels with a given hypothetical inflow hydrograph and compared with the solutions of the St. Venant equations. The results show that this discrete cascade model can take into account the non-linearity of flood wave better than the multilinear Muskingum flood routing method [Perumal, 1992] and is able to reproduce the solution of the St. Venant equations closely when the rating curve of the inlet of the channels is characterized by a narrow loop.

Camacho and Lees [1999] added a discrete linear channel in the multilinear discrete cascade model to lag a routed hydrograph by an explicit time interval specified by the time delay parameter, making it a three-parameter model. The overall performance of the multilinear discrete lag-cascade model to match the solution of the St. Venant equation was better than that of the multilinear discrete cascade model in uniform channels with very low slopes and high

resistance effects, which were characterized by open looped-rating curve at both inlet and outlet. In addition, the test result shows that a considerable portion of the flood wave advection process can be well explained by the explicit time delay of the discrete channel.

In summary, the kinematic model and the diffusion model are limited to steady flows. They cannot account for non-linearity of flood waves and unsteadiness showing substantial rating curve loops. Although the multilinear discrete lag-cascade model showed improvement over the multilinear discrete model in reproducing the St Venant solutions in ideal channels, the applicability of the models to real rivers is somewhat limited due to a high demand for quantity and quality flow/channel data.

## **2.2 Hydraulic routing model**

The hydraulic routing models are categorized by the numerical methods used to solve the Saint-Venant equations of unsteady flow. The method of characteristics transforms the simplified Saint-Venant equations in  $x$  (space) and  $t$  (time) space to ordinary differential equations in characteristic directions. The characteristic curves must satisfy the differential equations  $dx/dt$ , which may change in time and space. The dependent variable, i.e., depth and velocity, can be found from the simultaneous solution of the ordinary differential equations of two characteristic curves at position  $x$  and time  $t$ , where the two characteristic curves intersect. Therefore, the points on the time-distance space, where the solutions are obtained, are not known until the computations are performed. If the initial or boundary conditions or any derivatives in the differential equations are discontinuous, then the discontinuities propagate along the characteristic curves in the entire  $x-t$  space. In addition, the

characteristics are not usually straight lines. In some cases, the characteristics of the same family intersect, causing the dependent variables to have multiple values, which in turn generate shocks [Cunge *et al.*, 1980]. In the vicinity of the shocks, the following assumptions of the Saint-Venant equations are violated: (1) vertical accelerations are not negligible and (2) the hydrostatic pressure distribution is not valid [Cunge *et al.*, 1980]. The method of characteristics is most useful for an understanding of the behavior of the solutions of the simplified Saint-Venant equations of one-dimensional unsteady flow affected by initial and boundary conditions [Sturm, 2001]. In general, the time step in the method must satisfy the Courant stability criterion [Stoker, 1957; Strelkoff, 1970]. However, an implicit time-line interpolation, developed by Goldberg and Wylie [1983], relaxes the limit of the time step regulated by the Courant condition.

Another approach to solving the Saint-Venant equations numerically is explicit finite difference methods. These methods advance the solution of the equations point by point along the  $k^{\text{th}}$  time line in the  $x-t$  space until all the unknown variables, i.e., depth and velocity, related to the time have been calculated. After the procedure continues to the next time line,  $k+1^{\text{th}}$ , the unknown variables of the new time line are calculated, based on the values of the variables, evaluated along the  $k^{\text{th}}$  time line. In the explicit schemes, only the time derivatives include unknowns, and two linearly approximated equations are generated from the continuity and momentum equations at each node in the  $x-t$  domain so that two unknown variables at the next time line can be directly evaluated from the two equations [Anderson and Burt, 1985]. Descriptions and analyses of several explicit finite difference methods were presented by

*Sturm* [2001] who comments that, for any explicit scheme, the Courant stability criterion must be met for numerical stability.

The implicit finite difference method is the third scheme for solving the Saint-Venant equations. While the explicit finite methods approximate the spatial and temporal derivatives along one time line and one space line, respectively, the implicit scheme uses two adjacent time/space lines to calculate the spatial/temporal derivatives. Hence, the implicit schemes use all information in each of the four nodes in each computational grid. When the number of computational grids is  $N - 1$  and two dependent variables at  $N$  computational nodes of the forward time line need to be evaluated, the  $2N$  unknowns are simultaneously solved from  $2(N - 1)$  equations from the Saint-Venant equations for each grid and two equations from the boundary conditions along the current time line [*Sturm*, 2001]. The Newton-Raphson iterative method has been widely used to obtain simultaneous solutions.

Compared to the implicit schemes, the characteristic and explicit schemes can be applied relatively easily to unsteady flow. However, the size of the computational time step is restricted by the Courant condition for numerical stability. Being numerically stable means that round-off errors introduced in the computations are not amplified during successive computations. The Courant condition is

$$\Delta t \leq \frac{\Delta x}{V + \sqrt{gA/B}},$$

where  $A$  is the cross-sectional area of flow,  $B$  the top width of the water surface,  $V$  the velocity,  $\Delta x$  the finite difference distance interval, and  $\Delta t$  the computational time step. As seen in the above condition, the computational time step substantially decreases as hydraulic depth  $A/B$  increases. Thus, using such a small time step in a deep river that has a gradual flood wave of duration on the order of weeks is very inefficient in terms of computational time and accuracy [Fread, 1974]. In addition, future distance intervals of the method of characteristics and the explicit schemes are unknown and equal, respectively. This restriction is unfavorable for rivers with irregular cross-sections that vary rapidly in the  $x$ -direction along the waterway [Fread, 1974].

While *Abbott and Ionescu* [1966] and *Strelkoff* [1970] showed analytical stability analyses of various implicit schemes, *Amein and Fang* [1970] and *Fread* [1973a] tested the stability of implicit schemes through numerical experiments. *Fread* [1974] used the von Neumann technique to examine the numerical stability of four-point implicit schemes in which the Saint-Venant equations are linearized and then simplified. When the weighting factor  $\theta$  in the spatial derivatives is between 0.5 and 1, the implicit scheme is unconditionally (independent of the size of  $\Delta x$  and  $\Delta t$ ) linearly stable. When frictional effects (Manning's roughness coefficients) are negligible, the box scheme,  $\theta=0.5$ , is neutrally or weakly stable. *Fread* [1974] also investigated the accuracy of the various implicit schemes. The truncation error, or the difference between the solution of the difference equation and that of the partial differential equation, is determined by a Taylor series expansion. The truncation error indicates that the

box scheme has second-order accuracy and the backward scheme,  $\theta = 1$ , has first-order accuracy. This analysis indicates that accuracy decreases as  $\theta$  increases from 0.5 to unity. *Amein and Fang* [1970] applied a centered finite difference scheme, more recently referred to as the box implicit scheme, to the Neuse River, which flows from Goldsboro to Kingston in North Carolina, for flood routing. In addition, an explicit mesh method and the method of characteristics [*Amein*, 1966] were also used to compare the efficiency and the accuracy of each method. The channel geometry and bottom slopes were modeled in two ways. In the first model, a single cross-section was generated by averaging channel properties over the entire reach. Based on the elevations of the channel at the two ends of the reach, the average bottom slope was calculated. In the second model, the actual field data of the channel geometry was used from section to section, and so was the channel slope. At every three mile station, cross-sectional areas were measured from topographic maps and fitted to fourth-order polynomial equations as the functions of depth. Initial depths were estimated by backwater calculations from a downstream depth. The recorded stage hydrograph and a rating curve were used as the boundary conditions for upstream and downstream, respectively. Manning's roughness coefficients at the upstream and downstream boundaries were determined from fitted polynomial functions of depth. The values of Manning's  $n$  at intermediate points were assumed to be linearly varying between the two ends for a given depth. In the average cross-sectional model, the results of the three methods showed similar accuracy in estimating the downstream hydrographs. However, both the explicit method and the method of characteristics displayed instability with larger time increment, whereas the implicit method maintained stability. In the discrete cross-sectional model, the implicit scheme was the only method that handled the significant changes in the channel geometry and bottom slope.

One of the most efficient and accurate dynamic wave models for one-dimensional unsteady flows is FLDWAV. This model is a synthesis of the popular models, DWOPER [Fread, April 1978] and DAMBRK [Fread, 1980]. In addition, FLDWAV provides significant hydraulic simulation features not available in either of the other models [Anderson and Burt, 1985]. It is based on an implicit finite difference solution of the Saint-Venant equations of unsteady flow coupled with internal boundary conditions to take into account a wide spectrum of hydraulic structures along a waterway [Fread and Lewis, 1988]. The special features included are (1) an inactive cross-sectional area that accounts for embayment, ravines, or tributaries that store the flow but do not pass flow to the channel; (2) linearly interpolated cross-sections; (3) a calculation of Manning's  $n$  by comparing simulated and observed hydrographs and linear interpolation of the roughness coefficient for the intermediate values of the water elevation or discharge; (4) a special algorithm that subdivides a river reach into sub-reaches for treating mixed flow (from subcritical to supercritical or conversely); and (5) an efficient computational scheme that treats a dendritic (tree-type) network of channels or bifurcating channels.

The branch-network flow model, called BRANCH [Schaffranek et al., 1981], is also based on an implicit finite difference solution of the Saint-Venant equation of one-dimensional unsteady flow in the subcritical regime. By using branch-transformation equations that relate the unknown variables of flow rates and water-surface elevations at a current segment to the ones at the previous segment of a branch in a state-space representation, the solution of the finite difference equations can be obtained efficiently in terms of computational time and storage. The flow-resistance coefficient is calculated from the Manning equation for steady uniform flow, and it can be fine-tuned by comparing simulated and measured discharges. The

application of this flow model covers from a singular river reach to a multiple interconnected network of channels.

Another one-dimensional unsteady flow model for a complex network of channels is UNET [U.S. Army Corps of Engineers, 1995]. This flow model assumes that a compound channel is divided into two separate channels for the main channel and the floodplain. The two channels split the flows according to their conveyances [Fread, 1976; Smith, 1978].

*Barkau* [1982] extended the earlier work of *Fread* [1976] and *Smith* [1978], combining the separate continuity/momentum equations for the main channel and floodplain and defining a new set of continuity and momentum equations that were computationally more efficient. However, UNET solves only one-dimensional unsteady flow equations for the subcritical flow regime.

### **2.3 State-space model/optimal control theory in reservoir and river systems**

*Muzik* [1974] stated that the state space theory of systems was developed from the need of techniques to process a formidable task of the analysis and synthesis of multiple input-multiple output systems. Mathematically, the state variable approach is to use matrix analysis and vector calculus to provide a unifying basis for solving linear and nonlinear problems. Systems which are amenable to state space model are lumped and dynamic [Zadeh and Desoer, 1963; DeRusso et al., 1965; Ogata, 1967; Ogata, 1970]. Basically, lumped systems are described by ordinary differential equations, while distributed systems by partial differential equations to describe the dynamic behavior [Muzik, 1974]. In the strict sense, all physical systems are

distributed, but for practical purposes they can be approximated by means of ordinary differential equations [*Schwarz and Friedland, 1965*]. Dynamic systems generate outputs at any instant, which depend not only on the present inputs, but also on at least some of the previous inputs. *Derusso [1967]* explained that the state of a system separates the future from the past, so that the state contains all the relevant information of the past history of the system. *Ogata [1970]* defines the state of a dynamic system as the smallest set of variables (called state variables) such that the knowledge of these variables at time  $t = t_0$ , together with the input for  $t \geq t_0$ , completely determines the behavior of the system for any time  $t \geq t_0$ .

*Muzik [1974]* applied the state-space model to the kinematic routing scheme for routing overland flows in which the overland flow is represented by a series of interacting reaches of a uniform flow to simulate the unsteady nonuniform overland flows. *Hoos et al. [1989]* proposed a flood routing scheme that approximated the diffusion wave equation with lateral inflow, using explicit finite difference scheme. Then they represented the finite difference approximation in a state-space form to make the deterministic routing model fully adaptable to a stochastic updating procedure, Kalman filtering [*Kalman, 1960*], to account for modeling uncertainties related to (1) structure of the model, (2) model parameters, and (3) observed input/output data. *Georgakakos et al. [1990]* defined that the goal of stochastic models is to combine the system dynamics with the measurement information to optimally estimate the state vector. In addition, two desirable properties of these optimal estimates are unbiasedness and minimum error variance among all other unbiased estimators. In the case of linear systems with white Gaussian statistics, such optimal estimates are obtained from the Kalman Filter.

*Georgakakos and Bras* [1982] developed a statistical linearization technique, in conjunction with the Taylor-Gauss methodology, to convert a nonlinear routing model to an equivalent linear model. To improve the model performance in forecasting (e.g., time to the peak discharge, magnitude of the peak discharge), this linear model is represented by a state-space model in order to use filtering and optimal estimation techniques, utilizing observed hydrologic data in real time. *Georgakakos et al.* [1990] reformulated the multiple-reach Muskingum-Cunge routing model into a state-space model to estimate the optimal state (discharge) through the Kalman filter. They implemented the linear (constant routing coefficients) and the nonlinear (time-varying coefficients) state-space routing models to manmade channels with either mild or steep slopes and compared the results with those from the dynamic wave operational (DWOPER) model, developed by *Fread* [April 1978], as the benchmark. The results showed that both the linear and nonlinear models coupled with the Kalman filtering, using real-time discharge measurements, improved the model performance in channels with even very mild slopes. However, they concluded that further research was needed to relate the bottom slope, adjusted by the maximum likelihood estimation approach, to the actual bottom slope since the improvement of the model performance was mainly due to the adjusted bottom slopes which were not necessarily equal to the actual slopes.

According to *Kirk* [1970], “the objective of optimal control theory is to determine the control signals that will cause a process to satisfy the physical constraints and at the same time minimize (or maximize) some performance criterion.” *Lewis and Syrmos* [1995] also defined the goal of optimal control theory as the optimization of a performance index or an objective function associated with a system developing dynamically through time. *Babs and Miguel*

[1989] employed the feedback method of optimal control, found in the work by *Chow* [1981], to estimate optimal time series of piezometric heads in groundwater flow in a confined aquifer. The piezometric head is optimal in a sense that it tracks the target piezometric head best, while satisfying the governing equations of groundwater flow in a confined aquifer in two dimensions. They formulated a quadratic objective function with the constraints, represented by a linear state-space form for the governing equations, to be fully adaptable to the feedback method of optimal control. The case studies revealed that (1) feedback rules can be used for operational management of the aquifer; (2) feedback models can be applied to very complex aquifer systems using existing ground water models; (3) It is much easier to specify and interpret than any other objective functions found in groundwater hydraulic management models; and (4) other objective functions can be easily incorporated into the feedback model [*Makinde-Odusola and Mariño*, 1989].

*Wasimi and Kitanidis* [1983] investigated the applicability of the discrete-time linear quadratic Gaussian (LQG) control in the optimal operation of a multireservoir system under flood conditions to minimize the expected flood damage by tracking predefined storage/release sequences. The objective of the LQG is to optimize the expected value of a quadratic performance index, subject to linear equality constraints and Gaussian disturbance into a dynamic system. Using the Muskingum method of linear streamflow routing [*Chow*, 1964] and reduced-order state-space unit hydrographs to forecast Gaussian inputs (runoff) from effective rainfall, the actual river basin system was modeled as a network of actual reservoirs, linear reservoirs, and inflow-outflow points. Then this networked model was represented in a state-space form appropriate for the application of the LQG. Due to the difficulty of the direct

measurement of the model states, the Kalman filtering [Kalman, 1960] was used to update the states at each computational time step. They suggested some advantages of the methodology: (1) the reservoirs are operated in a coordinated way; (2) complete use of observed information is made in determining the optimal operation policy for flood regulation; and (3) the LQG control technique is computationally very efficient and flexible in a real-time operation of multi-dimensional reservoir systems. However, the model did not incorporate capacity and nonnegativity constraints so its applicability was limited to moderate floods.

To overcome this limitation, *Georgakakos and Marks* [1987] developed an extended linear quadratic Gaussian (ELQG) control technique, which is applicable to optimization problems with nonlinear dynamic systems with Gaussian disturbance, control/state equality and inequality constraints, and nonquadratic performance indices. In this paper, the ELQG control was applied for reservoir system management and identified optimal release (control) policy from reservoirs, maximizing hydropower generation while satisfying other operational objectives (e.g., flood protection and water supply). Further, *Georgakakos* [1989] expanded the ELQG control method to account for non-Gaussian disturbances of reservoir inputs and to handle more effectively state (e.g. storage) constraints by incorporating a new barrier function and high-order statistical moments.

## **2.4 Uncertainty characterization in hydrologic models**

The outputs (e.g., hydrograph) from deterministic hydrologic models are not useful because the models assume deterministic hydrologic inputs, approximated structure of the model, and calibrated model parameters all of which are not necessarily true in reality. Hydrologic input

data is intrinsically corrupted due to the limited ability to measure and process raw data (hydrologic input uncertainty). Models represent actual physical system in an approximated manner and incorporate parameters that are needed to be calibrated by using either input-output data or physical properties (model uncertainty). To make the outputs of deterministic models useful for practical applications, the uncertainties of the outcomes from the models must be quantified.

Many studies have analyzed the uncertainties of forecasts of hydrologic models (e.g., discharge or stage) associated with various hydrologic inputs [*Mills, 1980; CArdova and RodrAguiez-Iturbe, 1985; Hosking and Clarke, 1990; Lardet and Obled, 1994*]. As with the input uncertainty, many investigations have quantified the uncertainty associated with modeling [*Mills, 1980; Garen and Burges, 1981; Kuczera, 1988; Hromadka and McCuen, 1989; Hromadka and Whitley, 1989; Melching et al., 1990; Sarino and Serrano, 1990; Hromadka and Whitley, 1994; Lin and Wang, 1996*]. However, few research efforts have focused on how both input and model uncertainties affect the forecast of hydrologic models. *Wasimi and Kitanidis [1983]* and *Georgakakos et al. [1990]* approached this matter comprehensively. However, both approaches are limited to Gaussian inputs or the linearization of the governing equations for the use of the Kalman filter [*Kalman, 1960*].

To overcome these limitations and achieve computational efficiency, the analytic-numerical Bayesian forecasting system (BFS) is introduced [*Krzysztofowicz, 1999; Krzysztofowicz, 2002; Krzysztofowicz and Maranzano, 2004b*]. The BFS consists of three components: (1) the input uncertainty processor [*Kelly and Krzysztofowicz, 1994; Kelly and Krzysztofowicz, 2000*], (2)

the hydrologic (model) uncertainty processor [*Krzysztofowicz and Kelly, 2000; Krzysztofowicz and Herr, 2001; Krzysztofowicz and Maranzano, 2004; Krzysztofowicz and Maranzano, 2004a*], and (3) the integrator [*Krzysztofowicz, 2001*]. The BFS quantifies the uncertainties of the model forecast associated with input (by the input processor) and model uncertainties (by the model processor) independently and then integrate, through the integrator, into a conditional predictive distribution to identify the total uncertainty of the forecast. Another special feature of BFS is a meta-Gaussian distribution model built by normal quantile transform. Using this model, the analytical form of a posterior distribution from the Bayes theorem can be obtained for any form of the marginal distribution of simulated or measured data. Except special distribution families (e.g. exponential family), most of posterior distributions are obtained numerically if the normal quantile transform is not used. Therefore, the meta-Gaussian model save the computation time significantly and can be applied for various systems. The model also allows for a nonlinear and heteroscedastic relationship between model and realized forecasts. The parameters of the model can also be easily estimated via linear regressions.

## CHAPTER 3

### A NONLINEAR HYDROLOGIC RIVER ROUTING MODEL

This chapter describes the development of a new nonlinear hydrologic river routing model. It begins with a list of the modeling assumptions, describes a general algorithm for parameter estimation using control theory methods (Linear Quadratic Regulator, LQR), and presents an application with a three reservoir system (in the equatorial lake region of East Africa) and a river reach (Main Nile). The chapter concludes with a summary of findings and a discussion of hydrologic uncertainties.

#### 3.1 Modeling framework

##### 3.1.1 Assumptions

A new deterministic hydrologic river routing model is developed based on assumptions that 1) a river reach can be thought of as a cascaded series of interacting conceptual reservoirs in which outflow and water loss depend on storage (i.e., stored water volume in a reservoir) in a non-decreasing form; and 2) the interaction between adjacent reservoirs is described by a water balance equation. In addition to these assumptions, this study hypothesizes that 1) the representation of a river reach in the cascaded series makes it possible to effectively describe the nonlinear characteristics of flood waves like other cascade models [*Becker and Kundzewicz, 1987; Perumal, 1992; Perumal, 1994; Camacho and Lees, 1999*]; and 2) the dependence between outflow and storage, called a release function, and the dependence between loss and storage, called a loss function, can be identified from observed inflow and outflow data. This

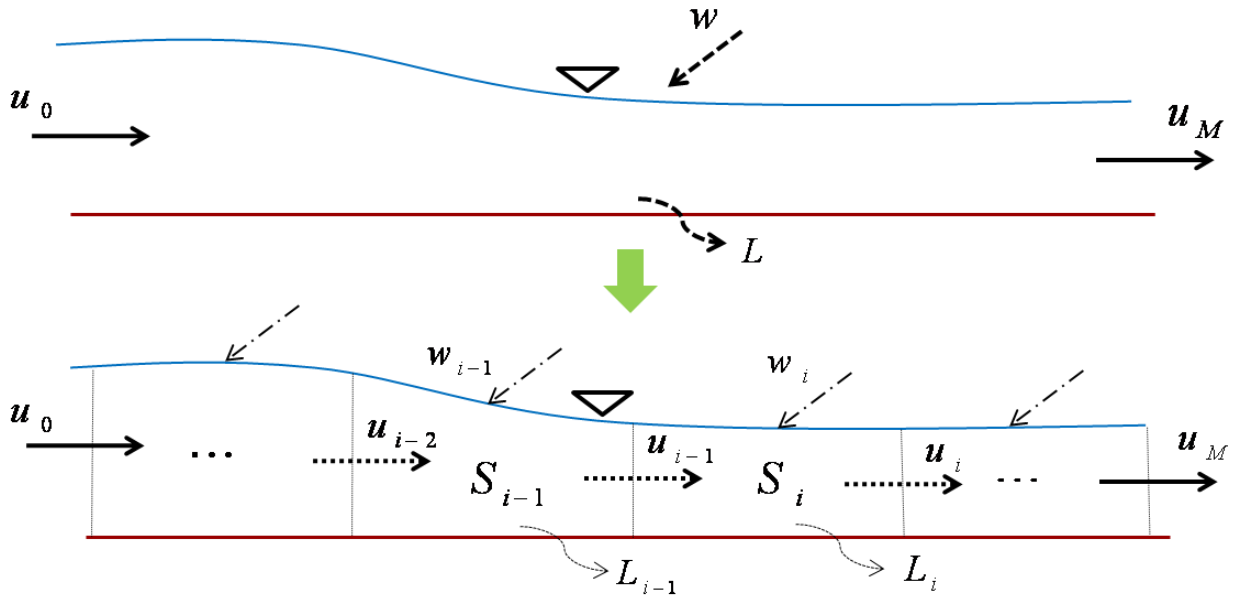
approach is different from current studies by *Cunge* [1969], *Muzik* [1974], and *Georgakakos* [1982] because they have predefined the types of the release functions as linear, exponential, or power laws and these properties are invariant over the entire range of flows through the reach. In this work, the cascaded conceptual reservoir approach is extended to allow for a more general nonlinear relationship between outflow and storage. The mathematical framework of this extension is developed and outlined below including a case study on the Equatorial Lake system. A second application on a general river reach is described in the next section.

Figure 3-1 shows a schematic interpretation of a river reach by a cascaded series of  $M$  conceptual reservoirs. Each  $i^{\text{th}}$  conceptual reservoir is characterized by its storage  $S_i(k)$  at the beginning of time step  $k$ , external inflow  $w_i(k)$ , outflow  $u_i(k)$ , and water loss  $L_i(k)$ .  $u_i(k)$  also become the inflow into the  $i+1^{\text{th}}$  reservoir. An external inflow can be a tributary inflow, watershed runoff, or hydrological inflow such as rainfall. Furthermore, a water loss is mainly caused by water seepage, retention on flood plains, net evaporation losses over the river surface, weir-controlled diversions, and others. The water balance response of the entire river reach can then be expressed by a set of coupled discrete-time dynamical equations:

$$\begin{aligned}
 S_1(k+1) &= S_1(k) + u_0(k) - u_1(k) - L_1(k) + w_1(k), \\
 &\dots \\
 S_i(k+1) &= S_i(k) + u_{i-1}(k) - u_i(k) - L_i(k) + w_i(k), \\
 &\dots \\
 S_M(k+1) &= S_M(k) + u_{M-1}(k) - u_M(k) - L_M(k) + w_M(k), \\
 k &= 1, \dots, N.
 \end{aligned} \tag{3.1}$$

In the above equations,  $u_0(k)$  is the reach inflow into the first conceptual reservoir of  $i = 1$ , and  $u_M(k) = Q(k)$  is the reach outflow from the last conceptual reservoir of  $i = M$ .  $u_0(k)$  and  $Q(k)$  are assumed known for all time steps  $k$ , as are  $w_i(k)$  for all reservoirs  $i$ . The reservoir release and loss terms,  $u_i(k)$  and  $L_i(k)$ , are only required to be non-decreasing functions of storage  $S_i(k)$  or a weighted storage between  $S_i(k)$  and  $S_i(k+1)$  that is  $x_i S_i(k) + (1-x_i) S_i(k+1)$ . When the change of storage between time step  $k$  and  $k+1$  is relatively insignificant, as in a lake or a very mild sloped river reach for a short time scale,  $S_i(k)$  alone can be used as the domain for the non-decreasing functions. Otherwise, the weighted storage should be used as the domain for taking into account a significant change of storage between time steps.

The development and calibration of this model consists of identifying the required number of conceptual reservoirs  $M$  and the associated functions  $u_i[S(k/k+1)]$  and  $L_i[S(k/k+1)]$  such that the model outflow  $u_M(k)$  simulate adequately well the observed outflow  $Q(k)$  for all  $k$ . (In what follows, the symbol  $S(k/k+1)$  denotes either  $S_i(k)$  or  $x_i S_i(k) + (1-x_i) S_i(k+1)$  whichever is applicable.)



**Figure 3-1.** Schematic view of a cascaded series of  $M$  conceptual reservoirs of a river reach.

### 3.1.2 Model identification and calibration procedure

First, the identification of the required number of conceptual reservoirs is addressed by developing models with progressively more reservoirs and determining the configuration that achieves satisfactory correspondence between  $u_M(k)$  and  $Q(k)$ , based on the principle of parsimony. For each conceptual reservoir configuration, the general model calibration procedure is outlined below:

#### Algorithm 3.1:

1. Assume that  $u_i[S_i(k/k+1)]$  and  $L_i[S_i(k/k+1)]$ ,  $i = 1, \dots, M$ , are equal to some initial non-decreasing functions of storage,  $f_{L_i}[S_i(k/k+1)]$  and  $f_{u_i}[S_i(k/k+1)]$ . These initial functions can be linear.

2. Fix the loss functions,  $f_{L_i} [S_i(k / k + 1)]$ , at their current nominal forms and determine the best outflows,  $u_i(k), i = 1, \dots, M$ , that solve the following sequence of iterative optimization problems:

$$\underset{u_i(k), i=1, \dots, M; k=1, \dots, N}{\text{Min}} \frac{1}{2} \sum_{k=1}^N \left\{ \theta_1 \left[ \frac{u_1(k) - f_{u_1} [S_1(k / k + 1)]}{Q^{\max}} \right]^2 + \dots + \theta_M \left[ \frac{u_M(k) - f_{u_M} [S_M(k / k + 1)]}{Q^{\max}} \right]^2 + \theta_{M+1} \left[ \frac{u_M(k) - Q(k)}{Q^{\max}} \right]^2 \right\} \quad (3.2)$$

subject to the system dynamics,

$$\begin{aligned} S_i(k+1) &= S_i(k) + u_{i-1}(k) - u_i(k) - f_{L_i} [S_i(k / k + 1)] + w_i(k), \\ i &= 1, \dots, M; k = 1, \dots, N. \end{aligned} \quad (3.3)$$

In the previous optimization problem,  $\theta_i, i = 1, \dots, M + 1$ , are coefficients properly specified to minimize the last error term in the objective function (simulated minus observed outflows) while keeping the decision variables  $u_i(k)$  in the vicinity of the initial non-decreasing function  $f_{u_i} [S_i(k / k + 1)], i = 1, \dots, M$ . This step involves a sequence of optimization problems, the solution of which creates a new set of non-decreasing release functions to be used in the next iteration of the optimization problems until no further improvement in the cumulative outflow error term estimated

by the new release functions and the fixed loss functions through the dynamical equations (3.1) can be achieved.

3. Fix the release functions,  $f_{u_i} [S_i(k/k+1)]$ , at their current nominal forms obtained in the previous step and determine the best water losses,  $L_i(k), i = 1, \dots, M$ , that solve the following sequence of iterative optimization problems:

$$\underset{L_i(k), i=1, \dots, M; k=1, \dots, N}{\text{Min}} \frac{1}{2} \sum_{k=1}^N \left\{ \theta_1 \left[ \frac{L_1(k) - f_{L_1} [S_1(k/k+1)]}{Q^{\max}} \right]^2 + \dots + \theta_M \left[ \frac{L_M(k) - f_{L_M} [S_M(k/k+1)]}{Q^{\max}} \right]^2 + \theta_{M+1} \left[ \frac{u_M(k) - Q(k)}{Q^{\max}} \right]^2 \right\} \quad (3.4)$$

subject to the system dynamics,

$$\begin{aligned} S_i(k+1) &= S_i(k) + f_{u_{i-1}} [S_{i-1}(k/k+1)] - f_{u_i} [S_i(k/k+1)] - L_i(k) + w_i(k), \\ i &= 1, \dots, M; k = 1, \dots, N. \end{aligned} \quad (3.5)$$

As before, the coefficients,  $\theta_i, i = 1, \dots, M+1$ , are used to minimize the last error term in the objective function while keeping the decision variables  $L_i(k)$  in the vicinity of initial non-decreasing functions  $f_{L_i} [S_i(k/k+1)], i = 1, \dots, M$ . It is noted that the decision variables of this problem are  $L_i(k), i = 1, \dots, M; k = 1, \dots, N$ , while releases  $u_i(k)$  are obtained from the release functions derived in Step 2. This step involves a sequence of optimization problems, the solution of which creates a new set of non-

decreasing loss functions used in the next iteration of the optimization problems until no further improvement of the cumulative outflow error term estimated by the new loss functions and the fixed release functions through the dynamical equations (3.1) can be achieved.

4. Iterate between Steps 2 and 3 until the release and loss functions  $f_{u_i} [S_i(k / k + 1)]$  and  $f_{L_i} [S_i(k / k + 1)]$  converge to stable forms, and the cumulative square error of the simulated outflows reaches a minimum value.

The following comments pertain to the previous model calibration procedure:

- i. The sequence of optimization problem in Steps 2 and 3 are solved *analytically*, using control theory methods for linear systems with quadratic cost. These methods, based on discrete-time linear quadratic regulator (LQR) theory, are herein modified to guarantee the non-decreasing function requirement. This modification is explained in comment iii below.
- ii. The previous procedure is flexible to identify various types of water losses and gains including net evaporation losses (or gains) over the river surface, weir-controlled diversions, groundwater seepage gains and losses, and others. The only requirement for these terms is that they be non-decreasing functions of the reach storage.
- iii. The new sets of non-decreasing release and loss functions for the  $i^{th}$  conceptual reservoir in Steps 2 and 3 respectively are generated by combining the solutions of the optimization problems  $S_i(k / k + 1)$  and  $u_i(k)$  or  $L_i(k)$  into pairs for each time  $k$  and reordering all pairs such that if  $S_i(k_1 / k_1 + 1) > S_i(k_2 / k_2 + 1)$ , then  $u_i(k_1) > u_i(k_2)$  or

$L_i(k_1) > L_i(k_2)$  for  $k_1 = 1, \dots, N, k_2 = 1, \dots, N$ , and  $k_1 \neq k_2$ . Finally, a nonlinear function or piecewise-defined nonlinear function is fitted against reordered data points. This function becomes the new non-decreasing release or loss function in each iteration of Step 2 or Step 3, respectively.

### 3.1.3 Discrete-time linear quadratic regulator (LQR)

A discrete-time linear quadratic regulator (LQR) applies to optimization problems involving systems with linear dynamics and quadratic cost functional. The cost could be 1) time to move from an initial state to a desired final state, 2) the energy of all intermediate and final states, and 3) any deviation of states or controls from their desired trajectories. In the linear dynamic system, a control is an input to the system and a state contains all information about the behavior of the system. In the context of river routing, the outflow and the storage are the control and state variables, respectively. Furthermore, the cost functional, as formulated in equation (3.4), is the sum of the square deviation of the simulated outflows of all conceptual reservoirs from their desired trajectories. For the last conceptual reservoir, this square difference is between simulated ( $u_M(k)$ ) and observed flows ( $Q(k)$ ). Finally, the dynamic system has linear dynamics, as illustrated by the water balance equation (3.1) when linearized around specific nominal state and control sequences.

Following *Lewis and Syrmos* [1995], the general LQR solution is derived next. The solution is general in that it applies to linear system of the following form:

$$x_{k+1} = A_k x_k + B_k u_k + C_k, \quad (3.6)$$

where the state is  $x_k \in R^n$ , the control  $u_k \in R^m$ , and the system matrices

$$A_k \in R^{n \times n}, B_k \in R^{n \times m}, C_k \in R^n.$$

The associated cost functional is quadratic:

$$\begin{aligned} J_1 &= \frac{1}{2} (x_N - \gamma_N)' P (x_N - \gamma_N) + \sum_{k=1}^{N-1} \left( \frac{1}{2} x_k' L_{xx}^k x_k + \frac{1}{2} u_k' L_{uu}^k u_k + u_k' L_{ux}^k x_k + L_x^{k'} x_k + L_u^{k'} u_k + \hat{L}^k \right) \\ &= \phi_N(x_N) + \sum_{k=1}^{N-1} L^k(x_k, u_k), \end{aligned} \quad (3.7)$$

where the weighting matrices are  $L_{xx}^k \in R^{n \times n}$ ,  $L_{uu}^k \in R^{m \times m}$ ,  $L_{ux}^k \in R^{m \times n}$ ,  $L_x^k \in R^n$ ,  $L_u^k \in R^m$ , and

$\hat{L}^k \in R^1$ , the terminal matrix is  $P \in R^{n \times n}$ , and the desired final state is  $\gamma_N \in R^n$ . The problem is

to find optimal solution  $u_k^*$ , which minimizes Equation (3.7) and simultaneously satisfies

Equation (3.6). To solve the problem, a Hamiltonian function is introduced to transform the

problem of minimizing the cost subject to the constraint, Equation (3.6), into the problem of

minimizing the Hamiltonian function without the constraint by introducing Lagrange

multipliers  $\lambda_{k+1}$ :

$$H^k(x_k, u_k) = \frac{1}{2} x_k' L_{xx}^k x_k + \frac{1}{2} u_k' L_{uu}^k u_k + u_k' L_{ux}^k x_k + L_x^{k'} x_k + L_u^{k'} u_k + \hat{L}^k + \lambda_{k+1}' (A_k x_k + B_k u_k + C_k).$$

$$(3.8)$$

In fact, through the transformation, the dependence of  $x_k$  and  $u_k$  is freed so that they behave as if they were independent variables by the extra degree of freedom  $\lambda_{k+1}$  [Lewis and Syrmos, 1995], so the gradients of  $H^k$  with respect to  $x_k$ ,  $u_k$ , and  $\lambda_{k+1}$  can be calculated independently. Then, the necessary conditions for the constrained minimum are given by

$$x_{k+1} = \frac{\partial H^k}{\partial \lambda_{k+1}} = A_k x_k + B_k u_k + C_k \quad (3.9)$$

$$\lambda_k = \frac{\partial H^k}{\partial x_k} = A_k' \lambda_{k+1} + L_{xx}^k x_k + L_{ux}^k u_k + L_x^k \quad (3.10)$$

$$0 = \frac{\partial H^k}{\partial u_k} = B_k' \lambda_{k+1} + L_{uu}^k u_k + L_{ux}^k x_k + L_u^k \quad (3.11)$$

$$\lambda_N = \frac{\partial \phi_N}{\partial x_N} = P(x_N - \gamma_N). \quad (3.12)$$

As illustrated in Appendix A, the optimal control and state sequences are calculated such that

$$S_k = L_{xx}^k + A_k' S_{k+1} A_k - \left( B_k' S_{k+1} A_k + L_{ux}^k \right)' \left( B_k' S_{k+1} B_k + L_{uu}^k \right)^{-1} \left( B_k' S_{k+1} A_k + L_{ux}^k \right), \quad S_N = P, \quad (3.13)$$

$$v_k = A_k' v_{k+1} - A_k' S_{k+1} C_k - L_x^k - \left( B_k' S_{k+1} A_k + L_{ux}^k \right)' \left( B_k' S_{k+1} B_k + L_{uu}^k \right)^{-1} \left( B_k' v_{k+1} - L_u^k - B_k' S_{k+1} C_k \right), \quad v_N = P \gamma_N, \quad (3.14)$$

$$u_k^* = - \left( B_k' S_{k+1} B_k + L_{uu}^k \right)^{-1} \left[ \left( B_k' S_{k+1} A_k + L_{ux}^k \right) x_k^* + B_k' S_{k+1} C_k - B_k' v_{k+1} + L_u^k \right], \quad (3.15)$$

$$x_{k+1}^* = A_k x_k^* + B_k u_k^* + C_k. \quad (3.16)$$

Equation (3.13) is called a Riccati equation. With boundary condition  $S_N = P$ , the solution of the Riccati equation  $S_k$  is defined by backward recursion. As with  $S_k$ , the auxiliary sequence  $\nu_k$  is computed recursively backward with the boundary condition  $\nu_N = P\gamma_N$ . Furthermore,  $S_k$  and  $\nu_k$  can be computed off-line even before optimal control  $u_k^*$  is calculated. Subsequently,  $u_k^*$  and  $x_k^*$  are computed by alternating Equations (3.15) and (3.16) in  $k$  with the already calculated  $S_k$ ,  $\nu_k$ , and a given initial state  $x_1$ . Optimal control  $u_k^*$  is a function of  $x_k^*$ , so it is called a state feedback or a close-loop control that decides current optimal control in terms of the state at the same time.

## 3.2 Application to the Equatorial Lake system

### 3.2.1 Approach

Flow data at both upstream and downstream gauge stations can be easily obtained, so the hypotheses in section 3.1.1 could be tested implicitly by comparing the simulated and observed flows at the downstream station. However, this test cannot fully evaluate the routing model's performance in identifying release or loss functions because their correspondences in the field are usually unavailable to be compared. This is because, in most cases, the related hydraulic data cannot be easily obtained due to high demand for quantity and quality of data.

Alternatively, a lake system can be utilized in testing the model's performance. First of all, the historical data of storage, discharge, and inflows have been well maintained in some lake systems. Furthermore, the system is compatible with the conceptual representation of a river reach in that 1) it consists of a series of cascading reservoirs each of which releases water depending on its storage; and 2) reservoirs operate based on water balance. Because most lakes are connected by rivers that have significant travel time between upstream and downstream lakes, a much longer time step is selected for the water balance equation in this test. Then it is reasonable to assume that the outflow from a given lake becomes the inflow into the next lake downstream at the same time step, which is consistent with the assumption of the model. The next sections provide a brief hydrological description of the Equatorial Lake system and proceed with the application of the river routing model.

### **3.2.2 Equatorial Lakes**

The Equatorial Lake system, as shown in Figure 3-2, encompasses Lakes Victoria, Kyoga, and Albert and their drainage basins. The system begins with Lake Victoria, shared by Uganda, Kenya, and Tanzania, with contributing catchment areas in Rwanda, Burundi, and the Democratic Republic of Congo (DRC). The lake has a surface area of about 70,000 km<sup>2</sup> and a total catchment area of nearly 193,000 km<sup>2</sup>. Because of its size, the magnitudes of rainfall and evaporation on the lake's surface are much greater than the magnitude of direct runoff from the catchments [*Hydromet*, 1992]. The Upper Victoria Nile drops 105 m over its 130 km course to carry the main outflow of Lake Victoria northerly towards Lake Kyoga. Lake Kyoga is a shallow lake, only a few meters deep, surrounded by mostly wetlands with a combined surface

area of 4,700 km<sup>2</sup>. The total area of catchments of the lake is approximately 75,000 km<sup>2</sup> [Shahin, 1985; Sutcliffe and Parks, 1999]. The lake is connected by the Lower Victoria Nile to Lake Albert, dropping 410 m along its 200 km course to the north and the west. Lake Albert has a surface area of nearly 5,300 km<sup>2</sup> and surrounding watersheds of 17,000 km<sup>2</sup> [Shahin, 1985]. The combined lake storage capacity is nearly 260 billion cubic meters (bcm), 215 bcm of which comprise Lake Victoria. The lake contributes almost 90% of the total equatorial lake outflow. The two rainy seasons over the watershed (in March-May and November-December) and the dampening storage effect from the vast size of the lake give rise to a seasonally uniform outflow. Table 3-1 lists the elevation ranges and active storages for the Equatorial Lake system [Hydromet, 1992]. In addition, the travel time between Lakes Victoria and Kyoga is less than half a day and that between Kyoga and Albert is nearly one day [SMEC, 1977].

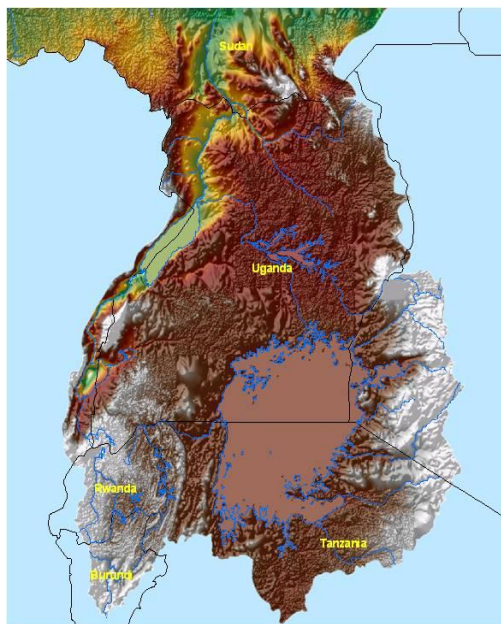


**Figure 3-2.** The Equatorial Lake system.

**Table 3-1.** Elevation ranges and active storages of the lakes (Hydromet 1992).

Lake	Min. Level (m)	Max. Level (m)	Active Storage (bcm)
Victoria	1133.08	1136.28	215.55
Kyoga	1030.31	1034.11	14.91
Albert	618.75	623.97	29.86

### 3.2.3 Model identification and calibration procedure

As a benchmark lake model, each lake in the Equatorial Lake system (Lake Victoria numbered by  $i = 1$ , Lake Kyoga by  $i = 2$ , and Lake Albert by  $i = 3$ ) is characterized by its storage  $S_i(k)$  at the beginning of monthly time step  $k$ , net basin supply  $w_i(k)$ , and outflow  $u_i(k)$ .  $u_i(k)$  also become the inflow into the  $i + 1^{th}$  lake. Net basin supply (NBS) that is the amount of net external input to a lake is estimated by

Net basin supply = runoff + precipitation - evaporation + human inflow - human outflow.

The water balance response of the Equatorial Lake system can be expressed by a set of coupled discrete-time linear dynamical equations:

$$\begin{aligned} S_1(k+1) &= S_1(k) - u_1(k) + w_1(k), \\ S_2(k+1) &= S_2(k) + u_1(k) - u_2(k) + w_2(k), \\ S_3(k+1) &= S_3(k) + u_2(k) - u_3(k) + w_3(k), \\ k &= 1, \dots, N. \end{aligned} \tag{3.17}$$

In the above equation,  $S_i(k), i = 1, 2, 3$ , and  $u_i(k), i = 1, 2, 3$ , are historically known and used to construct release rules for each lake by combining them into pairs for each time  $k$ . Hence, the lake release  $u_i(k)$  is a non-decreasing function of  $S_i(k)$ , as appeared by solid blue curves in

Figure 3-3. Since reasonably accurate estimates of each of the terms in the equation of NBS above are not available,  $w_i(k)$  is calculated by properly rearranging the dynamical equations with all the known terms,  $S_i(k)$  and  $u_{i-1}(k)$  or  $u_i(k)$ , on the right-hand side. Since water losses have been taken into account in the estimation of NBS, the benchmark lake model does not incorporate water loss terms  $L_i(k), i = 1, 2, 3$ .

For the new routing model,  $u_3(k) = Q(k)$  and  $w_i(k), i = 1, 2, 3$ , are the only model inputs. By identifying the release-storage functions estimated by the benchmark lake model, the validity of the model identification procedure can then be tested by comparing the model-derived release functions with the actual forms. The model identification and calibration procedure for this test is based on Algorithm 3.1 and skips the procedure of the identification of loss functions. The detailed procedure is outlined below:

1. Assume that  $u_i(k)$ , are equal to some linear non-decreasing functions of storage

$S_i(k), i = 1, 2, 3$ , that is  $u_i(k) = f_{u_i}[S_i(k)] = \alpha_i S_i(k) + \beta_i$ . Then, the best parameters

$\alpha_i$  and  $\beta_i, i = 1, 2, 3$ , that yields the smallest cumulative square error of the simulated

outflows from the Lake Albert are chosen among all feasible values of the parameters.

The dynamical system used in the process of finding the initial release rules is described by

$$\begin{aligned}
S_1(k+1) &= S_1(k) - [\alpha_1 S_1(k) + \beta_1] + w_1(k), \\
S_2(k+1) &= S_2(k) + [\alpha_1 S_1(k) + \beta_1] - [\alpha_2 S_2(k) + \beta_2] + w_2(k), \\
S_3(k+1) &= S_3(k) + [\alpha_2 S_2(k) + \beta_2] - [\alpha_3 S_3(k) + \beta_3] + w_3(k),
\end{aligned} \tag{3.18}$$

where  $\alpha_3 S_3(k) + \beta_3$  is the simulated outflow from the last lake.

2. Determine the best lake outflows,  $u_i(k), i = 1, 2, 3$ , that solve the following sequence of iterative optimization problems:

$$\begin{aligned}
\text{Min}_{u_i(k), i=1,2,3; k=1,\dots,N} \frac{1}{2} \sum_{k=1}^N \left\{ \theta_1 \left[ \frac{u_1(k) - f_{u_1}^k[S_1(k)]}{Q^{\max}} \right]^2 + \theta_2 \left[ \frac{u_2(k) - f_{u_2}^k[S_2(k)]}{Q^{\max}} \right]^2 + \theta_3 \left[ \frac{u_3(k) - f_{u_3}^k[S_3(k)]}{Q^{\max}} \right]^2 + \theta_4 \left[ \frac{u_3(k) - Q(k)}{Q^{\max}} \right]^2 \right\}
\end{aligned} \tag{3.19}$$

subject to the system dynamics,

$$\begin{aligned}
S_1(k+1) &= S_1(k) - u_1(k) + w_1(k), \\
S_2(k+1) &= S_2(k) + u_1(k) - u_2(k) + w_2(k), \\
S_3(k+1) &= S_3(k) + u_2(k) - u_3(k) + w_3(k), \\
k &= 1, \dots, N.
\end{aligned} \tag{3.20}$$

In the previous optimization problem,  $f_i^k[S_i(k)] = a_i^k S_i(k) + b_i^k, i = 1, 2, 3$ , are local linear functions defined by first-order Taylor expansion of  $f_{u_i}[S_i(k)]$  at their nominal values of  $S_i(k)$ . This linearization of the release functions is necessary to make the dynamics linear and the objective function (Equation (3.19)), quadratic so that LQR can yield the

optimal solutions of the sequence of optimization problems that are  $S_i^*(k)$  and  $u_i^*(k), i=1,2,3; k=1,\dots,N$ . Omitting the superscript  $k$  of the local linear functions, the system matrices used in LQR are

$$A^k = \begin{bmatrix} 1 & 0 & 0 \\ 0 & 1 & 0 \\ 0 & 0 & 1 \end{bmatrix}, \quad B^k = \begin{bmatrix} -1 & 0 & 0 \\ 1 & -1 & 0 \\ 0 & 1 & -1 \end{bmatrix}, \quad C^k = \begin{bmatrix} w_1(k) \\ w_2(k) \\ w_3(k) \end{bmatrix}, \quad (3.21)$$

and the weighting matrices are

$$L_{xx}^k = \begin{bmatrix} 2\theta_1 a_1^2 & 0 & 0 \\ 0 & 2\theta_2 a_2^2 & 0 \\ 0 & 0 & 2\theta_3 a_3^2 \end{bmatrix}, \quad L_{uu}^k = \begin{bmatrix} 2\theta_1 & 0 & 0 \\ 0 & 2\theta_2 & 0 \\ 0 & 0 & 2(\theta_3 + \theta_4) \end{bmatrix}, \quad L_{ux}^k = \begin{bmatrix} -2\theta_1 a_1 & 0 & 0 \\ 0 & -2\theta_2 a_2 & 0 \\ 0 & 0 & -2\theta_3 a_3 \end{bmatrix},$$

$$L_x^k = \begin{bmatrix} 2\theta_1 a_1 b_1 \\ 2\theta_2 a_2 b_2 \\ 2\theta_3 a_3 b_3 \end{bmatrix}, \quad L_u^k = \begin{bmatrix} -2\theta_1 b_1 \\ -2\theta_2 b_2 \\ -2\theta_3 b_3 - 2\theta_4 Q(k) \end{bmatrix}, \quad \hat{L}^k = \theta_1 b_1^2 + \theta_2 b_2^2 + \theta_3 b_3^2 + \theta_4 Q(k)^2,$$

$$P = \begin{bmatrix} 0 & 0 & 0 \\ 0 & 0 & 0 \\ 0 & 0 & 0 \end{bmatrix}.$$

(3.22)

3. Create non-decreasing release functions  $f_{u_i} [S_i(k)], i=1,2,3$ , by rearranging the orders of  $[S_i^*(k), u_i^*(k)], k=1,\dots,N$ , such that if  $S_i^*(k_1) > S_i^*(k_2)$ , then  $u_i^*(k_1) > u_i^*(k_2)$  for  $k_1 = 1,\dots,N, k_2 = 1,\dots,N$ , and  $k_1 \neq k_2$ .

4. Calculate local linear release functions from the new set of non-decreasing release functions obtained in Step 3 using first-order Taylor expansion and nominal sequence of  $S_i(k)$  calculated by the dynamical equations (3.17). The cumulative square error between modeled and actual outflows is also computed using the local linear release functions.
5. Iterate between Steps 2, 3, and 4 until the release functions converge to stable forms, and the cumulative square error calculated in Step 4 reaches a minimum value.

### 3.2.4 Results

A total of six different applications (experiments) of the river routing model are performed.

The list of given conditions in each application is as follows:

- Experiment 1: The following quantities are assumed perfectly known: Initial storages for all lakes; observed NBS sequences; Lake Albert outflows.
- Experiment 2: Observed NBS sequences and observed Lake Albert outflows are perfectly known; all other quantities are estimated by the model.
- Experiment 3: NBS sequences and Lake Albert outflows are assumed imperfectly known through sequences including random errors the strength of which is 5% of the actual sequence values.
- Experiment 4: NBS sequences and Lake Albert outflows are assumed imperfectly known through sequences including random errors with strength 10% of the actual sequence values.

- Experiment 5: NBS sequences and Lake Albert outflows are assumed imperfectly known through sequences including random errors with strength 15% of the actual sequence values.
- Experiment 6: NBS sequences and Lake Albert outflows are assumed imperfectly known through sequences including random errors with strength 15% of the actual sequence values.

In the first two cases, NBS's for all lakes are observed values. Moreover, the observed initial storages for all of the lakes are used in the last four cases. The entire 792 months (January 01, 1912 ~ December 01, 1977) is divided into two periods in which the first one is the calibration horizon, 700 months (January 01, 1912 ~ April 01, 1970), and the other is the validation horizon, 92 months (April 01, 1970 ~ December 01, 1977).

#### **3.2.4.1 Results for the first experiment**

As illustrated in Figure 3-3, the model identifies the release functions for all lakes very accurately in the calibration. Furthermore, the estimated storages and outflows sequences for all lakes are almost perfectly matched with the observed ones, as shown in Figure 3-4. To measure the accuracy of the model's prediction, three statistics are presented: 1) normalized root mean squared error (NRMSE) of storages and outflows; 2) time-to-peak error; and 3) peak discharge error in terms of NRMSE. All three measures are computed based on the difference between simulated and observed data over the calibration and validation periods, respectively. For example, NRMSE of the outflow at Albert is calculated using the model-identified release function from

$$\sqrt{\frac{1}{N} \sum_{k=1}^N \left( \frac{f_3^k(S_3(k)) - Q(k)}{Q(k)} \right)^2} \quad (3.23)$$

and quantifies the spread of the differences between simulated and observed outflows normalized by the observed outflow values. As illustrated in Table 3-2, most NRMSE exhibit a less than 1% mean relative error from the observed sequences. Kyoga has the largest spread in the storage, outflow, and peak errors, albeit less than 1%. The reason is that the slope of the release function curve is largest in Lake Kyoga, making it more sensitive to outflow changes than the other two lakes. Figure 3-4 shows a comparison of the simulated and observed sequences for the entire horizon (including both the calibration and the validation periods), and Figure 3-5 shows the sequences for the validation period only. The figures clearly show that the model can indeed identify the correct form of the release functions, given perfect knowledge of the other inputs.

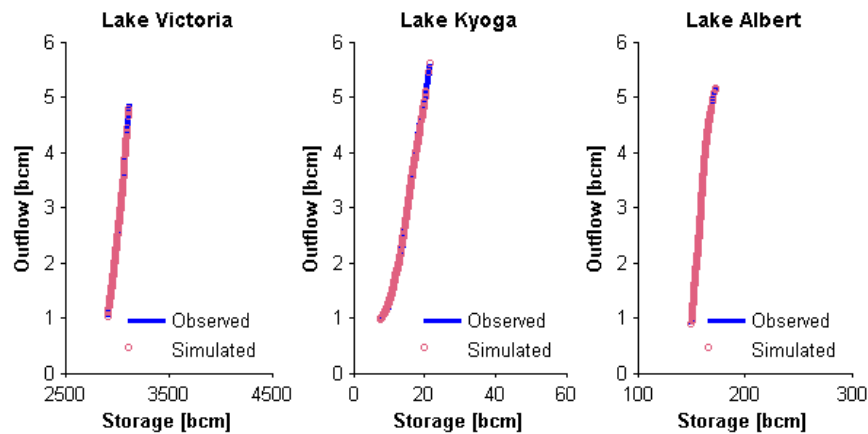


**Figure 3-3.** Estimated release functions for the first experiment.

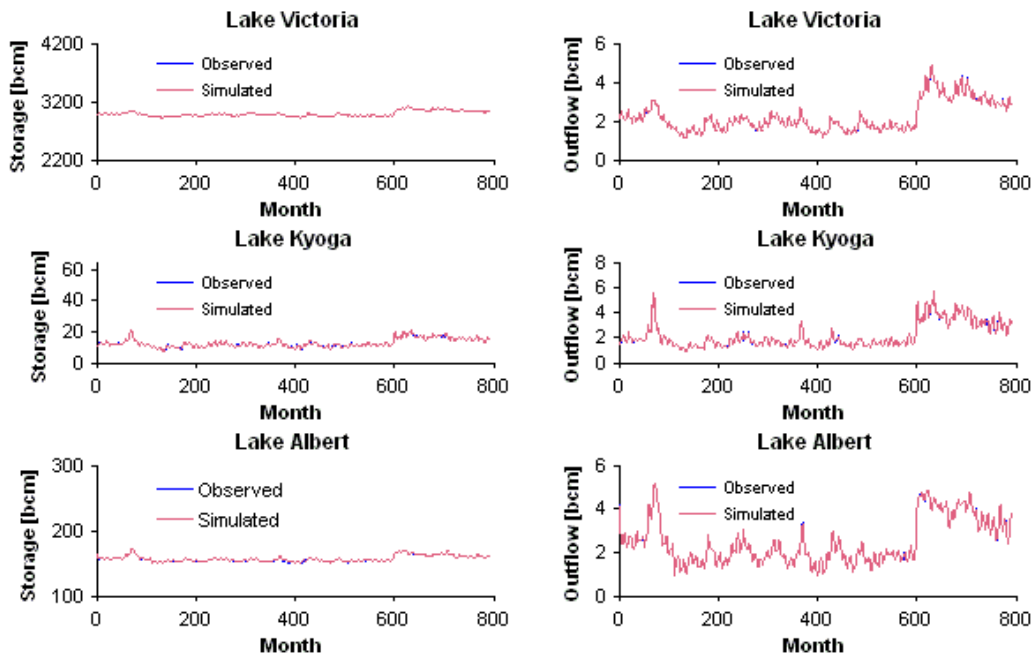


**Figure 3-4.** Model verification during the entire time period (calibration + validation) for the first experiment.

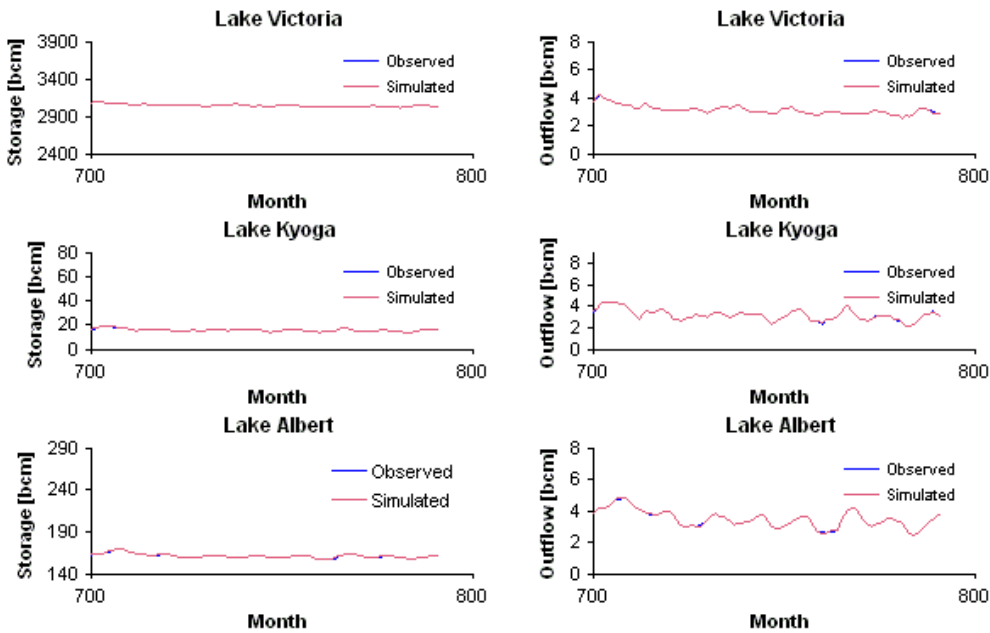
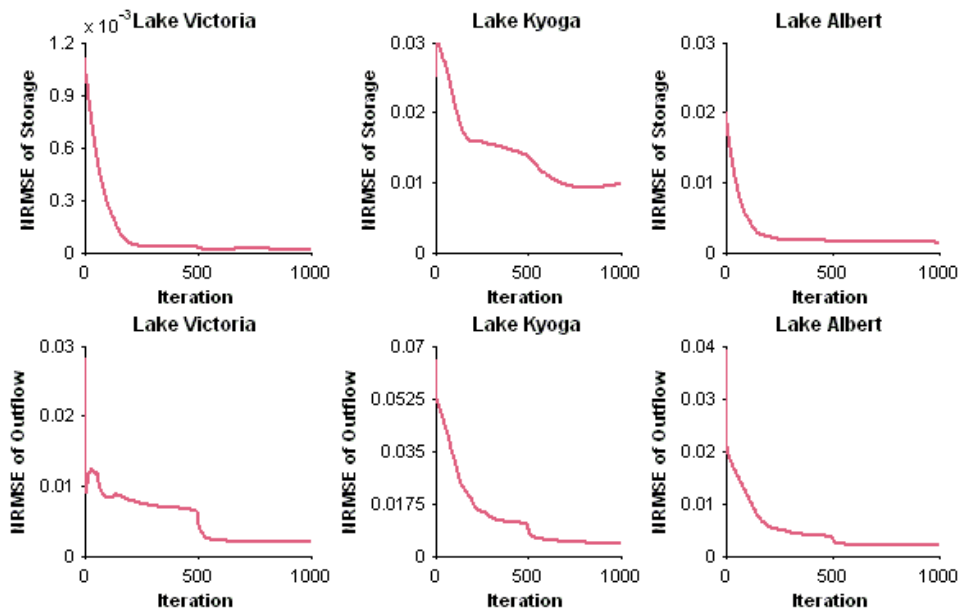


**Figure 3-5.** Model verification during validation for the first experiment.

**Table 3-2.** Evaluation of river routing model for the first experiment.

	Calibration			Validation		
	NRMSE, %	Time-To-Peak error, Months	NRMSE of peaks, %	NRMSE, %	Time-To-Peak error, Months	NRMSE of peaks, %
$S_1$	0.00	0.00	0.00	0.00	0.00	0.00
$S_2$	1.63	0.00	1.46	0.39	0.00	0.30
$S_3$	0.10	-0.01	0.10	0.05	0.00	0.02
$u_1$	0.23	0.00	0.28	0.20	0.00	0.17
$u_2$	0.54	0.00	0.49	0.77	0.00	0.48
$u_3$	0.16	-0.01	0.16	0.20	0.00	0.16

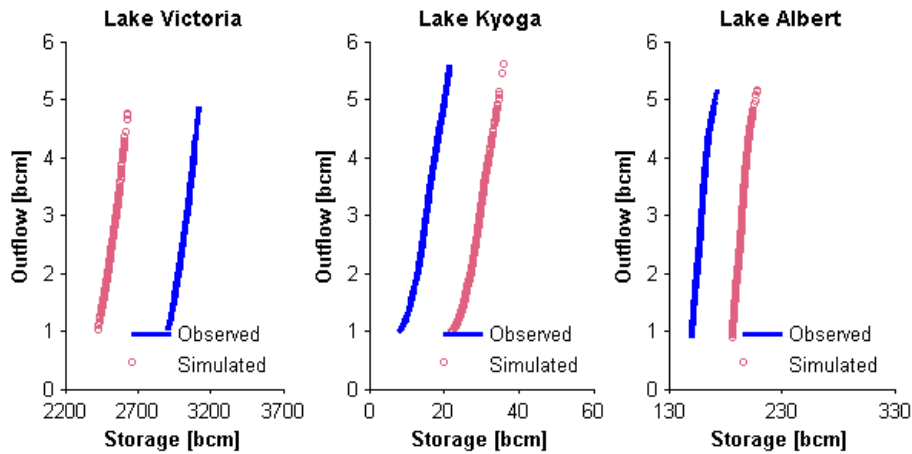
A sensitivity analysis for the first experiment is shown in Figure 3-6. In the figure, the NRMSE of the estimated storages and outflows with respect to the observed storages and outflows are calculated. This analysis shows that within 200 iterations, a rapid adjustment of the release functions takes place, and the functions converge to the right forms. After that, considerably slower improvement is made by mainly refining the shapes of the curves. Sudden drops and spikes in the sensitivity curves are reasonably expected in cases where the true release functions are more nonlinear.



**Figure 3-6.** Sensitivity analysis for the first experiments.

### 3.2.4.2 Results for the second experiment

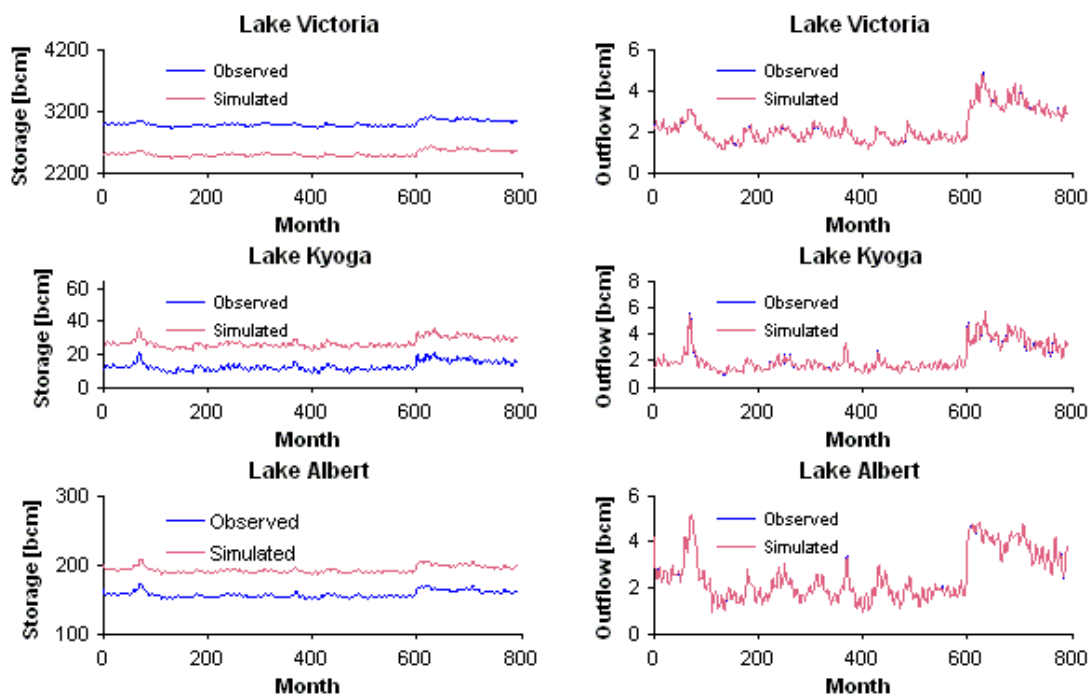
The observed initial storages are 2,986 bcm for Lake Victoria, 11.22 bcm for Lake Kyoga, and 163.81 bcm for Lake Albert. The initial storages in the second condition are changed by -486 bcm in Lake Victoria, 13.78 bcm in Lake Kyoga, and 36.19 bcm in Lake Albert. The purpose of this experiment is to see what effect the initial storage discrepancy will have on the identified release function forms. The results appear in Figure 3-7 to Figure 3-10 and Table 3-3.



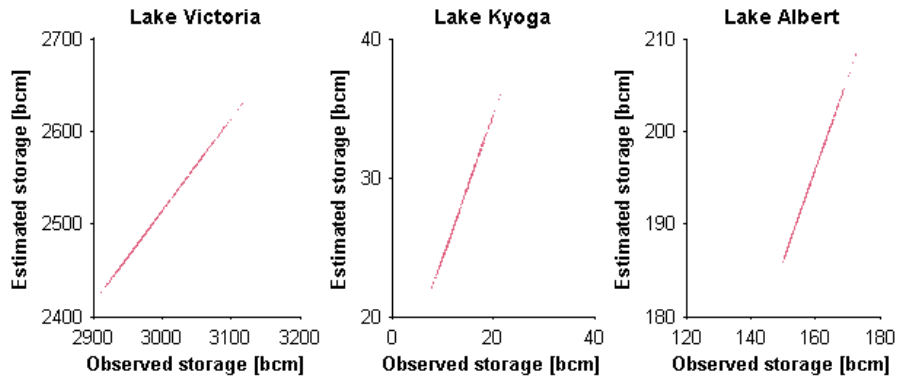
**Figure 3-7.** Estimated release functions for the second experiment.

Figure 3-7 clearly shows that, as a result of the imperfect initial storage information, the identified release functions are parallel to the actual forms but shifted by the amount of the initial storage discrepancies. In fact, the arithmetic average of the deviation of their storage sequences are -486.20 bcm for Lake Victoria, 14.25 bcm for Lake Kyoga, and 35.89 bcm for Lake Albert, respectively, very close to the initial storage discrepancies of -486 bcm, 13.78 bcm, and 36.19 bcm. Furthermore, the outflow NRMSE is 0.31%, 0.57%, 0.20%, respectively. Because of the proper positioning of the curves and equal slopes of the estimated and observed curves for a given outflow, the different initial storages release equal outflows at  $k = 1$  from the estimated and observed release functions, respectively, and the outflows cause equal changes in both storages at  $k = 2$  through the water balance equation. Then, the next storages at  $k = 2$  again generate equal outflows for the next time step. This process continues recursively for all  $k$ . Therefore, the model manages to match the observed outflow sequences, and the changes in both observed and estimated storages sequences are very similar, but translated by the initial storage error. Hence, Figure 3-9 shows almost perfect linear relationships between

the observed and estimated storage sequences for all lakes. Furthermore, the sample correlation coefficients for a set of their paired storage sequences are 1.0 for Lake Victoria, 0.999 for Lake Kyoga, and 0.999 for Lake Albert, and the sample standard deviations are 0.044 bcm, 0.110 bcm, and 0.083 bcm, respectively. The previous experiment shows that for this system, the model identification procedure cannot identify the initial storages, but can identify the correct release function shapes and observed outflows. From all of these observations, the predicted values of the storages by the estimated release functions are still very useful for forecasting changes in storage in the future. The figures in Table 3-3 also indicate that the model yields accurate estimates of outflows and time-to-peaks for all of the lakes.



**Figure 3-8.** Model verification over the entire time period for the second experiment.



**Figure 3-9.** Correlation analysis.

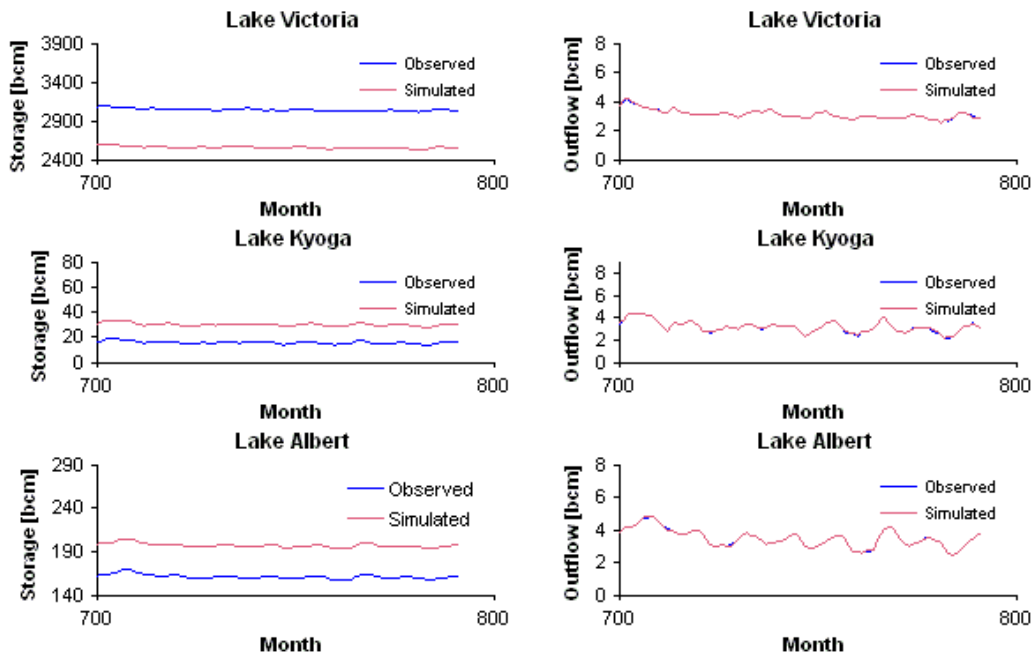


**Figure 3-10.** Model verification during validation for the second experiment.

**Table 3-3.** Evaluation of river routing model for the second experiment.

	Calibration			Validation		
	NRMSE, %	Time-To-Peak error, Months	NRMSE of peaks, %	NRMSE, %	Time-To-Peak error, Months	NRMSE of peaks, %
$S_1$	16.32	0.00	16.28	15.98	0.00	15.98
$S_2$	120.16	0.01	110.66	92.89	0.00	90.56
$S_3$	23.01	0.00	22.88	22.28	0.00	22.18
$u_1$	0.31	0.00	0.38	0.25	0.00	0.24
$u_2$	0.57	0.01	0.43	0.76	0.00	0.47
$u_3$	0.20	0.00	0.15	0.24	0.00	0.13

This, however, is a special system where the coefficient of the storage transition term is 1.

Most hydrologic or hydraulic systems are stable, so the system response, in the absence of any input, will approach zero as time goes infinity. The discrete-time state equation without any input is  $\mathbf{x}(k+1) = \mathbf{A}\mathbf{x}(k)$ ,  $\mathbf{x} \in R^n$ ,  $\mathbf{A} \in R^{n \times n}$ , and the solution is  $\mathbf{x}(k) = \mathbf{A}^k \mathbf{x}(0)$ ,  $k \geq 0$ . Since the system matrix used until now has been

$$\mathbf{A} = \begin{bmatrix} 1 & 0 & 0 \\ 0 & 1 & 0 \\ 0 & 0 & 1 \end{bmatrix},$$

system states  $\mathbf{x}(k)$  converge to  $\mathbf{x}(0)$ , the initial states, so the system is critically stable.

However, if the system matrix is

$$A = \begin{bmatrix} \alpha_1 & 0 & 0 \\ 0 & \alpha_2 & 0 \\ 0 & 0 & \alpha_3 \end{bmatrix}, \alpha_i < 1, i = 1, \dots, 3,$$

then all of the entries of  $\mathbf{x}(k)$  converge to zero as time  $k$  approaches infinity. Hence, the system is stable.

When the system is stable, and the model identification procedure can also identify the initial storages. To prove this argument, a stable version of the Equatorial Lake system is constructed:

$$\begin{aligned}
 S_1(k+1) &= \alpha_1 S_1(k) - u_1(k) + w_1(k), \\
 S_2(k+1) &= \alpha_2 S_2(k) + u_1(k) - u_2(k) + w_2(k), \\
 S_3(k+1) &= \alpha_3 S_3(k) + u_2(k) - u_3(k) + w_3(k), \\
 k &= 1, \dots, N.
 \end{aligned} \tag{3.24}$$

In the above equation, the values of storage coefficients  $\alpha_1, \alpha_2$ , and  $\alpha_3$  are 0.95, 0.93, and 0.92, respectively. In addition, different sets of initial storages are tested as follows:

1. Case 1: 2836 bcm / 4.805 bcm / 133.45 bcm for Lake Victoria, Kyoga, and Albert.
2. Case 2: 2936 bcm / 8.805 bcm / 153.45 bcm.
3. Case 3: 3036 bcm / 14.805 bcm / 173.45 bcm.
4. Case 4: 3136 bcm / 18.805 bcm / 193.45 bcm.
5. Observed initial storages: 2986 bcm / 11.22 bcm / 163.81 bcm.

For comparison purposes, these sets of initial storages are tested with the original system of Equation (3.20). The estimated release functions for the different sets of initial storages are

shown in Figure 3-11. The SSE of the estimated outflow of Lake Albert with respect to the observed outflow, calculated from all of the estimated release functions, are equal to one another. Therefore, the identifications of initial storages and actual release functions based on the SSE are impossible in the original system with storage coefficients equal to 1.

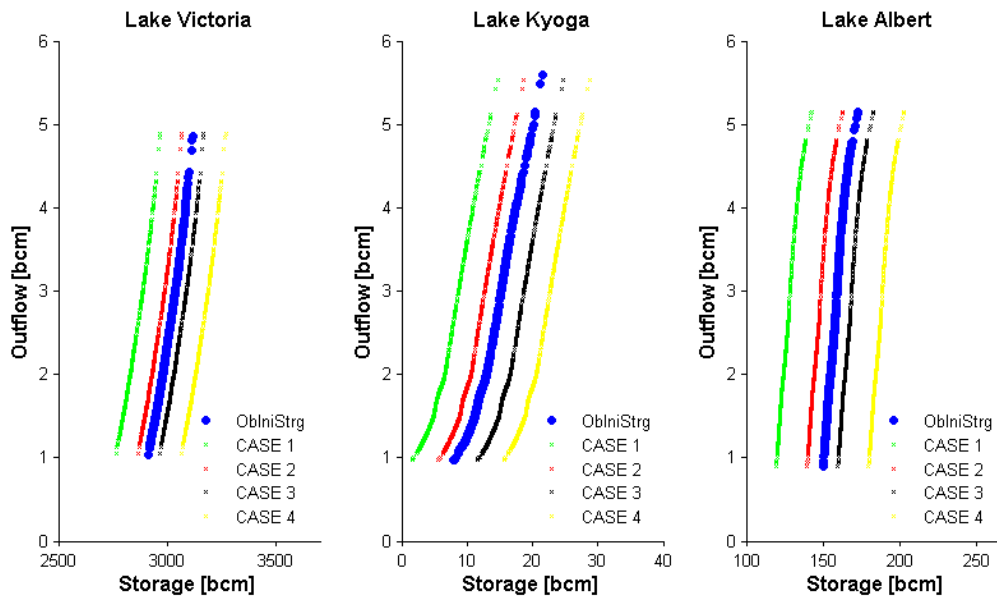


**Figure 3-11.** Release functions for the original system. ObIniStrg means observed initial storages.

However, the release functions estimated from the stable system, as seen in Figure 3-12, produce different SSE for different sets of initial storages. The SSE are  $23.4 \text{ bcm}^2$ ,  $2.8 \text{ bcm}^2$ ,  $3.06 \text{ bcm}^2$ , and  $21.3 \text{ bcm}^2$  for case 1, case 2, case 3, and case 4, respectively. As initial storages are assumed closer to the observed values, the estimated release functions produce much smaller SSE, thus making it possible to identify the observed initial storages and release functions based on the calculated SSE.

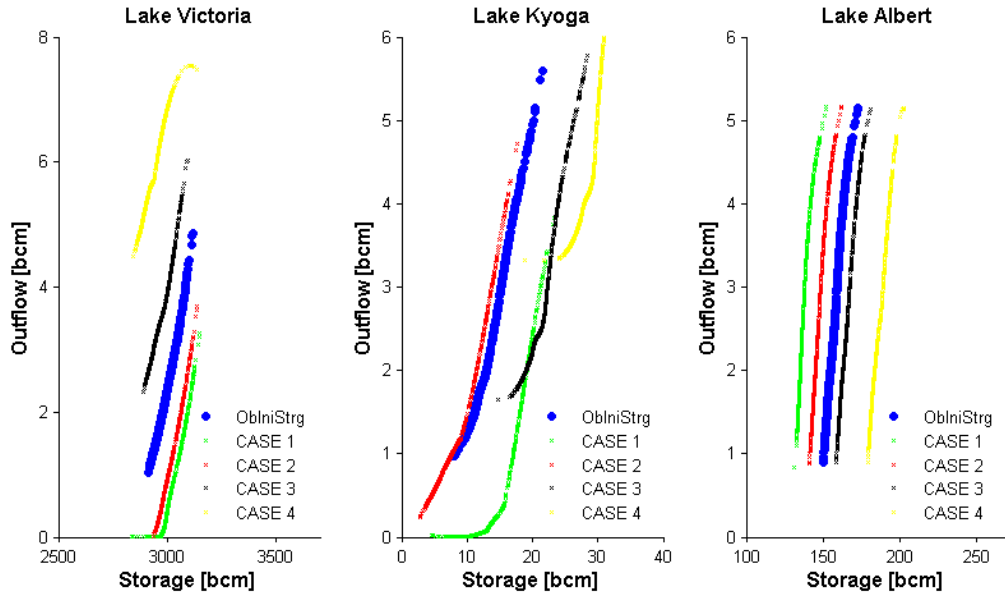


**Figure 3-12.** Release functions for stable systems. ObIniStrg means observed initial storages.

### 3.2.4.3 Results for the experiments three through six

In this and the following three sections, the river routing model identification procedure is applied with artificially perturbed inputs that mimic the uncertainty of observed or measured data. Assuming that measurement errors are normally distributed, the error perturbations are generated using standard normal random variates. Denoting by  $z_i(k)$  the random error of the  $i$ th input at time  $k$ , the perturbed inputs are obtained from:

$$\begin{aligned}
 \tilde{Q}(k) &= Q(k) + z_1(k) Q(k) \alpha \\
 \tilde{w}_1(k) &= w_1(k) + z_2(k) w_1(k) \alpha \\
 \tilde{w}_2(k) &= w_2(k) + z_3(k) w_2(k) \alpha \\
 \tilde{w}_3(k) &= w_3(k) + z_4(k) w_3(k) \alpha
 \end{aligned} \tag{3.25}$$

The value of  $\alpha$  signifies the perturbation intensity and in the experiments that follow takes on the values 0.05, 0.1, 0.15, and 0.2. These values respectively introduce a 5%, 10%, 15%, and 20% average discrepancy from the true input values. Figure 3-13 to Figure 3-16, show the perturbed NBSs and Lake Albert outflows for each value of  $\alpha$ . The paragraphs that follow assess the ability of the model identification procedure to correctly identify the release functions in the presence of a range of noise levels.

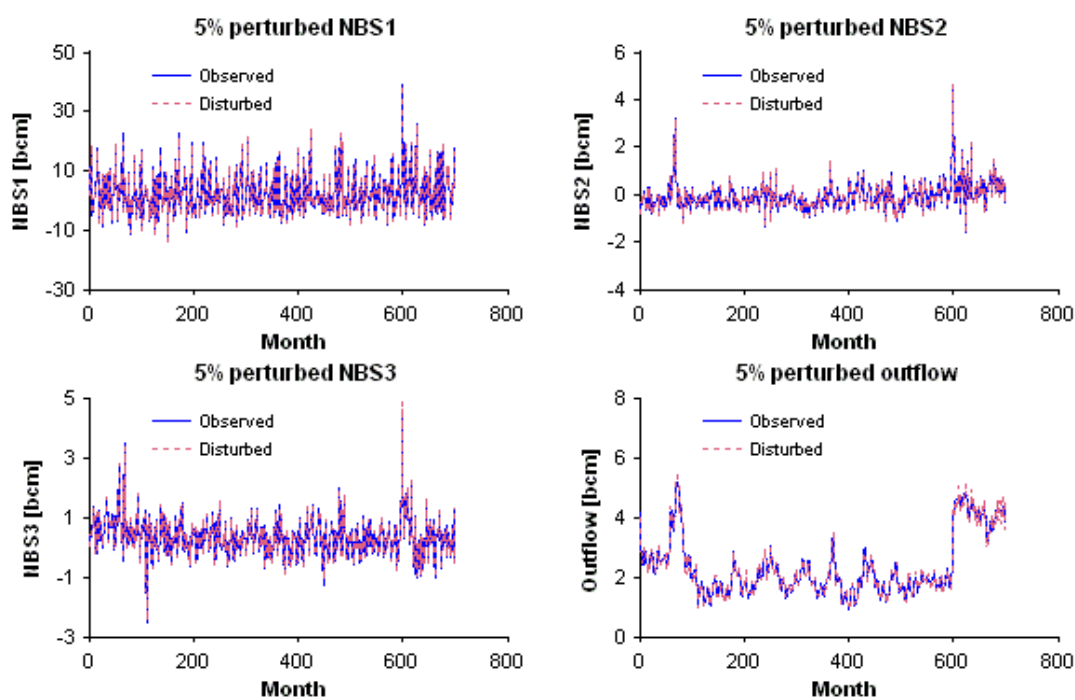


**Figure 3-13.** 5% disturbed NBS of each lake and 5% disturbed outflow of Lake Albert.

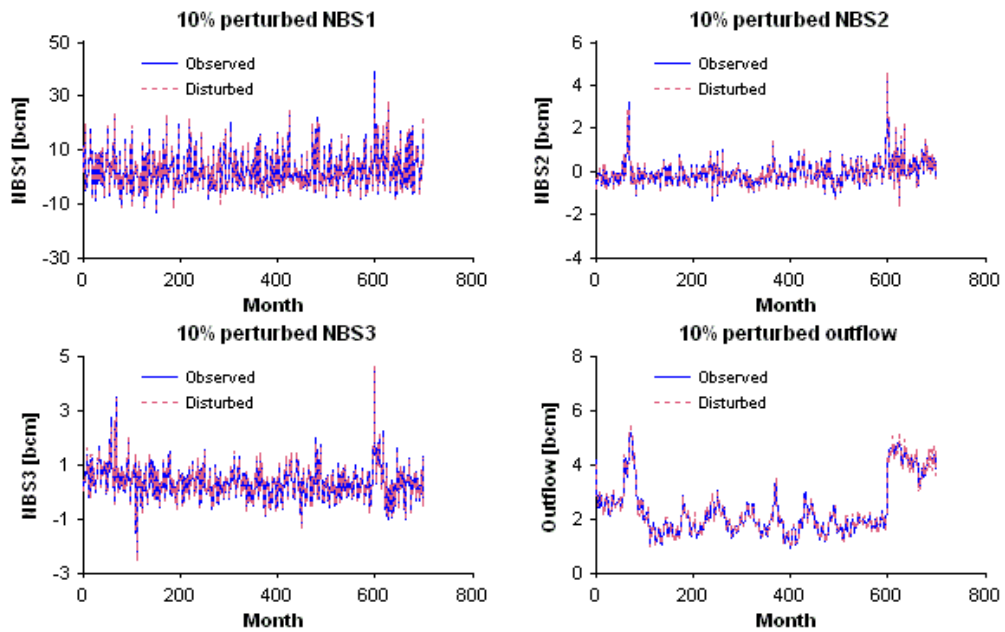


**Figure 3-14.** 10% disturbed NBS of each lake and 10% disturbed outflow of Lake Albert.

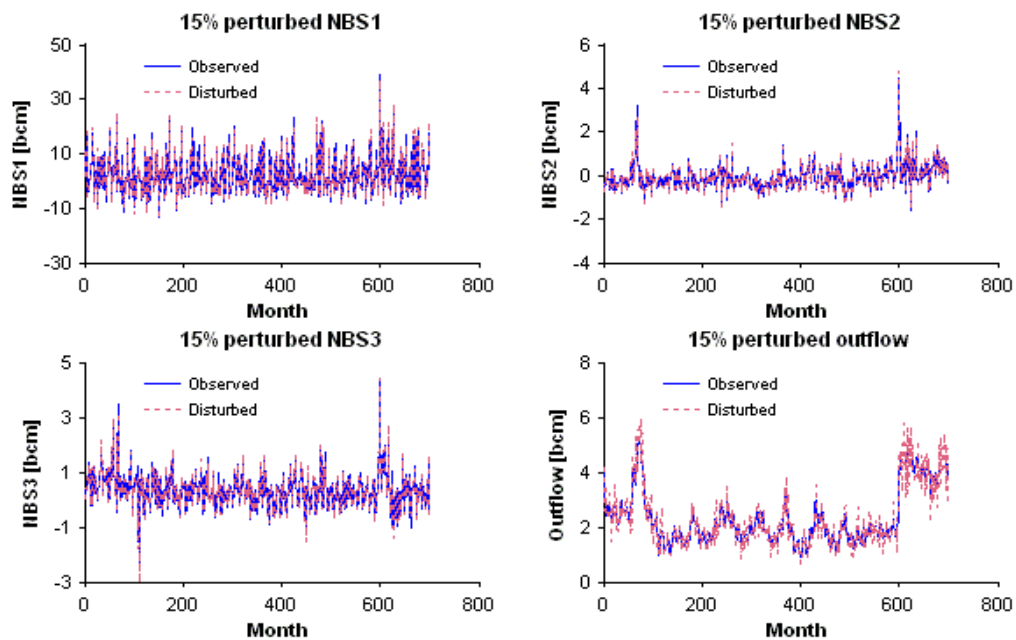


**Figure 3-15:** 15% disturbed NBS of each lake and 15% disturbed outflow of Lake Albert.

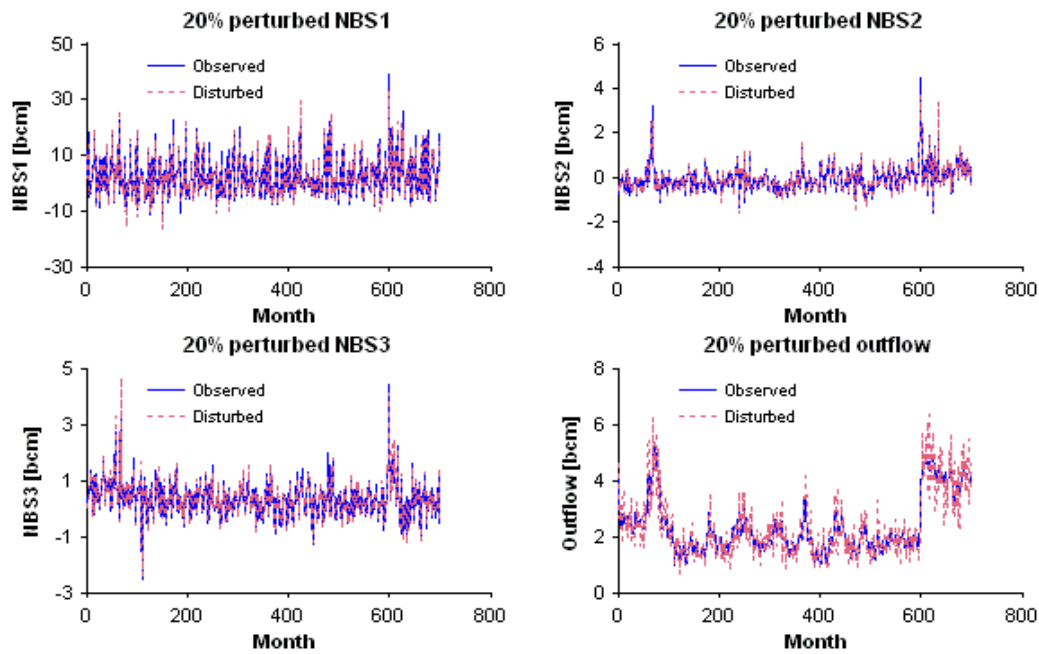


**Figure 3-16.** 20% disturbed NBS of each lake and 20% disturbed outflow of Lake Albert.

Figure 3-17 through Figure 3-20 compare the model-generated release functions with the observed (error free) rules for each magnitude of the disturbance from 5% to 20%, respectively. In addition, the corresponding results of the storage and outflow sequences are shown in Figure 3-21 through Figure 3-28. Even though the distortion of the shapes of the release rules increases as the size of the disturbance of the input data increases, the river routing model remarkably manages to identify the true release forms of the lake system.

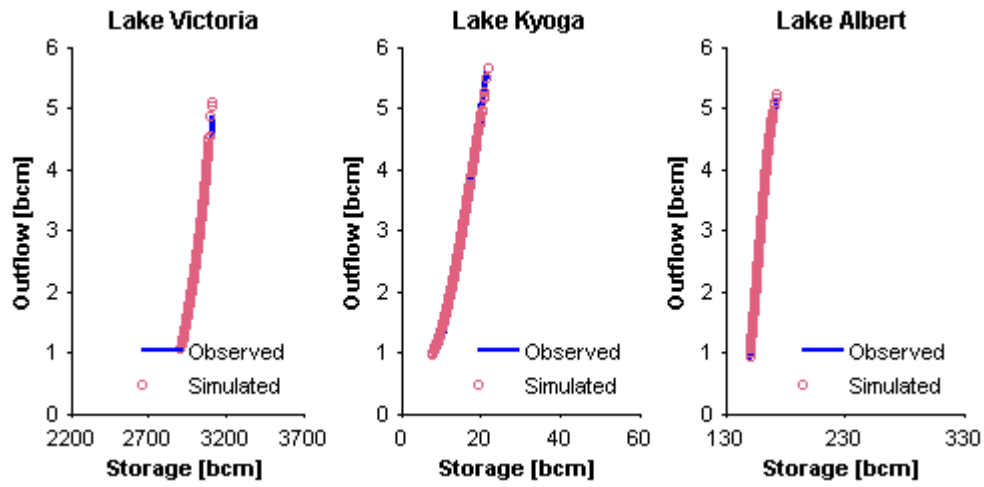


**Figure 3-17.** Simulated release functions for the third experiment.

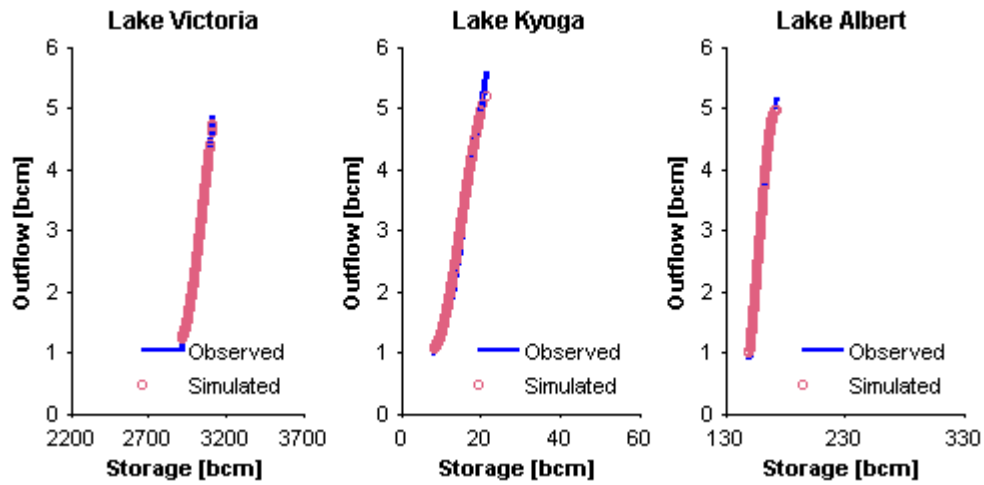


**Figure 3-18.** Simulated release functions for the fourth experiment.

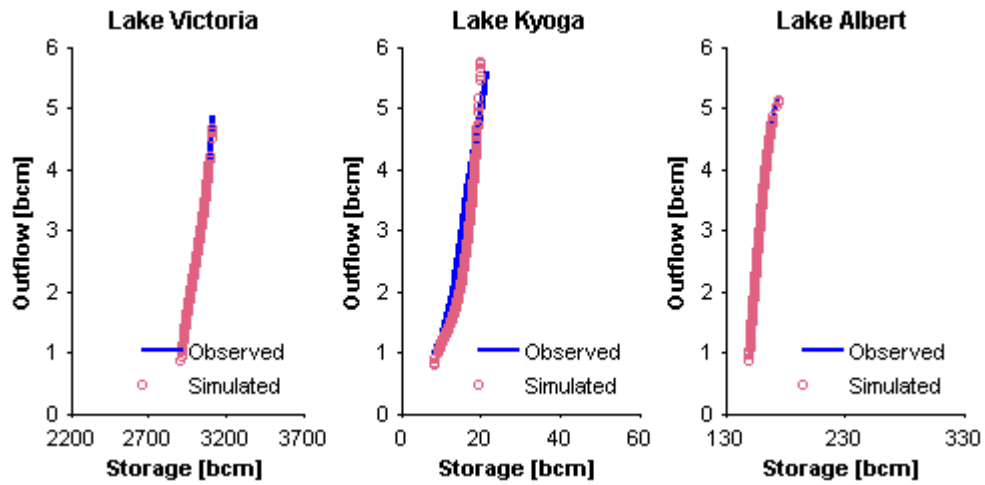


Figure 3-19. Simulated release functions for the fifth experiment.

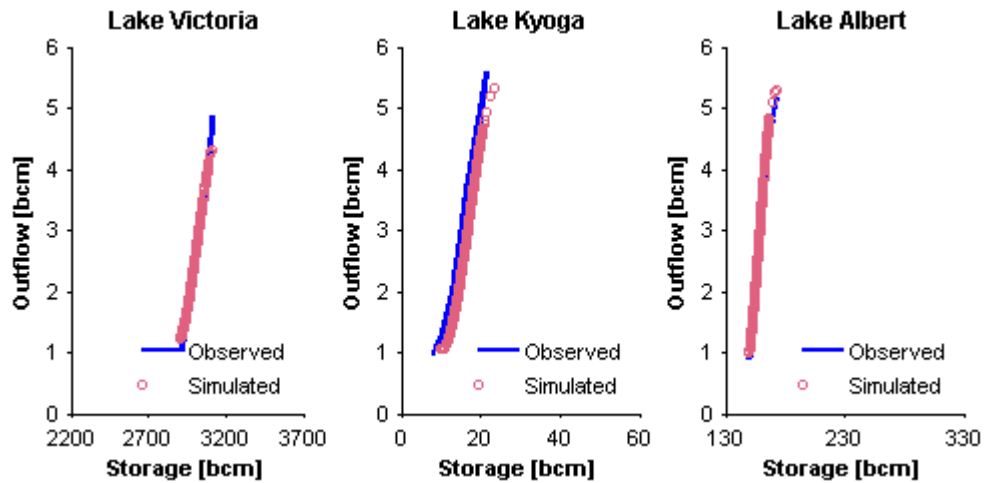
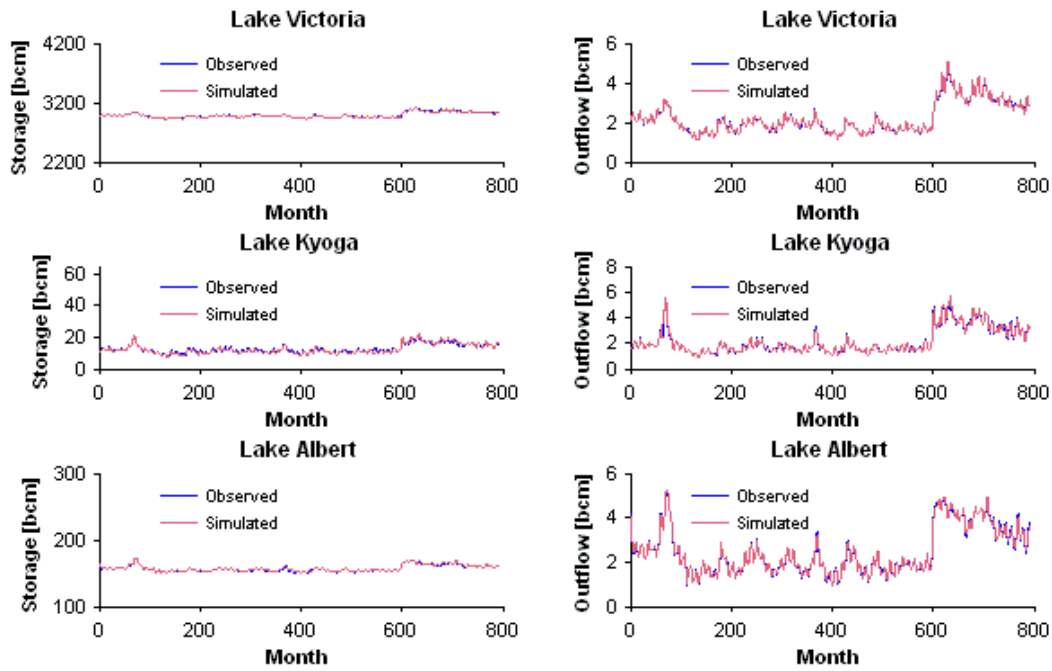


Figure 3-20. Simulated release functions for the sixth experiment.

These outcomes are due to the maintenance of the monotonically increasing property of the release functions through adaptive weighting policies. In fact, the weighting factors are determined in the following magnitude order:  $\theta_1 \approx \theta_2 \approx \theta_3 \leq \theta_4$ . Namely, for these

experiments, the last weighting factor  $\theta_4$  is assigned slightly higher than or equal value to the rest of the weighting factors, allowing the model to conform to the monotonicity of the release rules as much as to track  $\tilde{Q}$ .



**Figure 3-21.** Model verification during the entire time period (calibration + validation) for the third experiment.

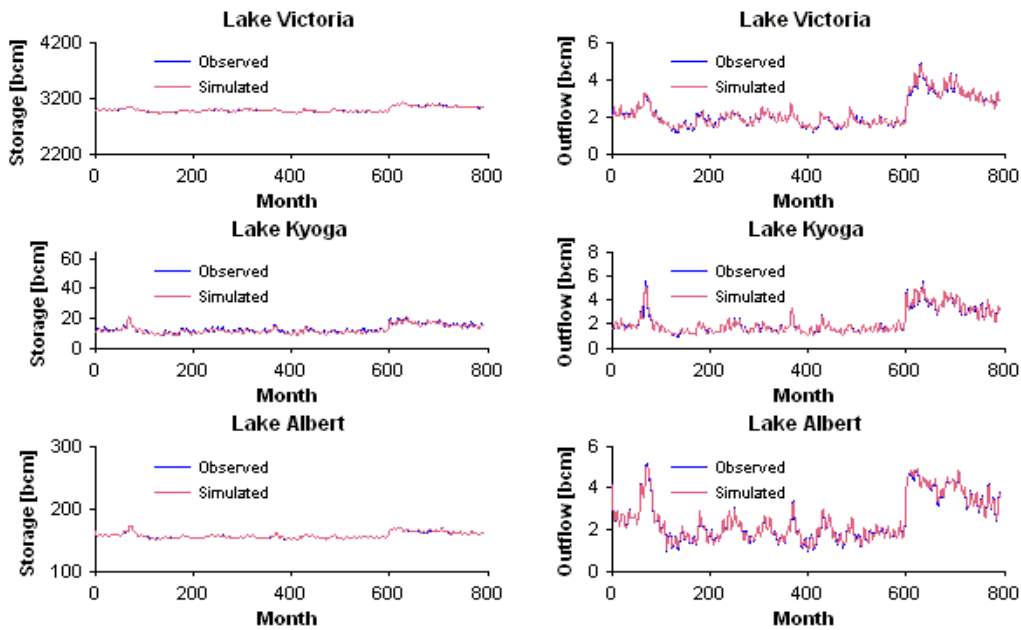


**Figure 3-22.** Model verification during the entire time period (calibration + validation) for the fourth experiment.

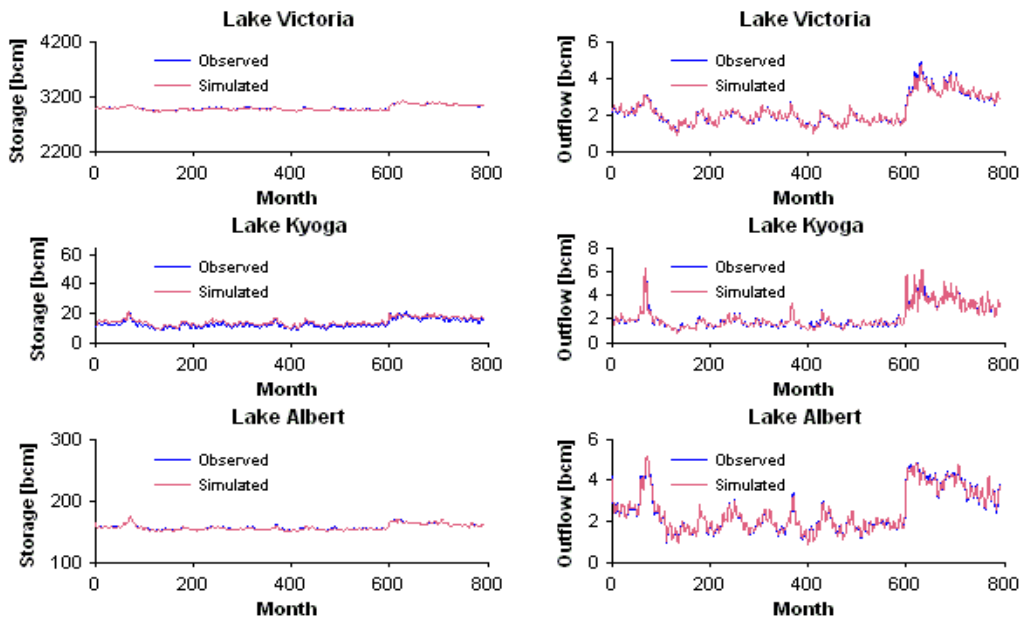


**Figure 3-23.** Model verification during the entire time period (calibration + validation) for the fifth experiment.

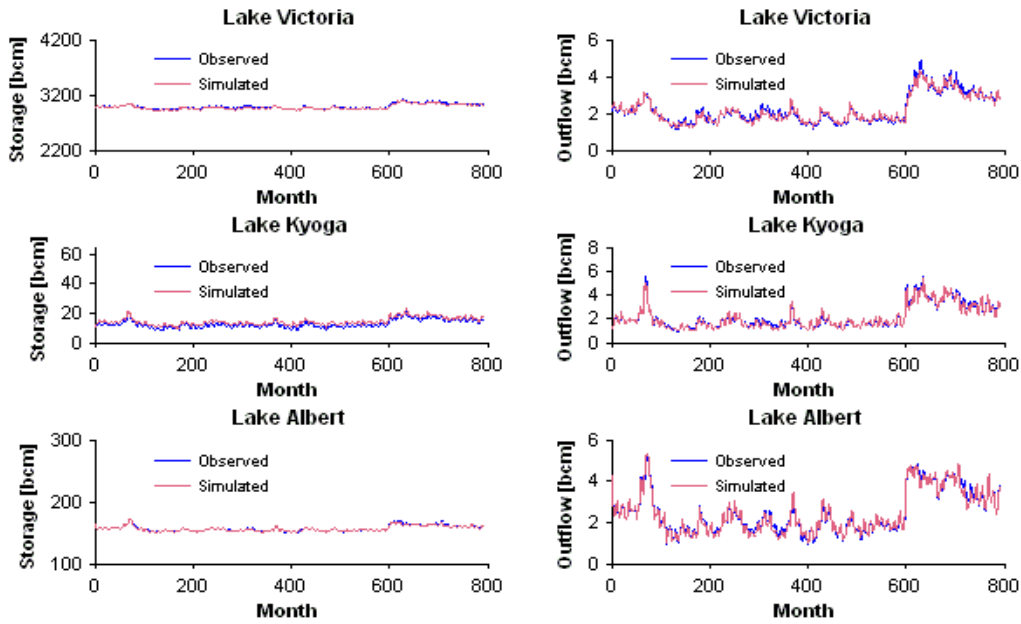


**Figure 3-24.** Model verification during the entire time period (calibration + validation) for the sixth experiment.

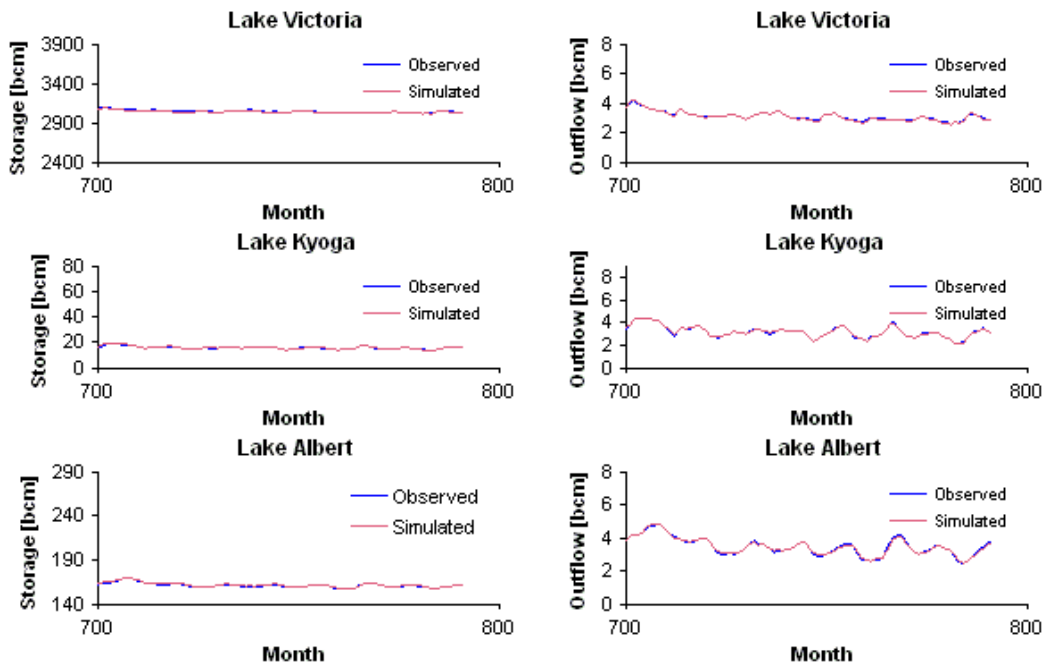


**Figure 3-25.** Model verification during validation for the third experiment.

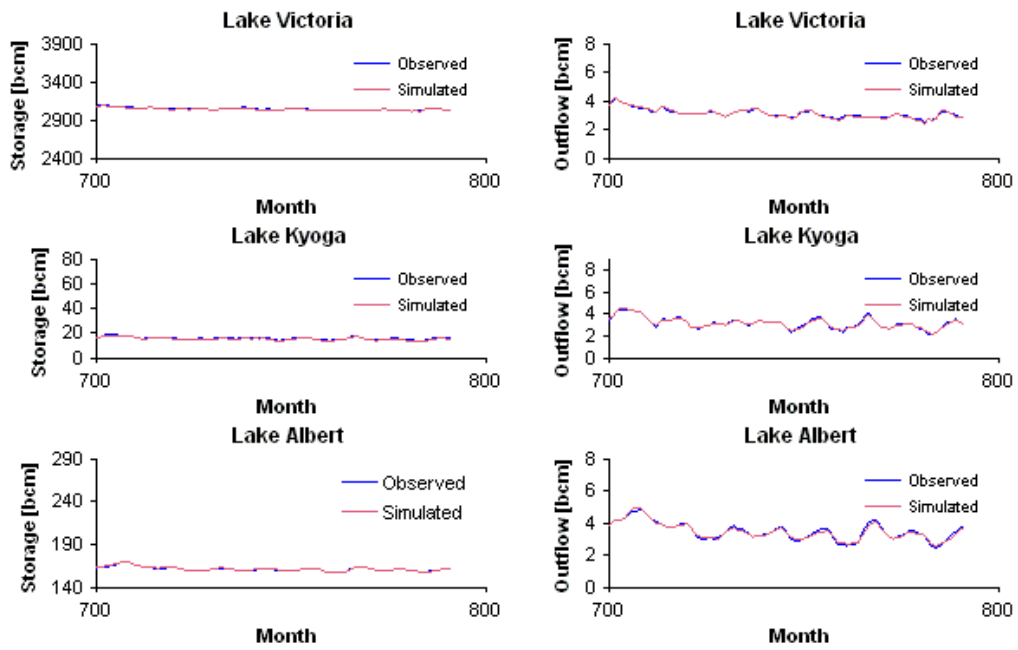


**Figure 3-26.** Model verification during validation for fourth experiment.

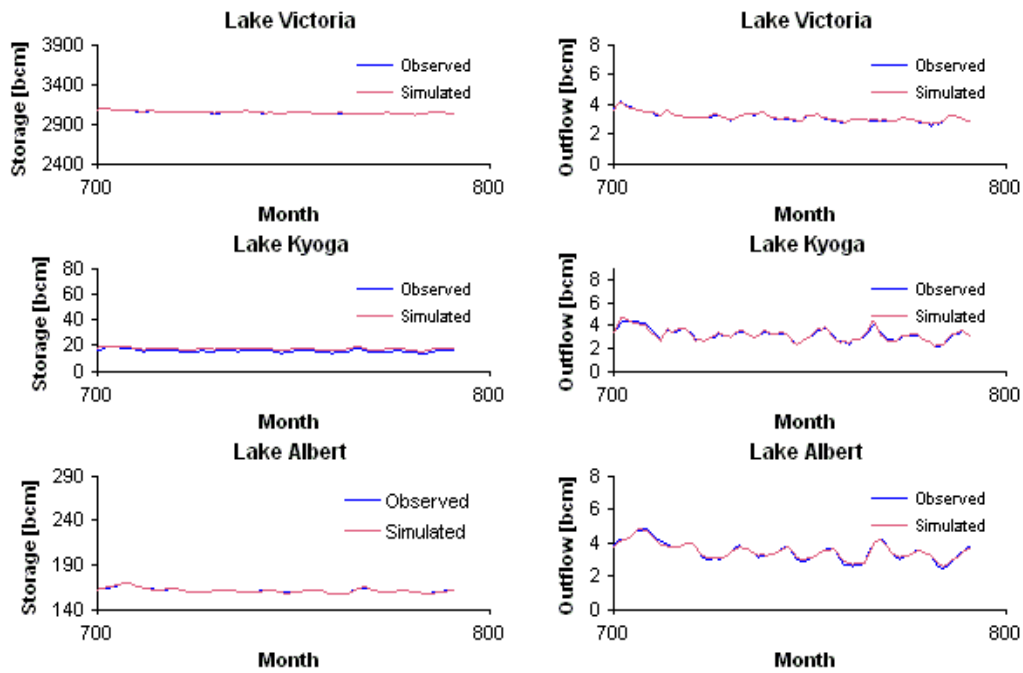


**Figure 3-27.** Model verification during validation for the fifth experiment.

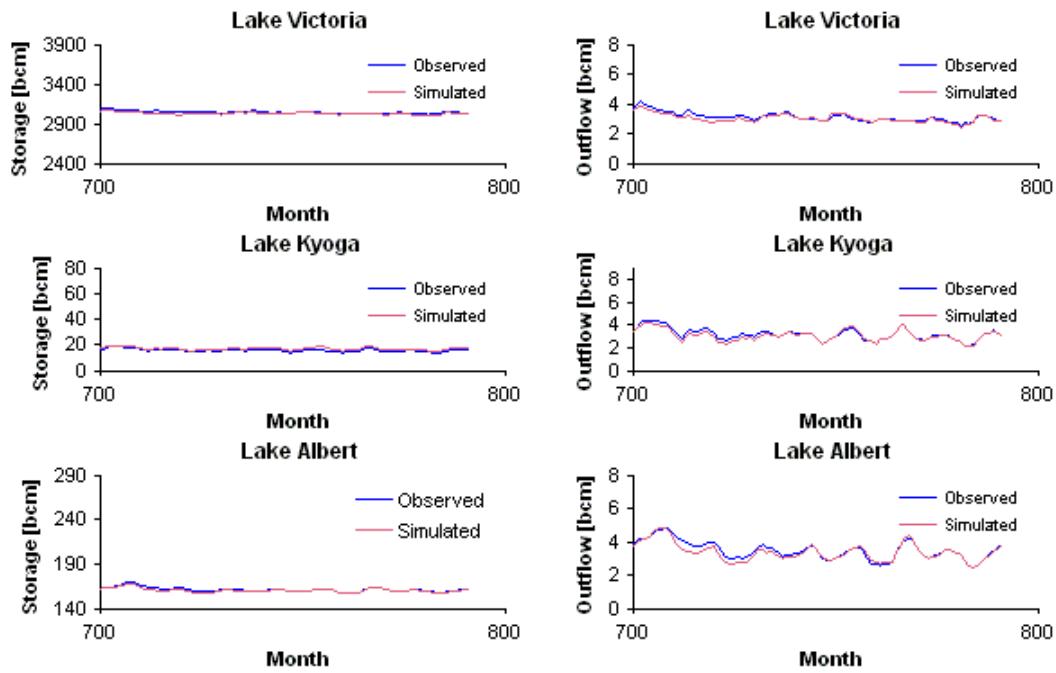


**Figure 3-28.** Model verification during validation for the sixth experiment.

The NRMSEs of the outflow of Lake Albert for all conditions never exceed approximately 7% during calibration and 6% during validation. The NRMSE's of the peaks never exceed 7% during calibration and 6% during validation. In addition, the magnitudes of the total NRMSE and the NRMSE of the peaks increase in the order of  $S_1, S_3,$  and  $S_2$  during calibration and validation for all experiments.

**Table 3-4.** Evaluation of river routing model for the third experiment.

	Calibration			Validation		
	NRMSE, %	Time-To-Peak error, Months	NRMSE of peaks, %	NRMSE, %	Time-To-Peak error, Months	NRMSE of peaks, %
$S_1$	0.08	0.00	0.08	0.18	0.00	0.17
$S_2$	3.92	-0.01	3.69	1.47	0.00	1.14
$S_3$	0.31	-0.01	0.30	0.34	0.00	0.30
$u_1$	0.88	0.00	1.00	1.21	0.00	1.11
$u_2$	1.73	-0.01	1.66	1.34	0.00	0.71
$u_3$	1.96	-0.01	1.80	1.93	0.00	1.38

**Table 3-5.** Evaluation of river routing model for the fourth experiment.

	Calibration			Validation		
	NRMSE, %	Time-To-Peak error, Months	NRMSE of peaks, %	NRMSE, %	Time-To-Peak error, Months	NRMSE of peaks, %
$S_1$	0.05	0.00	0.05	0.13	0.00	0.13
$S_2$	3.71	0.00	3.50	3.00	0.00	2.31
$S_3$	0.20	-0.01	0.17	0.21	0.00	0.19
$u_1$	2.01	0.00	1.97	1.37	0.00	1.18
$u_2$	2.40	0.00	1.91	2.26	0.00	2.04
$u_3$	2.68	-0.01	2.09	2.51	0.00	2.17

**Table 3-6.** Evaluation of river routing model for the fifth experiment.

	Calibration			Validation		
	NRMSE, %	Time-To-Peak error, Months	NRMSE of peaks, %	NRMSE, %	Time-To-Peak error, Months	NRMSE of peaks, %
$S_1$	0.15	0.00	0.14	0.09	0.00	0.08
$S_2$	11.97	-0.01	11.16	10.68	-0.17	10.54
$S_3$	0.43	-0.05	0.44	0.20	0.00	0.15
$u_1$	2.62	0.00	2.48	1.87	0.00	1.67
$u_2$	5.34	-0.01	5.51	4.42	-0.17	4.21
$u_3$	2.72	-0.05	2.44	2.50	0.00	2.26

**Table 3-7.** Evaluation of river routing model for the sixth experiment.

	Calibration			Validation		
	NRMSE, %	Time-To-Peak error, Months	NRMSE of peaks, %	NRMSE, %	Time-To-Peak error, Months	NRMSE of peaks, %
$S_1$	0.41	-0.01	0.41	0.54	-0.14	0.55
$S_2$	14.56	-0.09	13.08	8.24	0.00	8.86
$S_3$	0.44	-0.10	0.50	0.66	0.00	0.61
$u_1$	5.25	-0.01	5.29	4.83	-0.14	4.58
$u_2$	6.38	-0.09	6.42	5.71	0.00	5.55
$u_3$	5.77	-0.10	5.81	5.61	0.00	5.88

### 3.3 Application to the Main Nile

#### 3.3.1 Main Nile

In his book, entitled “Hydrology of the Nile River,” *Shahin* [1985] writes:

At Khartoum the Blue Nile joins the White Nile and the combined waters flow for 1,885 km to Aswan through a region of Nubian sandstone overlying an old eroded land surface of crystalline rocks which has been laid bare at places in the course of the still incomplete degradation of the river bed.

The Main Nile flows from Khartoum, Sudan, to Aswan, Egypt and extends upstream 400 km. From Khartoum, as depicted in Figure 3-29 and Figure 3-30, the course of the Main Nile runs northeast to Atbara (323 km), where the Atbara River joins the Main Nile. The river turns northwest to Abu-Hamed (578 km) and proceeds to where it abruptly turns southwest to Korti (872 km). From Korti, the river swings around a bend back to the north at Dongola (1083 km) and flows in a northerly direction to Aswan [*Shahin*, 1985].



**Figure 3-29.** The Eastern Nile system with existing and planned development [Georgakakos and Yao, 2000].



**Figure 3-30.** The Main Nile system with existing and planned development [Georgakakos and Yao, 2000].

### 3.3.2 Model identification and calibration procedure

First, the identification of the proper number of conceptual reservoirs,  $M$ , is addressed by developing models with progressively more reservoirs until the configuration achieves satisfactory correspondence between simulated and observed outflows at the outlet of a river reach (or at the last conceptual reservoir) of interest, based on the principle of parsimony.

Afterwards, the model calibration procedure, based on Algorithm 3.1, is followed as outlined below:

1. Assume that  $u_i [S_i(k / k + 1)]$  and  $L_i [S_i(k / k + 1)]$ ,  $i = 1, \dots, M$ , are equal to some initial non-decreasing functions of storage,  $f_{L_i} [S_i(k / k + 1)]$  and  $f_{u_i} [S_i(k / k + 1)]$ .  $S_i(k / k + 1) = x_i S_i(k) + (1 - x_i) S_i(k + 1)$  is a weighted storage that is employed to account for rapid changes in storage, even between time step  $k$  and  $k + 1$ .  $x_i, i = 1, \dots, M$ , are weighting factors ranging from zero to one. These additional parameters can be identified by determining the values that achieve satisfactory estimates of outflow at Dongola using the trial and error method. The linear initial release and loss functions that yield the smallest square error between simulated and observed outflows among all feasible linear functions are chosen.
2. Fix loss functions  $f_{L_i}^k [S_i(k / k + 1)]$ ,  $i = 1, \dots, M$ , at their current normal forms and determine the best outflows,  $u_i(k), i = 1, \dots, M$ , which solve the following sequence of iterative optimization problems:

$$\underset{u_i(k), i=1, \dots, M; k=1, \dots, N}{\text{Min}} \frac{1}{2} \sum_{k=1}^N \left\{ \theta_1 \left[ \frac{u_1(k) - f_{u_1}^k [S_1(k/k+1)]}{Q^{\max}} \right]^2 + \dots + \theta_M \left[ \frac{u_M(k) - f_{u_M}^k [S_M(k/k+1)]}{Q^{\max}} \right]^2 + \theta_{M+1} \left[ \frac{u_M(k) - Q(k)}{Q^{\max}} \right]^2 \right\} \quad (3.26)$$

subject to the system dynamics,

$$\begin{aligned} S_1(k+1) &= S_1(k) + h_k u_0(k) - h_k u_1(k) - h_k f_{L_1}^k [S_1(k/k+1)] + w_1(k), \\ &\dots \\ S_i(k+1) &= S_i(k) + h_k u_{i-1}(k) - h_k u_i(k) - h_k f_{L_i}^k [S_i(k/k+1)] + w_i(k), \\ &\dots \\ S_M(k+1) &= S_M(k) + h_k u_{M-1}(k) - h_k u_M(k) - h_k f_{L_M}^k [S_M(k/k+1)] + w_M(k), \\ k &= 1, \dots, N. \end{aligned} \quad (3.27)$$

In the optimization problem for  $M = 2$ ,  $u_0(k)$  is the reach inflow at Khartoum and  $u_M(k)$  is the reach outflow at Dongola.  $w_1(k) = 0, k = 1, \dots, N$ , and  $w_2(k)$  is the tributary inflow at Atbara.

$$f_{u_i}^k [S_i(k/k+1)] = a_i^k [x_i S_i(k) + (1-x_i) S_i(k+1)] + b_i^k \text{ and}$$

$$f_{L_i}^k [S_i(k/k+1)] = p_i^k [x_i S_i(k) + (1-x_i) S_i(k+1)] + q_i^k \text{ are local linear functions defined by}$$

the first-order Taylor expansions of  $f_{u_i} [S_i(k/k+1)]$  and  $f_{L_i} [S_i(k/k+1)]$ , respectively,

at their nominal values of  $x_i S_i(k) + (1-x_i) S_i(k+1)$ .  $h_k$  is a unit converter that is used to

convert the units of  $u_i(k)$  and  $L_i(k)$  from mcm/day to bcm, which represents the units

of both  $S_i(k)$  and  $w_i(k)$ . In addition, the system matrices of the LQR are

$$A^k = \begin{bmatrix} \gamma_1^k \lambda_1^k & 0 \\ 0 & \gamma_2^k \lambda_2^k \end{bmatrix}, B^k = \begin{bmatrix} -\gamma_1^k h_k & 0 \\ \gamma_2^k h_k & -\gamma_2^k h_k \end{bmatrix}, C^k = \begin{bmatrix} \gamma_1^k h_k u_0(k) + \gamma_1^k [w_1(k) - h_k q_1^k] \\ \gamma_2^k [w_2(k) - h_k q_2^k] \end{bmatrix}, \quad (3.28)$$

$$\gamma_i^k = 1 / [1 + h_k p_i^k (1 - x_i)], \lambda_i^k = 1 - h_k p_i^k x_i,$$

and the weighting matrices are

$$L_{xx}^k = \begin{bmatrix} 2\theta_1 \rho_1^{k^2} & 0 \\ 0 & 2\theta_2 \rho_2^{k^2} \end{bmatrix}, L_{uu}^k = \begin{bmatrix} 2\theta_1(1 + \varepsilon_1^k)^2 + 2\theta_2 \varepsilon_2^{k^2} & -2\theta_2 \varepsilon_2^k (1 + \varepsilon_2^k) \\ -2\theta_2 \varepsilon_2^k (1 + \varepsilon_2^k) & 2\theta_2(1 + \varepsilon_2^k)^2 + 2\theta_3 \end{bmatrix}, L_{ux}^k = \begin{bmatrix} -2\theta_1(1 + \varepsilon_1^k) \rho_1^k & 2\theta_2 \varepsilon_2^k \rho_2^k \\ 0 & -2\theta_2(1 + \varepsilon_2^k) \rho_2^k \end{bmatrix},$$

$$L_x^k = \begin{bmatrix} 2\theta_1 \varepsilon_1^k \rho_1^k u_0(k) - 2\theta_1 \pi_1^k \rho_1^k \\ -2\theta_2 \pi_2^k \rho_2^k \end{bmatrix}, L_u^k = \begin{bmatrix} -2\theta_1 \varepsilon_1^k (1 + \varepsilon_1^k) u_0(k) + 2\theta_1(1 + \varepsilon_1^k) \pi_1^k - 2\theta_2 \varepsilon_2^k \pi_2^k \\ 2\theta_2(1 + \varepsilon_2^k) \pi_2^k - 2\theta_3 Q(k) \end{bmatrix},$$

$$\hat{L}^k = \theta_1 (\varepsilon_1^k u_0(k) - \pi_1^k)^2 + \theta_2 \pi_2^{k^2} + \theta_3 Q(k)^2, P = \begin{bmatrix} 0 & 0 & 0 \\ 0 & 0 & 0 \\ 0 & 0 & 0 \end{bmatrix},$$

$$\psi_i^k = \frac{1}{\frac{1}{1 - x_i} + h_k p_i^k},$$

$$\varepsilon_i^k = a_i^k h_k \psi_i^k,$$

$$\rho_i^k = \frac{a_i^k \psi_i^k}{1 - x_i},$$

$$\pi_i^k = a_i^k h_k \psi_i^k q_i^k - a_i^k \psi_i^k w_i(k) - b_i^k.$$

(3.29)

3. Create non-decreasing release functions  $f_{u_i}^k [S_i(k / k + 1)], i = 1, \dots, M$ , by rearranging

the orders of a set of optimal solutions  $[S_i^*(k / k + 1), u_i^*(k)], k = 1, \dots, N$ , such that if

$S_i^*(k_1/k_1+1) > S_i^*(k_2/k_2+1)$ , then  $u_i^*(k_1) > u_i^*(k_2)$  for  $k_1 = 1, \dots, N, k_2 = 1, \dots, N$ , and  $k_1 \neq k_2$ .

4. Calculate new local linear release functions  $f_{u_i}^k [S_i(k/k+1)]$ ,  $i = 1, \dots, M$ ;  $k = 1, \dots, N$ , by the first-order Taylor expansion of the new set of non-decreasing release functions (from Step 3) about the nominal values of  $S_i(k/k+1)$  calculated by the following dynamical equations:

$$\begin{aligned}
 S_1(k+1) &= S_1(k) + h_k u_0(k) - h_k f_{u_1}^k [S_1(k/k+1)] - h_k f_{L_1}^k [S_1(k/k+1)] + w_1(k), \\
 &\dots \\
 S_i(k+1) &= S_i(k) + h_k f_{u_{i-1}}^k [S_{i-1}(k/k+1)] - h_k f_{u_i}^k [S_i(k/k+1)] - h_k f_{L_i}^k [S_i(k/k+1)] + w_i(k), \\
 &\dots \\
 S_M(k+1) &= S_M(k) + h_k f_{u_{M-1}}^k [S_{M-1}(k/k+1)] - h_k f_{u_M}^k [S_M(k/k+1)] - h_k f_{L_M}^k [S_M(k/k+1)] + w_M(k), \\
 k &= 1, \dots, N.
 \end{aligned} \tag{3.30}$$

The cumulative square error between modeled outflow  $f_{u_M}^k [S_M(k/k+1)]$  and actual outflow  $Q(k)$ ,  $k = 1, \dots, N$ , is also computed from Equation (3.30). Steps 2, 3, and 4 are iterated until the cumulative square error reaches a minimum value.

6. Fix release functions  $f_{u_i}^k [S_i(k/k+1)]$ ,  $i = 1, \dots, M$ , at their current normal forms obtained in the previous steps and determine the best water losses,  $L_i(k)$ ,  $i = 1, \dots, M$ , which solve the following sequence of iterative optimization problems:

$$\text{Min}_{L_i(k), i=1, \dots, M; k=1, \dots, N} \frac{1}{2} \sum_{k=1}^N \left\{ \theta_1 \left[ \frac{L_1(k) - f_{L_1}^k [S_1(k/k+1)]}{Q^{\max}} \right]^2 + \dots + \theta_M \left[ \frac{L_M(k) - f_{L_M}^k [S_M(k/k+1)]}{Q^{\max}} \right]^2 + \theta_{M+1} \left[ \frac{a_M^k S_M(k/k+1) + b_M^k - Q(k)}{Q^{\max}} \right]^2 \right\} \quad (3.31)$$

subject to the system dynamics,

$$\begin{aligned} S_1(k+1) &= S_1(k) + h_k u_0(k) - h_k f_{u_1}^k [S_1(k/k+1)] - h_k L_1(k) + w_1(k), \\ &\dots \\ S_i(k+1) &= S_i(k) + h_k f_{u_{i-1}}^k [S_{i-1}(k/k+1)] - h_k f_{u_i}^k [S_i(k/k+1)] - h_k L_i(k) + w_i(k), \\ &\dots \\ S_M(k+1) &= S_M(k) + h_k f_{u_{M-1}}^k [S_{M-1}(k/k+1)] - h_k f_{u_M}^k [S_M(k/k+1)] - h_k L_M(k) + w_M(k), \\ k &= 1, \dots, N. \end{aligned}$$

For  $M = 2$ , the system matrices of the LQR are

$$\begin{aligned} A^k &= \begin{bmatrix} \gamma_1^k \lambda_1^k & 0 \\ \gamma_2^k \frac{h_k a_1^k \psi_1^k}{1-x_1} & \gamma_2^k \lambda_2^k \end{bmatrix}, B^k = \begin{bmatrix} -\gamma_1^k h_k & 0 \\ -\gamma_2^k h_k^2 a_1^k \psi_1^k & -\gamma_2^k h_k \end{bmatrix}, C^k = \begin{bmatrix} c_1^k \\ h_k a_1^k \psi_1^k c_1^k + h_k (b_1^k - b_2^k) + w_2(k) \end{bmatrix}, \\ \gamma_i^k &= \frac{1}{1 + h_k a_i^k (1-x_i)}, \\ \lambda_i^k &= 1 - h_k a_i^k x_i, \\ \psi_i^k &= \frac{1}{\frac{1}{1-x_i} + h_k a_i^k}, \\ c_1^k &= h_k u_0(k) + w_1(k) - h_k b_1^k. \end{aligned} \quad (3.32)$$

And the weighting matrices are

$$\begin{aligned}
L_{xx}^k &= \begin{bmatrix} 2\varepsilon_1^{k^2} \left[ \theta_1 p_1^{k^2} + h_k^2 a_1^k \psi_2^{k^2} \left[ \theta_2 p_2^{k^2} + \theta_3 a_2^{k^2} \right] \right] & 2h_k a_1^k \varepsilon_1^k \psi_2^k \varepsilon_2^k \left[ \theta_2 p_2^{k^2} + \theta_3 a_2^{k^2} \right] \\ 2h_k a_1^k \varepsilon_1^k \psi_2^k \varepsilon_2^k \left[ \theta_2 p_2^{k^2} + \theta_3 a_2^{k^2} \right] & 2\varepsilon_2^{k^2} \left[ \theta_2 p_2^{k^2} + \theta_3 a_2^{k^2} \right] \end{bmatrix}, \\
L_{xx}^k &= \begin{bmatrix} 2\theta_1 \mu_1^2 + 2h_k^4 \psi_1^{k^2} a_1^{k^2} \psi_2^{k^2} \left[ \theta_2 p_2^{k^2} + \theta_3 a_2^{k^2} \right] & 2h_k^2 a_1^k \psi_1^k \psi_2^k \left[ \theta_2 \mu_2 p_2^k + \theta_3 h_k \psi_2^k a_2^{k^2} \right] \\ 2h_k^2 a_1^k \psi_1^k \psi_2^k \left[ \theta_2 \mu_2 p_2^k + \theta_3 h_k \psi_2^k a_2^{k^2} \right] & 2\theta_2 \mu_2^2 + 2\theta_3 h_k^2 \psi_2^{k^2} a_2^{k^2} \end{bmatrix}, \\
L_{xx}^k &= \begin{bmatrix} -2\varepsilon_1^k \left[ \theta_1 \mu_1^k p_1^k + h_k^3 a_1^k \psi_1^k \psi_2^{k^2} \left[ \theta_2 p_2^{k^2} + \theta_3 a_2^{k^2} \right] \right] & -2h_k^2 a_1^k \varepsilon_2^k \psi_1^k \psi_2^k \left[ \theta_2 p_2^{k^2} + \theta_3 a_2^{k^2} \right] \\ -2h_k a_1^k \varepsilon_1^k \psi_2^k \left[ \theta_2 \mu_2^k p_2^k + \theta_3 \psi_2^k a_2^{k^2} \right] & -2\varepsilon_2^k \left[ \theta_2 \mu_2^k p_2^k + \theta_3 h_k a_2^{k^2} \psi_2^k \right] \end{bmatrix}, \\
L_x^k &= \begin{bmatrix} -2\varepsilon_1^k \left[ \theta_1 \rho_1^k p_1^k + h_k a_1^k \psi_2^k \left[ \theta_2 \rho_2^k p_2^k - \theta_3 \beta_2^k a_2^k \right] \right] \\ -2\varepsilon_2^k \left[ \theta_2 \rho_2^k p_2^k - \theta_3 \beta_2^k a_2^k \right] \end{bmatrix}, L_x^k = \begin{bmatrix} 2\theta_1 \mu_1^k \rho_1^k + 2h_k \psi_1^k a_1^k \left[ \theta_2 \mu_2^k \rho_2^k - \theta_3 h_k \beta_2^k \psi_2^k a_2^k \right] \\ 2\theta_2 \mu_2^k \rho_2^k - 2\theta_3 h_k \beta_2^k \psi_2^k a_2^k \end{bmatrix}, \\
\hat{L}^k &= \theta_1 \rho_1^{k^2} + \theta_2 \rho_2^{k^2} + \theta_3 \beta_2^{k^2}, P = \begin{bmatrix} 0 & 0 \\ 0 & 0 \end{bmatrix}, \\
\beta_i^k &= \psi_i^k a_i^k c_i^k + b_i^k - Q(k), \\
\varepsilon_i^k &= \frac{\psi_i^k}{1 - x_i}.
\end{aligned}
\tag{3.33}$$

6. Create non-decreasing loss functions  $f_{L_i}^k [S_i(k/k+1)]$  by rearranging the orders of a set

of optimal solutions  $[S_i^*(k/k+1), L_i^*(k)]$ ,  $k = 1, \dots, N$ , such that if

$S_i^*(k_1/k_1+1) > S_i^*(k_2/k_2+1)$ , then  $L_i^*(k_1) > L_i^*(k_2)$  for  $k_1 = 1, \dots, N, k_2 = 1, \dots, N$ , and

$k_1 \neq k_2$ .

7. Calculate new local linear release functions  $f_{L_i}^k [S_i(k / k + 1)]$ ,  $i = 1, \dots, M$ ;  $k = 1, \dots, N$ , by the first-order Taylor expansion of the new set of non-decreasing loss functions (from Step 6) about the nominal values of  $S_i(k / k + 1)$  calculated by Equation (3.30). The cumulative square error between modeled outflow  $f_{u_M}^k [S_M(k / k + 1)]$  and actual outflow  $Q(k)$ ,  $k = 1, \dots, N$ , is also computed from Equation (3.30). Then Steps 5, 6, and 7 are iterated until the cumulative square error reaches a minimum value.
8. Iterate between Steps 2, 3, 4 and 5, 6, 7 until the release and loss functions converge to stable forms and the cumulative square error between the simulated and observed outflows at Dongola reaches a minimum value.

### 3.3.3 Results

In this application, the river routing model is utilized for routing flows from Khartoum past the confluence of Atbara to Dongola, a distance of about 1,083 km, as shown in Figure 3-29 and Figure 3-30. Except for the discharges at Khartoum and Atbara, no significant inflows to the Main Nile are assumed to exist along the water course of interest. Figure 3-31 shows a corresponding inflow-outflow hydrograph from January 1, 1914, to December 21, 1963, in 10-day time intervals with a total of 1,800 data points, which were used as input to the routing model. Water loss takes place mainly due to free water surface evaporation, retention on flood plains, water seepage and some minimal irrigation abstractions. Without specific knowledge of the amount of lost water of the river reach, the purpose of this application is to assess if the routing model can identify the required number of conceptual reservoirs and the underlying release and loss functions on the basis of the available inflow-outflow hydrographs.

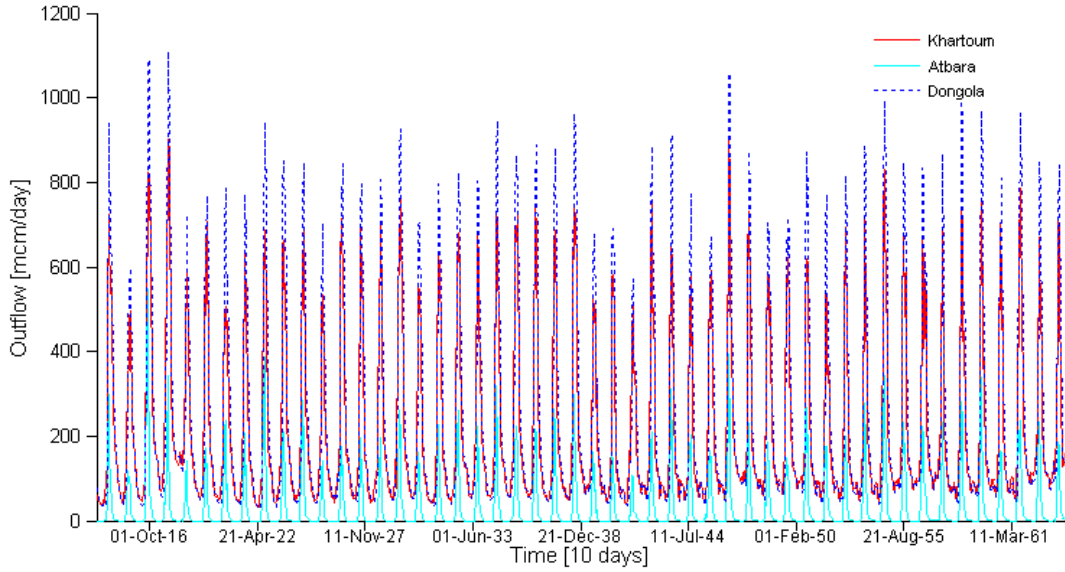


**Figure 3-31.** Inflow-Outflow hydrograph for the river routing application, January 1, 1914 to December 21, 1963. Time in 10-day intervals; 10-day average discharge in million cubic meters per day.

The routing model was implemented and calibrated as described in Section 3.3.2 above. The best reservoir configuration was found to be a cascade of three conceptual reservoirs with the optimal release and loss functions shown in Figure 3-32 and the system dynamics is

$$\begin{aligned}
 S_1(k+1) &= S_1(k) + h_k u_0(k) - h_k u_1(k) - h_k L_1(k) + w_1(k), \\
 S_2(k+1) &= S_2(k) + h_k u_1(k) - h_k u_2(k) - h_k L_2(k) + w_2(k), \\
 S_3(k+1) &= S_3(k) + h_k u_2(k) - h_k u_3(k) - h_k L_3(k) + w_3(k), \\
 k &= 1, \dots, N.
 \end{aligned} \tag{3.34}$$

In the above equation,  $u_0(k)$  is the reach inflow at Khartoum and  $u_3(k)$  is the reach outflow at Dongola.  $w_1(k) = w_3(k) = 0$  for  $k = 1, \dots, N$  and  $w_2(k)$  is the tributary inflow at Atbara. The

first conceptual reservoir extends from Khartoum to just upstream of the confluence with Atbara. The second reservoir, receiving input from Atbara and from the first reservoir, runs from Atbara to somewhere in-between Atbara and Dongola. Finally, the third reservoir proceeds from the end of the second reservoir to Dongola. The corresponding outflow at Dongola, estimated via Equation(3.30), is shown in Figure 3-33. It was found that the root mean squared error (RMSE) between modeled and observed outflows, defined by Equation (3.35), decreased with increasing number of conceptual reservoirs. The RMSE are 20.71 mcm/day for one conceptual reservoir, 19.68 mcm/day for two conceptual reservoirs (one from Khartoum to upstream of the Atbara confluence and the other from downstream of the confluence to Dongola), and 19.49 mcm/day for the three conceptual reservoirs.

$$\sqrt{\frac{\sum_{k=1}^N [f_M^k(S_M(k)) - Q(k)]^2}{N}}. \quad (3.35)$$

Furthermore, as the reservoir configuration increases from one reservoir to two, the RMSE decreases by about 5%. On the other hand, as the configuration increases from two reservoirs to three, it decreases only by 1%. These findings show that configurations with more conceptual reservoirs can better represent the observed flow, but there is point beyond which adding more reservoirs adds to the cost of the calibration procedure without significantly improving the RMSE.

Figure 3-32 demonstrates the unique ability of the new river routing model to identify general nonlinear release and loss function forms. As the figure shows, the optimal release functions do not follow a particular form (e.g., a power law) throughout their range, but they comprise several convex and concave regions. Furthermore, the loss functions become active (i.e., they begin to attain relatively significant values) when the storage is around 14.3 bcm for the first reservoir, 16 bcm for the second reservoir, and 11 bcm for the last reservoir, with corresponding outflow at about 425 mcm/day, 430 mcm/day, and 780 mcm/day, respectively. These functions generally exhibit the behavior expected of river losses which may be due to several sources (e.g., free water surface evaporation or retention on flood plains) but occur as *aggregate* losses across each reservoir. Lastly, the effect of the loss functions on the release functions is clearly discernible by the convex modification of the latter over the active loss function regions. This modification lowers the release rates compared to those that would have been expected in the absence of the water losses.

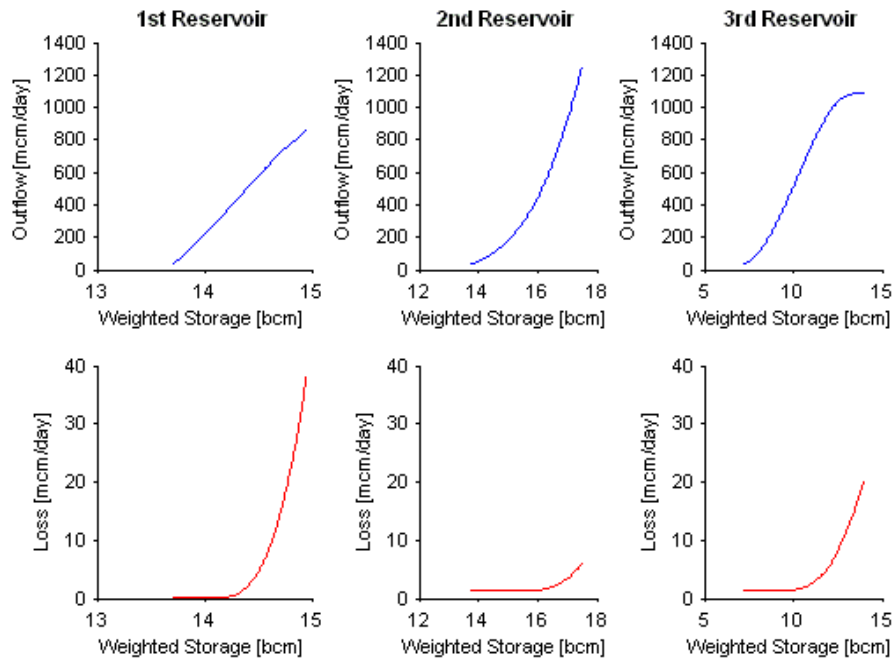


**Figure 3-32.** Optimal release and loss functions for the application reach modeled as a cascade of three conceptual reservoirs with a calibration time from January 1, 1914 to December 21, 1963.

Figure 3-33 compares the simulated and observed hydrographs from January 1, 1914 to December 21, 1963 in 10-day time intervals and shows that the model performs well. As shown in Table 3-8, the time-to-peak error is 3.6 days, which is less than the unit time interval of this application, the RMSA of peaks is 39.5 mcm/day, and the average of the peaks is 833.3 mcm/day. The total water losses during the simulation time are 11,036.9 mcm/day for observed losses, defined by Equation (3.36), and 7,607.9 mcm/day for estimated losses, defined by Equation (3.37) with  $N = 1,800$ . A potential reason for this discrepancy is that the procedure to compute the flow data at the reach outlet changed in 1970 when the High Aswan Dam filled up and submerged the original measurement site (Wadi Halfa).

$$\sum_{k=1}^N [u_0(k) + w_2(k) - Q(k)] \quad (3.36)$$

$$\sum_{k=1}^N [u_0(k) + w_2(k) - u_3(k)] \quad (3.37)$$

**Table 3-8.** Evaluation of the river routing model for the Main Nile from January 1, 1914 to December 21, 1963.

RMSEA of outflow, mcm/day	Time-to-Peak error, 10 days	RMSE of peaks, mcm/day
19.49	3.56	39.48

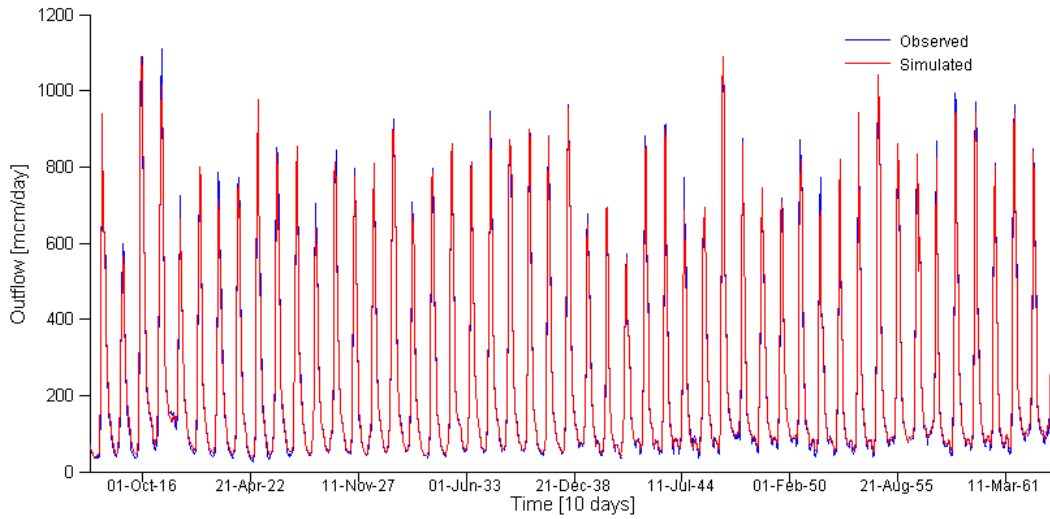


**Figure 3-33.** Comparison of observed and simulated outflows of the application reach (at Dongola) modeled as a cascade of three conceptual reservoirs from January 1, 1914 to December 21, 1963 in 10-day intervals.

To verify the calibrated model, the time period for the previous calibration procedure is divided into two periods, the first of which is the calibration period with 1400 data points (January 1, 1914 ~ November 11, 1952), and the second the validation period with 400 data points

(November 11, 1952 ~ December 11, 1963). Figure 3-34 shows the calibrated optimal release and loss functions of the cascade of three conceptual reservoirs. Compared with the optimal functions in Figure 3-32, all of the release and loss functions remain virtually equal except the first and last loss functions, which have a slight decrease and a slight increase in the loss rate, respectively, especially in their convex regions. The calibrated and observed outflows for calibration are compared in Figure 3-35. The RMSE of the calibrated outflow with respect to the observed outflow is 19.06 mcm/day. Similarly, the RMSE of the validated outflow with respect to the observed outflow is 20.90 mcm/day, as shown in Figure 3-36. These findings establish the robustness of the routing model and show its general applicability.

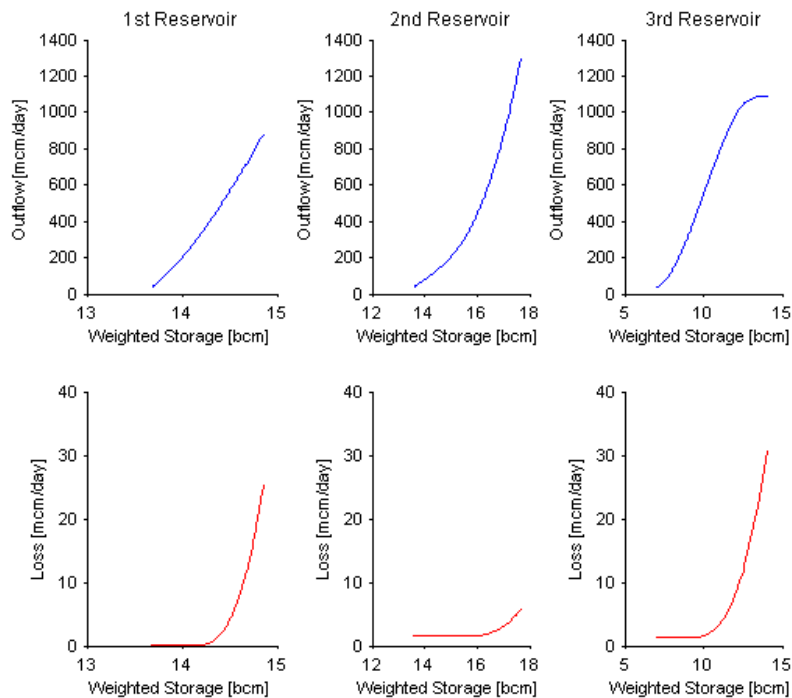


**Figure 3-34.** Optimal release and loss functions for the application reach modeled as a cascade of three conceptual reservoirs over a calibration time from January 1, 1914 to November 11, 1952.

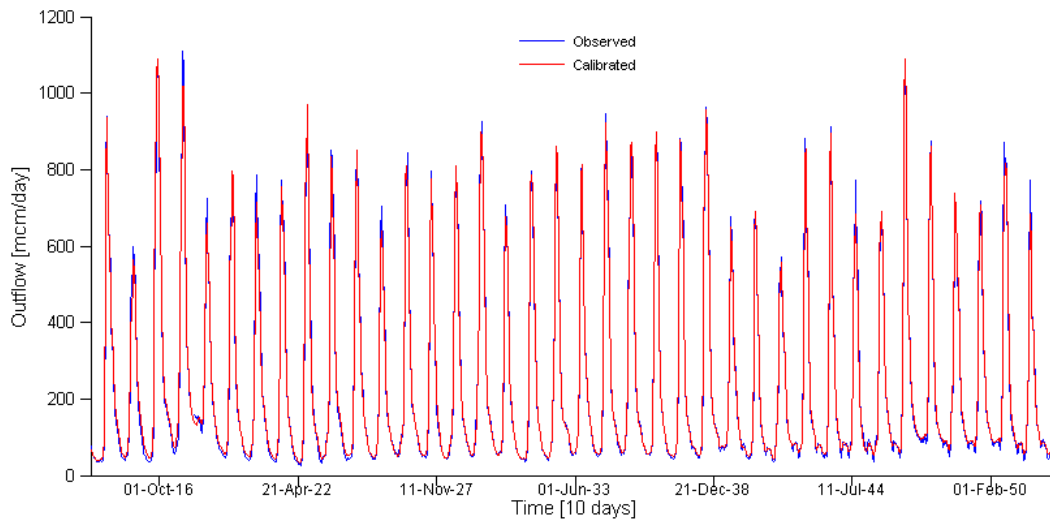


**Figure 3-35.** Comparison of observed and calibrated outflows of the application reach (at Dongola), modeled as a cascade of three conceptual reservoirs over a calibration time from Jan. 1, 1914 to Nov. 11, 1952 in 10-day intervals.

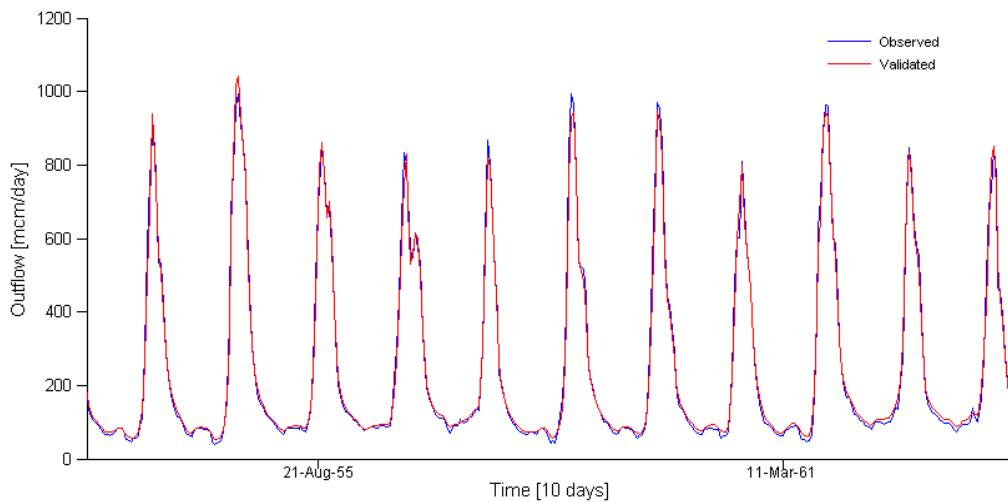


**Figure 3-36.** Comparison of observed and validated outflows of the application reach (at Dongola) modeled as a cascade of three conceptual reservoirs over a validation time from Nov. 11, 1952 to Dec. 11, 1963 in 10-day intervals.

Furthermore, three quantitative measures for evaluating the simulated outflows for both periods appear in Table 3-9. The time-to-peak errors for both time periods are less than the

unit time interval of this application. The average of the peaks is 819.9 mcm/day for calibration and 880.9 mcm/day for validation. For calibration with  $N = 1400$  for Equations (3.36) and (3.37), the total observed water losses are 9,104 mcm/day, and the total estimated water losses is 6,031.7 mcm/day. Likely, the total observed and estimated water losses for validation with  $N = 400$  are 1933 mcm/day and 1576.2 mcm/day, respectively.

**Table 3-9.** Evaluation of the new river routing model for the Main Nile.

Calibration			Validation		
RMSE of outflow, mcm/day	Time-to-Peak error, 10 days	RMSE of peaks, mcm/day	RMSE of outflow, mcm/day	Time-to-Peak error, 10 days	RMSE of peaks, mcm/day
19.06	4.36	39.13	20.90	4.54	43.48

### 3.3.4 Summary remarks on the river routing model

Conceptual reservoir cascade models are attractive because they usually include a few conceptual reservoirs in the management model state variable set. The outflow of each conceptual reservoir is usually related to its storage through linear, exponential, or power laws so that the model matches the observed inflow-outflow hydrographs. However, these predefined relationships can be limiting because they assume that these properties between outflow and storage are invariant over the entire range of flows through the river reach. The new hydrologic river routing model was developed to allow for a more general nonlinear relationship between outflow and storage. In addition, the routing model employs loss

functions to account for water losses mainly caused by water seepage, free water surface evaporation, and other phenomena.

In its application to the Equatorial Lake system, the known release rules generated from the benchmark lake model was compared with the model estimated release functions. Given only the data of the hydrologic inputs (NBS) and the outflow of the last lake (Lake Albert), the routing model successfully and accurately identified the nonlinear release functions of not only the last lake but also the other two lakes in the upstream using the LQR optimization scheme. Furthermore, the robustness of the routing model in erroneous input data was quantified by perturbing the model inputs by normally distributed errors to different degrees and applying the identification algorithm. Even though the NRMSEs of the outflow of Lake Albert with respect to the observed outflow increases with increasing perturbation error strength, the NRMSEs do not exceed 7%, demonstrating the model robustness in actual applications.

In its second application to the Main Nile, a cascade of three conceptual reservoirs was selected as the optimal reservoir configuration. For each conceptual reservoir, the nonlinear properties of release and loss functions were adequately identified because the routing model has no limitation in defining the properties of the relationships between outflow and storage and between loss and storage. Indeed, the loss functions were found to represent the integrated effect of water losses rather well.

## CHAPTER 4

### BAYESIAN FORECASTING FRAMEWORK

A Bayesian forecasting framework (BFF) is developed around the nonlinear river routing model introduced earlier to generate river or lake outflow forecasts in a multi-trace ensemble form. This chapter begins with a description of uncertainty sources associated with such forecasts, followed by a general procedure of BFF development. Forecast applications for the Equatorial Lakes in East Africa and the Main Nile are presented in the final sections.

#### 4.1 Uncertainty characterization

Two major uncertainty sources associated with forecasting river or lake outflows are model uncertainty and input uncertainty. Model uncertainty results from the approximated representation of an actual system and the imperfect calibration of model parameters; input uncertainty is associated with measurement errors of various inputs to the model.

Most river routing models use simplified representations of actual physical systems, introducing errors in the estimation of actual reach outflow. In addition, model parameters need to be calibrated against measured field data. Even if field data are accurate, incomplete calibration schemes often produce imperfect estimation of model parameters. In this work, forecast uncertainty due to model error is probabilistically quantified by a sequence of conditional distributions of actual future outflow generated by a model uncertainty processor (MUP) [Krzysztofowicz and Kelly, 2000; Krzysztofowicz and Herr, 2001; Krzysztofowicz and Maranzano, 2004; Krzysztofowicz and Maranzano, 2004a]. Based on historical and simulated

data samples chosen by a historical analog method, the conditional distributions are computed off-line so that they are readily available for real-time forecasting [Krzysztofowicz, 2002].

Input uncertainty stems from a lack of accuracy in measuring field data used as model inputs. Field measurements are often temporally or spatially aggregated and disaggregated, adding to the overall uncertainty. This type of uncertainty is quantified by a sequence of marginal distributions of model-estimated outflow generated by an input uncertainty processor (IUP) [Kelly and Krzysztofowicz, 2000]. In the IUP, given the forecasts of inflows to a reach or a lake in multi-trace ensemble forms, each inflow trace is simulated with the nonlinear river routing model in Chapter 3 to generate ensemble forecasts of outflows.

These uncertainty characterization components comprise the main elements of the Bayesian Forecasting Framework.

## 4.2 General BFF procedure

In the Bayesian forecasting system (BFS) [Krzysztofowicz, 1999; Krzysztofowicz, 2002; Krzysztofowicz and Maranzano, 2004b], as shown in Figure 4-1, the product of a meta-Gaussian posterior distribution,  $\Phi_j(u_j^* | u_j, u_{j-1}^*)$ ,  $j = 1, \dots, m$ , estimated by MUP and a marginal density of model-estimated outflow,  $\pi_j(u_j)$ ,  $j = 1, \dots, m$ , estimated by IUP is integrated over all feasible ranges of the model-estimated outflow in an integrator (INT) [Krzysztofowicz, 1999; Krzysztofowicz, 2001; Krzysztofowicz and Maranzano, 2004b]. Integration takes place for all the families of meta-Gaussian posterior distributions and marginal distributions to form

a sequence of predictive one-step transition distributions,  $\Theta_j(u_j^* | u_{j-1})$ ,  $j = 1, \dots, m$ ,

[*Krzysztofowicz and Maranzano, 2004b*] that probabilistically measure the combined effect of both model and input uncertainty in forecasts of the evolution of outflow process over time.

However, the derived sequences of the BFS distributions can provide only reliable ranges of the future outflows, not reliable traces. However, forecasted traces are required in the real-time operational management of any water resources system. Hence, a sequence of the linear one-step transition models is derived for generating these traces. The BFS incorporating this new feature is called a Bayesian forecasting framework (BFF). Furthermore, while the BFS is applied to short-term forecasting (6-h or 24-h time step for 3 days) [*Krzysztofowicz and Herr, 2001; Krzysztofowicz, 2002; Krzysztofowicz and Maranzano, 2004a; Krzysztofowicz and Maranzano, 2004b*], the BFF can be also applied to mid- or long-term forecasting by modifying the likelihood functions of the MUP. The details of the modification will be illustrated in Section 4.3.2.

The general BFF identification and calibration procedure is illustrated and outlined below:

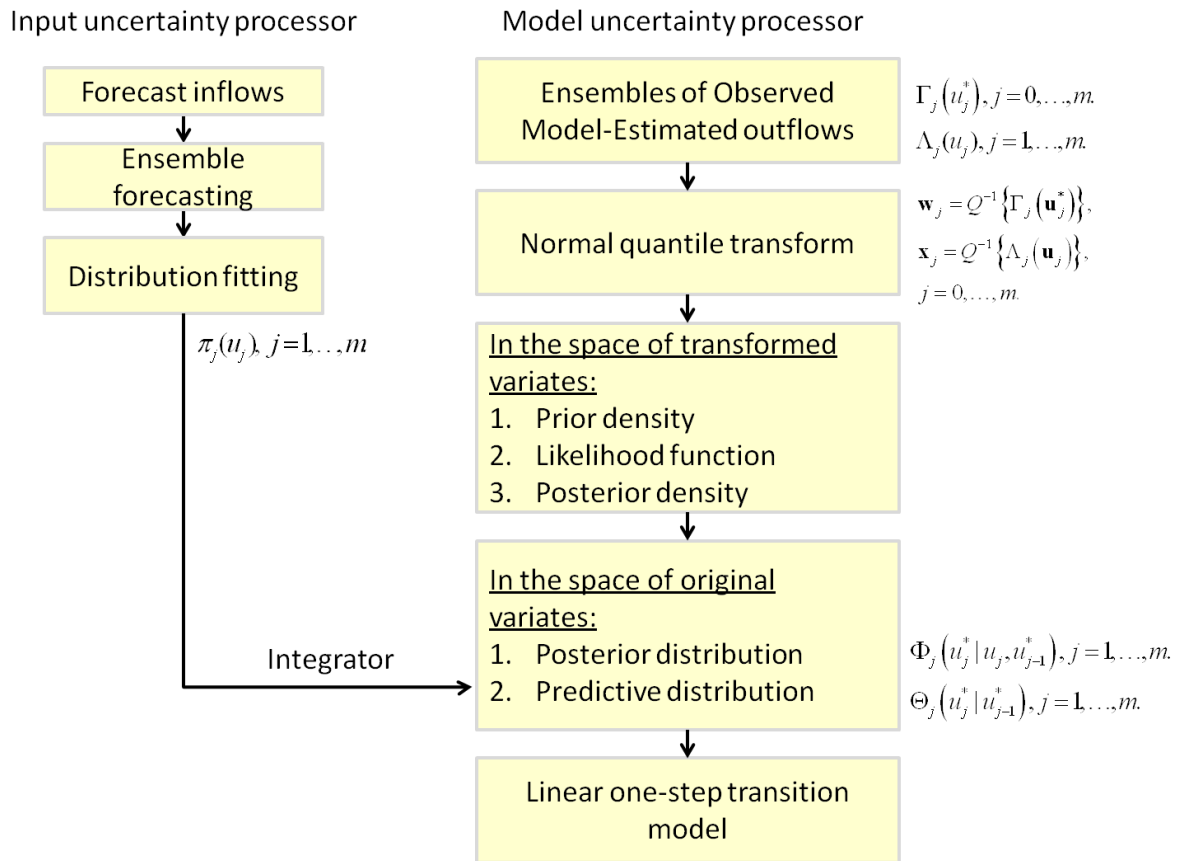


**Figure 4-1.** The Bayesian forecasting framework methodology.

Input uncertainty processor:

1. Since forecasting inflows to a river or a lake system by any advanced model is beyond the scope of this research, a much simpler method, a historical analog method, is used for selecting an ensemble of system inflows to be used as forecasts.
2. Each inflow trace is then simulated with the previously calibrated nonlinear river routing model for generating ensemble forecasts of outflows.
3. Then, for a set of the forecasted values for each time  $j$  in the ensemble, an empirical distribution is calculated, which is later fitted by a Weibull distribution  $\Pi_j(u_j)$  or

Weibull densities  $\pi_j(u_j)$ . Subscript  $j$  indicates the time steps in the forecasting horizon, spanning from 1 to  $m$ . It is noted that  $j=0$  indicates the last observation time before forecasting.

Model uncertainty processor:

4. A historical analog method is used to select the ensembles of actual and corresponding model-estimated outflows. From the ensembles, the empirical distributions of actual outflow  $u_j^*$  and model-estimated outflow  $u_j$  are estimated. With a fitting scheme, the two families of the empirical distributions are fitted by Weibull distributions  $\Gamma_j(u_j^*), j = 0, \dots, m$ , and  $\Lambda_j(u_j), j = 1, \dots, m$ .
5. By normal quantile transform (NQT in APPENDIX B) [*Moran, 1969; Kelly and Krzysztofowicz, 1994*], the random variables of actual future outflow  $\mathbf{u}_j^*, j = 0, \dots, m$ , and those of model-estimated outflow  $\mathbf{u}_j, j = 1, \dots, m$ , are transformed into standard normal variates  $\mathbf{w}_j$  and  $\mathbf{x}_j$ , respectively.
6. A sequence of prior densities in the space of the transformed variates is calculated from Equation (4.2). The theoretical background is explained in Section 4.3.1. Second, likelihood functions in the same space are estimated by Equation (4.5) of Section 4.3.2. Lastly, the sequence of posterior densities is generated by Bayes' theorem from Equation (4.11) of Section 4.3.3, which illustrates the derivation of the posterior densities.

7. By the Jacobian of the transformation, a sequence of meta-Gaussian posterior distributions of the original variates,  $\mathbf{u}_j^*$  and  $\mathbf{u}_j$ , is generated by Equation (4.15). More details on the meta-Gaussian function can be found in Section 4.3.4.

Integrator:

8. Based on the total probability law, a sequence of predictive one-step transition distributions is calculated from Equation (4.16).
9. Based on an ensemble generator [*Krzysztofowicz and Maranzano, 2004b*], the feasible values of  $\mathbf{u}_j^*$ ,  $j = 1, \dots, m$ , and then the sequence of predictive distributions are simulated. The detailed procedure is described in Section 4.4.4.

Linear one-step transition model:

10. First, a sampling window is configured by a specified sampling interval as the length and the feasible average ranges of  $\mathbf{u}_s^*$ ,  $s = s_1, \dots, s_n$ , as the heights. Subscript  $s$  indicates sampling start time  $s_1$  though sampling end time  $s_n$  for the sampling window. While sliding every sampling interval, the sampling window draws actual outflows that fall within the frame of the window from the ensemble of the actual outflow in Step 4. Finally, based on the drawn samples, a sequence of the linear one-step transition model of actual future flows is formulated and simulated by the Monte Carlo technique in Section 4.4.5 for generating realistic future traces of actual outflows.

### 4.3 Theoretical background

The derivation and validation of a normal-linear model are illustrated in APPENDIX C.

#### 4.3.1 Prior density in the space of transformed variates

A normal-linear model [Krzysztofowicz, 1987; Krzysztofowicz, 1999; Krzysztofowicz and Maranzano, 2004b] characterizes the stochastic linear dependence between standard normal variates.  $\mathbf{w}$  is a standard normal variate transformed from an original variate of an actual outflow. Assuming that an actual outflow process in the transformed space is governed by a linear relationship between  $\mathbf{w}_j$  and  $\mathbf{w}_{j-1}$ , a sequence of linear regression equations for time step  $j = 1, \dots, m$  are formulated by

$$\mathbf{w}_j = c_j \mathbf{w}_{j-1} + z_j + \Xi_j. \quad (4.1)$$

In the above equation,  $c_j$  and  $z_j$  are linear regression parameters calibrated by the observed values of  $\mathbf{w}_j$  and  $\mathbf{w}_{j-1}$ . The error variable  $\Xi_j$  is assumed to be stochastically independent of  $\mathbf{w}_{j-1}$  and normally distributed with mean zero and variance  $\varepsilon_j^2$ . Based on the linear regression equations, the normal-linear model has prior densities for  $j = 1, \dots, m$  in the form of

$$r_{Q^j}(w_j | w_{j-1}) = \frac{1}{\varepsilon_j \sqrt{2\pi}} \exp \left\{ -\frac{(w_j - c_j w_{j-1} - z_j)^2}{2\varepsilon_j^2} \right\}. \quad (4.2)$$

Subscript  $Q$  indicates the space of standard normal variates. The conditional mean and variance are

$$\begin{aligned} E(\mathbf{w}_j | w_{j-1}) &= c_j w_{j-1} + z_j, \\ \text{Var}(\mathbf{w}_j | w_{j-1}) &= \varepsilon_j^2. \end{aligned} \tag{4.3}$$

#### 4.3.2 Likelihood function in the space of transformed variates

As with the prior density in the previous section, a normal-linear model is employed to construct likelihood functions that characterize the stochastic linear dependence between  $\mathbf{w}$  and  $\mathbf{x}$  [Krzysztofowicz and Kelly, 2000; Krzysztofowicz and Herr, 2001; Krzysztofowicz and Maranzano, 2004a; Krzysztofowicz and Maranzano, 2004b].  $\mathbf{w}$  is a standard normal variate transformed from an original variate of the actual outflow, and  $\mathbf{x}$  is a standard normal variate transformed from an original variate of the model-estimated outflow. Assuming that the model-estimated outflows in the transformed space are related to the actual outflows based on the linear relationships among  $\mathbf{x}_j$ ,  $\mathbf{w}_j$ , and  $\mathbf{w}_{j-1}$ , a sequence of linear regression equations for time step  $j = 1, \dots, m$  are formulated by

$$\mathbf{x}_j = a_j \mathbf{w}_j + e_j \mathbf{w}_{j-1} + b_j + \Theta_j, \tag{4.4}$$

where  $a_j$ ,  $b_j$ , and  $e_j$  are regression parameters calibrated with the observed values of  $\mathbf{x}_j$ ,  $\mathbf{w}_j$ , and  $\mathbf{w}_{j-1}$ . The error variate  $\Theta_j$  is assumed to be stochastically independent of  $(\mathbf{w}_j, \mathbf{w}_{j-1})$  and

normally distributed with mean zero and variance  $\sigma_j^2$ . Unlike the linear regression equations for the likelihood functions of BFS [Krzysztofowicz and Herr, 2001; Krzysztofowicz, 2002; Krzysztofowicz and Maranzano, 2004a; Krzysztofowicz and Maranzano, 2004b], these linear equations do not include  $\mathbf{w}_0$ , except  $j=1$ , so the BFF can be applied for short-range through long-range forecasts because the dependence of  $\mathbf{x}_j$  on  $\mathbf{w}_0$  fades away as time increases. Subscript  $j=0$  denotes the last observation time before forecasting. Based on the regression equations, the normal-linear model has a sequence of conditional densities for  $j=1, \dots, m$  in the form of

$$f_{Q^j}(x_j | w_j, w_{j-1}) = \frac{1}{\sigma_j \sqrt{2\pi}} \exp \left\{ -\frac{(x_j - (a_j w_j + e_j w_{j-1} + b_j))^2}{2\sigma_j^2} \right\}. \quad (4.5)$$

And the conditional mean and variance are

$$\begin{aligned} E(\mathbf{x}_j | w_j, w_{j-1}) &= a_j w_j + e_j w_{j-1} + b_j, \\ \text{Var}(\mathbf{x}_j | w_j, w_{j-1}) &= \sigma_j^2. \end{aligned} \quad (4.6)$$

### 4.3.3 Posterior density in the space of transformed variates

Bayes' theorem for probability density functions in general is

$$f(x|y) = \frac{f(y|x)f(x)}{\int_{-\infty}^{\infty} f(y|x)f(x)dx}. \quad (4.7)$$

Applying this theorem to the previously calculated prior and likelihood functions generates a sequence of posterior densities in the transformed space by

$$\phi_{Q^j}(w_j | x_j, w_{j-1}) = \frac{f_{Q^j}(x_j | w_j, w_{j-1})r_{Q^j}(w_j | w_{j-1})}{\int_{-\infty}^{\infty} f_{Q^j}(x_j | w_j, w_{j-1})r_{Q^j}(w_j | w_{j-1})dw_j}, \quad (4.8)$$

$j = 1, \dots, m,$

and the numerator and denominator are calculated by

$$f_{Q^j}(x_j | w_j, w_{j-1})r_{Q^j}(w_j | w_{j-1}) = \frac{1}{\sigma_j \varepsilon_j 2\pi} \exp \left\{ -\frac{(x_j - (a_j w_j + e_j w_{j-1} + b_j))^2}{2\sigma_j^2} - \frac{(w_j - (c_j w_{j-1} + z_j))^2}{2\varepsilon_j^2} \right\} \quad (4.9)$$

and

$$\begin{aligned} \kappa_{Q^j}(x_j | w_{j-1}) &= \int_{-\infty}^{\infty} f_{Q^j}(x_j | w_j, w_{j-1})r_{Q^j}(w_j | w_{j-1})dw_j \\ &= \frac{1}{\sqrt{2\pi} \sqrt{\varepsilon_j^2 a_j^2 + \sigma_j^2}} \exp \left\{ -\frac{(x_j - [a_j(c_j w_{j-1} + z_j) + e_j w_{j-1} + b_j])^2}{2(\varepsilon_j^2 a_j^2 + \sigma_j^2)} \right\}. \end{aligned} \quad (4.10)$$

respectively.  $\kappa_{Q^j}(x_j | w_{j-1})$ , the conditional expected density of  $w_j$ , makes the total area of  $\phi_{Q^j}(w_j | x_j, w_{j-1})$  equal to one. An integration rule shown below is used for deriving the posterior densities of Equation (4.8):

$$\int_{-\infty}^{\infty} d \exp(-fx^2 + gx + h) dx = d \sqrt{\frac{\pi}{f}} \exp\left(\frac{g^2}{4f} + h\right),$$

where  $f$  is strictly positive. Subsequently, the derived sequence of the posterior densities is

$$\phi_{Q^j}(w_j | x_j, w_{j-1}) = \frac{1}{T_j \sqrt{2\pi}} \exp\left\{-\frac{(w_j - A_j x_j - E_j w_{j-1} - B_j)^2}{2T_j^2}\right\}, \quad (4.11)$$

$j = 1, \dots, m.$

The parameters of the posterior densities are

$$A_j = \frac{a_j \varepsilon_j^2}{a_j^2 \varepsilon_j^2 + \sigma_j^2}, \quad B_j = \frac{z_j \sigma_j^2 - a_j b_j \varepsilon_j^2}{a_j^2 \varepsilon_j^2 + \sigma_j^2}$$

$$E_j = \frac{c_j \sigma_j^2 - a_j e_j \varepsilon_j^2}{a_j^2 \varepsilon_j^2 + \sigma_j^2}, \quad T_j^2 = \frac{\sigma_j^2 \varepsilon_j^2}{a_j^2 \varepsilon_j^2 + \sigma_j^2}.$$

With all the densities derived here in the transformed space, they are sent back to the original space by the Jacobian of the transformation in the next section.

#### 4.3.4 Prior and posterior functions in the space of the original variates

A sequence of prior densities of the original variates is derived by the Jacobian of the transformation [Moran, 1969; Kelly and Krzysztofowicz, 1994]:

$$g_j(u_j^* | u_{j-1}^*) = \frac{r_{Q^j}(w_j | w_{j-1})}{\left| \frac{\partial u_j^*}{\partial w_j} \right|} = \frac{\gamma_j(u_j^*)}{\varepsilon_j q \left[ Q^{-1}(\Gamma_j(u_j^*)) \right]} q \left( \frac{Q^{-1}(\Gamma_j(u_j^*)) - c_j Q^{-1}(\Gamma_{j-1}(u_{j-1}^*)) - z_j}{\varepsilon_j} \right), \quad (4.12)$$

$j = 1, \dots, m.$

In addition, the corresponding prior distributions are

$$G_j(u_j^* | u_{j-1}^*) = Q \left( \frac{Q^{-1}(\Gamma_j(u_j^*)) - c_j Q^{-1}(\Gamma_{j-1}(u_{j-1}^*)) - z_j}{\varepsilon_j} \right), \quad (4.13)$$

$j = 1, \dots, m.$

In the above equation,  $Q$  is the standard normal distribution with density  $q$ , and  $\Gamma_j$  is the marginal distribution of actual future outflow  $\mathbf{u}_j^*$  for time  $j$ , and  $u_j^*$  defines a value taken by  $\mathbf{u}_j^*$ . The density of  $\mathbf{u}_j^*$  is  $\gamma_j$ . The prior densities and distributions are called meta-Gaussian prior densities and distributions, respectively [Moran, 1969; Kelly and Krzysztofowicz, 1994; Kelly and Krzysztofowicz, 1997]. The meta-Gaussian models have a strong advantage in that (1) they can assume any form of a marginal density (parametric or non-parametric) of an

original variate; (2) they offer an analytic solution to Bayes' theorem (both prior and posterior density/distribution functions are analytic, so they can be calculated quickly in real-time applications); and (3) they allow the parameters of these functions in the BFF to be approximately evaluated via linear regression.

As with the meta-Gaussian prior densities, a sequence of the meta-Gaussian posterior densities [Krzysztofowicz and Maranzano, 2004a; Krzysztofowicz and Maranzano, 2004b] is derived by

$$\begin{aligned} \phi_j(u_j^* | u_j, u_{j-1}^*) &= \frac{\phi_{Q^j}(w_j | x_j, w_{j-1})}{\left| \frac{\partial u_j^*}{\partial w_j} \right|} \\ &= \frac{\gamma_j(u_j^*)}{q[\mathcal{Q}^{-1}(\Gamma_j(u_j^*))]} \frac{1}{T_j} q \left( \frac{\mathcal{Q}^{-1}(\Gamma_j(u_j^*)) - A_j \mathcal{Q}^{-1}(\Lambda_j(u_j)) - E_j \mathcal{Q}^{-1}(\Gamma_{j-1}(u_{j-1}^*)) - B_j}{T_j} \right), \\ j &= 1, \dots, m, \end{aligned} \quad (4.14)$$

and the corresponding meta-Gaussian posterior distributions take the form of

$$\begin{aligned} \Phi_j(u_j^* | u_j, u_{j-1}^*) &= \mathcal{Q} \left( \frac{\mathcal{Q}^{-1}(\Gamma_j(u_j^*)) - A_j \mathcal{Q}^{-1}(\Lambda_j(u_j)) - E_j \mathcal{Q}^{-1}(\Gamma_{j-1}(u_{j-1}^*)) - B_j}{T_j} \right), \quad (4.15) \\ j &= 1, \dots, m. \end{aligned}$$

The posterior functions measure the impact of model uncertainty on the forecast of actual future outflows in terms of the one-step transition conditional functions of  $u_j^*$  given  $u_j$  and  $u_{j-1}^*$ . Random variable  $\mathbf{u}_j$  represents the model-estimated outflow for time  $j$ , and  $u_j$  defines a value taken by  $\mathbf{u}_j$ .

#### 4.3.5 Predictive distribution in the space of the original variates

Lastly, based on the total probability law,  $\Phi_j(u_j^* | u_j, u_{j-1}^*)$  and the marginal densities of model-estimated outflow  $\pi_j$ ,  $j=1, \dots, m$ , are combined into products as integrands, which are integrated over all feasible ranges of  $u_j$  [Krzysztofowicz, 2002; Krzysztofowicz and Maranzano, 2004b]:

$$\Theta_j(u_j^* | u_{j-1}^*) = \int_{-\infty}^{\infty} \Phi_j(u_j^* | u_j, u_{j-1}^*) \pi_j(u_j) du_j. \quad (4.16)$$

$\Theta_j(u_j^* | u_{j-1}^*)$ ,  $j=1, \dots, m$ , are conditional predictive one-step transition distributions that probabilistically quantify the combined effect of model and input uncertainties (total uncertainty) onto  $u_j^*$ ,  $j=1, \dots, m$ . Equation (4.16) is derived as follows:

Assuming that  $\pi_j(u_j) = \pi_j(u_j | u_{j-1}^*)$ , the density function of  $\Theta_j(u_j^* | u_{j-1}^*)$  is

$$\begin{aligned} \theta_j(u_j^* | u_{j-1}^*) &= \int_{-\infty}^{\infty} \phi_j(u_j^* | u_j, u_{j-1}^*) \pi_j(u_j | u_{j-1}^*) du_j \\ &= \int_{-\infty}^{\infty} \phi_j(u_j^* | u_j, u_{j-1}^*) \pi_j(u_j) du_j. \end{aligned}$$

In this density function,  $\phi_j(u_j^* | u_j, u_{j-1}^*)$  is the density function of  $\Phi_j(u_j^* | u_j, u_{j-1}^*)$ . Then,

$\theta_j(u_j^* | u_{j-1}^*)$  is integrated so that it has the following distribution function:

$$\begin{aligned}
\Theta_j(u_j^* | u_{j-1}^*) &= \int_{-\infty}^{\infty} \theta_j(\alpha | u_{j-1}^*) d\alpha \\
&= \int_{-\infty}^{u_j^*} \int_{-\infty}^{\infty} \phi_j(\alpha | u_j, u_{j-1}^*) \pi_j(u_j) du_j d\alpha \\
&= \int_{-\infty}^{\infty} \int_{-\infty}^{u_j^*} \phi_j(\alpha | u_j, u_{j-1}^*) d\alpha \pi_j(u_j) du_j \\
&= \int_{-\infty}^{\infty} \Phi_j(u_j^* | u_j, u_{j-1}^*) \pi_j(u_j) du_j.
\end{aligned}$$

Therefore, Equation (4.16) holds.

## 4.4 Application of BFF to the Equatorial Lakes

### 4.4.1 Introduction

Combined with the nonlinear river routing model in Chapter 3, the BFF procedure is applied to the Equatorial Lakes to generate a multi-trace ensemble forecast of Lake Albert outflow. The routing model was identified and calibrated with historical data from January 1, 1912 to August 1, 1975 (in monthly time intervals), as shown in Figure 4-2. The forecasting horizon is assumed to span from August 1, 1975, to November 1, 1977, so that the actual outflows (in the red-colored dotted line) of Lake Albert over the forecasting horizon can be compared with the forecasted outflow from the BFF. Hence, August 1, 1975 is assumed to coincide with the last observation time before the forecast initiation time.

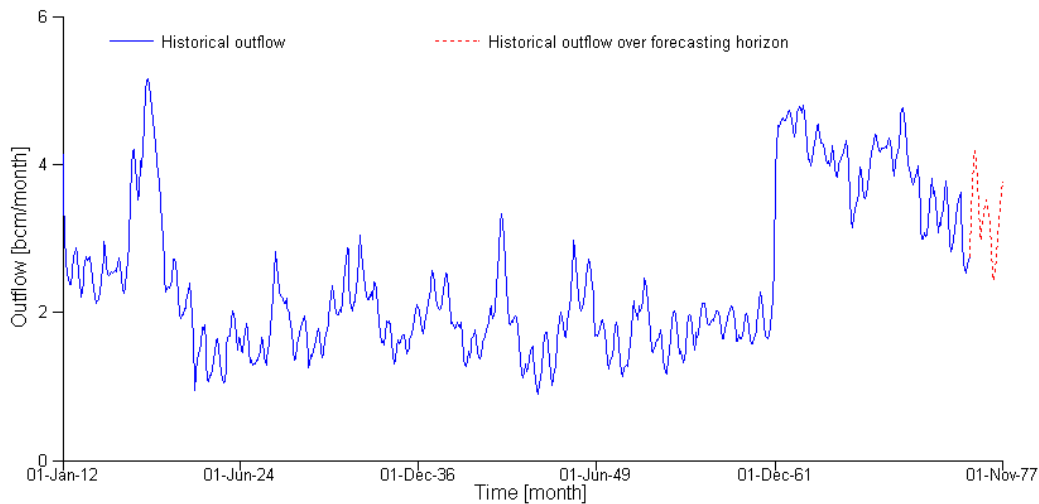


**Figure 4-2.** BFF application data: historical outflow from January 1, 1912 to August 1, 1975; forecasting horizon from August 1, 1975 to November 1, 1977; time in monthly intervals; monthly discharge in billions of cubic meters.

## 4.4.2 Input uncertainty processor

### 4.4.2.1 Inflow forecast

To estimate future NBS (net basin supply) of each lake by a historical analog method, we compare the most currently observed consecutive  $l$  NBS data points for each lake with the same number of consecutive inflows for the corresponding lake in past events. Then, NBS traces of the length of  $m$  succeeding the most similar events in history to the current situation are selected from the historical NBS data of each lake. The length of the forecasting horizon is  $m = 27$  (27 months). The collection of the selected traces becomes the ensemble of future NBS, as shown in Figure 4-3, Figure 4-4, and Figure 4-5 for Lake Victoria, Lake Kyoga, and Lake Albert, respectively. For the comparison, this approach uses  $l = 6$  data points (6 months).

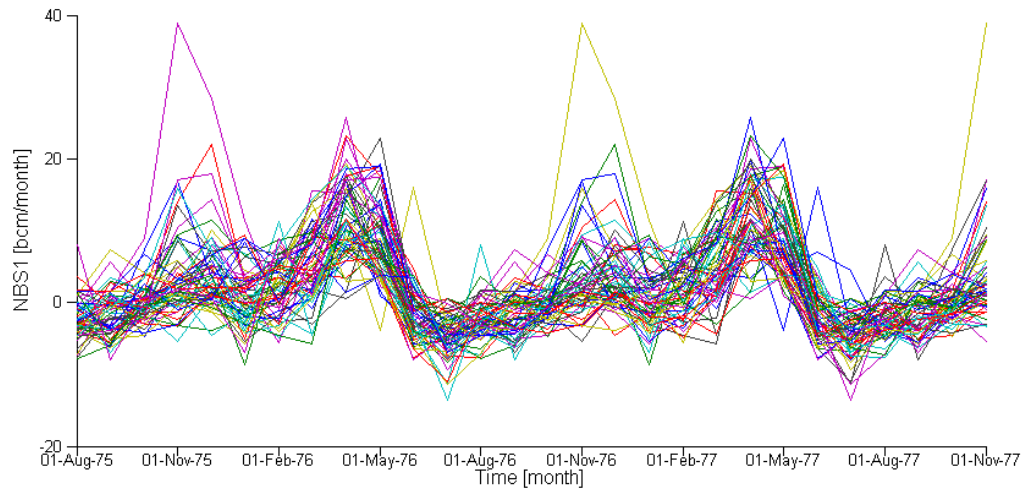


**Figure 4-3.** Ensemble forecasts of NBS for Lake Victoria over the forecasting horizon. Time is in monthly intervals.

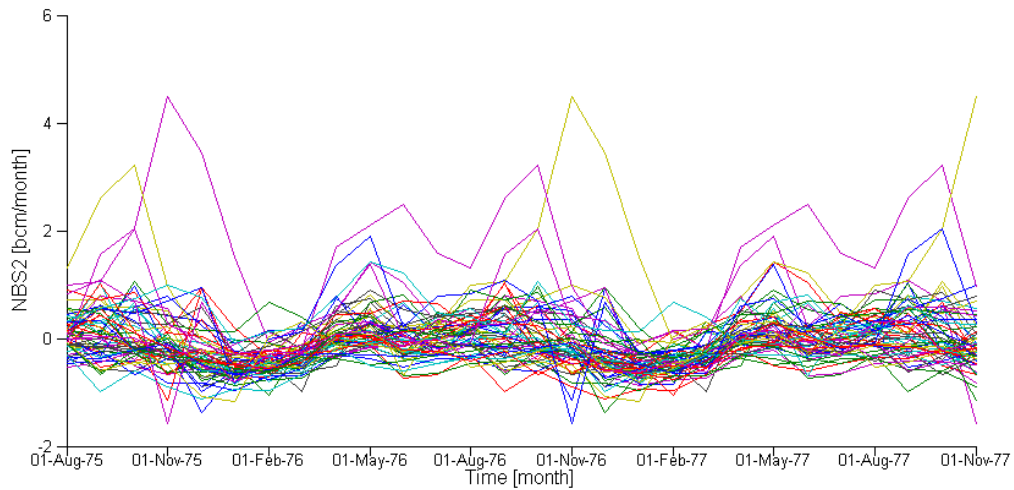


**Figure 4-4.** Ensemble forecasts of NBS for Lake Kyoga over the forecasting horizon. Time is in monthly intervals.

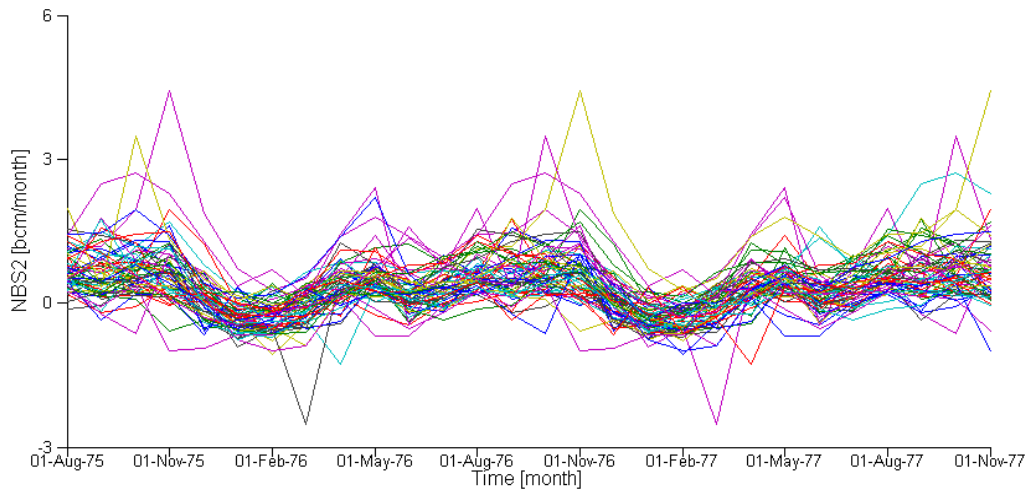


**Figure 4-5.** Ensemble forecasts of NBS for Lake Albert over the forecasting horizon. Time is in monthly intervals.

#### 4.4.2.2 Ensemble outflow forecast and distribution fitting

Each NBS trace in the ensemble is simulated with the calibrated nonlinear river routing model for generating a multi-trace ensemble of model-estimated outflows of Lake Albert, as shown in Figure 4-6, which is the result of the ensemble forecasting.

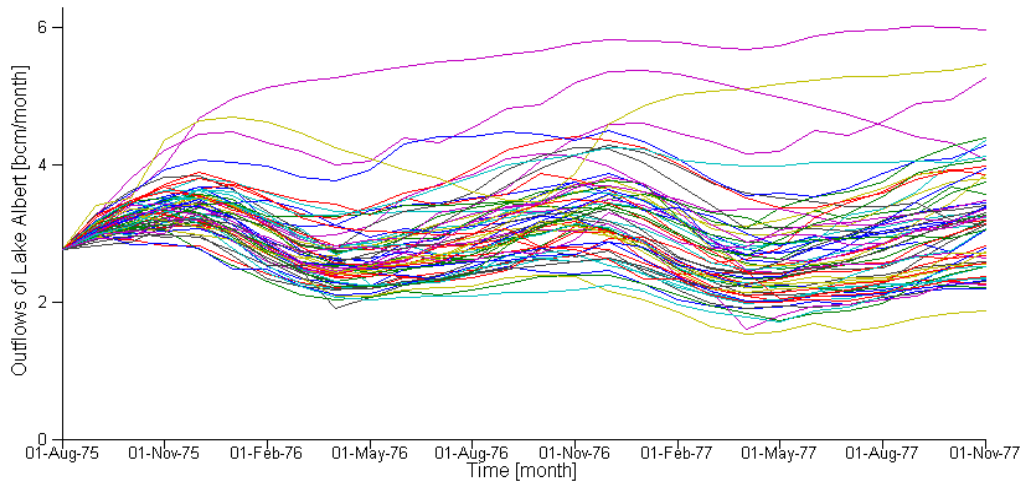


**Figure 4-6.** Simulated outflows of Lake Albert over the forecasting horizon. Time is in monthly intervals.

The general procedure for calculating an empirical distribution of a general random variable  $\mathbf{z}$ , is outlined below:

1. The observed values of  $\mathbf{z}$ ,  $z^i, i=1, \dots, d$ , are sorted into increasing order so that

$$z^1 < \dots < z^r < \dots < z^d, r=1, \dots, d.$$

2. Then, empirical distribution  $\hat{F}_{\mathbf{z}}(z^r)$  for each  $z^r$  is calculated by

$$\hat{F}_{\mathbf{z}}(z^r) = \frac{r}{d}.$$

From the forecasted values of the model-estimated outflow for each time  $j$  in the ensemble, a sequence of empirical distributions of  $\mathbf{u}_j, j=1, \dots, m$ , is calculated by the method presented above.  $\mathbf{u}_j$  is a random variable of the model-estimated outflow of Lake Albert for time step  $j$

of the forecasting horizon. A three-parameter Weibull distribution function [*Kelly and Krzysztofowicz, 2000*] is selected for fitting the empirical distributions:

$$Wb(x) = \begin{cases} 1 - \exp\left[-\left(\frac{x-\gamma}{\alpha}\right)^\beta\right], & x > \gamma. \\ 0, & x \leq \gamma \end{cases} \quad (4.17)$$

In the above equation, scale parameter  $\alpha > 0$ , shape parameter  $\beta > 0$ , and shift parameter  $r \in (-\infty, \infty)$ . Based on a parameter estimation method presented by *Kelly and Krzysztofowicz* [2000], a sequence of Weibull distributions  $\Pi_j(u_j)$ ,  $j = 1, \dots, m$ , is calculated and shown in Figure 4-7 for selected time steps with corresponding empirical distributions.

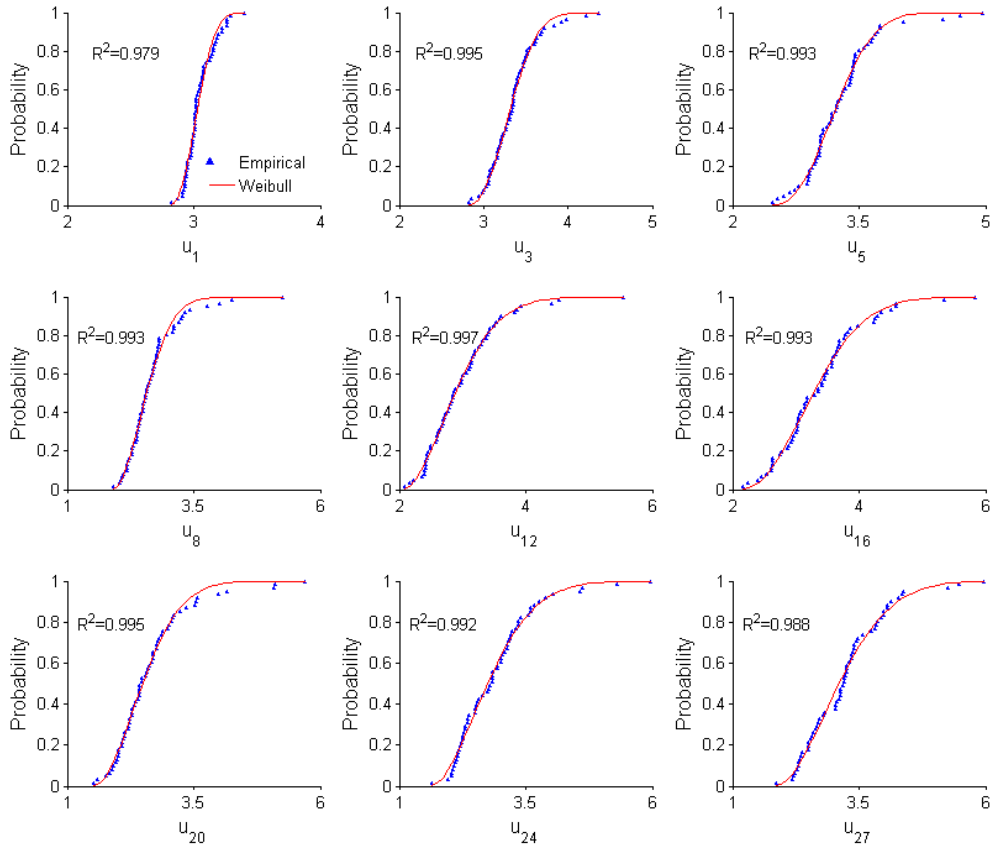


**Figure 4-7.** Empirical distributions of  $\mathbf{u}_j$  and the fitted Weibull distributions  $\Pi_j(u_j)$  for select time steps of the forecasting horizon.

In addition, coefficients of determinations  $R^2$  for all time steps are calculated in Table 4-1. In most cases,  $R^2$  are well above 0.98, indicating that Weibull distributions  $\Pi_j(u_j)$ ,  $j = 1, \dots, m$ , fit the corresponding empirical distributions well.

**Table 4-1.**  $R^2$  of fitted Weibull distributions  $\Pi_j(u_j)$  for  $j = 1, \dots, m$ .

$j$	$R^2$	$j$	$R^2$	$j$	$R^2$	$j$	$R^2$
1	0.979	8	0.993	15	0.992	22	0.995
2	0.993	9	0.992	16	0.993	23	0.997
3	0.995	10	0.995	17	0.993	24	0.992
4	0.995	11	0.995	18	0.989	25	0.992
5	0.993	12	0.997	19	0.993	26	0.992
6	0.991	13	0.996	20	0.995	27	0.988
7	0.994	14	0.992	21	0.996		

### 4.4.3 Model uncertainty processor

#### 4.4.3.1 Marginal distributions of actual and model-estimated outflows

A common practice in the ensemble forecasting of lake outflow is to calculate an ensemble of future outflow via simulating any lake model with each trace of the ensembles of future lake inflows. In light of the BFF, this ensemble forecasting method is equivalent to the input uncertainty processor of the BFF, which accounts for the influence of only input uncertainty on forecasted outflows [Krzysztofowicz, 1999; Krzysztofowicz and Maranzano, 2004b]. Hence, the following procedures and results show how the BFF improves the forecasting results from the input uncertainty processor, as shown in Figure 4-6, in terms of both accuracy and reliability.

First, the sequences of marginal distributions  $\Gamma_j(u_j^*)$  and  $\Lambda_j(u_j)$  need to be generated, where  $u_j^*$  and  $u_j$  are random variables of the actual future outflow and the model-estimated outflow of Lake Albert at time step  $j$ , respectively. To this end, a historical analog method is selected for constructing the ensembles of observed and model-estimated outflows. Figure 4-8 shows

the historical analogs most relevant to the current trend of the observed outflows of Lake Albert. Subsequently, the sequences of empirical and fitted Weibull distributions of  $\mathbf{u}_j^*$ ,  $j = 0, \dots, m$ , are calculated from analogous data points, and the results for selected time steps appear in Figure 4-10. The parameter estimation technique proposed by *Kelly and Krzysztofowicz* [2000] is used for fitting the empirical distributions by Weibull distributions. In addition,  $R^2$  values for the fitted Weibull distributions for all time steps appear in Table 4-2.

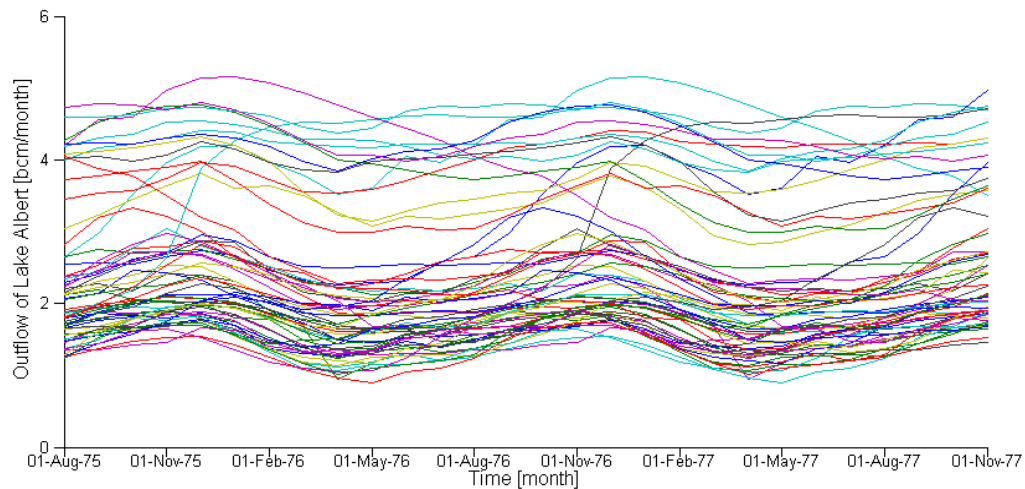


**Figure 4-8.** Historical analogs of actual outflows over the forecasting horizon. Time is in monthly intervals.

Similarly, Figure 4-9 shows the historical analogs of the model-estimated outflow of Lake Albert. The sequences of the empirical and fitted Weibull distributions of  $\mathbf{u}_j$ ,  $j = 0, \dots, m$ , calculated from analogous data points, are shown in Figure 4-11. In addition, the  $R^2$  values of the fitted Weibull distributions for all time steps appear in Table 4-3.

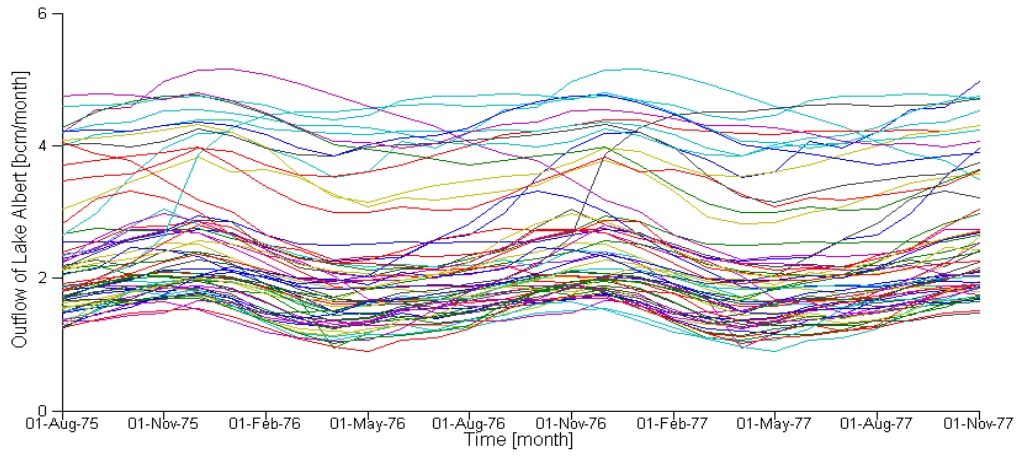


**Figure 4-9.** Historical analogs of model-estimated outflows over the forecasting horizon. Time is in monthly intervals.

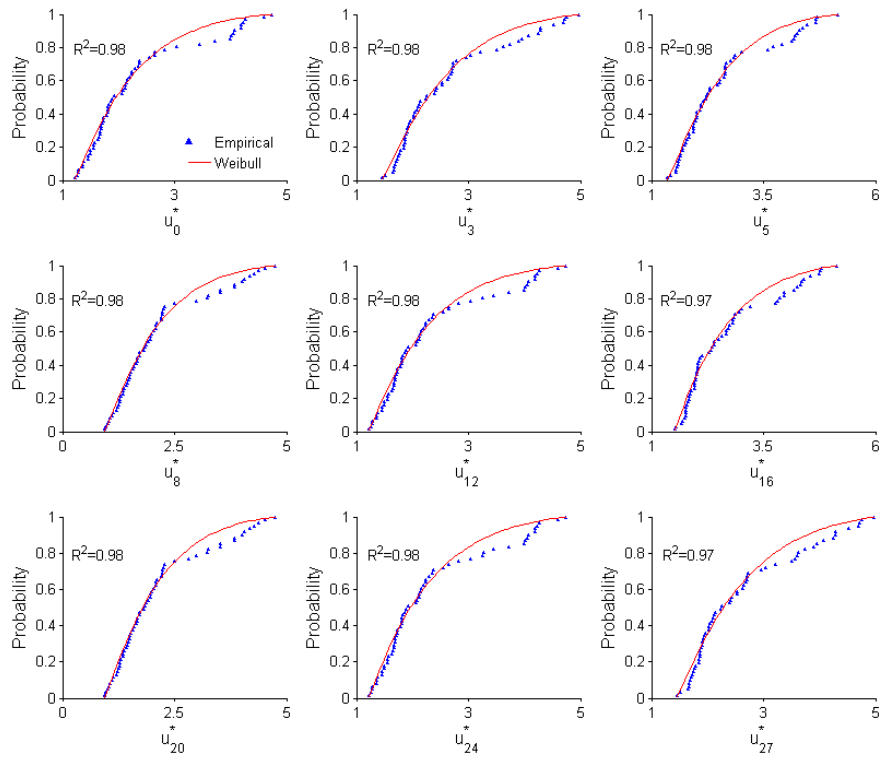


**Figure 4-10.** Empirical distributions of  $u_j^*$  and the fitted Weibull distributions  $\Gamma_j(u_j^*)$  for selected time steps of the forecasting horizon.

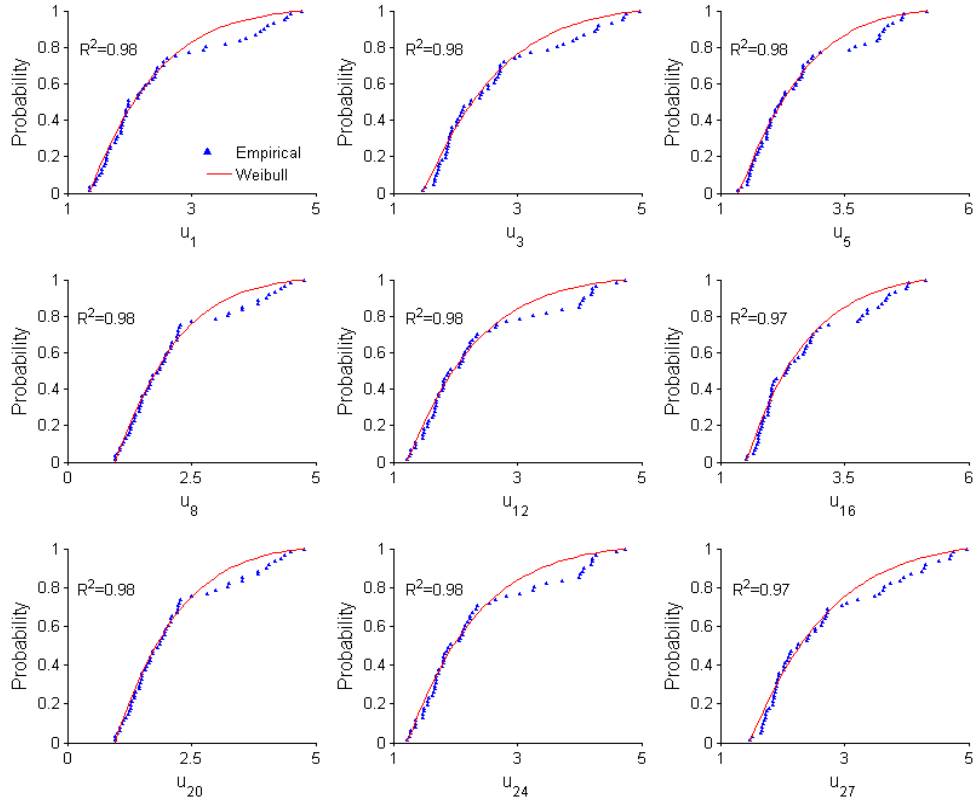


**Figure 4-11.** Empirical distributions of  $\mathbf{u}_j$  and fitted Weibull distributions  $\Lambda_j(u_j)$  for selected time steps of the forecasting horizon.

**Table 4-2.**  $R^2$  of fitted Weibull distributions  $\Gamma_j(u_j^*)$  for  $j = 0, \dots, m$ .

$j$	$R^2$	$j$	$R^2$	$j$	$R^2$	$j$	$R^2$
0	0.98	7	0.98	14	0.97	21	0.98
1	0.98	8	0.98	15	0.98	22	0.97
2	0.97	9	0.98	16	0.97	23	0.97
3	0.98	10	0.98	17	0.98	24	0.98
4	0.98	11	0.98	18	0.98	25	0.98
5	0.98	12	0.98	19	0.98	26	0.97
6	0.98	13	0.98	20	0.98	27	0.97

**Table 4-3.**  $R^2$  of fitted Weibull distributions  $\Lambda_j(u_j)$  for  $j = 1, \dots, m$ .

$j$	$R^2$	$j$	$R^2$	$j$	$R^2$	$j$	$R^2$
0	0.98	7	0.98	14	0.97	21	0.98
1	0.98	8	0.98	15	0.98	22	0.97
2	0.98	9	0.98	16	0.97	23	0.97
3	0.98	10	0.97	17	0.98	24	0.98
4	0.97	11	0.98	18	0.98	25	0.98
5	0.98	12	0.98	19	0.98	26	0.97
6	0.98	13	0.98	20	0.98	27	0.97

#### 4.4.3.2 Normal quantile transform

By the NQT,  $\mathbf{u}_j^*$  and  $\mathbf{u}_j$  are transformed into  $\mathbf{w}_j$  and  $\mathbf{x}_j$ ,  $j = 0, \dots, m$ , such that

$$\mathbf{w}_j = \begin{bmatrix} Q^{-1}\{\Gamma_j(u_j^*(1))\} \\ \vdots \\ Q^{-1}\{\Gamma_j(u_j^*(i))\} \\ \vdots \\ Q^{-1}\{\Gamma_j(u_j^*(s))\} \end{bmatrix}, \quad \mathbf{x}_j = \begin{bmatrix} Q^{-1}\{\Lambda_j(u_j(1))\} \\ \vdots \\ Q^{-1}\{\Lambda_j(u_j(i))\} \\ \vdots \\ Q^{-1}\{\Lambda_j(u_j(s))\} \end{bmatrix}, \quad (4.18)$$

$j = 0, \dots, m$ .

In the above equation,  $Q^{-1}$ , the inverse of the standard normal distribution function, can be approximated by a polynomial function [Abramowitz and Stegun, 1972]. As seen in Figure 4-8 and Figure 4-9,  $u_j^*(i)$  and  $u_j(i)$  are the value of the  $i$ th historical analogous trace of the observed outflow for time  $j$  and the value of the  $i$ th historical analogous trace of the corresponding model-estimated outflow for that time, respectively. The number of analogous data points for each time is indicated by  $s$ .

#### 4.4.3.3 Prior density in the transformed space and its validation

In the space of transformed variates  $\mathbf{w}_j$  and  $\mathbf{x}_j$ , a sequence of prior densities calculated from Equations (4.1), (4.2), and (4.3) is summarized by

$$\begin{aligned}
 r_{Q^j}(\mathbf{w}_j | \mathbf{w}_{j-1}) &= \frac{1}{\varepsilon_j \sqrt{2\pi}} \exp \left\{ -\frac{(\mathbf{w}_j - c_j \mathbf{w}_{j-1} - z_j)^2}{2\varepsilon_j^2} \right\}, \\
 E(\mathbf{w}_j | \mathbf{w}_{j-1}) &= c_j \mathbf{w}_{j-1} + z_j, \\
 Var(\mathbf{w}_j | \mathbf{w}_{j-1}) &= \varepsilon_j^2, \\
 j &= 1, \dots, m.
 \end{aligned} \tag{4.19}$$

The results of the values of the parameters in the above equation, estimated from linear regression models

$$\begin{aligned}
 \mathbf{w}_j &= c_j \mathbf{w}_{j-1} + z_j + \Xi_j, \Xi_j \sim N(0, \varepsilon_j^2), \\
 j &= 1, \dots, m.
 \end{aligned} \tag{4.20}$$

are shown in Table 4-4.

The assumption of linearity of the relationship between  $\mathbf{w}_j$  and  $\mathbf{w}_{j-1}$ ,  $j = 1, \dots, m$ , is justified by plotting the values of dependent variable  $\mathbf{w}_j$  against the values of independent variable  $\mathbf{w}_{j-1}$  and calculating the  $R^2$  value of a regression line that fits against the data points in each plot, as shown in both Figure 4-12 and Table 4-4. In most plots, the main bodies of the points lie

approximately on straight lines, and the values of  $R^2$  are high, so the linearity assumption is reasonably valid.

**Table 4-4.** Parameters of prior densities in the space of the transformed variates

$j$	$c_j$	$z_j$	$\varepsilon_j$	$R^2$	$j$	$c_j$	$z_j$	$\varepsilon_j$	$R^2$
1	0.959	0.019	0.278	0.93	15	0.964	-0.024	0.136	0.98
2	0.976	0.036	0.174	0.97	16	0.946	0.008	0.285	0.92
3	0.609	-0.024	0.527	0.74	17	0.993	-0.019	0.132	0.98
4	0.946	-0.003	0.287	0.92	18	1.010	-0.018	0.118	0.99
5	0.998	-0.009	0.134	0.98	19	1.028	-0.021	0.177	0.97
6	1.018	-0.017	0.120	0.99	20	0.954	0.017	0.340	0.90
7	1.010	-0.019	0.177	0.97	21	1.026	0.048	0.278	0.94
8	0.958	0.018	0.343	0.90	22	1.128	0.083	0.722	0.76
9	1.024	0.056	0.279	0.94	23	0.972	-0.021	0.152	0.98
10	0.990	-0.002	0.150	0.98	24	0.991	-0.007	0.149	0.98
11	0.936	-0.012	0.154	0.98	25	0.960	0.032	0.272	0.94
12	0.992	-0.001	0.151	0.98	26	0.983	0.032	0.168	0.97
13	0.956	0.021	0.274	0.93	27	0.603	-0.019	0.530	0.73
14	0.982	0.034	0.171	0.97					

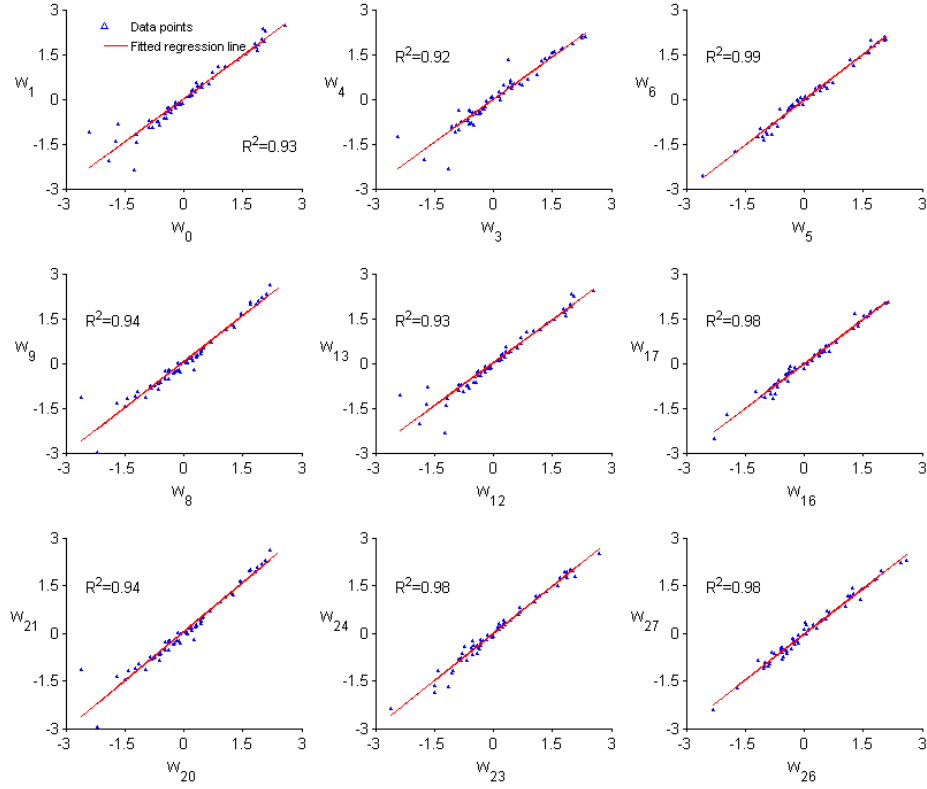


**Figure 4-12.** Linearity of  $w_j$  on  $w_{j-1}$  in the prior densities in the space of the transformed variates. Selected  $j$ 's are used.

To assess the normality assumption of error variable  $\Xi_j, j = 1, \dots, m$ , in Equation (4.20), we have drawn normal probability plots or normal scores plots, shown in Figure 4-13. In the plots, residual  $e_j(i)$  for time  $j$  and data  $i$  is calculated by

$$e_j^p(i) = w_j(i) - \hat{w}_j(i) = w_j(i) - (c_j w_{j-1}(i) + z_j), i = 1, \dots, s, j = 1, \dots, m, \quad (4.21)$$

where  $s$  is the number of observed values of variable  $w_j$  or  $w_{j-1}$ . In addition, the normal score of the  $r$ th smallest residual is calculated by [Hayter, 2002]

$$Q^{-1}\left(\frac{r - \frac{3}{8}}{s + \frac{1}{4}}\right). \quad (4.22)$$

In the above equation,  $Q$  is a standard normal distribution function. After outliers are removed, the  $R^2$  value of a regression line fitted against a data set of each plot is calculated in Table 4-5. The high values of  $R^2$  (the average is 0.96) in most time steps suggest that the normality assumption holds.

The assumption of constant variance  $\varepsilon_j^2, j = 1, \dots, m$ , can be verified by a visual examination of the data points in each residual plot. A residual plot is drawn with residual  $e_j$  on the vertical axis and independent variable  $w_{j-1}$  on the horizontal axis, shown in Figure 4-14. The main bodies of the data points in most residual plots are randomly dispersed around the horizontal axis through zero, so the homoscedasticity assumption will be reasonably valid. In fact, the fairly random patterns provide an acceptable justification for the assumption of independence of  $\Xi_j$  from independent variables  $w_{j-1}$  for  $j = 1, \dots, m$ .

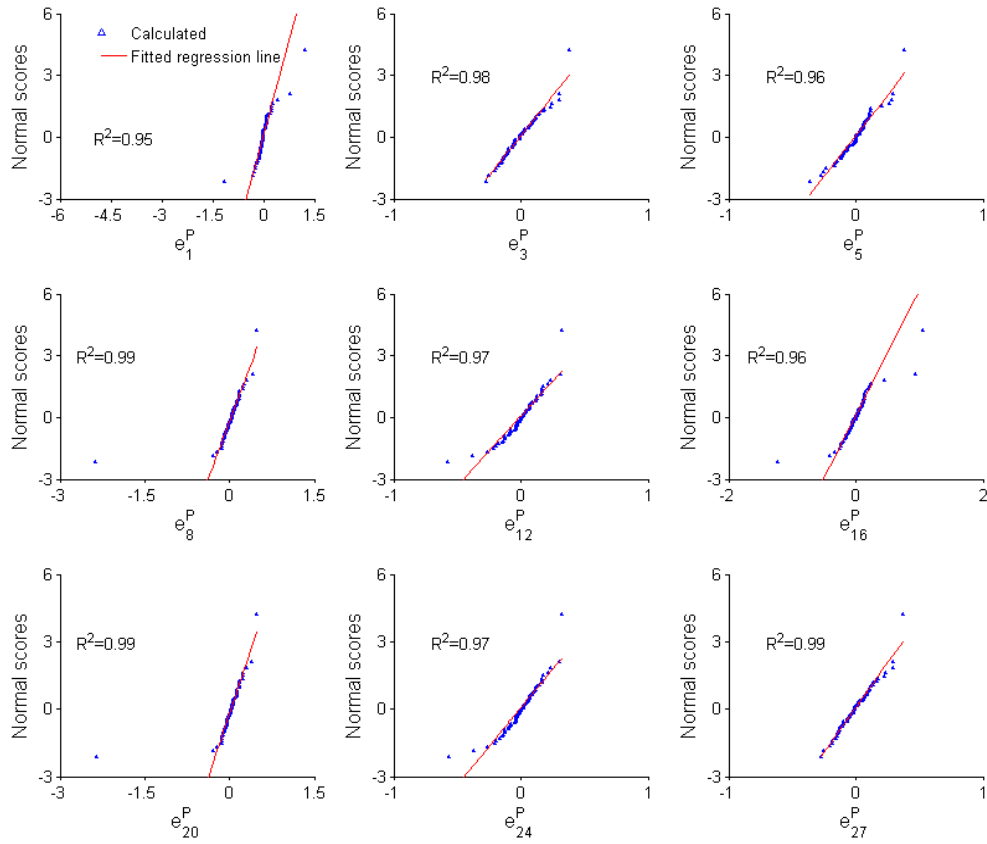


**Figure 4-13.** Normal probability plots for the prior densities in the space of the transformed variates. Selected  $j$ 's are used.

**Table 4-5.**  $R^2$  values of the regression lines in the normal probability plots for the prior densities in the space of the transformed variates.

$j$	$R^2$	$j$	$R^2$	$j$	$R^2$	$j$	$R^2$
1	0.95	8	0.99	15	0.99	22	0.97
2	0.99	9	0.95	16	0.96	23	0.92
3	0.98	10	0.98	17	0.97	24	0.97
4	0.96	11	0.93	18	0.97	25	0.95
5	0.96	12	0.97	19	0.86	26	0.98
6	0.97	13	0.95	20	0.99	27	0.99
7	0.86	14	0.98	21	0.95		

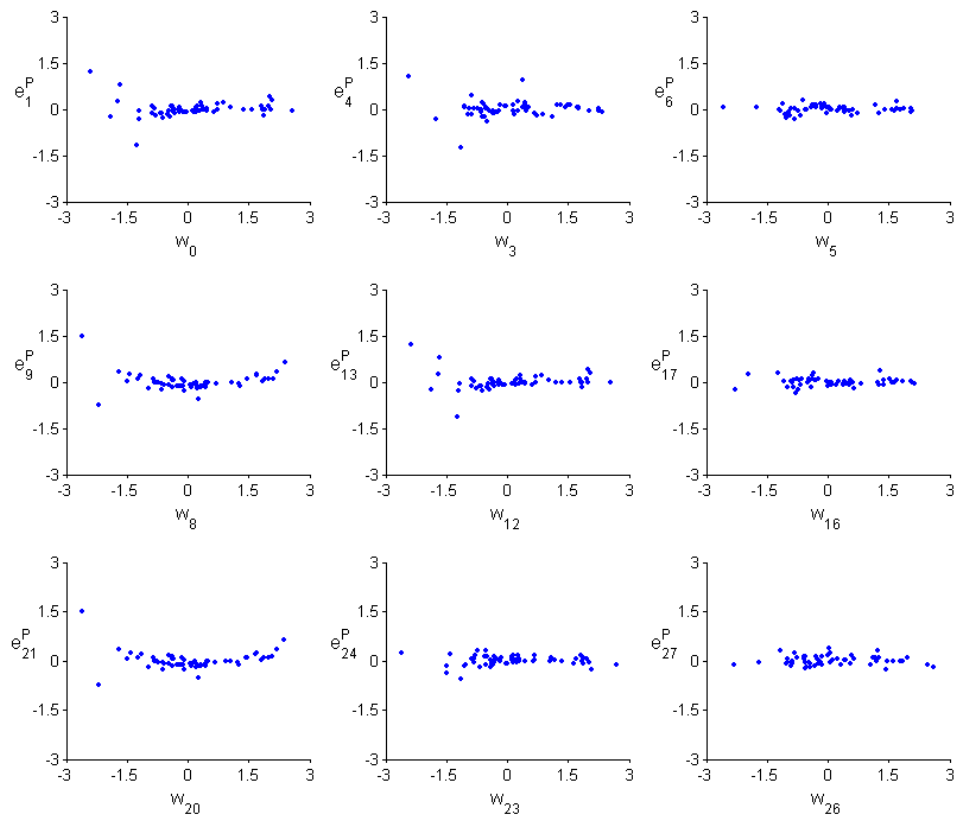


**Figure 4-14.** Residual plots for the prior densities in the space of the transformed variates.

#### 4.4.3.4 Likelihood function in the transformed space and its validation

As with the prior distributions, a sequence of likelihood functions in the space of the transformed variates calculated from Equations (4.4), (4.5), and (4.6) is summarized by

$$\begin{aligned}
f_{Q^j}(x_j | w_j, w_{j-1}) &= \frac{1}{\sigma_j \sqrt{2\pi}} \exp \left\{ -\frac{(x_j - (a_j w_j + e_j w_{j-1} + b_j))^2}{2\sigma_j^2} \right\}, \\
E(\mathbf{x}_j | w_j, w_{j-1}) &= a_j w_j + e_j w_{j-1} + b_j, \\
Var(\mathbf{x}_j | w_j, w_{j-1}) &= \sigma_j^2, \\
j &= 1, \dots, m.
\end{aligned} \tag{4.23}$$

The values of the parameters in the above equation are estimated from multiple linear regression models

$$\begin{aligned}
\mathbf{x}_j &= a_j \mathbf{w}_j + e_j \mathbf{w}_{j-1} + b_j + \Theta_j, \Theta_j \sim N(0, \sigma_j^2), \\
j &= 1, \dots, m.
\end{aligned} \tag{4.24}$$

the results of which appear in Table 4-6.

As shown in Figure 4-15 and Table 4-6, the assumption of linearity of  $\mathbf{x}_j$  on  $\mathbf{w}_j$  and  $\mathbf{w}_{j-1}$ ,  $j = 1, \dots, m$ , are assessed by plotting the values of dependent variable  $\mathbf{x}_j$  against the values of independent variables  $\mathbf{w}_j$  and  $\mathbf{w}_{j-1}$  and calculating the  $R^2$  value of a regression line that fits to the data points in each plot. In most plots, the main bodies of the data points lie approximately on straight planes, and the values of  $R^2$  are very high (approximately 1.00), so the linearity assumption holds reasonably.

**Table 4-6.** Parameters of the likelihood functions in the space of the transformed variates.

$j$	$a_j$	$e_j$	$b_j$	$\sigma_j$	$R^2$	$j$	$a_j$	$e_j$	$b_j$	$\sigma_j$	$R^2$
1	1.007	0.003	0.009	0.009	1.00	15	1.001	0.001	0.003	0.008	1.00
2	0.983	0.017	-0.005	0.009	1.00	16	1.001	-0.003	0.003	0.008	1.00
3	0.998	0.002	0.002	0.008	1.00	17	1.015	-0.015	-0.002	0.006	1.00
4	1.004	-0.003	0.000	0.008	1.00	18	0.985	0.003	0.005	0.006	1.00
5	1.014	-0.016	0.002	0.006	1.00	19	0.994	-0.003	0.003	0.005	1.00
6	0.993	0.005	0.001	0.006	1.00	20	0.992	0.005	-0.001	0.007	1.00
7	1.003	-0.001	0.003	0.005	1.00	21	0.990	0.003	-0.002	0.005	1.00
8	1.003	0.007	-0.006	0.007	1.00	22	1.018	-0.015	-0.004	0.006	1.00
9	0.997	0.007	-0.003	0.004	1.00	23	1.000	0.001	-0.001	0.006	1.00
10	0.997	-0.012	0.006	0.007	1.00	24	1.014	-0.004	-0.001	0.005	1.00
11	0.997	0.001	-0.001	0.006	1.00	25	0.996	0.002	-0.005	0.008	1.00
12	1.005	-0.003	-0.003	0.005	1.00	26	0.979	0.017	0.002	0.009	1.00
13	1.002	0.003	-0.006	0.009	1.00	27	1.002	0.001	-0.001	0.008	1.00
14	0.979	0.018	0.000	0.009	1.00						

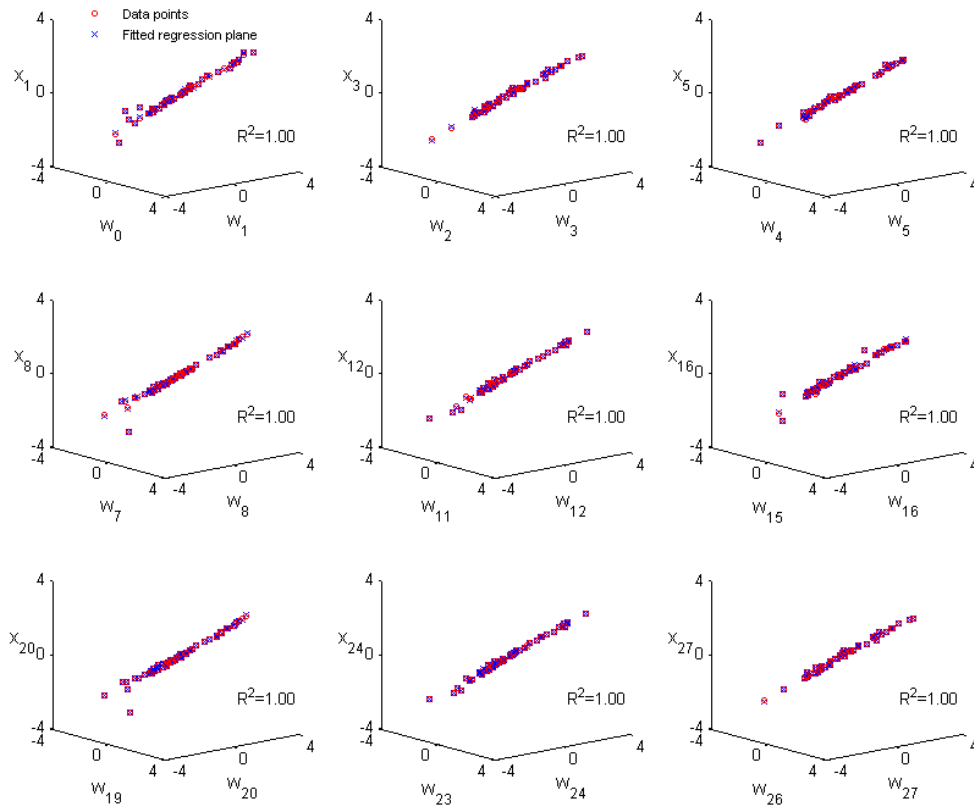


**Figure 4-15.** Linearity of  $x_j$  on  $w_{j-1}$  and  $w_{j-2}$  of likelihood functions in the space of the transformed variates. Selected  $j$ 's are used.

Figure 4-16 shows a sequence of normal probability plots that assesses the normality assumption of error variables  $\Theta_j, j = 1, \dots, m$ , in Equation (4.24). In each plot, residual  $e_j^L(i)$  for time  $j$  and data  $i$  is calculated by

$$e_j^L(i) = x_j(i) - \hat{x}_j(i) = x_j(i) - (a_j w_j(i) + e_j w_{j-1}(i) + b_j), i = 1, \dots, s, j = 1, \dots, m, \quad (4.25)$$

where  $s$  is the number of observed values of variable  $x_j, w_j$ , or  $w_{j-1}$ . Most of the plots show linear patterns of the main bodies of data points, indicating that linear models provide a decent fit to the data. Indeed, as seen in Table 4-7, the high values of  $R^2$  (the average is 0.94) in most time steps suggest that the normality assumption is valid.

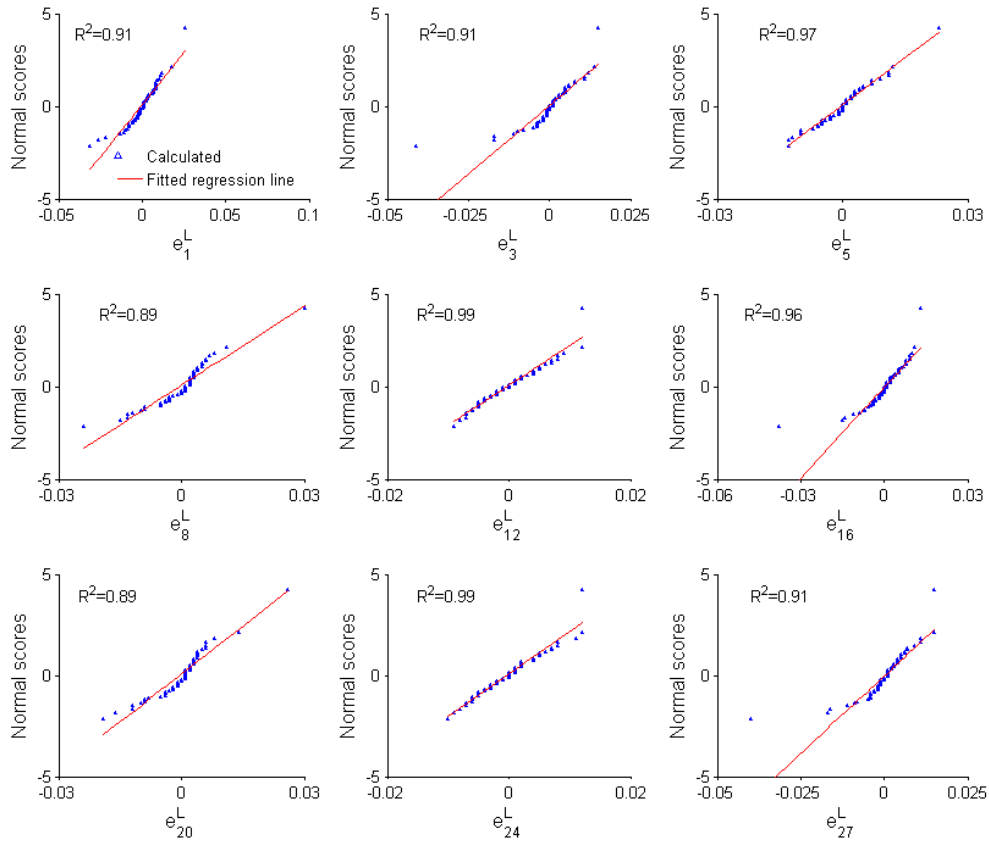


**Figure 4-16.** Normal probability plots for the likelihood functions in the space of the transformed variates. Selected  $j$ 's are used.

**Table 4-7.**  $R^2$  values of the regression lines in the normal probability plots for the likelihood functions in the space of the transformed variates.

$j$	$R^2$	$j$	$R^2$	$j$	$R^2$	$j$	$R^2$
1	0.91	8	0.89	15	0.91	22	0.94
2	0.89	9	0.95	16	0.96	23	0.94
3	0.91	10	0.94	17	0.98	24	0.99
4	0.97	11	0.94	18	0.98	25	0.92
5	0.97	12	0.99	19	0.94	26	0.89
6	0.99	13	0.91	20	0.89	27	0.91
7	0.90	14	0.90	21	0.99		

Figure 4-17 shows residual plots for selected time steps for verifying the assumption of constant variance  $\sigma_j^2, j = 1, \dots, m$ , by visual examination. A residual plot is drawn with residual  $e_j^L$  on the vertical axis and independent variables  $w_j$  and  $w_{j-1}$  on the horizontal axis, shown in Figure 4-17. The majority of data points in most residual plots are randomly dispersed around the horizontal axis through zero so that the assumption of homoscedasticity is reasonably valid. In fact, the fairly random patterns provide acceptable verification of the assumption of the independence of  $\Theta_j$  from independent variables  $w_j$  and  $w_{j-1}$  for  $j = 1, \dots, m$ .

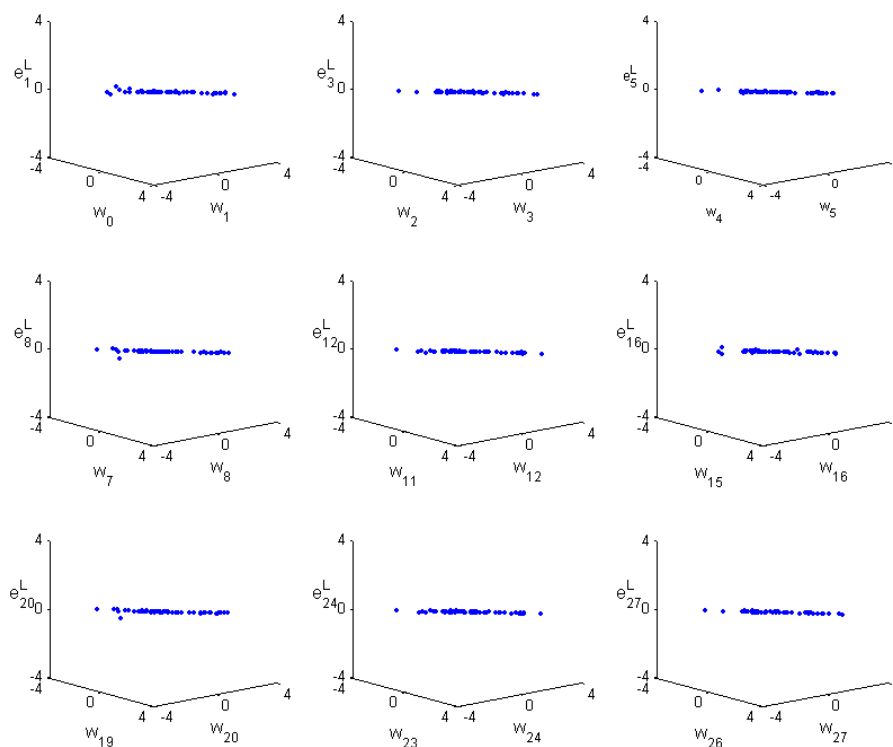


**Figure 4-17.** Residual plots for the likelihood functions in the space of the transformed variates. Selected  $j$ 's are used.

#### 4.4.4 Integrator

After calculating a sequence of posterior distributions in the transformed space by Bayes' theorem and then calculating a sequence of meta-Gaussian posterior distribution functions  $\Phi_j(u_j^* | u_j, u_{j-1}^*)$ ,  $j = 1, \dots, m$ , by Equation (4.15), we derive a sequence of predictive one-step transition distributions in the space of the original variates by

$$\Theta_j(u_j^* | u_{j-1}^*) = \int_{-\infty}^{\infty} \Phi_j(u_j^* | u_j, u_{j-1}^*) \pi_j(u_j) du_j, \quad (4.26)$$

$$j = 1, \dots, m.$$

In this equation,  $\pi_j(u_j)$  is the corresponding density for distribution  $\Pi_j(u_j)$ . Using the Romberg algorithm, the composition of the outcome from the MUP,  $\Phi_j(u_j^* | u_j, u_{j-1}^*)$ , and the outcome from the IUP,  $\pi_j(u_j)$ , are numerically integrated over any feasible range of  $u_j$  for quantifying the total uncertainty (the combined effect of the model and the input uncertainties). Because actual outflows in the future  $u_{j-1}^*$ ,  $j = 2, \dots, m$ , except  $u_0^*$ , are unknown at present, the Monte Carlo simulation method is used to materialize  $u_{j-1}^*$ ,  $j = 2, \dots, m$ , and thus to calculate  $\Theta_j(u_j^* | u_{j-1}^*)$ ,  $j = 1, \dots, m$ . In a Bayesian ensemble generator [Krzysztofowicz and Maranzano, 2004b], the simulation procedure is outlined below:

1. Generate a set of uniform random numbers  $(p_1, \dots, p_m)$ , where  $0 < p_j < 1$ .
2. Given observed  $u_0^*$ , realize  $u_1^*$  such that  $p_1 = \Theta_1(u_1^* | u_0^*)$ .

3. Realize  $u_j^*$  repeatedly on  $j = 2, \dots, m$  such that  $p_j = \Theta_j(u_j^* | u_{j-1}^*)$  given  $u_{j-1}^*$  in the preceding realization.

This single realization of  $u_{j-1}^*, j = 2, \dots, m$ , generates a single sequence of the predictive distributions  $\Theta_j(u_j^* | u_{j-1}^*), j = 1, \dots, m$ . Consequently, a  $M$  number of simulations generates an  $M$  number of sequences of  $\Theta_j(u_j^* | u_{j-1}^*), j = 1, \dots, m$ . Figure 4-18 shows an  $M$  number of simulated predictive distributions  $\Theta_j(u_j^* | u_{j-1}^*)$  over some number of discrete values of  $u_j^*$  (gray-colored solid curves) for  $j=4$  and 24. Subsequently, for each value of  $u_j^*$ , the values of  $\Theta_j(u_j^* | u_{j-1}^*)$  for  $M$  different realized values of  $u_{j-1}^*$  are arithmetically averaged. As a result, all discrete values of  $u_j^*, j = 1, \dots, m$ , have corresponding average values of  $\Theta_j(u_j^* | u_{j-1}^*)$ , depicted by red dots for  $j=4$  and 24 in Figure 4-18.

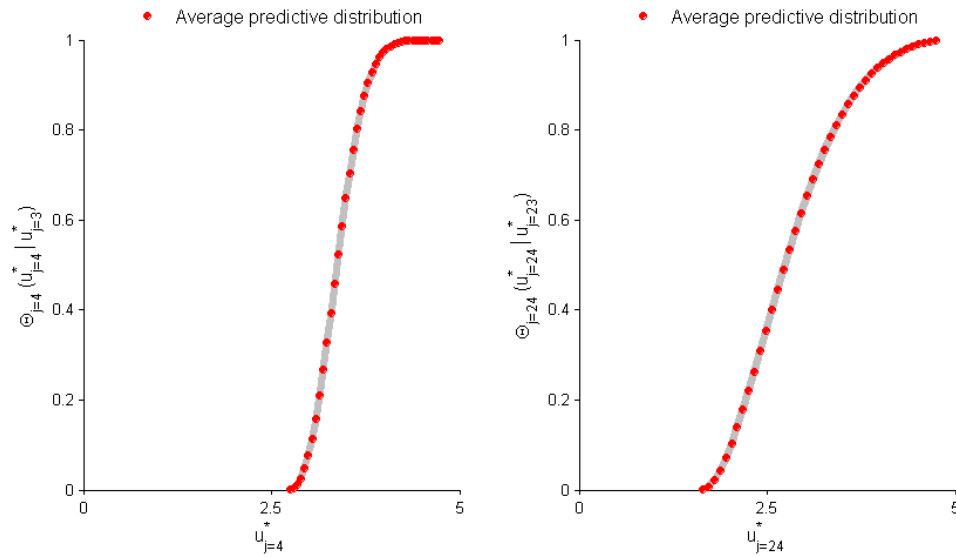


**Figure 4-18.** Simulated predictive one-step transition distributions from the Monte Carlo simulation and the corresponding average predictive distributions.  $j=4$  and  $24$  are used.

Next, the average predictive distributions (red dots) are approximated by Weibull distributions  $\Omega_j(u_j^* | u_{j-1}^*)$ ,  $j = 1, \dots, m$ , and then box plots are drawn from  $\Omega_j(u_j^* | u_{j-1}^*)$  as well as from distributions of the model-estimated outflow,  $\Pi_j(u_j)$  for all  $j$  in Figure 4-19. In light of the BFF,  $\Pi_j(u_j)$  represents pre-BFF distributions (blue box plots) and  $\Omega_j(u_j^* | u_{j-1}^*)$  represents BFF distributions (red box plots). A comparison of the two box plots clearly shows that the variances of the BFF distributions are smaller than those of the pre-BFF distribution, while the actual outflows that materialize (green dots) still fall within the forecasted ranges. Indeed, the value of  $R_1$  (the ratio of the range of  $u_j^*$  from the BFF distribution to that from the pre-BFF distribution) in either Table 4-8 or Figure 4-20 decreases and maintains the ratio of about 0.78 until the end of the forecasting time after the initial increase in the first few months. Therefore, the BFF-derived forecasts are more concise without significantly sacrificing reliability.

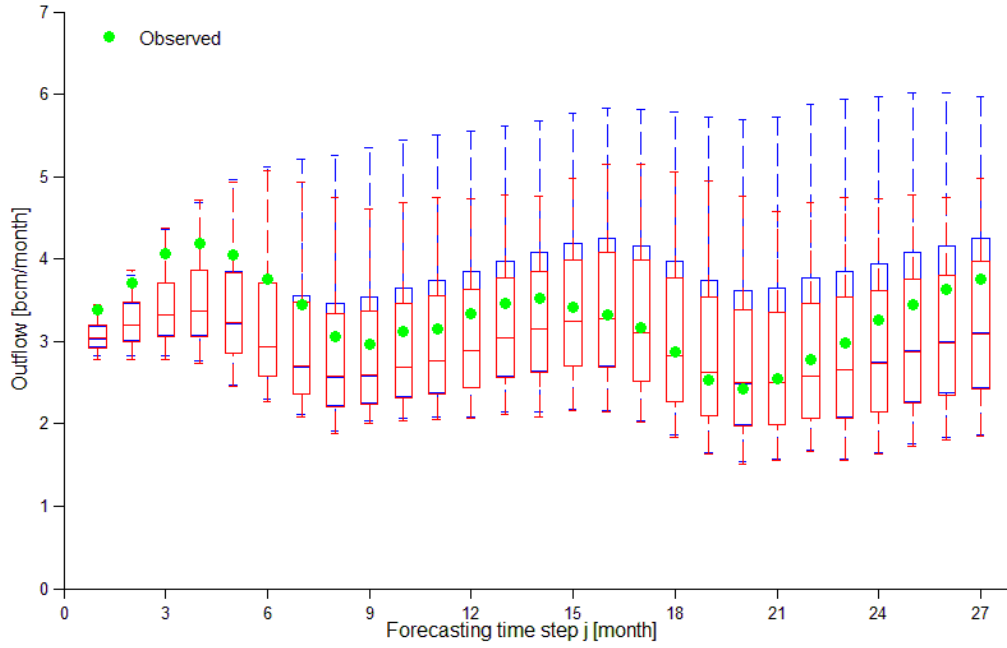


**Figure 4-19.** Box plots from the pre-BFF distributions  $\Pi_j(u_j)$  (blue) and the BFF predictive distributions  $\Omega_j(u_j^* | u_{j-1}^*)$  (red).

**Table 4-8.** Comparison of the ranges of  $u_j^*$  from the pre-BFF and BFF distributions. The O mark indicates that the observed outflow falls within the forecasted ranges.

$j$	$R_1$	Included	$j$	$R_1$	Included	$j$	$R_1$	Included	$j$	$R_1$	Included
1	1.149	O/O	8	0.857	O/O	15	0.786	O/O	22	0.718	O/O
2	1.121	O/O	9	0.784	O/O	16	0.820	O/O	23	0.728	O/O
3	1.033	O/O	10	0.783	O/O	17	0.831	O/O	24	0.720	O/O
4	1.037	O/O	11	0.785	O/O	18	0.821	O/O	25	0.717	O/O
5	0.996	O/O	12	0.774	O/O	19	0.814	O/O	26	0.707	O/O
6	0.996	O/O	13	0.771	O/O	20	0.783	O/O	27	0.763	O/O
7	0.920	O/O	14	0.757	O/O	21	0.727	O/O			

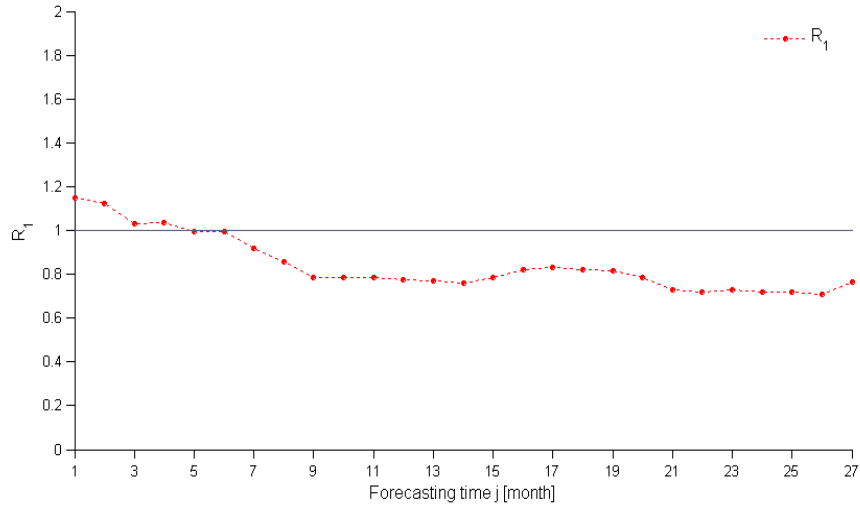


**Figure 4-20.** The values of ratio  $R_1$  over the forecasting horizon.

#### 4.4.5 Linear one-step transition model

The derived sequence of the BFF distributions can provide only reliable ranges of the future outflow of Lake Albert, not reliable traces. However, forecasted traces are required in the real-time operational management of river systems, necessitating the development of a proper model for generating such traces. Hence, a sequence of the linear one-step transition model is derived and the procedure outlined as follows:

1. For each  $j$ , some historical analogs of actual outflows are sampled from a moving window that is configured by a specified sampling interval  $l_s$  and average predictive ranges of  $u_j^*$  over the sampling interval. The average predictive ranges are specified by the BFF distributions  $\Omega_j(u_j^* | u_{j-1}^*)$ ,  $j = 1, \dots, m$ . Let's assume, for example, that the moving window stops at  $j = 15$  to collect samples of historical actual outflows, as

shown in Figure 4-21. Sampling interval  $l_s$  is assumed to be 10. The moving window then covers five time steps for both backward and forward directions from  $j = 15$ , which are represented in green-colored dashed lines in the figure (gray-colored lines are not considered for this moving window). Next, outflow traces that fall within the frame of the moving window are chosen for developing a linear model.

2. A linear one-step transition model for time  $j$  is given by

$$\mathbf{u}_j^* = a_{j-1}\mathbf{u}_{j-1}^* + b_{j-1} + \varepsilon_{j-1}. \quad (4.27)$$

In the equation,  $\varepsilon_{j-1}$  is assumed to be independent of  $\mathbf{u}_{j-1}^*$  and normally distributed with a zero mean and variance  $\sigma_{j-1}^2$ . From the selected traces in Step 1, the data of time  $j-1$  and time  $j$  are used in the regression analysis for estimating the values of  $a_{j-1}$ ,  $b_{j-1}$ , and sample variance  $\hat{\sigma}_{j-1}^2$ . Steps 1 and 2 proceed recursively on  $j$ , with  $j = 1, \dots, m$ , generating a sequence of linear one-step transition models.

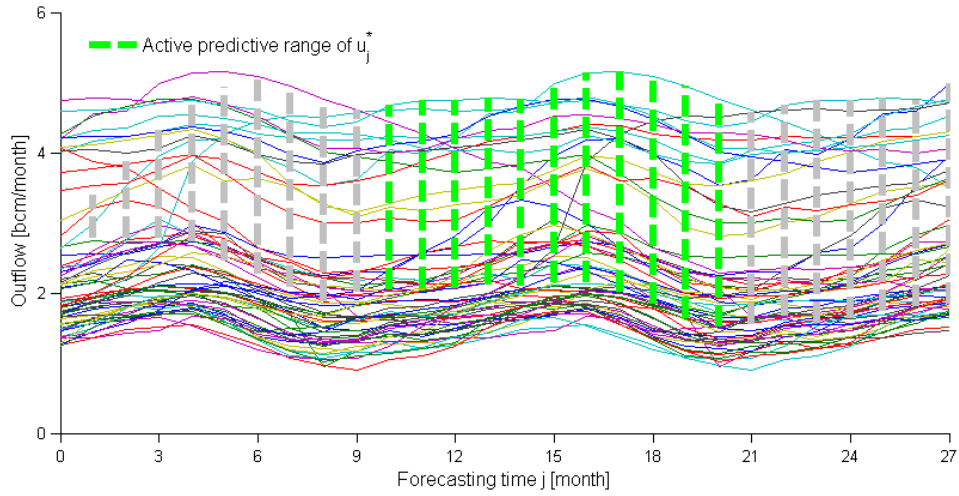


**Figure 4-21.** A moving window for the linear one-step transition model. Historical analogs of the actual outflow of Lake Albert are used.

Using the calibrated linear models in Equation (4.27) and the Monte Carlo simulation, we generate a single trace of future outflows according to the following algorithm:

1. A uniform random number  $(p_0, \dots, p_m)$ , where  $0 < p_j < 1, j = 0, \dots, m$ , are generated.
2. Given observed outflow  $u_0^*$ ,  $u_1^*$  is generated such that  $u_1^* = a_0 u_0^* + b_0 + \hat{\sigma}_0 Q^{-1}(p_0)$ .
3. Repeatedly on  $j = 2, \dots, m$ ,  $u_j^*$  are generated such that

$$u_j^* = a_{j-1} u_{j-1}^* + b_{j-1} + \hat{\sigma}_{j-1} Q^{-1}(p_{j-1}).$$

Figure 4-22 shows an ensemble of the realized outflow from the sampling with a moving window of  $l_s = 2$  and 2,000 simulations. Because the historical traces that fall within the average predictive ranges of the first few months are so scarce, a small interval size is selected.

A comparison between this figure and Figure 4-6 and computing the values of  $R_2$  (the ratio of

the range of  $u_j^*$  from simulated traces to that from a pre-BFF distribution, as shown in Figure 4-23) shows that the linear one-step transition models produce more concise and reliable forecasts of the outflow of Lake Albert and thus provide more economical and accurate inputs to the real-time operational models for the better management of lake systems.

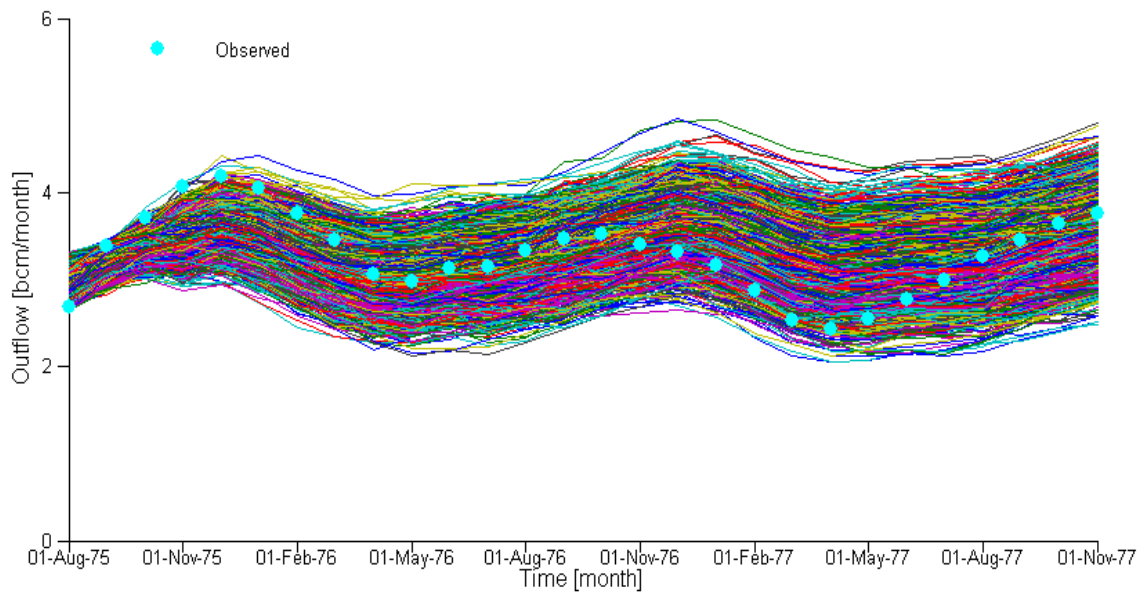


**Figure 4-22.** Ensemble forecasts of the actual outflow of Lake Albert over the forecasting horizon generated by a sequence of linear one-step transition models.

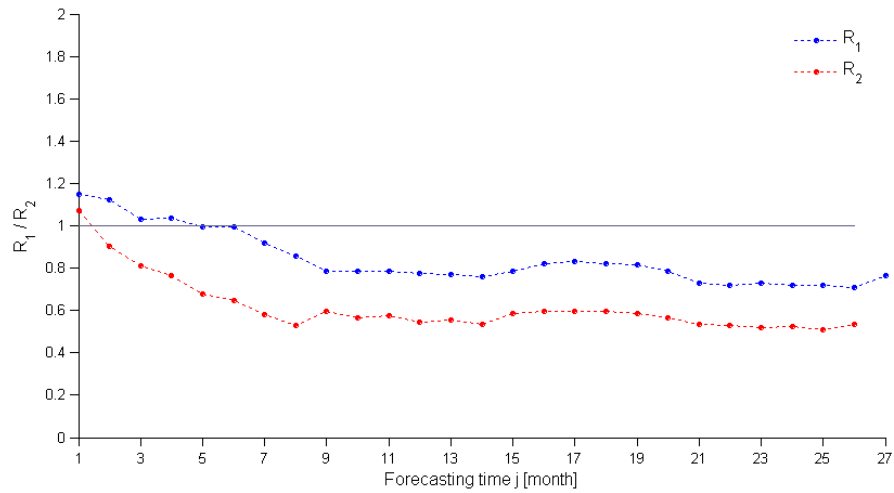


**Figure 4-23.** The values of ratio  $R_2$  over the forecasting horizon.

## 4.5 Application of the BFF to the Main Nile

### 4.5.1 Introduction

The BFF procedure is applied to the Main Nile for generating a multi-trace ensemble forecast of the reach outflow at Dongola. The river routing model in Chapter 3 was identified and calibrated using historical data from January 1, 1914 to November 1, 1952 (in 10-day time intervals), shown in Figure 4-24. The forecasting horizon is assumed to span from November 1, 1952 to December 11, 1953 so that the actual outflows (in red-colored dotted line) at Dongola over the forecasting horizon can be compared with the forecasted outflows from the BFF. Hence, November 1, 1952 is assumed to be the last observation time before the forecast initial time.

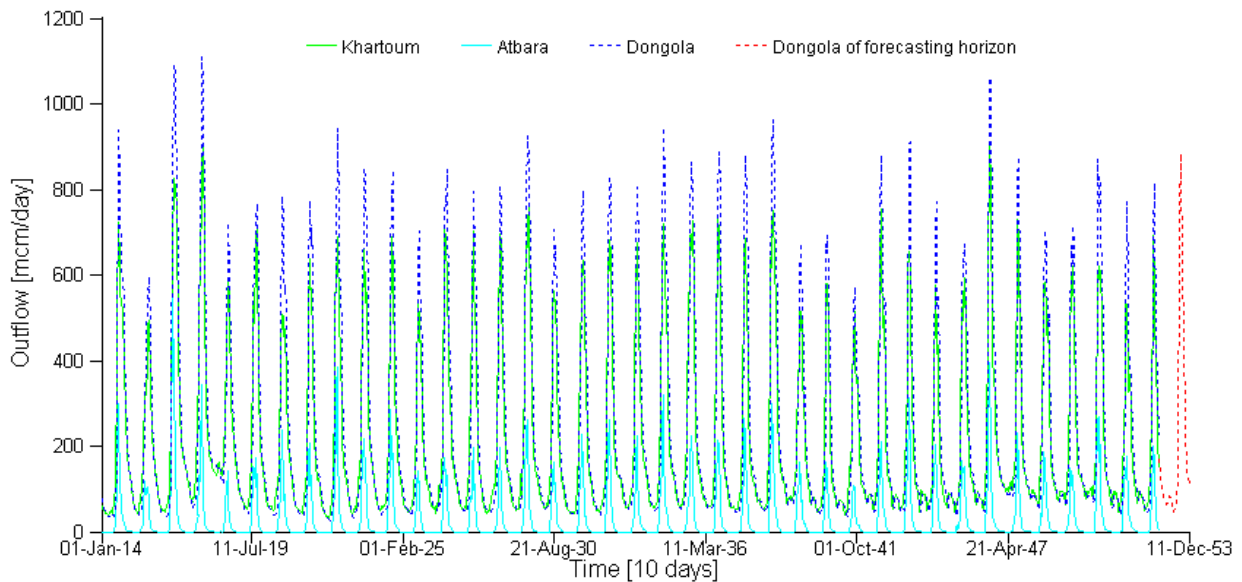


**Figure 4-24.** BFF application: the historical inflow-outflow hydrograph from January 1, 1914 to November 1, 1952; the forecasting horizon from November 1, 1952 to December 11, 1953; time in 10-day intervals; 10-day average discharge in million cubic meters.

## 4.5.2 Input uncertainty processor

### 4.5.2.1 Inflow forecast

Future inflows for Khartoum and Atbara are estimated using the historical analogs method in Section 4.4.2.1. Each inflow trace has a length of  $m$ , which is equivalent to the length of the forecasting horizon.  $m = 40$  (13 months span) is used in this application. Figure 4-25 and Figure 4-26 show the ensembles of future inflows of Khartoum and Atbara, respectively. In this approach,  $l = 24$  data points (8 months span) are used for the comparison.

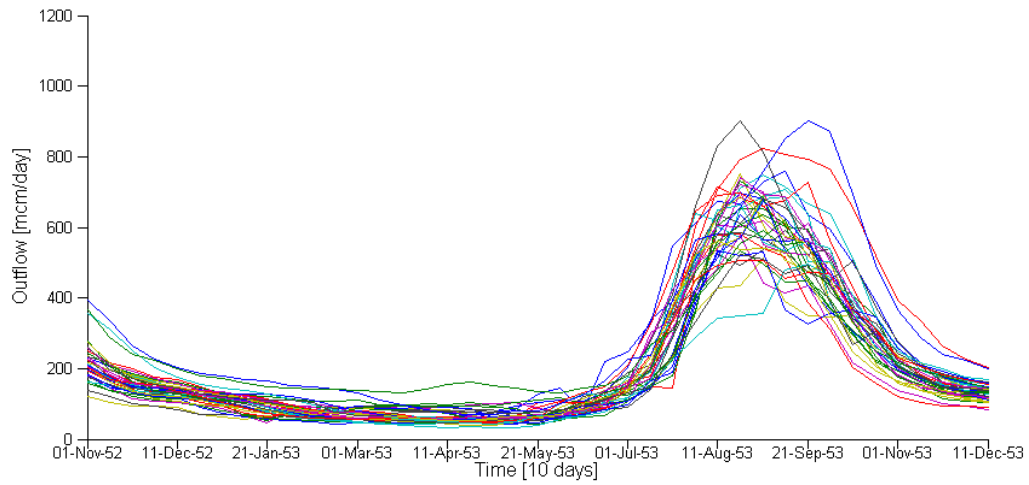


**Figure 4-25.** Ensemble forecasts of the Khartoum inflows over the forecasting horizon. Time is in 10-day intervals.

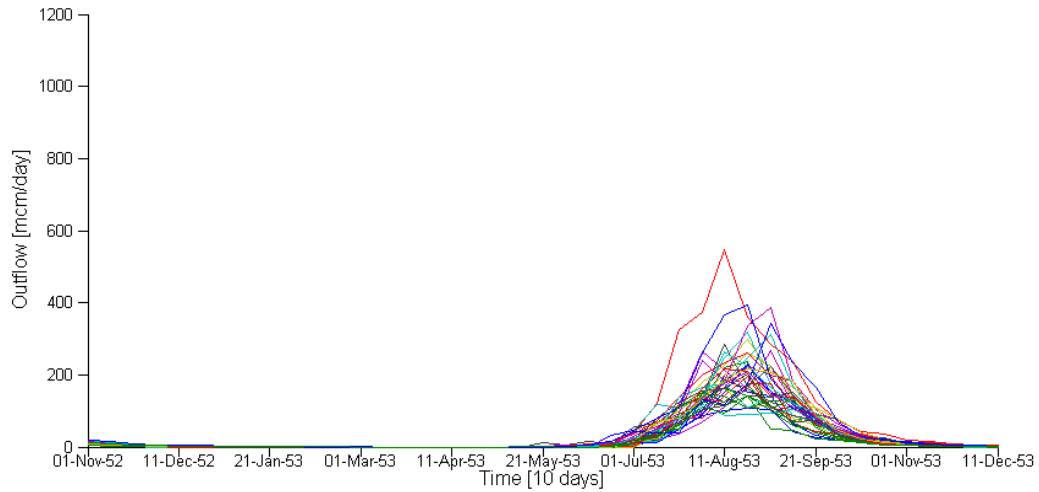


**Figure 4-26.** Ensemble forecasts of the Atbara inflows over the forecasting horizon. Time is in 10-day intervals.

#### 4.5.2.2 Ensemble forecast of outflow and distribution fitting

Next, each inflow trace of the Khartoum and Atbara ensembles is simulated with the calibrated nonlinear river routing model for generating an ensemble of model-estimated outflow at Dongola, illustrated in Figure 4-27.

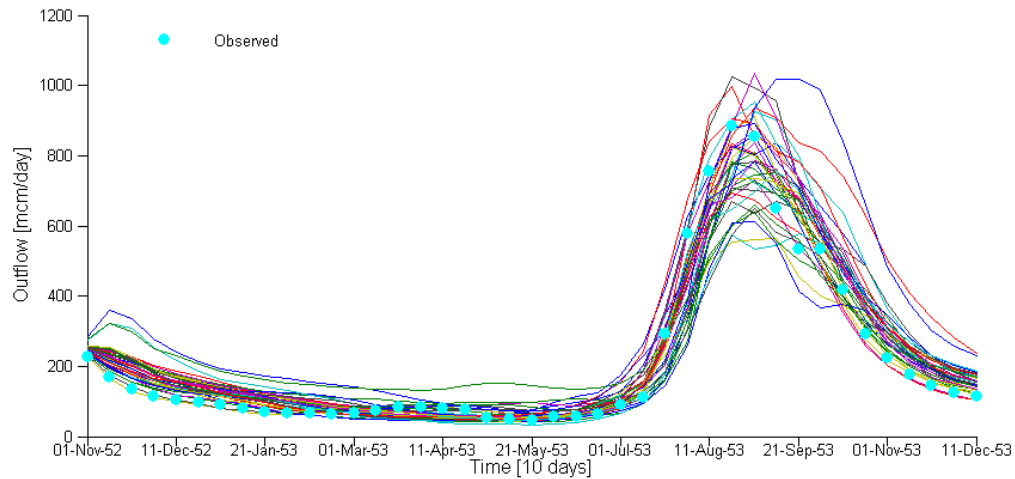


**Figure 4-27.** Simulated outflows at Dongola over the forecasting horizon. Time is in 10-day intervals.

Using the ensemble of the model-estimated outflow in Figure 4-27, we calculate a sequence of empirical distributions of  $\mathbf{u}_j, j = 1, \dots, m$ , by the method presented in Section 4.4.2.2.  $\mathbf{u}_j$  is a random variable of the model-estimated outflow at Dongola with time step  $j$  of the forecasting horizon. Next, based on the parameter estimation method presented by *Kelly and Krzysztofowicz* [2000] in Equation (4.17), a sequence of Weibull distributions  $\Pi_j(u_j), j = 1, \dots, m$ , is calculated and shown in Figure 4-28 for selected time steps with corresponding empirical distributions.

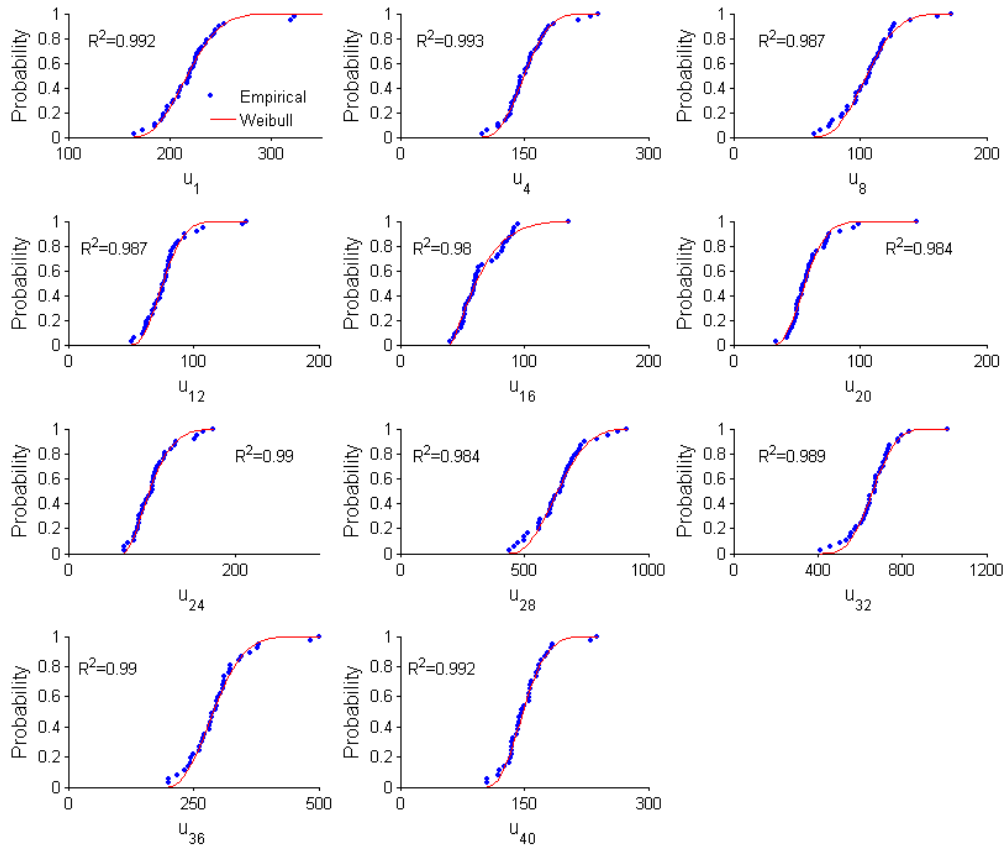


**Figure 4-28.** Empirical distributions of  $u_j$  and the fitted Weibull distributions  $\Pi_j(u_j)$  for select time steps of the forecasting horizon.

In addition, the coefficients of determinations,  $R^2$ , for all time steps are calculated in Table 4-9.

In most cases,  $R^2$  are well above 0.98, indicating that Weibull distributions

$\Pi_j(u_j)$ ,  $j = 1, \dots, m$ , fit the corresponding empirical distributions well.

**Table 4-9.**  $R^2$  of fitted Weibull distributions  $\Pi_j(u_j)$  for  $j = 1, \dots, m$ .

$j$	$R^2$	$j$	$R^2$	$j$	$R^2$	$j$	$R^2$
1	0.99	11	0.98	21	0.95	31	0.98
2	0.99	12	0.99	22	0.96	32	0.99
3	0.99	13	0.98	23	0.99	33	0.99
4	0.99	14	0.99	24	0.99	34	0.97
5	0.99	15	0.99	25	0.99	35	0.99
6	0.99	16	0.98	26	0.96	36	0.99
7	0.99	17	0.96	27	0.97	37	0.99
8	0.99	18	0.96	28	0.98	38	0.99
9	0.98	19	0.98	29	0.98	39	0.99
10	0.99	20	0.98	30	0.99	40	0.99

### 4.5.3 Model uncertainty processor

#### 4.5.3.1 Marginal distributions of actual and model-estimated outflows

To generate the sequences of marginal distributions  $\Gamma_j(u_j^*)$ ,  $j = 0, \dots, m$ , and  $\Lambda_j(u_j)$ ,  $j = 1, \dots, m$ , the historical analogs of the observed and model-estimated outflows, respectively, are selected by the historical analog method.  $\mathbf{u}^*$  is a random variable of the actual outflow. Figure 4-29 presents the most relevant historical analogs to the current trend of the observed outflow. Subsequently, the sequences of the empirical and fitted Weibull distributions of  $\mathbf{u}_j^*$ ,  $j = 0, \dots, m$ , are calculated from the analogous data points and the results for the selected time steps appear in Figure 4-31. The method proposed by *Kelly and Krzysztofowicz* [2000] is used for computing the parameters of the Weibull distributions fitted against the empirical distributions. In addition, the  $R^2$  values for the fitted Weibull distributions for all time steps appear in Table 4-10.

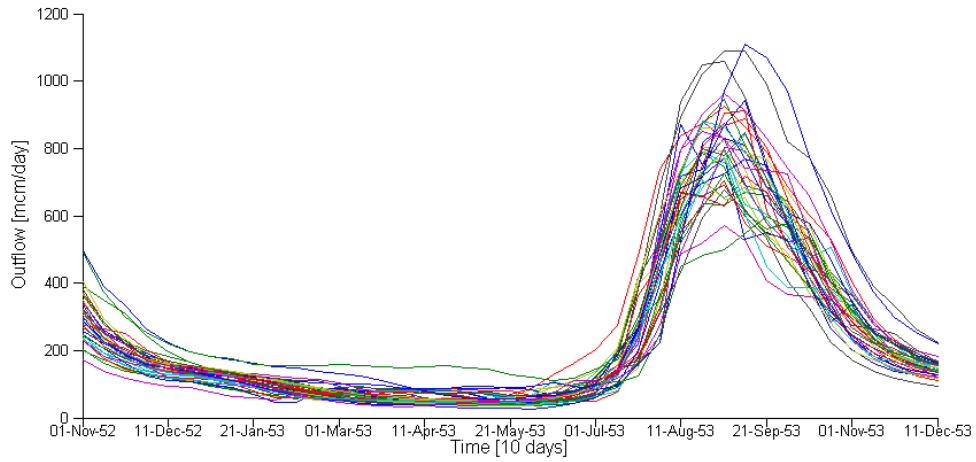


**Figure 4-29.** Historical analogs of the observe outflow at Dongola over the forecasting horizon. Time is in 10-day intervals.

Similarly, Figure 4-30 shows the historical analogs of the model-estimated outflow.

Subsequently, the sequences of empirical and fitted Weibull distributions of  $\mathbf{u}_j, j = 0, \dots, m$ , are calculated from the analogous data points and presented in Figure 4-32. In addition, the  $R^2$  values of the fitted Weibull distributions for all time steps appear in Table 4-11.

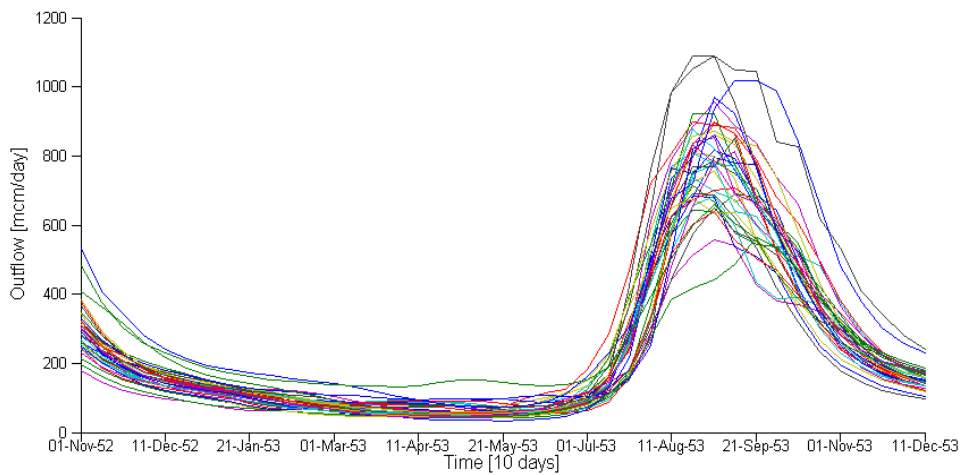


**Figure 4-30.** Historical analogs of the model-estimated outflow at Dongola over the forecasting horizon. Time is in 10-day intervals.

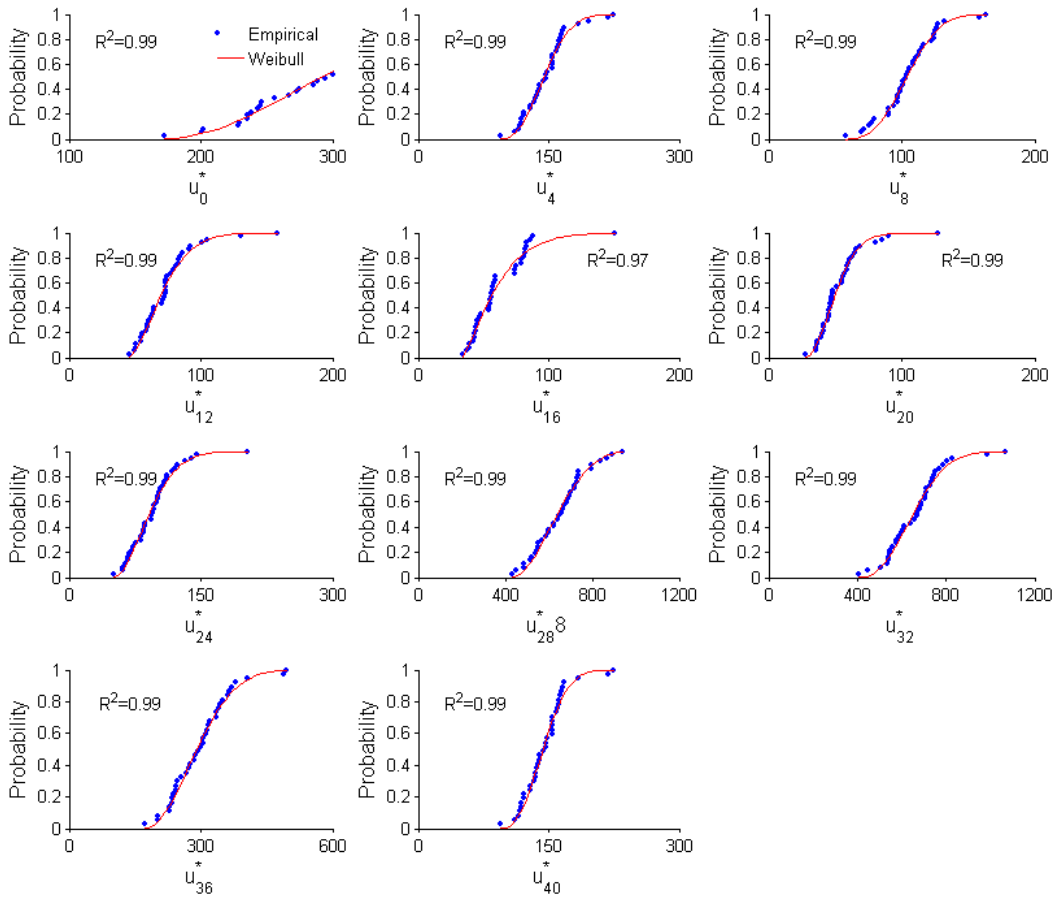


**Figure 4-31.** Empirical distributions of  $u_j^*$  and fitted Weibull distributions  $\Gamma_j(u_j^*)$  for the selected time steps of the forecasting horizon.

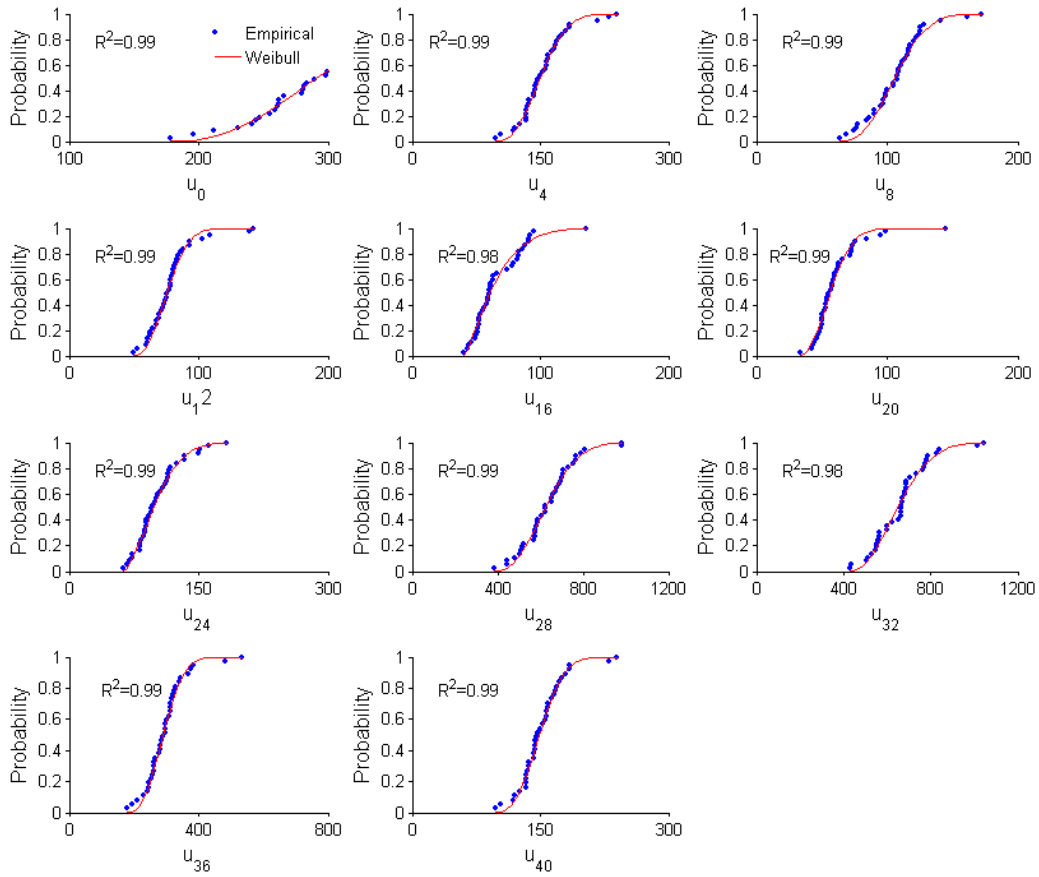


**Figure 4-32.** Empirical distributions of  $u_j$  and fitted Weibull distributions  $\Lambda_j(u_j)$  for the selected time steps of the forecasting horizon.

**Table 4-10.**  $R^2$  of fitted Weibull distributions  $\Gamma_j(u_j^*)$  for  $j = 0, \dots, m$ .

$j$	$R^2$	$j$	$R^2$	$j$	$R^2$	$j$	$R^2$
0	0.99	11	0.98	21	0.98	31	0.99
1	0.99	12	0.99	22	0.99	32	0.99
2	0.99	13	0.99	23	0.98	33	0.99
3	0.99	14	0.99	24	0.99	34	0.99
4	0.99	15	0.99	25	0.98	35	0.99
5	0.99	16	0.97	26	0.98	36	0.99
6	0.99	17	0.96	27	0.97	37	0.99
7	0.99	18	0.98	28	0.99	38	0.99
8	0.99	19	0.98	29	0.99	39	0.99
9	0.99	20	0.99	30	0.99	40	0.99
10	1.00						

**Table 4-11.**  $R^2$  of fitted Weibull distributions  $\Lambda_j(u_j)$  for  $j = 1, \dots, m$ .

$j$	$R^2$	$j$	$R^2$	$j$	$R^2$	$j$	$R^2$
1	0.99	11	0.98	21	0.95	31	0.99
2	0.99	12	0.99	22	0.97	32	0.98
3	0.99	13	0.98	23	0.99	33	0.97
4	0.99	14	0.99	24	0.99	34	0.98
5	1.00	15	0.99	25	0.99	35	0.99
6	0.99	16	0.98	26	0.93	36	0.99
7	0.99	17	0.96	27	0.95	37	0.99
8	0.99	18	0.96	28	0.99	38	0.99
9	0.98	19	0.98	29	0.99	39	0.99
10	0.99	20	0.99	30	0.99	40	0.99

#### 4.5.3.2 Normal quantile transform

Using the Normal Quantile Transform (NQT), we transform  $\mathbf{u}_j^*$  and  $\mathbf{u}_j$  into  $\mathbf{w}_j$  and

$\mathbf{x}_j$ ,  $j = 0, \dots, m$ , respectively, such that

$$\mathbf{w}_j = \begin{bmatrix} Q^{-1}\{\Gamma_j(u_j^*(1))\} \\ \vdots \\ Q^{-1}\{\Gamma_j(u_j^*(i))\} \\ \vdots \\ Q^{-1}\{\Gamma_j(u_j^*(s))\} \end{bmatrix}, \quad \mathbf{x}_j = \begin{bmatrix} Q^{-1}\{\Lambda_j(u_j(1))\} \\ \vdots \\ Q^{-1}\{\Lambda_j(u_j(i))\} \\ \vdots \\ Q^{-1}\{\Lambda_j(u_j(s))\} \end{bmatrix}, \quad (4.28)$$

$j = 0, \dots, m$ .

In the above equation,  $Q^{-1}$  is the inverse of the standard normal distribution function and can be approximated by *Abramowitz and Stegun* [1972]. As seen in Figure 4-29 and Figure 4-30,  $u_j^*(i)$  and  $u_j(i)$  are the values of the  $i$ th historical analogous trace of the observed outflow for

time  $j$  and the value of the  $i$  th historical analogous trace of the corresponding model-estimated outflow for that time, respectively.

#### **4.5.3.3 Prior density in the space of the transformed variates and its validation**

In the space of transformed variates  $\mathbf{w}_j$  and  $\mathbf{x}_j, j = 0, \dots, m$ , a sequence of prior densities is calculated from Equation (4.19). In addition, the values of the parameters of the prior densities are estimated from the linear regression models in Equation (4.20). The results are shown in Table 4-12.

The assumption of linearity of the relationship between  $\mathbf{w}_j$  and  $\mathbf{w}_{j-1}, j = 1, \dots, m$ , are justified by plotting the values of dependent variable  $\mathbf{w}_j$  against the values of independent variable  $\mathbf{w}_{j-1}$  and calculating the  $R^2$  value of a regression line that fits to the data points in each plot, shown in Figure 4-33 and Table 4-12. In most plots, the main bodies of the points lie approximately on straight lines, and the values of  $R^2$  are high, so the linearity assumption holds.

**Table 4-12.** Parameters of the prior densities in the space of the transformed variates.

$j$	$c_j$	$z_j$	$\varepsilon_j$	$R^2$	$j$	$c_j$	$z_j$	$\varepsilon_j$	$R^2$
1	1.052	-0.002	0.328	0.93	21	0.940	0.000	0.518	0.80
2	0.937	0.012	0.295	0.94	22	0.859	0.042	0.689	0.66
3	0.974	0.003	0.247	0.96	23	0.680	-0.125	0.602	0.67
4	0.983	-0.011	0.228	0.96	24	0.722	-0.011	0.721	0.53
5	0.985	-0.030	0.209	0.94	25	0.834	-0.027	0.636	0.65
6	0.985	-0.032	0.193	0.95	26	0.592	0.082	0.783	0.40
7	0.993	0.010	0.163	0.98	27	0.904	-0.151	0.812	0.56
8	0.979	-0.007	0.260	0.92	28	0.617	-0.013	0.819	0.45
9	1.072	-0.024	0.368	0.87	29	0.683	0.048	0.652	0.55
10	0.843	0.064	0.342	0.90	30	0.755	-0.010	0.551	0.59
11	0.625	-0.068	0.845	0.38	31	0.741	-0.055	0.706	0.48
12	0.884	0.016	0.476	0.80	32	0.851	-0.035	0.634	0.69
13	0.895	-0.025	0.431	0.83	33	1.026	-0.022	0.460	0.81
14	0.920	-0.004	0.252	0.94	34	0.868	0.032	0.622	0.69
15	0.953	0.019	0.181	0.96	35	0.973	0.028	0.597	0.72
16	0.876	-0.011	0.331	0.87	36	0.838	-0.065	0.462	0.84
17	0.989	0.044	0.255	0.93	37	1.009	-0.021	0.303	0.91
18	1.041	0.016	0.226	0.95	38	0.878	0.005	0.300	0.90
19	0.980	-0.008	0.398	0.86	39	0.988	0.012	0.260	0.95
20	0.956	0.008	0.462	0.83	40	0.984	0.008	0.258	0.95

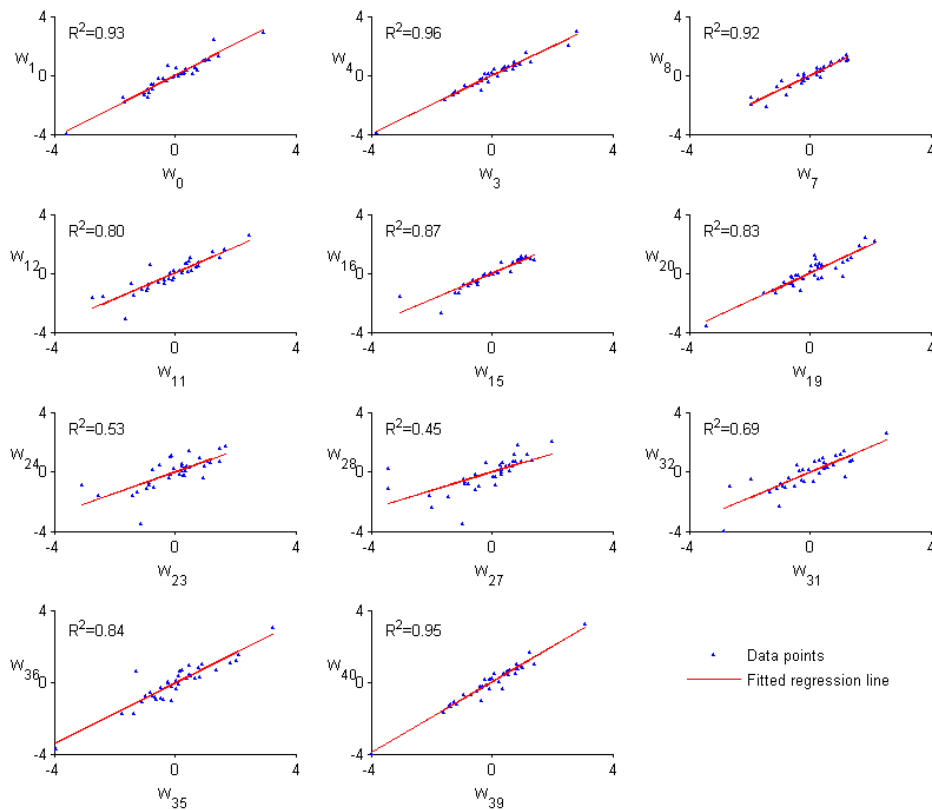


**Figure 4-33.** Linearity of  $w_j$  on  $w_{j-1}$  in the prior densities in the space of the transformed variates. Selected  $j$ 's are used.

To assess the normality assumption of error variable  $\Xi_j, j = 1, \dots, m$ , in Equation (4.20), we construct normal probability plots, shown in Figure 4-34. In the plots, residual  $e_j(i)$  for time  $j$  and data  $i$  is calculated by Equation (4.21), and the normal score of the  $r$ th smallest residual is calculated by Equation (4.22). Moreover, the  $R^2$  value of a regression line for a data set of each plot without the outliers is calculated in Table 4-13. The high values of  $R^2$  (the average is 0.97) in most time steps suggest that the normality assumption is reasonably valid.

The assumption of constant variance  $\varepsilon_j^2, j = 1, \dots, m$ , can be verified by a visual examination of the data points in each residual plot. A residual plot is drawn with residual  $e_j$  on the vertical axis and independent variable  $w_{j-1}$  on the horizontal axis, illustrated in Figure 4-35. Even though residual  $e_{28}^p$  show that the size slightly depends on the value of the corresponding independent variable, the points in most residual plots are randomly dispersed around the horizontal axis through zero, so the assumption of homoscedasticity remains reasonably valid. In fact, the fairly random patterns provide acceptable justification for the assumption of independence of  $\Xi_j$  from independent variables  $w_{j-1}$  for  $j = 1, \dots, m$ .

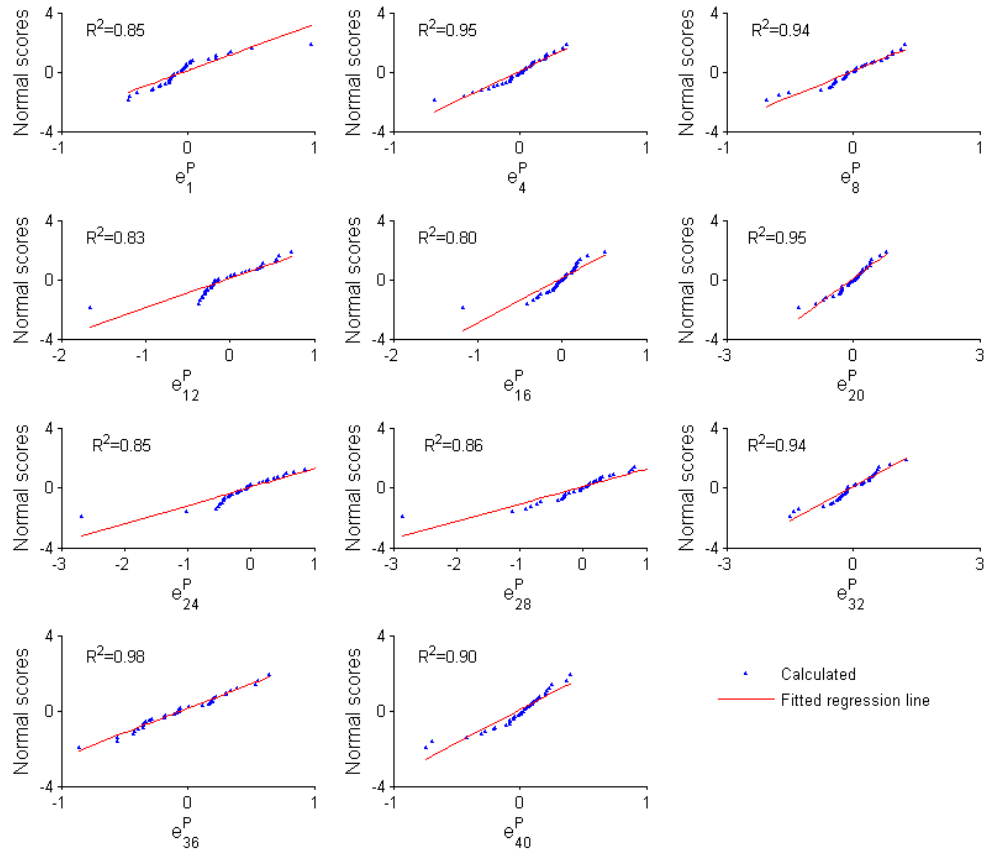


**Figure 4-34.** Normal probability plots for the prior densities in the space of the transformed variates. Selected  $j$ 's are used.

**Table 4-13.**  $R^2$  values of the regression lines in the normal probability plots for the prior densities in the space of the transformed variates.

$j$	$R^2$	$j$	$R^2$	$j$	$R^2$	$j$	$R^2$
1	0.85	11	0.98	21	0.98	31	0.90
2	0.96	12	0.83	22	0.94	32	0.94
3	0.94	13	0.82	23	0.90	33	0.97
4	0.95	14	0.98	24	0.85	34	0.98
5	0.98	15	0.96	25	0.99	35	0.94
6	0.96	16	0.80	26	0.94	36	0.98
7	0.98	17	0.93	27	0.87	37	0.96
8	0.94	18	0.99	28	0.86	38	0.97
9	0.67	19	0.95	29	0.98	39	0.92
10	0.98	20	0.95	30	0.99	40	0.90

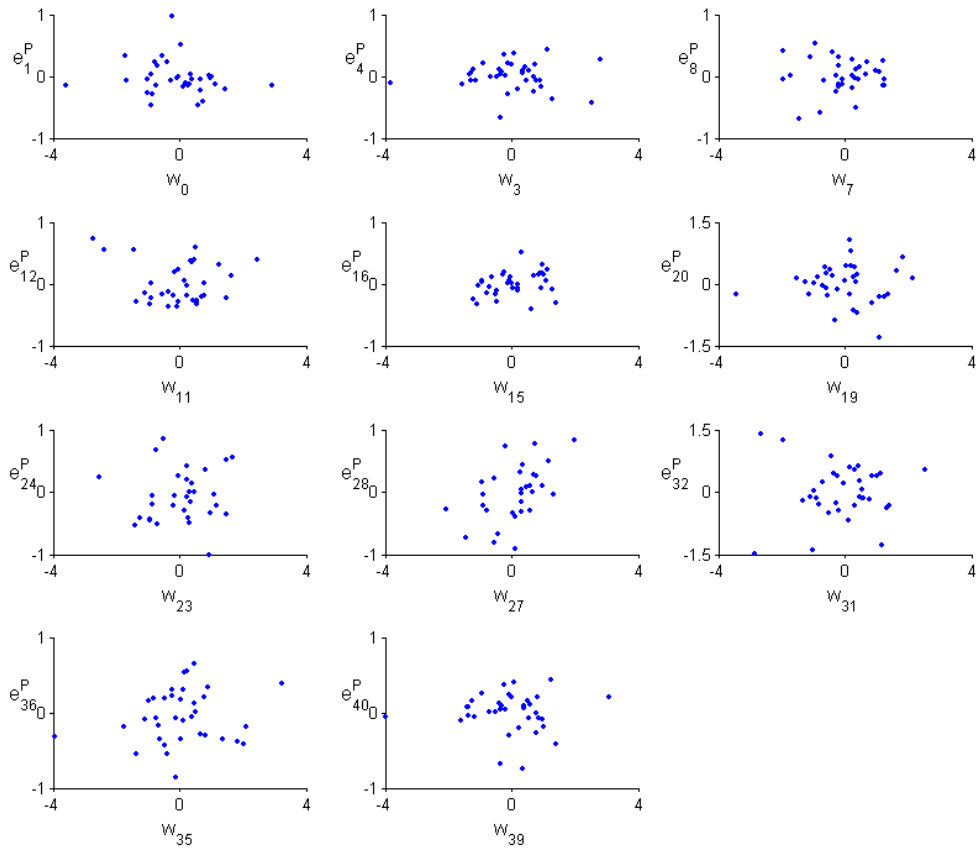


**Figure 4-35.** Residual plots for the prior densities in the space of the transformed variates.

#### 4.5.3.4 Likelihood function in the transformed space and its validation

As with the prior distributions, a sequence of likelihood functions in the space of the transformed variates is calculated from Equation (4.23). The values of the parameters in the likelihood functions are estimated from multiple linear regression models in Equation (4.24). The results appear in Table 4-14.

The assumption of the linearity of  $\mathbf{x}_j$  on  $\mathbf{w}_j$  and  $\mathbf{w}_{j-1}$ ,  $j = 1, \dots, m$ , are assessed by plotting the values of dependent variable  $\mathbf{x}_j$  against the values of independent variables  $\mathbf{w}_j$  and  $\mathbf{w}_{j-1}$  and calculating the  $R^2$  value of a regression line that fits to the data points in each plot, presents in both Figure 4-36 and Table 4-14. In most plots, the main bodies of the data points lie approximately on straight planes, and the values of  $R^2$  are very high (above 0.90), so the linearity assumption holds reasonably.

**Table 4-14.** Parameters of the likelihood functions in the space of the transformed variates.

$j$	$a_j$	$e_j$	$b_j$	$\sigma_j$	$R^2$	$j$	$a_j$	$e_j$	$b_j$	$\sigma_j$	$R^2$
1	0.926	0.152	0.015	0.256	0.95	21	0.861	0.309	0.128	0.420	0.87
2	0.765	0.354	0.029	0.296	0.94	22	0.511	0.529	0.063	0.418	0.88
3	0.597	0.452	0.016	0.311	0.92	23	0.618	0.284	0.017	0.448	0.81
4	0.383	0.659	0.013	0.382	0.88	24	0.765	0.211	0.042	0.496	0.80
5	0.652	0.391	-0.014	0.500	0.76	25	0.860	0.029	0.044	0.380	0.87
6	0.962	0.103	-0.003	0.506	0.77	26	0.751	0.270	0.014	0.444	0.83
7	0.095	0.954	-0.022	0.423	0.83	27	0.716	0.156	0.018	0.276	0.92
8	0.618	0.396	-0.050	0.346	0.87	28	0.775	0.168	-0.023	0.452	0.82
9	-0.030	1.070	-0.054	0.313	0.90	29	0.932	0.016	0.007	0.252	0.93
10	0.450	0.331	0.007	0.523	0.69	30	0.770	0.095	0.029	0.334	0.83
11	0.686	0.383	0.064	0.459	0.81	31	0.756	0.100	0.067	0.254	0.91
12	0.075	0.968	0.021	0.553	0.78	32	0.889	0.130	-0.021	0.270	0.94
13	0.549	0.446	-0.001	0.597	0.75	33	0.728	0.391	-0.037	0.316	0.93
14	0.097	0.813	-0.003	0.490	0.79	34	0.970	0.123	-0.014	0.331	0.91
15	-0.318	1.255	-0.009	0.436	0.83	35	1.042	0.028	-0.053	0.295	0.92
16	0.895	0.085	0.038	0.296	0.90	36	0.849	0.278	-0.013	0.237	0.96
17	0.805	0.207	0.039	0.250	0.93	37	0.728	0.338	0.016	0.249	0.95
18	0.731	0.257	0.044	0.222	0.95	38	0.563	0.473	0.022	0.283	0.93
19	0.490	0.609	0.052	0.290	0.94	39	0.653	0.363	0.022	0.331	0.90
20	0.585	0.470	0.056	0.339	0.92	40	0.547	0.489	0.011	0.406	0.86

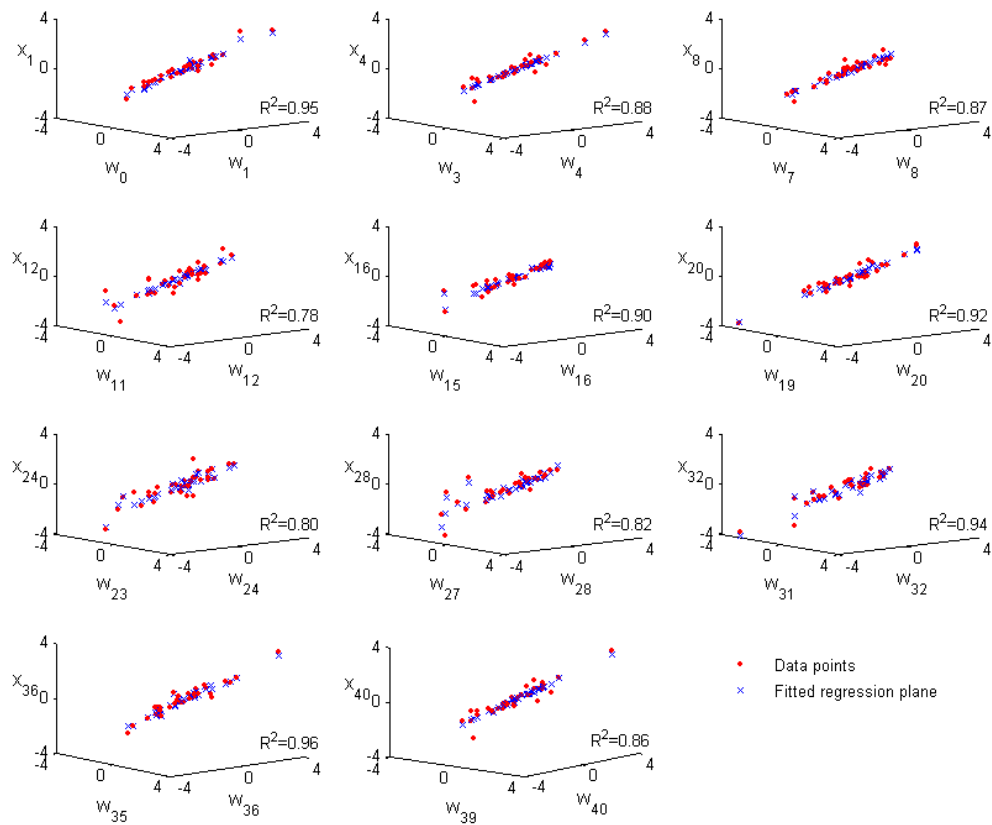


**Figure 4-36.** Linearity of  $x_j$  on  $w_{j-1}$  and  $w_{j-1}$  of the likelihood functions in the space of the transformed variates. Selected  $j$ 's are used.

Figure 4-37 shows a sequence of normal probability plots that assess the normality assumption of error variables  $\Theta_j$ ,  $j = 1, \dots, m$ , in Equation (4.24). In the plots, residual  $e_j^L(i)$  for time  $j$  and data  $i$  is calculated by Equation (4.25). Most of the plots show the linear patterns of the main bodies of the data points, indicating that linear models provide an acceptable fit to the data. Indeed, as Table 4-15 shows, the high values of  $R^2$  (the average is 0.98) in most time steps suggest that the normality assumption is valid.

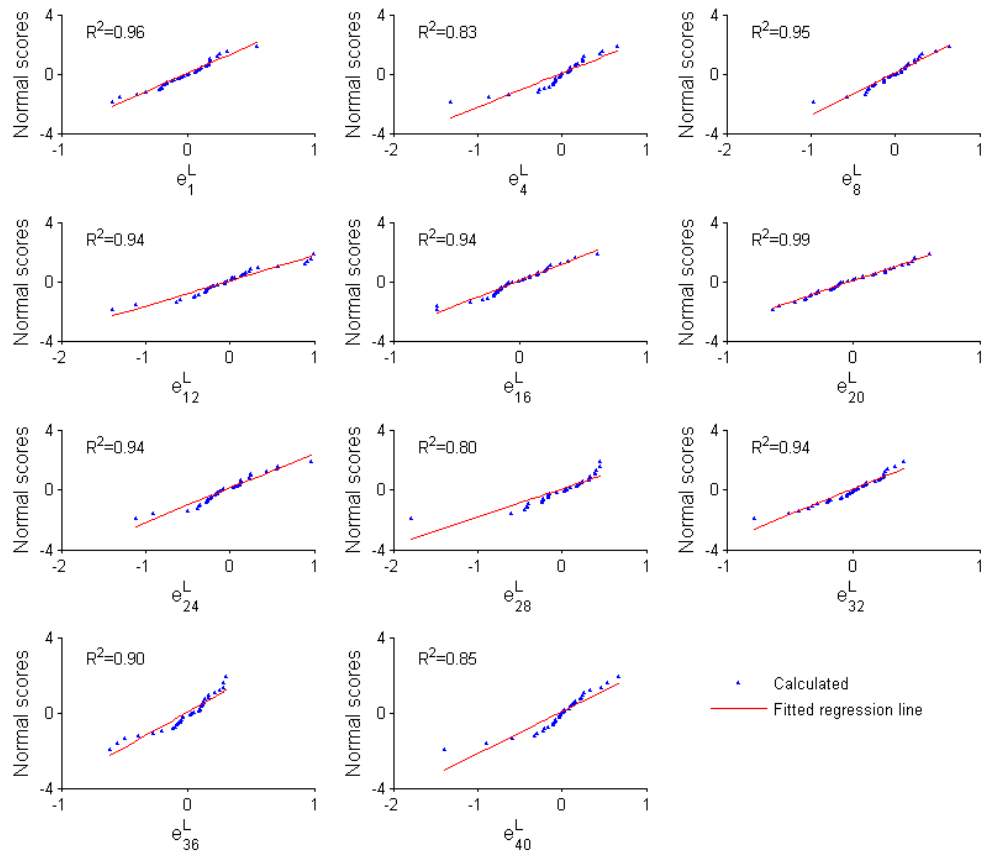


**Figure 4-37.** Normal probability plots for the likelihood functions in the space of the transformed variates. Selected  $j$ 's are used.

**Table 4-15.**  $R^2$  values of the regression lines in the normal probability plots for the likelihood functions in the space of the transformed variates.

$j$	$R^2$	$j$	$R^2$	$j$	$R^2$	$j$	$R^2$
1	0.96	11	0.95	21	0.97	31	0.98
2	0.94	12	0.94	22	0.98	32	0.94
3	0.87	13	0.88	23	0.99	33	0.96
4	0.83	14	0.84	24	0.94	34	0.94
5	0.82	15	0.94	25	0.99	35	0.87
6	0.88	16	0.97	26	0.90	36	0.90
7	0.95	17	0.97	27	0.96	37	0.95
8	0.95	18	0.96	28	0.80	38	0.96
9	0.96	19	0.96	29	0.97	39	0.88
10	0.78	20	0.99	30	0.95	40	0.85

Figure 4-38 shows residual plots for the selected time steps for verifying the assumption of constant variance  $\sigma_j^2, j = 1, \dots, m$ , in Equation (4.24) by visual examination. A residual plot is drawn with residual  $e_j^L$  on the vertical axis and independent variables  $w_j$  and  $w_{j-1}$  on the horizontal axis, shown in Figure 4-38. The majority of data points in most residual plots are randomly dispersed around the horizontal axis through zero, so the assumption of homoscedasticity is reasonably valid. In fact, the fairly random patterns provide a decent verification of the assumption of the independence of  $\Theta_j$  from independent variables  $w_j$  and  $w_{j-1}$  for  $j = 1, \dots, m$ .

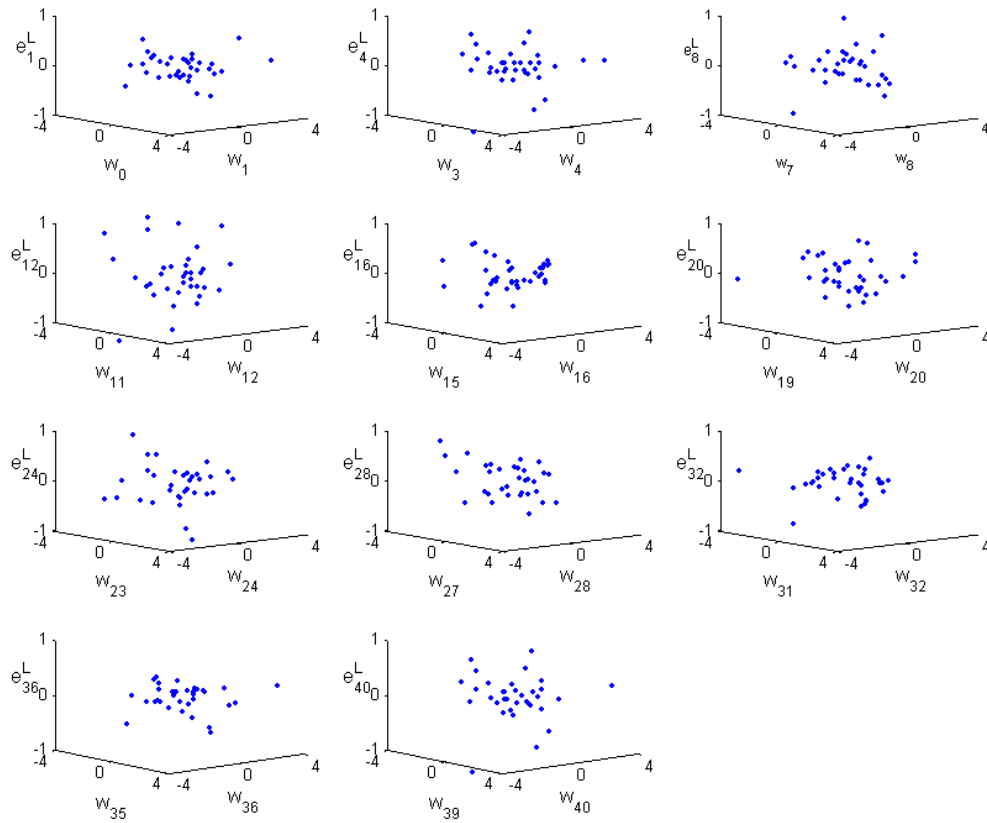


**Figure 4-38.** Residual plots for the likelihood functions in the space of the transformed variates.

#### 4.5.4 Integrator

After calculating a sequence of posterior distributions in the transformed space by Bayes' theorem and then calculating a sequence of meta-Gaussian posterior distribution functions  $\Phi_j(u_j^* | u_j, u_{j-1}^*)$ ,  $j = 1, \dots, m$ , in Equation (4.15), we derive a sequence of predictive one-step transition distributions by Equation (4.26). As with the BFF application to the Equatorial Lakes, the Bayesian ensemble generator [Krzysztofowicz and Maranzano, 2004b] is run to

simulate  $M$  number of predictive distributions  $\Theta_j(u_j^* | u_{j-1}^*)$ ,  $j = 1, \dots, m$ . By averaging the predictive distributions for each time step  $j$ , the average predictive distribution can be estimated and fitted by Weibull distributions  $\Omega_j(u_j^* | u_{j-1}^*)$ ,  $j = 1, \dots, m$ . Figure 4-39 shows  $M$  number of simulated predictive distributions  $\Theta_j(u_j^* | u_{j-1}^*)$  over some number of feasible discrete values of  $u_j^*$  (gray-colored solid curves) and the corresponding average predictive distribution (red dots) for  $j=8$  and 24, respectively.

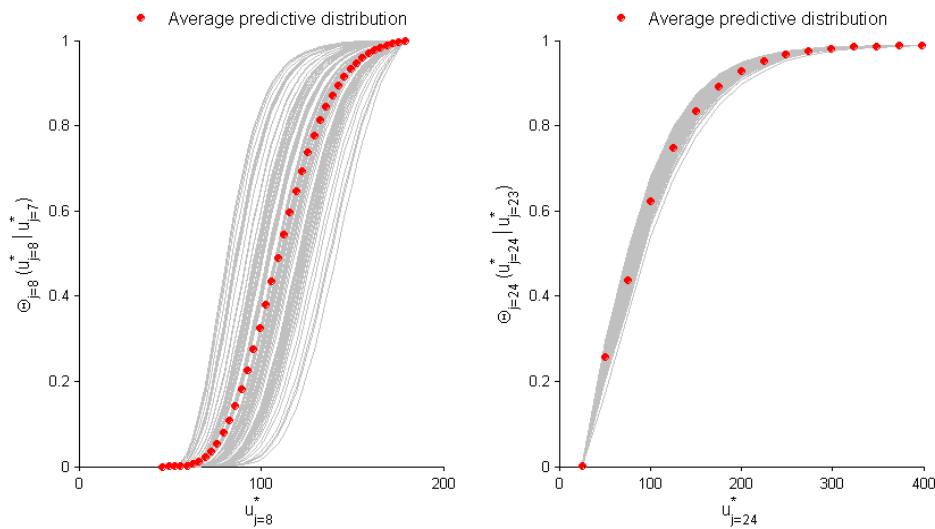


**Figure 4-39.** Simulated predictive one-step transition distributions from the Monte Carlo simulation and the corresponding average predictive distributions.  $j=8$  and 24 are used.

Next, box plots are drawn from the fitted average predictive distributions

$\Omega_j(u_j^* | u_{j-1}^*)$ ,  $j = 1, \dots, m$ , as well as from the distributions of the model-estimated outflow,

$\Pi_j(u_j)$ ,  $j = 1, \dots, m$ , in Figure 4-40. In a comparison of the two box plots, the variances of

nearly all BFF distributions  $\Omega_j(u_j^* | u_{j-1}^*)$  are smaller than those of the pre-BFF distributions

$\Pi_j(u_j)$ , while the actual outflows that materialized (green dots) still fall within the forecasted ranges. Indeed, the value of  $R_1$  (the ratio of the range of  $u_j^*$  from the BFF distribution to that from the pre-BFF distribution) in Table 4-16 and Figure 4-41 are significantly low at an average value of 0.47 up to  $j = 21$ , increases shortly during the peak discharge period, and then drops back until the end of the forecasting period. The average value of  $R_1$  across the forecasting period is 0.62. Even though the ranges of the BFF distributions at  $j = 23$  through  $j = 30$  are close to or slightly higher than those of the pre-BFF distributions, the corridor represented by the ranges of the BFF distributions among these time steps resembles the trend of the actual outflows more closely than that represented by the ranges of the pre-BFF distributions. Therefore, the BFF-derived forecasts provide more concise and accurate forecasts without a significant loss of reliability.

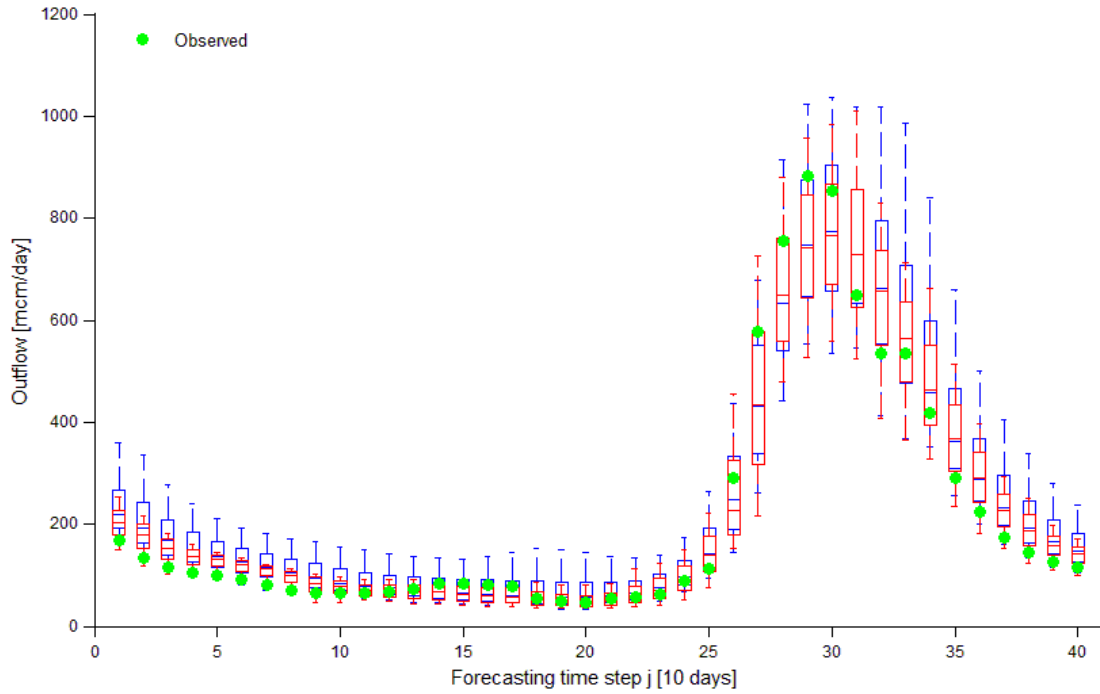


**Figure 4-40.** Box plots from pre-BFF distributions  $\Pi_j(u_j)$  (blue) and BFF predictive distributions  $\Omega_j(u_j^* | u_{j-1}^*)$  (red).

**Table 4-16.** Comparison of the ranges of  $u_j^*$  from the pre-BFF and BFF distributions.

$j$	$R_1$	Included	$j$	$R_1$	Included	$j$	$R_1$	Included	$j$	$R_1$	Included
1	0.52	O/O	11	0.42	O/O	21	0.47	O/O	31	1.03	O/O
2	0.47	O/O	12	0.47	O/O	22	0.76	O/O	32	0.70	O/O
3	0.48	O/O	13	0.54	O/O	23	0.90	O/O	33	0.56	O/O
4	0.44	O/O	14	0.52	O/O	24	0.91	O/O	34	0.68	O/O
5	0.40	O/O	15	0.57	O/O	25	0.85	O/O	35	0.70	O/O
6	0.42	O/O	16	0.50	O/O	26	1.04	O/O	36	0.72	O/O
7	0.40	O/O	17	0.46	O/O	27	1.22	O/O	37	0.58	O/O
8	0.46	O/O	18	0.43	O/O	28	0.85	O/O	38	0.63	O/O
9	0.54	O/O	19	0.40	O/O	29	0.91	O/O	39	0.53	O/O
10	0.51	O/O	20	0.41	O/O	30	0.85	O/O	40	0.52	O/O

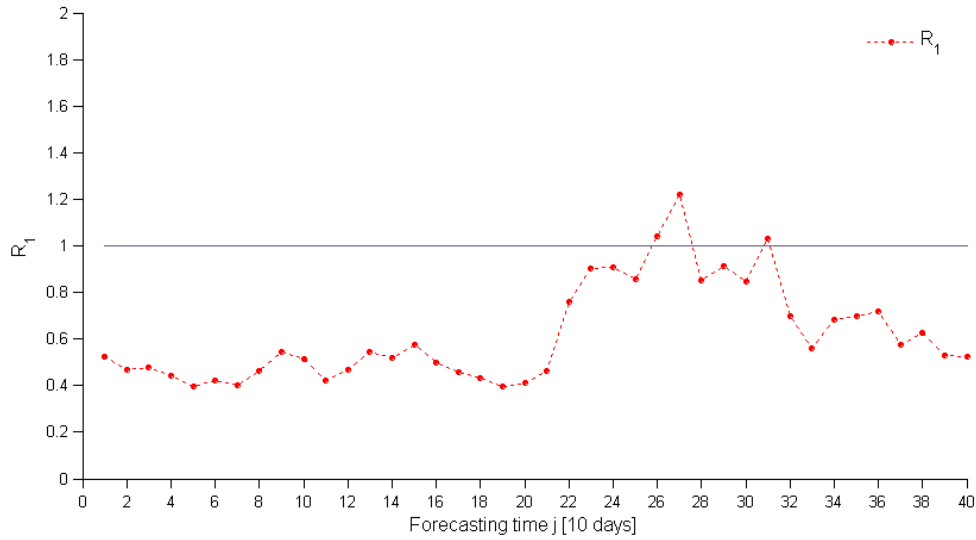


**Figure 4-41.** The values of ratio  $R_1$  over the forecasting horizon.

#### 4.5.5 Linear one-step transition model

In order to obtain reliable traces of future outflow at Dongola, we derive a sequence of linear one-step transition model according to the procedure outlined in Section 4.4.5. Figure 4-42 displays the configuration of a moving window that is sampling outflow data from historical analogs of actual outflow. Specifically, the moving window stops at  $j = 26$  with sampling interval  $l_s$  of 16. The green dashed lines represent the activated heights of the moving window, but the gray lines are not considered in this sampling. After sampling the necessary data for all time steps, a sequence of the linear one-step transition models in Equation (4.27) is generated by the least square fit and then combined with the Monte Carlo simulation, yielding the multi-trace ensemble of actual future outflow, shown in Figure 4-43.

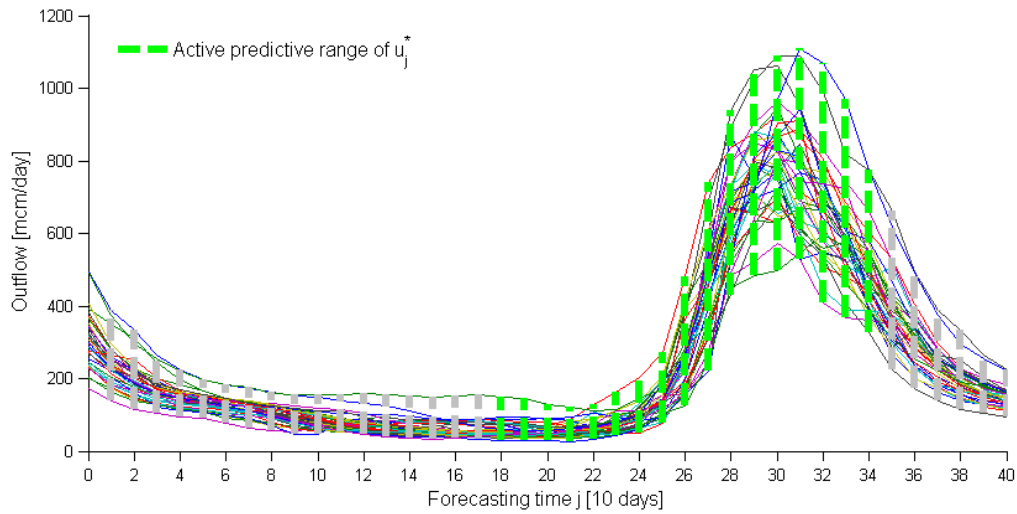


**Figure 4-42.** A moving window for the linear one-step transition model.

This figure shows an ensemble of the realized outflow from the sampling with a moving window of  $l_s = m = 2,000$  simulations. Compared with Figure 4-27, Figure 4-43 presents clearly visible, much smaller ranges of the actual outflow, but the ranges still include the realized values of the outflow for the forecasting horizon. Furthermore, plotting  $R_1$  and  $R_2$  together in Figure 4-44 shows that the linear one-step transitional model can provide more concise but still more reliable forecasts of the reach outflow than the BFF distribution alone. Indeed, the average value of  $R_2$  across the forecasting period is 0.55.

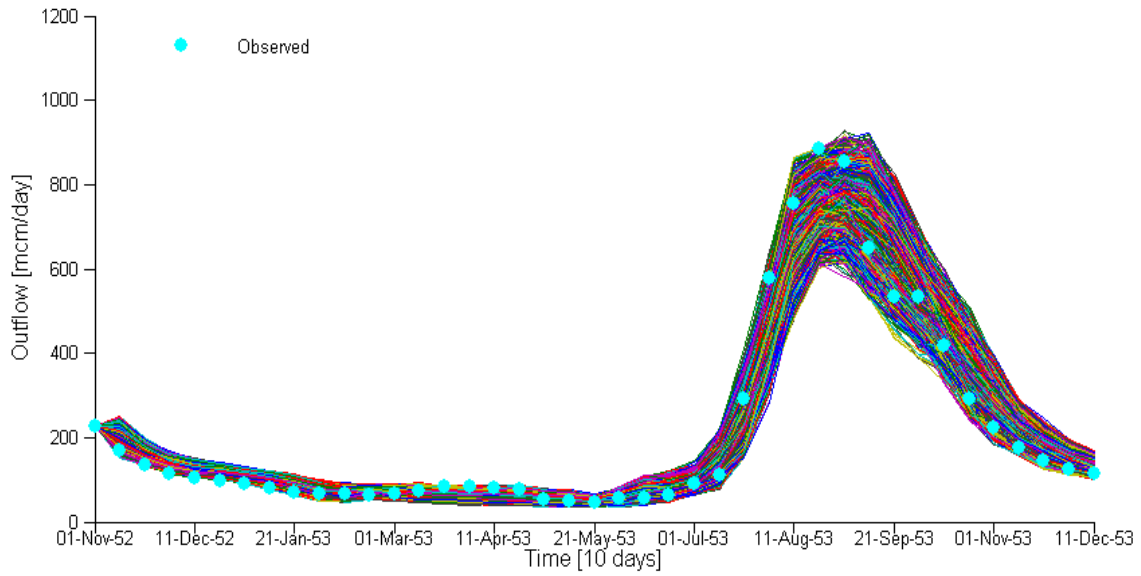


**Figure 4-43.** Ensemble forecast of the actual outflow at Dongola over the forecasting horizon, generated by a sequence of linear one-step transition models.

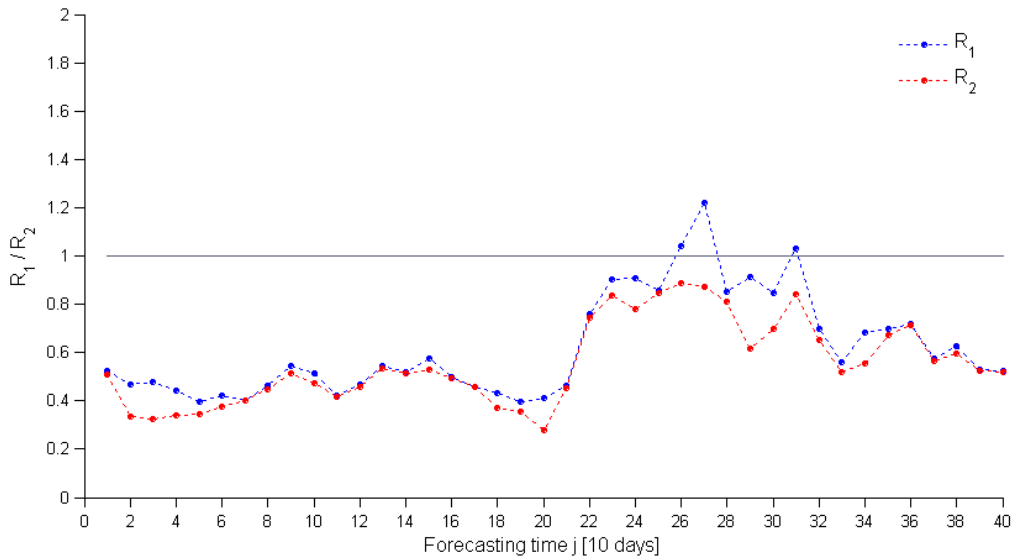


**Figure 4-44.** The values of  $R_1$  and  $R_2$  over the forecasting horizon.

#### 4.6 Summary remarks on the BFF

A common practice in the ensemble forecasting of outflow of a river reach or a lake is to simulate traces of outflow via a calibrated river routing model from forecasted inflow traces. The accuracy and reliability in this forecasting can be improved by 1) utilizing the observation of outflow at the beginning of the forecasting; 2) employing the knowledge of relationships between model-estimated outflow and actual outflow in previous historical events; and 3) characterizing the evolution of outflow process over time from historical analogs. The Bayesian forecasting framework (BFF) utilizes this information in order to build a sequence of conditional distributions, called predictive distributions, and to generate traces of reliable future outflow by a sequence of linear one-step transition models. Because the conditional distributions can increase the probability of the occurrence of certain values of outflow for current time when outflow at the previous time is known to be a particular value, they can decrease the magnitude of variances around their means. In addition, using likelihood functions that are constructed based on linear relationships between model-estimated and actual outflows, the BFF can identify the impact of model uncertainty on the final outcomes from the river routing model, thus enhancing the credibility of the forecasted results. Finally, historical findings of the evolution of outflow process over time, applied in the generation of a sequence of linear one-step transition models, contribute to yielding a more concise and reliable forecast of the outflow.

Applications of the BFF to the Equatorial Lakes and the Main Nile clearly show that the BFS combined with the linear one-step transition model outperforms the BFS alone in the forecasting of river or lake outflow. Although the values of both  $R_1$  and  $R_2$  are much smaller

than one throughout the forecasting horizons in both applications, all of the materialized outflows for the forecasting period fall within the forecasted ranges. These results show that the BFF can be expanded to any hydrological or hydraulic model to produce less expensive and more reliable outcomes, thus contributing to more efficient real-time operation for water resource management.

## CHAPTER 5

### ACCOMPLISHMENTS, CONCLUSIONS, AND RECOMMENDATIONS

#### 5.1 Accomplishments and Conclusions

A comprehensive new approach for simulating the flow routing process through natural open channels and characterizing the uncertainties of outflow forecasts is developed. Specific accomplishments include:

1. Development of a physically-based, spatially-distributed, conceptual, and easy to implement nonlinear hydrologic river routing model for reliable simulations of river flows.
2. Development of an efficient model identification approach to identify the most effective model structure and estimate its storage-outflow and storage-loss relationships and other parameters.
3. Characterization of conditions under which reservoir cascade models are identifiable.
4. Demonstration that the new routing model and identification approach are robust even in the presence of model and input uncertainties.
5. Successful applications of the routing model to real world systems.
6. Development of a modified Bayesian forecasting framework (BFF) for medium- and long-range forecasting of outflows of a river reach or a lake system.
7. Demonstration that the BFF generates reliable multi-trace ensemble flow forecasts potentially useful in operational river basin management.

Unlike previous multi-linear methods and cascade models, the new river routing model identifies the hidden or internal storage-outflow and storage-loss relationships without assuming linear, exponential, or power laws. It is shown that these functions comprise convex and concave regions, depending on topography and other natural river features.

While the model applications exhibit strong evidence that the identified model structure and parameters are directly related to physical system features, such relationships were not systematically explored. Furthermore, detailed comparisons with hydraulic routing models over a wide range of physical conditions will be undertaken as part of future research efforts.

While the Bayesian forecasting framework provided more accurate and useable outflow forecasts than the ensemble forecasting, more retrospective forecasting needs to be performed for further validation.

## **5.2 Recommendations for future work**

This work can be expanded in various ways that involve hydrology, hydraulics, climate, and water resource components as outlined below:

1. ***Apply the new routing model to various river systems with different computational time scales.*** The current study incorporated a single tributary inflow and used monthly or ten-day time scales for computational time steps. Experiments for a dendritic network of channels or bifurcating channels with time scales from seconds to hours would help improve the validation of the routing model through comparison of outflow

differences. Furthermore, experiments for a weir- or dam-controlled river reach would facilitate the characterization of the operations of hydraulic structures based on only inflow-outflow hydrograph data.

2. ***Compare the new routing model with existing routing models for an additional validation step.*** The new routing models will be compared with and evaluated against existing routing models such as lag-and-K routing schemes and fully dynamic methods.
3. ***Extend the optimization scheme of the routing model to hydrologic systems, climate systems, and other water resource components that have non-decreasing properties among related variables.*** It is common to observe in nature that a variable with an approximate non-decreasing relationship with another variable describes a particular phenomenon (e.g., subsurface flow versus soil moisture or temperature versus evaporation). Therefore, extending the optimization scheme used in the routing model to other hydrologic and climate systems would help identify interdependences among related variables without any restrictions imposed by presumed mathematical forms.
4. ***Apply the BFF to other forecasting applications.*** Other process models can be integrated into the BFF for improved, multi-trace ensemble forecasts. Among others, such forecasting applications may be related to rainfall-runoff processes, agricultural planning, and groundwater-surface water response.

## APPENDIX A

### DERIVATION OF THE OPTIMAL CONTROL OF DISCRETE-TIME SYSTEMS

This section presents the derivation of the optimal control and the state of a general discrete-time linear quadratic (LQ) optimal control problem. This LQ problem is to minimize the discrete-time quadratic cost function

$$J = \frac{1}{2} x_N' S_N x_N + \sum_{k=1}^{N-1} \left( \frac{1}{2} x_k' L_{xx}^k x_k + \frac{1}{2} u_k' L_{uu}^k u_k + u_k' L_{ux}^k x_k + L_x^{k'} x_k + L_u^{k'} u_k + \hat{L}^k \right), \quad (\text{A.1})$$

subject to the linear dynamical equation with inputs

$$x_{k+1} = A_k x_k + B_k u_k + C_k, \quad (\text{A.2})$$

where  $x_k \in R^n$  and  $u_k \in R^m$ ;  $L_{xx}^k \in R^{n \times n}$ ,  $L_{uu}^k \in R^{m \times m}$ ,  $L_{ux}^k \in R^{m \times n}$ ,  $L_x^k \in R^n$ ,  $L_u^k \in R^m$ , and  $S_N \in R^{n \times n}$ ;  $A_k \in R^{n \times n}$ ,  $B_k \in R^{n \times m}$  and  $C_k \in R^n$ ; and  $\hat{L}^k$  is a scalar quantity. All weighting matrices of the cost function and the matrices of dynamical system (or plant) vary for time  $k$ .  $S_N \geq \mathbf{0}$ ,  $L_{xx} \geq \mathbf{0}$ , and  $L_{uu} > \mathbf{0}$  are assumed to derive optimal control of the general LQ problem. To solve the LQ problem, the Hamiltonian function is defined by

$$H^k(x_k, u_k) = \frac{1}{2} x_k' L_{xx}^k x_k + \frac{1}{2} u_k' L_{uu}^k u_k + u_k' L_{ux}^k x_k + L_x^{k'} x_k + L_u^{k'} u_k + \hat{L}^k + \lambda_{k+1}' (A_k x_k + B_k u_k + C_k). \quad (\text{A.3})$$

Then the necessary conditions for minimizing the cost function, which also satisfies the constraint of Equation (A.2), are given by the state equation, the costate equation, the stationary condition, and the boundary condition as follows [Lewis and Syrmos, 1995].

State equation:

$$x_{k+1} = \frac{\partial H^k}{\partial \lambda_{k+1}} = A_k x_k + B_k u_k + C_k. \quad (\text{A.4})$$

Costate equation:

$$\lambda_k = \frac{\partial H^k}{\partial x_k} = A_k' \lambda_{k+1} + L_{xx}^k x_k + L_{ux}^k u_k + L_x^k. \quad (\text{A.5})$$

Stationary condition:

$$0 = \frac{\partial H^k}{\partial u_k} = B_k' \lambda_{k+1} + L_{uu}^k u_k + L_{ux}^k x_k + L_u^k. \quad (\text{A.6})$$

Boundary condition:

$$\lambda_N = \frac{\partial \phi}{\partial x_N} = S_N x_N, \quad (\text{A.7})$$

where the terminal cost  $\phi$  is  $\frac{1}{2}x'_N S_N x_N$ .

At this point, the subscripts on the plant matrices and the superscripts on the weighting matrices are dropped to simplify the notation. Rearranging Equation (A.6) yields

$$u_k = -L_{uu}^{-1} L_{ux} x_k - L_{uu}^{-1} B' \lambda_{k+1} - L_{uu}^{-1} L_u, \quad (\text{A.8})$$

and substituting Equation (A.8) into Equation (A.4) yields

$$\begin{aligned} x_{k+1} &= Ax_k + B(-L_{uu}^{-1} L_{ux} x_k - L_{uu}^{-1} B' \lambda_{k+1} - L_{uu}^{-1} L_u) + C \\ &= (A - BL_{uu}^{-1} L_{ux}) x_k - BL_{uu}^{-1} B' \lambda_{k+1} - BL_{uu}^{-1} L_u + C. \end{aligned} \quad (\text{A.9})$$

Following the same procedure used in the application of the sweep method [Bryson and Ho, 1975] to LQ problems by Lewis and Syrmos [1995], it is assumed that for all  $k \leq N$

$$\lambda_k = S_k x_k + v_k. \quad (\text{A.10})$$

This assumption will be valid if consistent equations can be found for auxiliary sequences  $S_k$  and  $v_k$ . To find these equations, use Equation (A.10) in Equation (A.9) to obtain

$$x_{k+1} = (A - BL_{uu}^{-1} L_{ux}) x_k - BL_{uu}^{-1} B' S_{k+1} x_{k+1} - BL_{uu}^{-1} B' v_{k+1} - BL_{uu}^{-1} L_u + C, \quad (\text{A.11})$$

which is rearranged to yield

$$x_{k+1} = \Xi^{-1} (A - BL_{uu}^{-1} L_{ux}) x_k - \Xi^{-1} BL_{uu}^{-1} B' v_{k+1} - \Xi^{-1} BL_{uu}^{-1} L_u + \Xi^{-1} C, \quad (\text{A.12})$$

where  $\Xi^{-1} = (I + BL_{uu}^{-1} B' S_{k+1})^{-1}$ .

Now substituting equation (A.8) into equation (A.5) generates

$$\lambda_k = (A' - L'_{ux} L_{uu}^{-1} B') \lambda_{k+1} + (L_{xx} - L'_{ux} L_{uu}^{-1} L_{ux}) x_k - L'_{ux} L_{uu}^{-1} L_u + L_x. \quad (\text{A.13})$$

Next, substituting Equations (A.10) and (A.12) into this equation yields

$$\begin{aligned} S_k x_k + v_k &= (A' - L'_{ux} L_{uu}^{-1} B') (S_{k+1} x_{k+1} + v_{k+1}) + (L_{xx} - L'_{ux} L_{uu}^{-1} L_{ux}) x_k - L'_{ux} L_{uu}^{-1} L_u + L_x \\ &= \left[ (A' - L'_{ux} L_{uu}^{-1} B') S_{k+1} \Xi^{-1} (A - BL_{uu}^{-1} L_{ux}) + (L_{xx} - L'_{ux} L_{uu}^{-1} L_{ux}) \right] x_k \\ &\quad + \left[ -\Pi \Xi^{-1} BL_{uu}^{-1} B' v_{k+1} - \Pi \Xi^{-1} BL_{uu}^{-1} L_u + \Pi \Xi^{-1} C + (A' - L'_{ux} L_{uu}^{-1} B') v_{k+1} - L'_{ux} L_{uu}^{-1} L_u + L_x \right], \end{aligned} \quad (\text{A.14})$$

or

$$\begin{aligned} &\left[ -S_k + (A' - L'_{ux} L_{uu}^{-1} B') S_{k+1} \Xi^{-1} (A - BL_{uu}^{-1} L_{ux}) + (L_{xx} - L'_{ux} L_{uu}^{-1} L_{ux}) \right] x_k \\ &+ \left[ -v_k - \Pi \Xi^{-1} BL_{uu}^{-1} B' v_{k+1} - \Pi \Xi^{-1} BL_{uu}^{-1} L_u + \Pi \Xi^{-1} C + (A' - L'_{ux} L_{uu}^{-1} B') v_{k+1} - L'_{ux} L_{uu}^{-1} L_u + L_x \right] = 0, \end{aligned} \quad (\text{A.15})$$

where  $\Pi = (A' - L'_{ux}L^{-1}_{uu}B')S_{k+1}$ . This equation must hold for all state sequences  $x_k$  given any  $x_0$ , so the bracketed terms must go to zeros. Therefore,

$$S_k = (A' - L'_{ux}L^{-1}_{uu}B')S_{k+1}\Xi^{-1}(A - BL^{-1}_{uu}L_{ux}) + (L_{xx} - L'_{ux}L^{-1}_{uu}L_{ux}), \quad (\text{A.16})$$

and

$$\begin{aligned} v_k = & \left[ (A' - L'_{ux}L^{-1}_{uu}B') - \Pi\Xi^{-1}BL^{-1}_{uu}B' \right] v_{k+1} \\ & + \left[ -\Pi\Xi^{-1}BL^{-1}_{uu}L_u + \Pi\Xi^{-1}C - L'_{ux}L^{-1}_{uu}L_u + L_x \right]. \end{aligned} \quad (\text{A.17})$$

To calculate much simpler forms of Equations (A.16) and (A.17), the following lemmas are introduced:

*Lemma A.1: Matrix inversion*

$$(A + BCD)^{-1} = A^{-1} - A^{-1}B(C^{-1} + DA^{-1}B)^{-1}DA^{-1}.$$

*Lemma A.2: Short form of Lemma A.1*

$$(X^{-1} + BD)^{-1} = X - XB(I + DXB)^{-1}DX.$$

*Lemma A.3:*

$$I - A(I + A)^{-1} = (I + A)^{-1}.$$

Using these lemmas, the auxiliary sequences can be written as

$$S_k = L_{xx} + A'S_{k+1}A - (B'S_{k+1}A + L_{ux})' (B'S_{k+1}B + L_{uu})^{-1} (B'S_{k+1}A + L_{ux}), \quad (\text{A.18})$$

and

$$v_k = A'v_{k+1} + A'S_{k+1}C + L_x - (B'S_{k+1}A + L_{ux})' (B'S_{k+1}B + L_{uu})^{-1} [B'v_{k+1} + B'S_{k+1}C + L_u]. \quad (\text{A.19})$$

The boundary conditions for these auxiliary sequences are computed by comparing Equations (A.7) and (A.10):

$$S_N = S_N, \quad (\text{A.20})$$

$$v_N = \mathbf{0}, \quad (\text{A.21})$$

where  $\mathbf{0}$  is a zero vector. By using the computed auxiliary sequences, the optimal control can be derived from Equation (A.8):

$$\begin{aligned}
u_k &= -L_{uu}^{-1}L_{ux}x_k - L_{uu}^{-1}B'(S_kx_k + v_k) - L_{uu}^{-1}L_u \\
&= -L_{uu}^{-1}L_{ux}x_k - L_{uu}^{-1}B'S_{k+1}(Ax_k + Bu_k + C) - L_{uu}^{-1}B'v_{k+1} - L_{uu}^{-1}L_u,
\end{aligned} \tag{A.22}$$

which is rearranged by

$$u_k = -(B'S_{k+1}B + L_{uu})^{-1}[(B'S_{k+1}A + L_{ux})x_k + B'S_{k+1}C + B'v_{k+1} + L_u]. \tag{A.23}$$

To obtain a solution for Equation (A.23), the inverse of the first bracketed term on the right side of the equation must exist. To do so, first,  $S_k$  must be positive semidefinite or positive definite because if  $S_k \geq 0$ , then  $B'S_{k+1}B \geq 0$ , which is based on the following lemma [Bernstein, 2005].

*Lemma A.4:*

Let  $Z \in R^{m \times n}$ . If  $C \leq D$ , then  $ZCZ' \leq ZDZ'$ . Note that  $C \leq D$  denotes that  $D - C$  is positive semidefinite.

Hence, it can be easily shown that when  $C, D$ , and  $Z$  in *Lemma A.4* become  $\mathbf{0}, S_{k+1}$ , and

$B$ , respectively,  $B'S_{k+1}B$  is always positive semidefinite. Second, if  $L_{uu} > 0$ , then

$B'S_{k+1}B + L_{uu} > 0$ . Therefore, the inverse always exists. The Joseph stabilized version of

Equation (A.18), called the Riccati equation, has much better numerical performance in terms

of satisfying the positive semidefiniteness of  $S_k$ . To convert the Riccati equation into the Joseph stabilized version, Equation (A.16) is rearranged to obtain

$$S_k = \bar{A}' \left[ S_{k+1} - S_{k+1} B (B' S_{k+1} B + L_{uu})^{-1} B' S_{k+1} \right] \bar{A} + \bar{Q}, \quad (\text{A.24})$$

where  $\bar{A} = A - B L_{uu}^{-1} L_{ux}$  and  $\bar{Q} = L_{xx} - L'_{ux} L_{uu}^{-1} L_{ux}$ . Denoting  $K_k = (B' S_{k+1} B + L_{uu})^{-1} B' S_{k+1} \bar{A}$ ,

Equation (A.24) becomes

$$S_k = \bar{A}' S_{k+1} (\bar{A} - B K_k) + \bar{Q}. \quad (\text{A.25})$$

However,

$$\begin{aligned} & (\bar{A} - B K_k)' S_{k+1} (\bar{A} - B K_k) + K'_k L_{uu} K_k + \bar{Q} \\ &= \bar{A}' S_{k+1} \bar{A} - \bar{A}' S_{k+1} B K_k \underbrace{- K'_k B' S_{k+1} \bar{A} + K'_k B' S_{k+1} B K_k + K'_k L_{uu} K_k}_{= \Gamma} + \bar{Q} \\ &= \bar{A}' S_{k+1} (\bar{A} - B K_k) + \bar{Q} \\ &= S_k, \end{aligned}$$

where

$$\begin{aligned} \Gamma &= -K'_k \left[ B' S_{k+1} \bar{A} - (B' S_{k+1} B + L_{uu}) K_k \right] \\ &= -K'_k \left[ B' S_{k+1} \bar{A} - (B' S_{k+1} B + L_{uu}) (B' S_{k+1} B + L_{uu})^{-1} B' S_{k+1} \bar{A} \right] \\ &= \mathbf{0}. \end{aligned}$$

Therefore, the Joseph stabilized version is

$$S_k = (\bar{A} - BK_k)' S_{k+1} (\bar{A} - BK_k) + K_k' L_{uu} K_k + \bar{Q}. \quad (\text{A.26})$$

The second term on the right-hand side are always positive definite according to both Lemma 4 and the assumptions of  $L_{uu} > 0$ . For  $k = N - 1$ , the assumption of  $S_N \geq 0$  with Lemma A.4 results in the first term  $(\bar{A} - BK_k)' S_{k+1} (\bar{A} - BK_k) \geq 0$ , which results in  $S_{N-1} \geq 0$  by the combination of the assumption of  $\bar{Q} \geq 0$ . This reasoning applies from  $k = N - 1$  to  $k = 2$ , proving that  $S_k$  is positive semidefinite for all  $k$ . Therefore, with the assumptions of  $S_N \geq 0, L_{uu} > 0$ , and  $\bar{Q} \geq 0$ , the Joseph stabilized version guarantees that Equation (A.23) will yield unique optimal control sequences.

*Lewis and Syrmos* [1995] showed that the sufficient condition for the constrained minimization problem is given by

$$B'S_{k+1}B + H_{uu} > 0, \quad (\text{A.27})$$

where the superscript of  $H^k$  is also dropped for the simplicity of the notation. Since  $H_{uu}$  is calculated by

$$H_{uu} = \frac{\partial}{\partial u_k} \left( \frac{\partial H}{\partial u_k} \right) = L_{uu} + \frac{\partial (L_{ux} x_k)}{\partial u_k} + \frac{\partial L_u}{\partial u_k} = L_{uu},$$

then the sufficient condition becomes  $B'S_{k+1}B + L_{uu} > 0$ , which is proven by the Joseph stabilized version.

## APPENDIX B

### NORMAL QUANTILE TRANSFORMS

*Papoulis* [1991] explains how to determine a random variable of a specified distribution from a original random variable of a known distribution in the following inverse problem:

Given the distribution  $F_x(x)$  of random variable  $\mathbf{x}$ , find the distribution of a new random variable  $\mathbf{u} = F_x(x)$ . Since  $F_x(x)$  monotonically increases as  $\mathbf{x}$  increases, it follows that

$\mathbf{P}\{\mathbf{u} \leq u\} = \mathbf{P}\{\mathbf{x} \leq x\}$ . Consequently,  $F_u(u) = \mathbf{P}\{\mathbf{u} \leq u\} = \mathbf{P}\{\mathbf{x} \leq x\} = F_x(x) = \mathbf{u}$ . However,  $\mathbf{u}$  is uniformly distributed in the interval  $(0, 1)$  because the density  $f_u(u)$  is such that

$$f_u(u) = \frac{dF_u(u)}{du} = \frac{du}{du} = 1.$$

Hence, the distribution of  $\mathbf{u}$  is uniform in the interval  $(0, 1)$ , proving the following lemma.

*Lemma B.1:* If  $\mathbf{u} = F_x(x)$ , then  $F_u(u) = \mathbf{u}$ , and  $f_u(u) = 1$  in the interval  $(0, 1)$ .

From the monotonicity of  $F_x(x)$ , there exists a unique inverse of  $F_x(x)$ , which is  $\mathbf{x} = F_x^{-1}(\mathbf{u})$ .

Then, *Lemma B.1* can be expanded into *Lemma B.2* with  $\mathbf{u} = F_x(x)$  and  $F_u(u) = \mathbf{P}\{\mathbf{x} \leq x\}$ .

*Lemma B.2:* If  $\mathbf{x} = F_x^{-1}(\mathbf{u})$ , then  $\mathbf{P}\{\mathbf{x} \leq x\} = F_x(x)$ .

Since  $F_x(x)$  is arbitrary,  $F_x(x)$  can be replaced by  $F_y(y)$ , yielding *Lemma B.3*.

*Lemma B.3:* If  $\mathbf{y} = F_y^{-1}(\mathbf{u})$ , then  $\mathbf{P}\{\mathbf{y} \leq y\} = F_y(y)$ .

By combining  $\mathbf{u} = F_x(x)$  and *Lemma B.3*, it can be concluded that

$$\text{if } \mathbf{y} = F_y^{-1}(F_x(x)), \text{ then } \mathbf{P}\{\mathbf{y} \leq y\} = F_y(y).$$

Hence, an original random variable  $\mathbf{x}$  can be transformed into  $\mathbf{y}$  by the composition of the inverse of the distribution of  $\mathbf{y}$  and the marginal distribution of  $\mathbf{x}$ . Therefore, any random variable of a parametric or non-parametric (empirical) marginal distribution can be converted into a standard normal variable using the inverse of the standard normal distribution. This composition is called the normal quantile transform (NQT).

## APPENDIX C

### VALIDATION OF THE NORMAL-LINEAR MODEL

Based on Papoulis' explanation [Papoulis, 1991], the theoretical justification for normal linear models are presented in this section. Let  $\mathbf{s}, \mathbf{x}_1, \dots, \mathbf{x}_n$  represent random variables. Random variable  $s$  needs to be estimated in terms of a function  $g(\mathbf{X})$  of random vector  $\mathbf{X} = [\mathbf{x}_1, \dots, \mathbf{x}_n]$ . Among related estimation methods, only the mean square (MS) estimation method is considered because it yields simple results. By the MS estimation method,  $g(\mathbf{X})$  can be found by minimizing the MS error

$$P = E \left\{ \left[ \mathbf{s} - g(\mathbf{X}) \right]^2 \right\}. \quad (\text{A.28})$$

The solution that minimizes  $P$  is

$$g(\mathbf{X}) = E \{ \mathbf{s} | \mathbf{X} \} = \int_{-\infty}^{\infty} s f_s(s | X) ds. \quad (\text{A.29})$$

Moreover, if  $\mathbf{s}, \mathbf{x}_1, \dots, \mathbf{x}_n$  are jointly normal with the zero mean, the linear and nonlinear estimators of  $\mathbf{s}$  are equal to

$$\hat{\mathbf{s}} = a_1 \mathbf{x}_1 + \dots + a_n \mathbf{x}_n = g(\mathbf{X}) = E \{ \mathbf{s} | \mathbf{X} \}. \quad (\text{A.30})$$

Furthermore, the joint normality with the zero mean makes the orthogonality of  $\mathbf{s} - \hat{\mathbf{s}}$  and  $\mathbf{x}_i$ ,  $i = 1, \dots, n$ , possible, so they are independent. Therefore, the conditional variance of  $\mathbf{s}$  is

$$\text{var}(\mathbf{s} | \mathbf{X}) = E\left\{(\mathbf{s} - E(\mathbf{s} | \mathbf{X}))^2 | \mathbf{X}\right\} = E\left\{(\mathbf{s} - \hat{\mathbf{s}})^2 | \mathbf{X}\right\} = E\left\{(\mathbf{s} - \hat{\mathbf{s}})^2\right\} = P. \quad (\text{A.31})$$

Conditional density  $f_s(s | \mathbf{X})$  is also normal because both  $f(\mathbf{s}, \mathbf{x}_1, \dots, \mathbf{x}_n)$  and  $f(\mathbf{x}_1, \dots, \mathbf{x}_n)$  are jointly normal. Thus, it is given by

$$f(s | x_1, \dots, x_n) = \frac{1}{\sqrt{2\pi P}} e^{-[s - (a_1 x_1 + \dots + a_n x_n)]^2 / 2P}. \quad (\text{A.32})$$

In the above equation, parameters  $a_1, \dots, a_n$  are determined by solving

$$\frac{\partial P}{\partial a_i} = E\left\{-2[s - (a_1 x_1 + \dots + a_n x_n)]x_i\right\} = 0, \quad i = 1, \dots, n. \quad (\text{A.33})$$

In summary, if the RVs  $\mathbf{s}, \mathbf{x}_1, \dots, \mathbf{x}_n$ , are jointly normal with the zero mean, then

$$\textcircled{1} \quad E(\mathbf{s} | \mathbf{X}) = \hat{\mathbf{s}} = a_1 \mathbf{x}_1 + \dots + a_n \mathbf{x}_n$$

$$\textcircled{2} \quad \text{var}(\mathbf{s} | \mathbf{X}) = E\left\{(\mathbf{s} - \hat{\mathbf{s}})^2\right\} = P$$

$$\textcircled{3} \quad \mathbf{s} - \hat{\mathbf{s}} \text{ and } \mathbf{x}_i \text{ are independent}$$



Then parameter estimates  $\hat{a}_1, \dots, \hat{a}_n$  are found by taking the partial derivative of  $T$  with respect to each parameter equal to zero, which results in the same estimates as those from the least square fit. Consequently, a normal-linear model can be justified by showing that it satisfies the necessary conditions in light of linear regression models [*Kelly and Krzysztofowicz, 1997*]:

- Condition ① can be met by showing that the conditional mean is linear.
- Conditions ② and ④ can be met by showing that residuals  $\mathbf{s} - \hat{\mathbf{s}}$  have a normal distribution with a zero mean and a finite variance (to assess the homoscedasticity of a variance).
- Condition ③ can be met by assessing the independence of residuals  $\mathbf{s} - \hat{\mathbf{s}}$  and  $\mathbf{x}_i, i = 1, \dots, n$ .
- Condition ⑥ can be met by showing that each random variable is normally distributed.

## REFERENCES

- Abbott, M. B. and F. Ionescu (1966). "On the Numerical Computation of Nearly Horizontal Flows." J. Hydraulic Res. **5**(2): 97-117.
- Abramowitz, M. and I. A. Stegun (1972). Handbook of Mathematical Functions. Dover, Mineola, New York.
- Adomian, G. (1994). Solving frontier problems in physics-The decomposition method. Dordrecht, The Netherlands, Kluwer Academics.
- Amein, M. (1966). "Streamflow Routing on Computer by Characteristics." Water Resour. Res. **2**(1): 123-130.
- Amein, M. and C. S. Fang (1970). "Implicit Flood Routing in Natural Channels." Journal of Hydraulic Engineering **96**(HY12): 2481-2500.
- Anderson, M. G. and T. P. Burt (1985). Hydrological Forecasting, John Wiley & Sons Ltd.
- Barkau, R. L. (1982). Simulation of the July 1981 Flood Along the Salt River. Report for CE695BV. Ft. Collins, CO, Special Problems in Hydraulics, Department of Civil Engineering, Colorado State University.
- Becker, A. (1976). "Simulation of nonlinear flow systems by combining linear models." IAHS **116**: 135-142.
- Becker, A. and Z. Kundzewicz (1987). "Nonlinear Flood Routing With Multilinear Models." Water Resour. Res. **23**(6): 1043-1048.
- Bernstein, D. S. (2005). Matrix Mathematics: Theory, Facts, and Formulas with Application to Linear Systems Theory. Princeton, Princeton University Press.
- Bryson, A. E., Jr. and Y. C. Ho (1975). Applied Optimal Control. New York, Hemisphere.

- Camacho, L. A. and M. J. Lees (1999). "Multilinear discrete lag-cascade model for channel routing." Journal of Hydrology **226**(1-2): 30-47.
- Cardova, J. and I. Rodriguez-Iturbe (1985). "On the Probabilistic Structure of Storm Surface Runoff." Water Resour. Res. **21**(5): 755-763.
- Chow, G. C. (1981). Econometric Analysis by Control Methods. New York, John Wiley.
- Chow, V. T. (1959). Open-channel hydraulics. New York, McGraw-Hill.
- Chow, V. T. (1964). Handbook of Applied Hydrology. New York, McGraw-Hill.
- Craya, A. (1952). The criterion for the possibility of roll-wave formation. Gravity Waves. Washington, D.C., National Bureau of Standards. **Circular No. 521**: 141-151.
- Cunge, J. A. (1969). "On the subject of a flood propagation computation method (Muskingum method)." J. Hydraulic Res. **7**(2): 205-230.
- Cunge, J. A., J. F.M. Holly and A. Verwey (1980). Practical Aspects of Computational River Hydraulics. London, Pitman Publishing Limited.
- Derusso, P. M., R. J. Roy, and Ch. M. Close (1967). State Variables for Engineers. New York, N.Y., Wiley, 608 pp.
- DeRusso, P. M., R. J. Roy and C. M. Close (1965). State variables for engineers. New York,, Wiley.
- Dooge, J. C. I. (1973). Linear theory of hydrologic systems. USDA Tech. Bull. . Washington, D.C., U.S. Department of Agriculture. **1468**.
- Dooge, J. C. I., W. G. Strupczewski and J. J. Napi?kowski (1982). "Hydrodynamic derivation of storage parameters of the Muskingum model." Journal of Hydrology **54**(4): 371-387.

- Fread, D. L. (1973a). "Effects of Time Step Size in Implicit Dynamic Routing." Water Resour. Bull. **9**(2): 338-351.
- Fread, D. L. (1974). Numerical Properties of Implicit Four-point Finite Difference Equations of Unsteady Flow. NOAA Tech. Memo NWS HYDRO-18. Silver Spring, Maryland, U.S. Department of Commerce, National Weather Service.
- Fread, D. L. (1976). Theoretical Development of an Implicit Dynamic Routing Model. Silver Spring, MD, Hydrologic Research Laboratory, Office of Hydrology, U.S. Department of Commerce, NOAA, NWS: 13-17.
- Fread, D. L. (1980). Capabilities of NWS model to forecast flash floods caused by dam failures. Proc. of 2nd Conf. on Flash Floods. Atlanta, Georgia, American Met. Soc.: 171-178.
- Fread, D. L. (1984). DAMBRK: The NWS dam-break flood forecasting model. Silver Spring, Md, Office of Hydrology, National Weather Service, National Oceanic and Atmospheric Administration, U.S. Department of Commerce.
- Fread, D. L. (April 1978). National Weather Service operational dynamics wave model. Silver Spring, Md., NOAA. **W23**.
- Fread, D. L. and J. M. Lewis (1988). FLDWAV: A Generalized Flood Routing Model. Proceedings of the 1988 National Conference on Hydraulic Engineering. S. R. Abt and J. Gessler. Colorado Springs, CO, ASCE: 668-73.
- Garbrecht, J. and G. Brunner (1991). "Hydrologic Channel-Flow Routing for Compound Sections." Journal of Hydraulic Engineering **117**(5): 629-642.
- Garen, D. C. and S. J. Burges (1981). "Approximate Error Bounds For Simulated Hydrographs." Journal of Hydraulic Engineering **107**(HY11): 1519-1534.
- Georgakakos, A. (1989). "Extended Linear Quadratic Gaussian Control: Further Extensions." Water Resour. Res. **25**(2): 191-201.

- Georgakakos, A., K. Georgakakos and E. Baltas (1990). "A State-Space Model for Hydrologic River Routing " Water Resour. Res. **26**(5): 827-838.
- Georgakakos, A. and D. Marks (1987). "A New Method for the Real-Time Operation of Reservoir Systems." Water Resour. Res. **23**(7): 1376-1390.
- Georgakakos, K., and R. Bras (1982). "Real-Time, Statistically Linearized, Adaptive Flood Routing." Water Resour. Res. **18**(3): 513-524.
- Goldberg, D. E. and E. B. Wylie (1983). "Characteristics Method Using Time-Line Interpolations." Journal of Hydraulic Engineering **109**(5): 670-83.
- Guang-Te, W. and V. P. Singh (1992). "Muskingum method with variable parameters for flood routing in channels." Journal of Hydrology **134**(1-4): 57-76.
- Hayami, S. (1951). On the propagation of flood waves. Bulletin of the Disaster Prevention Research Institute. Kyoto, Japan, Disaster Prevention Research Institute. **1**(1): 1-16.
- Hayter, A. J. (2002). Probability and Statistics for Engineers and Scientists 2nd Edition, DUXBURY.
- Henderson, F. M. (1966). "Open Channel Flow". New York, McMillan Publishing Co., Inc.
- Hoos, A., A. Koussis and G. Beale (1989). "A Channel Dynamics Model for Real-Time Flood Forecasting." Water Resour. Res. **25**(4): 691-705.
- Hosking, J. R. M. and R. T. Clarke (1990). "Rainfall-Runoff Relations Derived From the Probability Theory of Storage." Water Resour. Res. **26**(7): 1455-1463.
- Hromadka, T. V. and R. H. McCuen (1989). "Evaluation of Rainfall-Runoff Performance Using the Stochastic Integral Equation Method." Stochastic Hydrology and Hydraulics **3**(3): 217-226.

- Hromadka, T. V. I. and R. J. Whitley (1989). Stochastic Integral Equations and Rainfall-Runoff Models. Berlin, Springer-Verlag.
- Hromadka, T. V. I. and R. J. Whitley (1994). "A Stochastic Integral Equation Analog of Rainfall-Runoff Processes for Evaluating Modeling Uncertainty." Stochastic Hydrology and Hydraulics **8**(4): 259-268.
- Hydromet (1992). Hydromet Survey Project (Hydromet). Hydrometeorological Survey of the Catchments of Lake Victoria, Kyoga and Albert. Hydrological Summaries For Sub-Catchments of the Project Area. Entebbe, Uganda, Hydromet Survey Project.
- Kalinin, G. P. and P. I. Milyukov (1957). On the computation of unsteady flow in open channels. Leningrad, USSR, Meteorologiya Gidrologiya Zhurnal **10**: 10-18.
- Kalman, R. E. (1960). "A new approach to linear filtering and prediction problems." J. Basic Eng. **82D**: 35-45.
- Keefer, T. N. and R. S. McQuivey (1974). "Multiple linearization flow routing model." Journal of Hydraulic Engineering **100**(HY7): 1031-1046.
- Kelly, K. and R. Krzysztofowicz (1997). "A bivariate meta-Gaussian density for use in hydrology." Stochastic Hydrology and Hydraulics **11**(1): 17-31.
- Kelly, K. S. and R. Krzysztofowicz (1994). "Probability distributions for flood warning systems." Water Resour. Res. **30**(4): 1145-1152.
- Kelly, K. S. and R. Krzysztofowicz (2000). "Precipitation uncertainty processor for probabilistic river stage forecasting." Water Resour. Res. **36**(9): 2643-2653.
- Kirk, D. E. (1970). Optimal Control Theory. Englewood Cliffs, New Jersey, Prentice-Hall.
- Krzysztofowicz, R. (1987). "Markovian Forecast Processes." Journal of the American Statistical Association **82**(397): 31-37.

- Krzysztofowicz, R. (1999). "Bayesian Theory of Probabilistic Forecasting Via Deterministic Hydrologic Model." Water Resour. Res. **35**(9): 2739-2750.
- Krzysztofowicz, R. (2001). "Integrator of uncertainties for probabilistic river stage forecasting: precipitation-dependent model." Journal of Hydrology **249**(1-4): 69-85.
- Krzysztofowicz, R. (2002). "Bayesian system for probabilistic river stage forecasting." Journal of Hydrology **268**(1-4): 16-40.
- Krzysztofowicz, R. and H. D. Herr (2001). "Hydrologic uncertainty processor for probabilistic river stage forecasting: precipitation-dependent model." Journal of Hydrology **249**(1-4): 46-68.
- Krzysztofowicz, R. and K. S. Kelly (2000). "Hydrologic uncertainty processor for probabilistic river stage forecasting." Water Resources Research **36**(11): 3265-3277.
- Krzysztofowicz, R. and C. J. Maranzano (2004). "Hydrologic uncertainty processor for probabilistic stage transition forecasting." Journal of Hydrology **293**(1-4): 57-73.
- Krzysztofowicz, R. and C. J. Maranzano (2004a). "Hydrologic uncertainty processor for probabilistic stage transition forecasting." Journal of Hydrology **293**(1-4): 57-73.
- Krzysztofowicz, R. and C. J. Maranzano (2004b). "Bayesian system for probabilistic stage transition forecasting." Journal of Hydrology **299**(1-2): 15-44.
- Kuczera, G. (1988). "On the validity of first-order prediction limits for conceptual hydrologic models." Journal of Hydrology **103**(3-4): 229-247.
- Kundzewicz, Z. W. (1984). "Multilinear flood routing." Acta, Geophys. Pol. **32**: 419-445.
- Lardet, P. and C. Obled (1994). "Real-time flood forecasting using a stochastic rainfall generator." Journal of Hydrology **162**(3-4): 391-408.
- Lewis, F. L. and V. L. Syrmos (1995). Optimal control. New York, J. Wiley.

- Lighthill, M. J. and G. B. Whitham (1955). "On kinematic waves I: Flood movement in long rivers." Proc., Royal Society(A229): 281-316.
- Lin, G.-F. and Y.-M. Wang (1996). "General stochastic instantaneous unit hydrograph." Journal of Hydrology **182**(1-4): 227-238.
- Makinde-Odusola, B. A. and M. A. Mariño (1989). "Optimal control of groundwater by the feedback method of control." Water Resour. Res. **25**(6): 1341-1352.
- McCarthy, G. T. (1938). The unit hydrograph and flood routing. Paper presented at Conf. of the North Atlantic Div. of US Corps of Engineers. New London, Connecticut.
- Melching, C., B. Yen and H. W. Jr. (1990). "A Reliability Estimation in Modeling Watershed Runoff With Uncertainties." Water Resour. Res. **26**(10): 2275-2286.
- Miller, W. A. and J. A. Cunge (1975). Simplified Equations of Unsteady Flow. In Unsteady Flow in Open Channels. K. Mahmood and V. Yevjevich. Fort Collins, CO, Water Resources Publications. **vol. 1**: 89-182.
- Mills, W. C. (1980). Coupling Stochastic and Deterministic Hydrologic Models for Decision Making. Reports on Natural Resource Systems. Tucson, Arizona, University of Arizona. **No. 36**.
- Moran, P. A. P. (1969). "Statistical Inference with Bivariate Gamma Distributions." Biometrika **56**(3): 627-634.
- Muzik, I. (1974). "State variable model of overland flow." Journal of Hydrology **22**(3-4): 347-364.
- Nash, J. E. (1960). "A unit hydrograph study with particular reference to British catchments." Proc. Inst. Civ. Eng. **17**: 249-282.
- O'Connor, K. M. (1976). "A discrete linear cascade model for hydrology." Journal of Hydrology **29**: 203-242.

- O'Donnell, T. (1985). "A direct three-parameter Muskingum procedure incorporating lateral flow." Hydrological Sciences Journal **30**(4): 479-96.
- Ogata, K. (1967). State Space Analysis of Control Systems. Englewood Cliffs, N.J., Prentice-Hall, 608 pp.
- Ogata, K. (1970). Modern Control Engineering. Englewood Cliffs, N.J., Prentice-Hall, 836 pp.
- Papoulis, A. (1991). Probability, Random Variables, and Stochastic Processes, McGraw-Hill, Inc.
- Perumal, M. (1992). "Multilinear muskingum flood routing method." Journal of Hydrology **133**(3-4): 259-272.
- Perumal, M. (1994). "Multilinear discrete cascade model for channel routing." Journal of Hydrology **158**(1-2): 135-150.
- Ponce, V. M. (1989). Engineering Hydrology. Englewood Cliffs, NJ, Prentice-Hall.
- Ponce, V. M. (1991). "New perspective on the Vedernikov Number." Water Resour. Res. **27**(7): 1777-1779.
- Ponce, V. M. and P. V. Changanti (1994). "Variable-parameter Muskingum-Cunge method revisited." Journal of Hydrology **162**(3-4): 433-439.
- Ponce, V. M., Y. H. Chen and D. B. Simons (1979). "Unconditional Stability in Convection Computations." Journal of Hydraulic Engineering **105**(HY9): 1079-86.
- Ponce, V. M., R. M. Li and D. B. Simons (1978). "Applicability of Kinematic and Diffusion Models." Journal of Hydraulic Engineering **104**(HY3): 353-360.
- Ponce, V. M. and A. Lugo (2001). "Modeling Looped Ratings in Muskingum-Cunge Routing." Journal of Hydrologic Engineering **6**(2): 119-124.

- Ponce, V. M. and V. Yevjevich (1978). "Muskingum-Cunge method with variable parameters." Journal of Hydraulic Division, ASCE **104**(HY12): 1663-1667.
- Price, R. K. (2009). "An optimized routing model for flood forecasting." Water Resour. Res. **45**(2): W02426.
- Roache, P. (1972). Computational Fluid Dynamics. New Mexico: Albuquerque, Hermosa Publisher.
- Sarino and S. E. Serrano (1990). "Development of the Instantaneous Unit Hydrograph Using Stochastic Differential Equations." Stochastic Hydrology and Hydraulics **4**(2): 151-160.
- Schaffranek, R. W., R. A. Baltzer and D. E. Goldberg (1981). A Model for Simulation of Flow in Singular and Interconnected Channels. G. P. Office. Washington, DC, Techniques of Water Resources Investigations of the U.S. Geological Survey. **Chapter C3**
- Schwarz, R. J. and B. Friedland (1965). Linear systems. New York, McGraw-Hill.
- Serrano, S. E. (2006). "Development and Verification of an Analytical Solution for Forecasting Nonlinear Kinematic Flood Waves." Journal of Hydrologic Engineering **11**(4): 347-353.
- Shahin, M. (1985). Hydrology of the Nile Basin. Developments in Water Science, 21, 575 pp, Amsterdam/Oxford/New York/Tokyo:Elsevier.
- Singh, V. P. and R. C. McCann (1980). "Some notes on Muskingum method of flood routing." Journal of Hydrology **48**(3): 343-361.
- Singh, V. P., G. T. Wang and D. D. Adrian (1997). "Flood routing based on diffusion wave equation using mixing cell method." Hydrological Processes **11**: 1881-1894.
- SMEC (1977). Hydrologic Model of the Upper Nile Basin. WMO, Geneva, Snowy Mountain Engineering Corporation.

- Smith, R. H. (1978). Development of a Flood Routing Model for Small Meandering Rivers. Department of Civil Engineering. MO, University of Missouri at Rolla. **Ph.D.**
- Stephenson, D. (1979). "Direct optimization of Muskingum routing coefficients." Journal of Hydrology **67**: 1-11.
- Stoker, J. J. (1957). Water Waves. New York, Interscience Pub.
- Strelkoff, T. (1970). "Solution of Saint-Venant Equations." Journal of Hydraulic Engineering **96**(HY1): 223-252.
- Sturm, T. W. (2001). Open Channel Hydraulics, McGraw-Hill.
- Sutcliffe, J. V. and Y. P. Parks (1999). The Hydrology of the Nile. IAHS Press, Wallingford, UK, 180 pp.
- U.S. Army Corps of Engineers (1995). One-dimensional Unsteady Flow Through a Full Network of Open Channels. UNET User's Manual. Davis, CA, Hydrologic Engineering Center.
- Vedernikov, V. V. (1945). "Conditions at the front of a translation wave disturbing a steady motion of a real fluid." U.S.S.R. Acad. Of Sci. Comptes Rendus (Doklady) **48**(4): 239-242.
- Vedernikov, V. V. (1946). "Characteristic features of a liquid flow in an open channel." U.S.S.R. Acad. Of Sci. Comptes Rendus (Doklady) **52**(3): 207-210.
- Wang, G. T., S. Chen and J. Boll (2003). "A semianalytical solution of the Saint-Venant equations for channel flood routing." Water Resour. Res. **39**(4): 1076.
- Wasimi, S. and P. Kitanidis (1983). "Real-Time Forecasting and Daily Operation of a Multireservoir System During Floods by Linear Quadratic Gaussian Control." Water Resour. Res. **19**(6): 1511-1522.

Weinmann, P. E. and E. M. Laurenson (1979). "Approximate flood routing methods: A review." Journal of Hydraulic Engineering **105**(12): 1521-1536.

Zadeh, L. A. and C. A. Desoer (1963). Linear system theory; the state space approach. New York, McGraw-Hill.